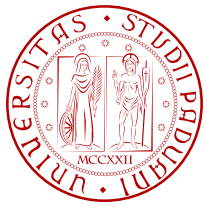

Università degli Studi di Padova

Dipartimento di Fisica e Astronomia "G. GALILEI"

SCUOLA DI DOTTORATO DI RICERCA IN ASTRONOMIA

CICLO XXV

SUPERMASSIVE BLACK HOLES, STAR CLUSTERS, AND STELLAR DISCS IN GALACTIC NUCLEI

Direttore della Scuola: Prof. Giampaolo Piotto
Supervisori: Prof. Enrico Maria Corsini
Dott.ssa Elena Dalla Bontà

Dottoranda: Elisa Portaluri

Riassunto

Questa tesi è dedicata allo studio della struttura delle regioni centrali delle galassie. Attraverso metodi differenti si è proceduto a caratterizzare alcuni aspetti degli oggetti centrali massicci (CMO) che risiedono nei nuclei galattici investigando, ad esempio, i loro possibili scenari di formazione, le proprietà delle loro popolazioni stellari le relazioni che li legano all'intera galassia.

Nel primo capitolo si è evidenziata l'importanza di capire le proprietà fisiche dei CMO riassumendo i risultati degli studi precedenti in cui si discutono gli scenari di formazione, le relazioni di scala e le proprietà dei buchi neri supermassicci (SBH), degli ammassi stellari nucleari (NSC) e dei dischi stellari nucleari (NSD) che costituiscono gli oggetti massicci centrali conosciuti fino ad oggi. La massa dei SBH è compresa nell'intervallo tra 10^6 e 10^{10} $M_\odot$ e si può misurare in diversi modi. Si pensa che essi risiedano in tutte le galassie, alle quali sono legate mediante una serie di relazioni. Per questo motivo è plausibile che abbiano formazione ed evoluzione comuni. Tuttavia gli scenari proposti rimangono incerti. I NSC sono, invece, oggetti massicci ($M_{\rm NSC}\sim 10^5 - 10^8$ $M_\odot$), molto compatti ($r_{\rm e} \sim 5$ pc) e molto brillanti ($-14 < M_I < -10$). Essi possono essere costituiti da popolazioni stellari multiple, ossia possono avere una componente vecchia di forma sferoidale ed una componente giovane a forma di disco o ad anello. La loro massa e la loro luminosità sono correlate a varie proprietà della galassia che li ospita. Lo scenario di formazione più plausibile sembra essere quello in cui il gas migra verso il centro della galassia, dove ha luogo la formazione stellare. Accanto a questi processi dissipativi, la loro massa può aumentare tramite eventi di fusione che coinvolgono ammassi globulari. I NSD, invece, sono dischi stellari piccoli ($h \sim 10 - 50$ pc) e luminosi ($\mu^0_{0,V} \sim 16 - 19$ mag arcsec^{-2}). Essi contribuiscono al massimo alla metà della luminosità del nucleo e sono sistemi fragili che non sopravvivono ad eventi di fusione galattica. La popolazione stellare, di cui sono costituiti, è stata studiata in dettaglio solo

per pochi oggetti e gli esiti hanno mostrato risultati non omogenei. La loro brillanza superficiale centrale è legata al raggio di scala, come mostrano anche i dischi galattici delle spirali o delle galassie lenticolari, o i dischi immersi nelle galassie ellittiche. I NSD sembrano essersi formati dal gas che si è accumulato nel nucleo dalla galassia e che ha cominciato a formare stelle. Tale gas può avere avuto origine interna alla galassia, provenendo da regioni periferiche, oppure può essere stato catturato dall'esterno a seguito di eventi di fusione. SBH, NSC e NSD possono risiedere nello stesso nucleo galattico, che porta a chiedersi se essi siano manifestazioni di uno stesso oggetto e condividano lo stesso scenario di formazione.

Nel secondo capitolo della tesi si sono studiate la formazione e le proprietà dei NSD analizzando una serie di simulazioni che studia eventi di fusione non dissipativi di ammassi stellari nei nuclei galattici. Un ammasso stellare massiccio e un disco compatto nucleare vengono fatti accrescere dalla fusione con una decina di ammassi stellari, i quali hanno dimensioni e masse comparabili a quelle degli ammassi globulari osservati nella Via Lattea. In questo modo, le simulazioni riescono a riprodurre strutture che si osservano nei nuclei galattici. Sono, poi, state analizzate le immagini e le mappe cinematiche ricavate come se fossero realmente state osservate alla distanza dell'Ammasso della Vergine e come se avessero caratteristiche simili al nucleo di NGC 4244. Mediante il metodo di Scorza & Bender, si è proceduto alla decomposizione fotometrica delle immagini per ottenere i parametri strutturali degli eventuali NSD. Le simulazioni riguardanti l'accrescimento di ammassi globulari in un disco nucleare pre-esistente hanno mostrato la presenza di un NSD le cui proprietà cinematiche e fotometriche sono in accordo con quelle misurate per i NSD di galassie reali. Ciò è indice del fatto che i NSD possano essere frutto di eventi di fusione che coinvolgono ammassi stellari nei nuclei galattici. Le simulazioni realizzate a partire dalla struttura sferoidale, invece, mostrano un nucleo allungato che presenta caratteristiche dissimili da quelle dei NSD. Ciò evidenzia l'importanza di utilizzare il metodo di Scorza & Bender per verificare la presenza di NSD.

Nel terzo capitolo della tesi si è proceduto ad analizzare la struttura e le proprietà della popolazione stellare del nucleo galattico di NGC 1023, una galassia interagente di tipo SB0. A tale scopo è stata condotta un'analisi fotometrica accurata delle immagini d'archivio ottenute con l'*Hubble Space Telescope* (*HST*) nonché uno studio spettroscopico dettagliato mediante spettri a campo integrale ottenuti con telescopi da terra. Le stelle del NSD sono significativamente più giovani e più metalliche rispetto a quelle dello sferoide. Ciò supporta uno scenario in cui il NSD è il risultato della formazione stellare avvenuta con il gas che è stato trasportato nel centro della galassia. Tale gas può avere avuto origine interna o esterna: può, infatti, provenire dal disco galattico di NGC 1023 o

dalla galassia satellite NGC 1023A. Le caratteristiche del NSD di NGC 1023 escludono, dunque, un'origine non dissipativa, quale può essere la fusione di ammassi stellari nel nucleo.

Il quarto capitolo della tesi è dedicato all'analisi dinamica della galassia di tipo lenticolare NGC 383, che dista 63.4 Mpc, allo scopo di misurare le masse dei CMO che sono presenti nel suo nucleo. La dispersione di velocità centrale di NGC 383 è consistenze con una massa del SBH di $M_\bullet = 5.8 \times 10^8$ $M_\odot$. L'analisi è stata condotta utilizzando le immagini d'archivio ottenute con la camera *Wide Field and Planetary Camera 2* e grazie agli spettri ottenuti con lo spettrografo *Space Telescope Imaging Spectrograph* di *HST*. Tali dati hanno fornito informazioni dettagliate sulla struttura, il profilo di massa della componente stellare, la profondità ottica delle regioni dominate dalla polvere e la distribuzione spaziale e cinematica del gas ionizzato presente nelle regioni centrali della galassia. Per riprodurre il profilo cinematico che è stato derivato dalla riga di emissione [N II]λ6583 lungo tre aperture parallele all'asse maggiore della galassia e di cui una passante per il centro, sono stati costruiti modelli dinamici che hanno incluso i profili di massa della componente stellare, del NSC e del SBH. Quando si è considerato un unico CMO, si è ottenuta una massa del SBH pari a $M_\bullet = 8.5^{+1.8}_{-1.3} \times 10^8$ $M_\odot$. Quando, invece, si è tenuto conto anche della presenza del NSC, si sono ricavate masse pari a $M_\bullet = 6.0^{+1.8}_{-1.2} \times 10^8$ $M_\odot$ e $M_{\rm NSC} = 8.9^{+5.0}_{-3.9} \times 10^7$ $M_\odot$ per il SBH e il NSC, rispettivamente. In entrambi i casi le masse dei CMO ottenute sono in accordo con le relazioni di scala che le legano ad alcune proprietà dell'intera galassia. Questi risultati costituiscono un importante passo in avanti nel contesto della caratterizzazione dei CMO e provano che i SBH possono coesistere con i NSC in alcune galassie.

Le principali conclusioni della tesi possono, quindi, essere riassunte in tre punti: 1) I NSD possono formarsi anche attraverso eventi di fusione, ma una certa quantità di gas è comunque necessaria; 2) NGC 1023 ospita un NSD che ha una popolazione giovane e metallica, frutto di una formazione dovuta a processi dissipativi; 3) un SBH e un NSC coesistono nel nucleo di NGC 383 e seguono relazioni diverse se confrontate con le proprietà della galassia che li ospita. Per la prima volta le masse di questi oggetti sono state misurate in maniera simultanea mediante l'utilizzo di modelli dinamici.

Abstract

In this thesis we investigated the structures of the central regions of galaxies. This was done by characterising some aspects of the central massive objects (CMOs) found to live in the galactic nuclei, such as studying the possible formation scenarios, stellar properties and scaling relations using a variety of methods.

In Chapter 1 we highlighted the importance of understanding the physical properties of CMOs in galaxies by exploring their possible connection with the host galaxies. We reviewed the previous works on the properties, formations scenarios, and scaling relations of supermassive black holes (SBHs), nuclear star clusters (NSCs), and nuclear stellar discs (NSDs) which reside in galactic nuclei. SBHs are believed to be the cause of the past or present activity of the galaxies. The masses of the SBHs range between 10^6 and 10^{10} $M_\odot$ and can be measured with several methods. SBHs are found to correlate with several properties of their host galaxy and their formation is still unclear. NSCs are commonly found in the centres of both elliptical and disc galaxies. They are very massive ($M_{\rm NSC}\sim 10^5 - 10^8$ $M_\odot$), very compact ($r_{\rm e} \sim 5$ pc), and very bright ($-14 < M_I < -10$). They can have multiple stellar populations, possessing both an old spheroidal component and a younger elongated disc or ring component. The mass of NSCs tightly correlates with the total mass of the galaxy, but several other correlations have been proposed to link the properties of the NSCs with those of the host galaxy. A combined scenario where star formation occurs in the centre of galaxies after dissipation processes and mass accretes via the mergers of globular clusters seems the more plausible way to form NSCs. NSDs are small ($h \sim 10 - 50$ pc) and bright ($\mu^0_{0,V} \sim 16 - 19$ mag arcsec^{-2}) discs. They never dominate the light distribution of the galactic nuclei, and locally contribute at most half the galaxy surface brightness. They are fragile systems

and do not survive a major merger. Their stellar population has been studied in details in only a few objects, showing a variety of phenomena. NSDs follow the same relation between the central face-on surface-brightness and the scalelength as the main discs of lenticular and spiral galaxies and embedded discs of early-type galaxies. No other relation was found with the properties of the host galaxy. The external capture or the secular infall of gas into the centre where it accumulates, dissipates and forms stars are the most studied scenarios to form NSDs. SBHs, NSCs, and NSDs have been observed to coexist in some galaxies, rising the question whether they are incarnations of the same object and share a common formation scenario.

Then in Chapter 2 we investigated the formation and properties of NSDs by looking for their presence in a set of $N-$body simulations studying the dissipationless merging of multiple star clusters in galactic nuclei. A few tens of star clusters with sizes and masses comparable to those of globular clusters observed in the Milky Way are accreted onto a pre-existing nuclear stellar component: either a massive super star cluster or a rapidly rotating, compact disc with a scalelength of a few parsecs, mimicking the variety of observed nuclear structures. Images and kinematic maps of the simulation time-steps were then built and analysed as if they were real and at the distance of the Virgo cluster. We used the Scorza-Bender method to search for the presence of disc structures via photometric decomposition. In one case the merger remnant had all the observed photometric and kinematic properties of NSDs observed in real galaxies. This shows that current observations are consistent with most of the NSD mass being assembled from the migration and accretion of star clusters into the galactic centre. In the other simulation instead, we detected an elongated structure from the unsharp masked image, that does not develop the photometric or kinematic signature of an NSD. Thus, in the context of searches for a disc structure, the Scorza-Bender method is a robust and necessary tool.

In Chapter 3 we investigated the structure and properties of the stellar population of the nuclear regions of the interacting SB0 galaxy NGC 1023 through a detailed analysis of archival *Hubble Space Telescope* (*HST*) imaging and ground-based integral-field spectroscopy. The stars of the nuclear disc are remarkably younger and more metal-rich with respect to the host bulge. These findings support a scenario in which the nuclear disc is the end result of star formation in gas piled up in the galaxy centre. The gas can be of either internal or external origin, i.e. from either the main disc of NGC 1023 or the nearby interacting satellite NGC 1023A. The dissipationless formation from already formed stars through the migration and accretion of star clusters into the galactic centre is rejected.

In Chapter 4 we presented a dynamical analysis aimed at constraining the

mass of the CMOs in the lenticular galaxy NGC 383 at a distance of 63.4 Mpc. The central stellar velocity dispersion is consistent with a putative SBH with a mass of $M_\bullet = 5.8 \times 10^8$ M$_\odot$. We presented archival *HST* imaging and spectroscopic observations obtained with the *Wide Field and Planetary Camera 2* mounting the F814W filter and the *Space Telescope Imaging Spectrograph* using the G570M grism, respectively. The data provide detailed information on the structure and mass profile of the stellar component, the dust optical depth, and the spatial distribution and kinematics of the ionised gas within the innermost region of the galaxy. Dynamical models, which account for the observed stellar mass profile and include the contribution of a NSC and a central SBH, were constructed to reproduce the kinematics derived from the [N II]λ6583 emission line along three slit positions crossing the nucleus and parallel to the galaxy major axis. A secure SBH detection with $M_\bullet = 8.5^{+1.8}_{-1.3} \times 10^8$ M$_\odot$ was obtained when a single CMO is considered. If we account for the presence of the NSC, then the masses of the SBH and NSC were $M_\bullet = 6.0^{+1.8}_{-1.2} \times 10^8$ M$_\odot$ and $M_{\rm NSC} = 8.9^{+5.0}_{-3.9} \times 10^7$ M$_\odot$, respectively. Both are consistent with the scaling relations linking the mass of CMOs with the properties of their host galaxy. These measurements prove that SBHs can coexist with NSCs and represent an important step forward in the characterisation of CMOs.

The main conclusions of this thesis can be summarised as follows: 1) NSDs can form via accretion events, but a certain amount of gas is necessary; 2) the young stellar population of the NSD of NGC 1023 suggests a formation via gas dissipation; 3) a SBH and a NSD coexist in NGC 383 and follow different scaling relations with the host galaxy. For the first time we were able to disentangle simultaneously the mass of both the CMOs using dynamical modelling.

Contents

Riassunto **i**

Abstract **v**

1 Introduction **1**

1.1 Studying the galactic nuclei 2

1.2 Supermassive black holes 4

1.2.1 Search and properties 5

1.2.2 Scaling relations 9

1.2.3 Formation 12

1.3 Nuclear star clusters 14

1.3.1 Search and properties 15

1.3.2 Scaling relations 17

1.3.3 Formation 19

1.4 Nuclear stellar discs 22

1.4.1 Search and properties 22

1.4.2 Scaling relations 23

1.4.3 Formation 24

1.5 Coexistence 28

1.5.1 Supermassive black holes and nuclear star clusters 28

1.5.2 Supermassive black holes and nuclear stellar discs 30

1.5.3 Nuclear star clusters and nuclear stellar discs 31

1.5.4 Supermassive black holes, nuclear star clusters, and nuclear stellar discs 32
1.6 Aim of the thesis 33

2 Nuclear stellar discs in simulations 39
2.1 Introduction 40
2.2 Simulations 42
2.2.1 Bulge model 43
2.2.2 Star cluster models 44
2.2.3 Numerical parameters 44
2.2.4 Properties of models A1 and A2 44
2.3 Pseudo surface photometry and stellar kinematics 49
2.3.1 Luminosity weighted images 49
2.3.2 Kinematic maps 53
2.4 Analysis 54
2.4.1 Detection of the nuclear stellar disc 54
2.4.2 Photometric decomposition 62
2.4.3 Estimate of expected total luminosity and mass of the nuclear stellar disc in model A2 78
2.4.4 The evolution of galaxy components 79
2.4.5 Two-dimensional photometric decomposition 80
2.4.6 Rotation parameter 84
2.5 Discussion 92
2.5.1 The $\mu_0 - h$ relation for nuclear stellar discs 93
2.5.2 The Tully-Fisher relation for nuclear stellar discs 94
2.5.3 Nuclear cluster discs and nuclear stellar discs 99
2.6 Conclusions 100

3 The young NSD in the SB0 galaxy NGC 1023 103
3.1 Introduction 103
3.2 Structural properties of the nuclear stellar disc 105
3.2.1 Broad-band imaging 105
3.2.2 Photometric model 107
3.3 Properties of the stellar populations of the NSD 112

3.3.1 Integral-field spectroscopy . . . 112
3.3.2 Stellar population model . . . 114
3.4 Discussion and conclusions . . . 116

4 The SBH and NSC of NGC 383 121
4.1 Introduction . . . 122
4.2 Galaxy selection . . . 124
4.2.1 Sample selection . . . 124
4.2.2 NGC 383 . . . 137
4.3 Spectroscopy: observations, data reduction, and analysis . . . 139
4.3.1 HST/STIS observations . . . 139
4.3.2 Data reduction . . . 140
4.3.3 Location of the slits . . . 141
4.3.4 Measurement of the emission lines . . . 144
4.3.5 Ionised-gas kinematics . . . 151
4.4 Imaging: observations, data reduction, and analysis . . . 153
4.4.1 HST/WFPC2 observations . . . 153
4.4.2 Data reduction . . . 154
4.4.3 Isophotal analysis of the surface brightness . . . 155
4.4.4 Correction for dust obscuration . . . 157
4.4.5 Deprojected stellar density without a nuclear star cluster 161
4.4.6 Photometric decomposition with a nuclear star cluster . 166
4.4.7 Deprojected stellar density with a NSC . . . 171
4.5 Dynamical modelling . . . 177
4.5.1 Ionised-gas dynamics . . . 177
4.5.2 Dynamical model with a single CMO . . . 182
4.5.3 Dynamical model with SBH and NSC . . . 184
4.6 Discussion and conclusions . . . 186

Bibliography 195

List of Tables

1.1 Stellar population properties of NSDs. 27

2.1 The merger models. 46
2.2 Models of star clusters used in the simulations. 46
2.3 Properties of models A1 and A2. 47
2.4 Selection of the *HST* instrument. 51
2.5 Photometric parameters of the nuclear stellar discs derived from the photometric decomposition of the mock images of model A2. 77
2.6 Photometric parameters of the nuclear stellar discs derived from the photometric decomposition of the mock images of model A1 for a flattened distribution of star cluster particles. 77
2.7 Lower and upper limits of the mass of the measured nuclear stellar discs of model A2. 79
2.8 Kinematic parameters of the nuclear elongated structure observed in models A1 and A2. 88
2.9 Photometric parameters of nuclear stellar discs for the $\mu^0_{0,V} - h$ diagram. 94
2.10 Photometric and kinematic parameters of nuclear stellar discs for the Tully-Fisher relation. 98

3.1 Photometric parameters of the nuclear stellar disc. 111
3.2 Line-strength indices and stellar population properties in the concentric circular rings centred on the galaxy nucleus. 113

4.1 Properties of the sample galaxies which are candidate to host a NSC. 127
4.2 Predicted SBH parameters and details of *STIS* observations for the sample galaxies candidates to host a nuclear star cluster. . . 133
4.3 Log of the *STIS* observations of NGC 383. 140
4.4 Properties of the spectral lines in the region of the G750M grism 150
4.5 Measured [N II] λ6583 kinematics of NGC 383. 150
4.6 Log of the *WFPC2* observations of NGC 383 155
4.7 Parameters of the decomposition of the surface-brightness distribution of NGC 383 obtained from MGE. 166
4.8 Parameters of the surface brightness of the NSC of NGC 383 obtained from the multi-Gaussian expansion. 177
4.9 Masses of coexisting SBHs and NSCs. 189

List of Figures

2.1 TIPSY screen-shots of the simulated galaxies for models A1 and A2 48
2.2 $B - I$ colour map of the simulated galaxies models A1 and A2 . 53
2.3 Graphic description of the assumption of the Scorza-Bender method 54
2.4 Line-of-sight stellar velocity and velocity dispersion maps for the simulated galaxy in model A1 55
2.5 Line-of-sight stellar velocity and velocity dispersion maps for the simulated galaxy in model A2 56
2.6 Mock *WFC3/UVIS* I-band and unsharp-masked images of model A1 58
2.7 Mock *WFC3/UVIS* I-band and unsharp-masked images of model A2 59
2.8 Graphic description of distortion on the isophotes parametrised by the Fourier coefficients 61
2.9 Isophotal parameters of the nuclear region of model A1 as a function of the isophotal semi-major axis 63
2.10 Isophotal parameters of the nuclear region of model A1 as a function of the isophotal semi-major axis, including the best fit of the nuclear stellar disc model 64
2.11 Analysis of the position angle for the model A1 after 10 star clusters accretions. 65

2.12 Analysis of the position angle for the model A1 after 20 and 27 star cluster accretions. 66
2.13 Analysis of the position angle for the model A2 after 10 and 30 star cluster accretions. 67
2.14 Analysis of the position angle for the model A2 after 50 star cluster accretions. 68
2.15 Impact of a disc component on the isophote shape and radial profiles in the ($L_{\rm D}/L_{\rm B}$, $\cos(i)$) plane. 69
2.16 Graphic description of the assumption of the Scorza-Bender method 70
2.17 χ^2 distribution of the photometric decomposition of the nuclear stellar disc for model A2 72
2.18 Surface-brightness distribution of the nuclear region of model A2 as a function of the isophotal semi-major axis, obtained varying the stellar population of the last star cluster 73
2.19 Isophotal parameters of the nuclear region of model A1 obtained with a galaxy inclination of $i = 90°$ as a function of the isophotal semi-major axis 75
2.20 Isophotal parameters of the nuclear region of model A1 as a function of the isophotal semi-major axis obtained flattening the distribution of the star cluster particles. 76
2.21 Isophotal parameters of the galaxy components of model A1 as a function of the isophotal semi-major axis 81
2.22 Isophotal parameters of the galaxy components of model A2 as a function of the isophotal semi-major axis 82
2.23 Mock images of the galaxy of models A1 and A2, as seen face on 83
2.24 Mock image of the galaxy of models A1 and A2 with a galaxy inclination of 75° 83
2.25 Mock image of the galaxy of models A1 and A2 with a galaxy inclination of 90° 84
2.26 Best fit of the surface-brightness distribution assuming Sérsic + exponential profiles 85

2.27 Two-dimensional best-fitting of model A2 obtained using a Sérsic and an exponential profile 86
2.28 Radial profiles of the velocity, velocity dispersion, and V/σ of models A1 and A2 considering all the galaxy components 89
2.29 Radial profiles of the velocity, velocity dispersion, and V/σ of models A1 and A2 excluding the contribution of the bulge 90
2.30 Radial profiles of the velocity, velocity dispersion, and V/σ of models A1 and A2 excluding the contributions of the bulge and of the nuclear stellar cluster 91
2.31 The face-on central surface brightness of discs as a function of scalelength 93
2.32 Total magnitude as a function of the rotation width for the nuclear stellar discs 97

3.1 Isophotal parameters of the nuclear region of NGC 1023 109
3.2 χ^2 distribution for the photometric decomposition of the archival multiband images of NGC 1023 110
3.3 Equivalent width of the Hβ and [MgFe]$'$ and $\langle$Fe$\rangle$ and Mgb line-strength indices 117
3.4 Radial profiles of metallicity, age, magnesium overabundance, and nuclear disc-to-total luminosity ratio 118

4.1 Comparison between $M_\bullet$ upper limits of Beifiori et al. (2009) and $M_\bullet - \sigma_c$ relation by Ferrarese & Ford (2005) 126
4.2 Comparison between the *STIS*/F28x50LP surface-brightness profiles of the sample galaxies which are candidate to host a NSC and the PSF luminosity profile. 129
4.2 – Continued. 130
4.2 – Continued. 131
4.2 – Continued. 132
4.2 – Continued. 133
4.3 Comparison between the *STIS*/F28x50LP surface brightness profile of NGC 383 which do not host a NSC and the PSF luminosity profile. 134

4.4 The radius of the sphere of influence of a SBH as a function of the velocity dispersion and distance of the host galaxy. The dashed lines correspond to the radii ranging from 0.001 to 1.0 arcsec. 134
4.5 Predicted values of the SBH mass $M_\bullet$ of the sample galaxies candidates to host a NSC as a function of the radius of their sphere of influence 135
4.6 Measured values of the half-light radius for galaxies of the sample of Böker et al. (2004) as a function of the galaxy distance. . . . 136
4.7 Unsharp masked images of the sample galaxies. 138
4.8 *HST STIS*/F28X50LP acquisition image of NGC 383 and nuclear spectrum 141
4.9 Location of the slits with respect to the *STIS*/F28x50LP acquisition images. 142
4.10 Surface-brightness profile of the *STIS*/G750M spectrum compared with the best-matching profile extracted from two adjacent columns of the acquisition image. 143
4.11 Measurement of the instrumental resolution for the adopted *STIS*/G750M set up 147
4.12 Some of continuum-subtracted G750M spectra of NGC 383 illustrating the multi Gaussian fitting procedure. 148
4.12 Continued. 149
4.13 Parametric model of the rotation curve of NGC 383 to derive the systemic velocity 153
4.14 [N II] λ6583 kinematics of NGC 383 154
4.15 *WFPC2*/F555W and *WFPC2*/F814W images of the galaxies . . 156
4.16 Normalised passbands including system response for *WFPC2*/F555W (on the left) and *WFPC2*/F814W (on the right) filters. 157
4.17 Isophotal parameters for NGC 383 160
4.18 *WFPC2*/F814W mosaic image of NGC 383 161
4.19 *WFPC2*/F814W image and contour plots of the PSF obtained with TINYTIM. 162
4.20 Surface-brightness profiles of the PSF along sectors. 163

4.21 Contour plots of the *WFPC2*/F814W images of NGC 383 after the convolution with the PSF. 164
4.22 Surface brightness profiles of NGC 383 along sectors. 165
4.23 Surface brightness profiles of NGC 383 as sum of Gaussians. . . 167
4.24 Deprojection steps for the stellar mass profile of NGC 383 . . . 168
4.25 One-dimensional photometric decomposition of NGC 383 170
4.26 Two-dimensional photometric decomposition of NGC 383 172
4.27 Images of the NSC of NGC 383 without the galaxy and of the galaxy without the NSC 173
4.28 Contour plots of the images of the NSC of NGC 383 and of the galaxy without the contribution of the NSC. 173
4.29 Surface brightness profiles along sectors of the model NSC of NGC 383 174
4.30 Surface brightness profiles along sectors of the galaxy without the NSC 175
4.31 Deprojection steps for the stellar mass profile of the NSC of NGC 383 and of the galaxy without the NSC. 176
4.32 Schematic representation of the velocity shift caused by the non-zero width of the slit. 180
4.33 Observed [N II] $\lambda\lambda 6548, 6583$ kinematics along with the best-fitting model for the SBH mass of NGC 383. 182
4.34 The locus of points of equal χ^2 values around the minimum χ^2_{min} value in the $M_\bullet$-$(M/L)_*$, $i-(M/L)_*$, i-$M_\bullet$ planes. 183
4.35 χ^2 distribution for NGC 383 as a function of $M_\bullet$, inclination, and $(M/L)_*$. 184
4.36 Observed [N II] $\lambda\lambda 6548, 6583$ kinematics along with the best-fit model for the SBH and NSC masses of NGC 383. 185
4.37 The locus of points of equal χ^2 values around the minimum χ^2_{min} value in the planes obtained combining $M_\bullet$, i, $(M/L)_*$, and $(M/L)_{\rm NSC}$. 187
4.38 χ^2 distribution for NGC 383 as a function of $M_\bullet$, inclination, and $(M/L)_*$. 188

4.39 $M_{\rm NSC}$ and $M_\bullet$ as a function of velocity dispersion σ for galaxies where CMOs coexist 190
4.40 I-band absolute magnitude of nuclear star clusters as a function of the absolute magnitude of the galaxies 191
4.41 $M_{\rm CMO}$ as a function of galaxy magnitude, stellar velocity dispersion, and dynamical mass. 192

Chapter 1

Introduction

Abstract

One of the key questions of the extragalactic research in the last years is how galaxies formed and evolved and how the physics of the central region of galaxies is related to these processes. Indeed, the nuclei of galaxies occupy a privileged position at the bottom of the galactic potential well and their morphology, dynamics, star formation, and chemical enrichment provide important insight into the evolutionary history of galaxies. In this picture, the study of central massive objects (CMOs), namely supermassive black holes (SBHs), nuclear star clusters (NSCs), and nuclear stellar discs (NSDs) is particularly relevant.

SBHs can be detected with high-resolution observations and are believed to be the cause of the past or present activity of the galaxies. The masses of the SBHs range between 10^6 and 10^{10} $M_\odot$ and can be measured with several methods. Stellar and/or gas dynamical models, spectro-astrometry, and analysis of water megamasers are adopted for quiescent galaxies. Reverberation mapping is used for active galaxies and allows to measure the mass of SBHs at high redshift. SBHs are found to correlate with several properties of their host galaxy. The formation of such kind of objects is still unclear. They can form from massive primordial stars, or due to the collapse or merging of massive objects, such as star clusters.

NSCs are commonly found in the centres of both elliptical and disc galaxies. They are very massive ($M_{\rm NSC}\sim 10^5 - 10^8$ $M_\odot$), very compact ($r_{\rm e} \sim 5$ pc), and very bright ($-14 < M_I < -10$). They can have multiple stellar populations, possessing both an old spheroidal component and a younger elongated disc

or ring component. The mass of NSCs tightly correlates with the total mass of the galaxy, but several other correlations have been proposed to link the properties of the NSCs with those of the host galaxy. A combined scenario where star formation occurs in the centre of galaxies after dissipation processes and accumulates mass via the mergers of globular clusters seems the more plausible way to form NSCs.

NSDs are small ($h \sim 10 - 50$ pc) and bright ($\mu^0_{0,V} \sim 16 - 19$ mag arcsec^{-2}) discs. They never dominate the light distribution of the galactic nuclei, and locally contribute at most half the galaxy surface brightness. They are fragile systems and do not survive a major merger. Therefore, their age could constrain the epoch of the last major merger of the host galaxy. About 20% of elliptical and spiral galaxies hosts a NSD. Their stellar population has been studied in details in only a few objects, showing a variety of phenomena. NSDs follow the same relation between the central face-on surface-brightness and the scalelength as the main discs of lenticular and spiral galaxies and embedded discs of early-type galaxies. No other relations were found with the properties of the host galaxy. The external capture or the secular infall of gas into the centre where it accumulates, dissipates and forms stars are the most studied scenarios to form NSDs.

SBHs, NSCs, and NSDs have been observed to coexist in some galaxies. The most investigated case is the coexistence of SBHs with NSCs, rising the question whether they are two incarnations of a same object and share a common formation scenario. In galaxies where a SBH coexists with a NSD, such a disc can be used to measure the SBH mass. NSCs can be also surrounded by central discs of stars, i.e. NSDs. The three types of CMOs are found to coexist only in a very few galaxies. But a full statistics is still missing and detailed studies of objects with SBHs, NSCs, and NSDs are required.

1.1 Studying the galactic nuclei

Understanding the formation and evolution of galaxies is a lively debated topic in astrophysics, because the advent of more powerful telescopes stimulated more detailed theories and numerical simulations to interpret new observations. The main issue concerns the role of two competing scenarios in shaping galaxies. Large protogalaxies formed early through a dissipational collapse according to the "monolithic" scenario, whereas galaxies are the result of successive mergers between small structures in the "hierarchical" merging process.

In this thesis we focus on the study of galactic nuclei to investigate how their properties are connected with those of the host galaxy. In fact, the nuclei

of galaxies occupy a privileged position at the bottom of the galactic potential well. They contain a small fraction of the total mass of the galaxies, but they harbour the highest density regions and thus the morphology, dynamics, star formation, and chemical enrichment of the nuclei provide important insight into the evolutionary history of galaxies themselves. Galactic nuclei record the history of the material, whether coming from neighbouring galactic regions or accreted through mergers, that has sunk to the dynamical centre over the lifetime of the parent system. In this sense, core and galaxy environment are linked through some scaling relations. Furthermore, dynamical timescales are shorter in the nuclei than elsewhere in the galaxy and therefore, they can provide vital constraints on galaxy formation processes. But, to date, no clear explanation exists for the variety of phenomena they show.

Active galactic nuclei (AGN) are named usually the energetic phenomena discovered in the centre of galaxies. It is commonly accepted that AGNs powered by gas fuelling a central SBH (Rees 1984). SBHs are relics of the past activity of galaxies (e.g., Soltan 1982; Shankar et al. 2004) and are expected to be ubiquitous in all the galactic nuclei as a fundamental component of both massive-quiescent and active galaxies (Kormendy & Ho 2013a). Although less common in low-mass systems, they have been also identified in some late-type spirals (e.g., Shields et al. 2008; Barth et al. 2009).

Not less important is the fact that the galactic centres may host massive stellar structures, such as dense NSCs, with typical $L_V \sim 10^6 - 10^7$ $L_\odot$ and effective radius of a few parsecs, and/or NSDs, with luminosities up to 10^7 $L_\odot$ and scalelengths of a few tens of parsecs.

Ferrarese et al. (2006a); Wehner & Harris (2006) first referred as central massive objects (CMO) the structural components, i. e., stellar objects or SBHs that reside in the centres of galaxies. It leads to the idea of a continuity between their properties. For example, Ferrarese et al. (2006a) found that the masses of CMOs tightly correlate with those of the host galaxies, being $M_{\rm CMO} \approx 0.002$ $M_{\rm gal}$. They also showed that galaxies with masses $M_{\rm gal} > 10^{10} M_\odot$ usually host a SBH, while NSCs preferentially reside in less massive galaxies. This suggests CMOs may form from the same processes, i.e., gravitational collapse of a massive clump of gas at the centre of the galaxy. But NSCs are more than the low-mass analogs of SBHs, and albeit they share some basic ingredients in the formation processes, whether there is a connection between them and how CMOs relate to host galaxies are still open questions. In fact, other authors stated that no correlations between the various incarnations of CMOs exist (e.g., Balcells et al. 2007; Leigh et al. 2012; Scott & Graham 2013) leading to different scenarios for explaining their formation or evolution with the host galaxy.

Due to its superb spatial resolution, the *Hubble Space Telescope (HST)* was used extensively to study the inner regions of nearby galaxies, until a spatial scale of ≈ 10 pc. *HST* images showed a number of variety of structural features in the centre of galaxies, such as bars, dust irregular features or regular dust discs. Numerous surveys were carried out to investigate their structure on scales of 10-100 pc over a wide range of morphological types. During the past two decades, SBHs were detected in about 90 nearby quiescent galaxies and in about 150 active galaxies of all morphological types, using gas and stellar dynamical methods. *HST* imaging proved that NSCs and NSDs populate the nuclei of a large fraction of galaxies, and galaxies with neither a SBH nor a NSC/NSD are the exception. Several studies were aimed at understanding some aspects of CMOs, revealing also that they can live together in the nucleus of both early- and late-type galaxies.

The details about searching techniques, properties, and formation scenarios of SBHs, NSCs, and NSDs are discussed in Section 1.2, Section 1.3, and Section 1.4, respectively. Section 1.5 describes the properties of galaxies where different CMOs coexist. The aim and summary of the thesis are presented in Section 1.6.

1.2 Supermassive black holes

Black holes exist in several mass ranges: stellar BHs having $4\ \mathrm{M}_\odot \lesssim M_\bullet \lesssim 25\ \mathrm{M}_\odot$ are the evolutionary end point of massive stars (Bailyn et al. 1998; Özel et al. 2010; Farr et al. 2011); intermediate mass BHs with a mass $100\ \mathrm{M}_\odot \lesssim M_\bullet \lesssim 10^5\ \mathrm{M}_\odot$ are suggested to reside at the centres of globular clusters (Gebhardt et al. 2000a, 2005; van der Marel & Anderson 2010; Vesperini & Trenti 2010), SBHs with $10^6\ \mathrm{M}_\odot \lesssim M_\bullet \lesssim 10^9\ \mathrm{M}_\odot$ (see Kormendy & Ho 2013a,b for a list) and ultra massive BHs, with $M_\bullet > 10^{10}\ \mathrm{M}_\odot$ (McConnell et al. 2011; van den Bosch et al. 2012) sit in the centre of galaxies.

The existence of SBHs was first proposed to explain the prodigious energy outputs of quasars, and SBHs are now understood to be the primary source of energy in all types of AGNs and therefore relics of the past activity of nowadays quiescent galaxies (e.g., Lynden-Bell 1969; Rees 1978, 1984; Soltan 1982; Shankar et al. 2004). In fact, although the fraction of local galaxies that are active is small, we now know that most if not all galaxies have SBHs in their nucleus.

The sphere of influence of a black hole is the region of space within which the gravitational potential of the SBH dominates over that of the surrounding

stars. It is given by

$$r_{\rm infl} = GM_\bullet/\sigma^2 \approx 11.2 \frac{(M_\bullet/10^8\ {\rm M}_\odot)}{(\sigma/200\ {\rm km\ s^{-1}})^2}\ {\rm pc} \tag{1.1}$$

where σ is the velocity dispersion of the stars of the inner part of the galaxy. For a $M_\bullet = 10^7$ $\mathrm{M}_\odot$, it is $r_{\rm infl} \approx 20$ pc, which corresponds to an angular size of about 0.2 arcsec at a distance of the Virgo cluster, showing the importance that high-resolution instruments have in the study of SBHs.

1.2.1 Search and properties

The strongest dynamical evidence for a SBH comes from the centre of our Galaxy. To go through the dust obscuration of the galactic centre, observations in the infrared, radio, and X-ray bands were made and revealed a non-stellar source of radiation in the place of Sgr A* (e.g., Balick & Brown 1974; Ekers et al. 1975; Eckart & Genzel 1997; Genzel et al. 1997, 2000; Ghez et al. 1998, 2000). It has a diameter of about 10 light minutes (Bower et al. 2004; Shen et al. 2005) and it is surrounded by a cluster of stars. Genzel & Townes (1987) emphasised the phenomena in the central few parsecs and discussed the emerging dynamical evidence for a central mass, mainly based at that time on observations of gas motions. Genzel et al. (1994) first measured the mass distribution of the central star cluster, using resolved stellar kinematic. But thanks to their vicinity, Schödel et al. (2002, 2003); Ghez et al. (2003, 2005, 2008) mapped the proper motions and radial velocities of about 40 stars orbiting in the central few arcseconds (1 arcsec = 0.04 pc) with the *New Technology Telescope (NTT)*, *Very Large Telescope (VLT)*, *Keck Telescope*, and *HST*. Alternatives to a SBH are ruled out by astrophysical constraints: brown dwarf stars would collide, merge, and become luminous, whereas clusters of white dwarf stars, neutron stars, or stellar black holes would evaporate too quickly (Maoz et al. 1995; Maoz 1998; Genzel et al. 1997, 2000). Therefore, the Galaxy is the most evident signature of the existence of a SBH with a mass of $4.31 \pm 0.06 \times 10^6$ $\mathrm{M}_\odot$ (Gillessen et al. 2009). The compact radio emission and X-ray flares produced by Sgr A* comes from gas accretion onto the black hole at a low rate.

Over the two past decades, thanks to the spectroscopic and photometric observations made with *HST* and 8-m class ground-based telescopes, SBHs have been detected in many galaxies. The *HST* contribution is predominant for the searching of BH masses in quiescent galaxies. Until 1997 the main spectrograph mounted on *HST* was the *Faint Object Spectrograph (FOS)* (M87: Harms et al. 1994, NGC 4261: Ferrarese et al. 1996, NGC 7052: van der Marel & van den

Bosch 1998), and then the *Space Telescope Imaging Spectrograph (STIS)* was installed. Ground-based SBH detections were performed in about ten nearby galaxies, (e.g., our Galaxy, M31, M32, and NGC 4258). Some of them were re-observed with *HST* and an agreement within a factor of 2 was found for the mass measurement.

The sphere of influence for $M_\bullet \gtrsim 10^8$ $M_\odot$ is resolved for galaxies at distance of few Mpc with the current facilities (Ferrarese & Ford 2005). Most of these galaxies are luminous and have total masses larger than 10^{12} $M_\odot$. Depending on the activity of the host galaxies, the measure of $M_\bullet$ is done using several techniques, each one shows benefits and difficulties. In quiescent galaxies, $M_\bullet$ is measured using gas (e.g., Barth et al. 2001; Coccato et al. 2006; Neumayer et al. 2007; Dalla Bontà et al. 2009) and stellar dynamical modelling (e.g., Gebhardt et al. 2003; Houghton et al. 2006; Nowak et al. 2009; Cappellari et al. 2009), whereas in active galaxies $M_\bullet$ is measured from the reverberation mapping (Peterson 2004) and water megamasers techniques (Cheung et al. 1969). Kormendy & Richstone (1995), Ferrarese & Ford (2005), Kormendy & Ho (2013a), and Kormendy & Ho (2013b) reviewed the BH search techniques and summarised both the ground-based and space-based detections.

Stellar dynamics is a good way to constrain the central potential of a galaxy because the stars are always present and their motion is always gravitational. The method is based on the knowledge of the line-of-sight velocity distribution (LOSVD), that gives information about the orbital structure of a galaxy. The current dynamical models of stellar kinematics are based on the orbit superposition method (Schwarzschild 1979). Stellar motions are obtained by measuring the absorption lines in high signal-to-noise (S/N) spectra of galaxies and unfortunately are subject to high degeneracy that can produce a range of possible $M_\bullet$ (Valluri et al. 2004). Moreover the assumptions made in the models can contribute to potential biases in the inferred black hole masses (McConnell et al. 2013). In addition, authors use different absorption lines, ranging from optical to NIR, and there is the possibility that the mass estimates are not consistent. For example, optical stellar kinematics gives larger velocity dispersions than NIR one due to dust extinction (Silge & Gebhardt 2003; Nowak et al. 2009). Stellar analysis is also demanding for observational and computational requirements (Kormendy 2004). For example, giant ellipticals are hard to observe because of their low surface brightnesses, and they are difficult to interpret because of their high velocity anisotropy (e.g., Kormendy & Richstone 1992; Crane et al. 1993; Ferrarese et al. 1994; Lauer et al. 1995; Rest et al. 2001). The study of SBHs in giant ellipticals and dusty spirals was improved thanks to the 8-m class NIR telescopes and adaptive optics (Davies et al. 2006; Houghton et al. 2006; Nowak et al. 2007, 2008, 2009; Cappellari et al. 2009; Krajnović

et al. 2009).

SBH detections in high luminosity ellipticals are also based on gas dynamics. Following the work of Gebhardt & Thomas (2009), recent studies on SBH dynamics focus on the need of including the contribution of the dark matter halo in modelling (Shen & Gebhardt 2010; McConnell et al. 2011; Gebhardt et al. 2011; Rusli et al. 2013). For example, due to the degeneracy of the mass components (i.e., SBH, dark and luminous matter), the $M_\bullet$ estimate of M87 increases by more than a factor of 2 when the dark halo is taken into account. Excluding the dark component forces the stellar mass to be higher. Since it is assumed to be constant at all radii, $M_\bullet$ decreases to compensate this effect. Rusli et al. (2013) measured $M_\bullet$ in 10 nearby early-type galaxies. They used three-integral axisymmetric orbit-superposition models with *Spectrograph for INtegral Field Observations in the Near Infrared (SINFONI)* observations and extensively discussed whether including or ignoring a dark matter halo with a cored logarithmic profile in the dynamical models. The measurements and analysis of gas kinematics are simpler than the stellar kinematic ones. Dust and gaseous discs with regular morphology suggest that the gas is rotating onto circular orbits in a thin disc, and its kinematics can be used to trace the gravitational potential of galaxy nuclei. Tran et al. (2001) found gaseous discs in 18% of early-type galaxies. All the galaxies hosting a dust disc show nuclear activity and in most of cases the discs are aligned with the major axis of the galaxy in which they reside. The origin of the nuclear dust could be internal from stellar mass loss or external from merging or interactions with other galaxies (Tran et al. 2001). The typical optical lines used to trace the gas kinematics are Hα λ6563 Å and [N II] $\lambda\lambda$6548, 6583 Å, while in the NIR they are Fe II $\lambda1.64\,\mu$m, [S II] $\lambda1.96\,\mu$m, and H_2 $\lambda2.12\,\mu$m. The analysis can be complicated by the possible presence of broad-line components that must be subtracted in order to derive the actual rotation curve of the gas disc. Once the regularity of the gas kinematics is observationally verified, one can model the ionised gas assuming that it is rotating in a Keplerian disc (e.g., Dalla Bontà et al. 2009). Similarly, Davis et al. (2013) modelled the effect of the SBH on the kinematics of molecular gas in the early-type galaxy NGC 4526 by fitting interferometric observations of CO emissions. This method can be extensively adopted with the millimetre and submillimetre interferometers (*Atacama Large Millimeter Array (ALMA*). The use of molecular gas as a kinematic tracer can dramatically increase the number of SBH mass measurements.

The spectro-astrometrical method to measure $M_\bullet$ was proposed by Bailyn et al. (1998) and revised by Gnerucci et al. (2010). Spectro-astrometry consists in measuring the photocentre of the emission lines at different wavelengths or in different velocity channels. Its capability in overcoming the spatial resolution

limit is illustrated by the fact that two spatially unresolved sources can be separated when extracting absorption or emission lines at different wavelengths from the light spatial profile. The difference in the centroid positions at these wavelengths gives the separation between the two sources even if this is much smaller than the spatial resolution. Therefore, such an approach offers the possibility of measuring the BH mass below the conventional spatial resolution limit. For example, Gnerucci et al. (2011) mapped the rotating gas disc of the nearby active galaxy Centaurus A, measuring a BH mass of $M_\bullet$=$9.6^{+2.5}_{-1.8} \times 10^7$ $M_\odot$ consistent with other studies based on kinematic analysis.

The analysis of kinematics of water megamasers hosted in some galaxies and observed with the *Very-Long-Baseline Interferometry (VLBI)* technique is another way to identify the presence of SBHs. Water masers are the result of collisional excitation of warm interstellar gas and dust (Neufeld & Melnick 1991) and were first detected by Cheung et al. (1969). But this method is limited mainly because water-maser discs are not common (Braatz et al. 1994, 1996) and can be observed if the plane of the rotating gas is aligned with the line of sight.

State-of-the-art instruments fail in resolving the SBH sphere of influence in galaxies farther than $cz \gtrsim 10000$ km s^{-1}. But, the reverberation mapping technique overcomes this lack in active galaxies. This method consist in measuring the time lag between the light curve of the continuum and broad-emission lines coming from the broad line region (BLR; Peterson & Bentz 2006). In fact, the central black hole and accretion disc are completely surrounded by an obscuring, geometrically thick molecular torus, that contains the BLR, extended from a few light days to several tens of light weeks from the centre (Antonucci 1993; Urry & Padovani 1995). According to the standard model, the BLR consists of many dense cold photoionised clouds (e.g., Ferland et al. 1992; Murray & Chiang 1997; Peterson 2004) and is spatially unresolved (Denney et al. 2010; Bentz et al. 2010; Grier et al. 2012). Instead, the narrow line region (NLR) is extended further out from a few to several thousands parsecs. The distance of the host galaxy does not matter because the BLR size is measured directly in physical units from the time delay. The redshift to which reverberation mapping measurements can be pushed is limited only by the fact that the AGN must be bright enough to be detected. This method is potentially the most powerful and allows authors to measure $M_\bullet$ at high redshift by studying the high luminosity of quasars and tracing material within only a few hundred Schwarzschild radii from the SBH. This is a factor 10^3 closer than radii mapped by stellar and gas dynamical studies using *HST* (Ferrarese & Ford 2005). However, there are some factors that affect this technique, such as the unknown geometry of the BLR, the need of long-time monitoring, and a not complete understanding of

the scaling relations.

The masses of SBHs measured with different methods are in agreement in a few galaxies. This is the case of the SBH of Centaurus A, which is measured within a factor ≈ 2 from the kinematics of stars (Silge et al. 2005; Cappellari et al. 2009), gas (Marconi et al. 2006; Neumayer et al. 2007) and spectro-astrometry (Gnerucci et al. 2011). NGC 4258 also represented a good test for the reliability of SBH mass estimators. Miyoshi et al. (1995) and Herrnstein (1999) used the *Very Long Baseline Array (VLBA)* to observe the water maser emission in a thin, warped, and nearly edge-on gas annulus in the centre of this galaxy. They determined that a central SBH with a mass $M_\bullet = (3.9 \pm 0.1) \times 10^7$ $M_\odot$ is needed to account for the observed velocity profile, proper motions, and accelerations. Siopis et al. (2009) estimated the mass of the SBH modelling the stellar dynamics of the galaxy. They obtained $M_\bullet = (3.3 \pm 0.2) \times 10^7$ $M_\odot$. Pastorini et al. (2007) estimated the mass range of the SBH using gas kinematics as $2.5 \times 10^7 - 2.6 \times 10^8 M_\odot$ at the 95% confidence level. On the contrary the $M_\bullet$ of IC 1459 measured from the gaseous kinematics (Verdoes Kleijn et al. 2000) is 5 times smaller than the one measured from stars (Cappellari 2002). Thus, more determinations with different methods are needed to test the validity of the methods themselves. Unfortunately, comparing stellar-dynamical estimates to gas-dynamical estimates of SBH masses to other methods is not usually possible, as few galaxies have properties that permit more than one method to be applied with confidence.

1.2.2 Scaling relations

Searching for scaling relations between the different components of galaxies is fundamental to provide clues about the physical mechanisms that drive their evolution. The demography of SBHs accounts for about 90 masses measured in quiescent galaxies (Kormendy & Ho 2013a) and about 150 masses in AGNs (Ho 2008).

The most studied relation is between the masses of SBHs and the central stellar velocity dispersion σ of their host spheroid (Ferrarese & Merritt 2000; Gebhardt et al. 2000b). Different slopes were found for the relation, due to the different methods for measuring the velocity dispersion and to the choice of the sample. However, because of its small scatter, the $M_\bullet - \sigma$ relation is fundamental for many issues related to the studies of SBHs. Indeed, it allows to infer SBH masses with 30% accuracy from a single measurement of the bulge velocity dispersion (Ferrarese & Ford 2005) and constitutes a test for modelling the SBH formation and evolution. In fact, a discriminating factor in choosing models of galaxy evolution is the ability to reproduce its slope, normalisation

and scatter (e.g., Monaco et al. 2000; Di Matteo et al. 2008; Dubois et al. 2012). In general, elliptical galaxies and bulges of disc galaxies share many structural and kinematical properties (e.g., Wyse et al. 1997; Kormendy & Kennicutt 2004) and they show the same correlations. However, there are two types of bulges in disc galaxies: "classical" bulges and "pseudobulges". Classical bulges are believed to be formed via merging of sub-galactic clumps, satellites and clusters. They are elliptical galaxies around which a disc has reformed (e.g., Steinmetz & Navarro 2002). Instead, pseudobulges are mainly formed by the secular evolution of disc structures, such as bars and spirals (Combes & Sanders 1981). Greene et al. (2008) and Hu (2008) found that SBHs in pseudobulges show a significant offset from the $M_\bullet - \sigma$ relation, maybe due to the presence of bars. Graham (2008) and Graham & Li (2009) discovered that by excluding barred galaxies, the intrinsic scatter is reduced, and Graham et al. (2011) defined a barless $M_\bullet - \sigma$ relation from a sample of 64 galaxies, where barred galaxies located about 0.5 dex below their unbarred counterparts. On the contrary, Beifiori et al. (2009), measuring upper limits on the $M_\bullet$ in a sample of 105 galaxies did not find this difference in the $M_\bullet - \sigma$ relation. The upper limits run parallel and above the $M_\bullet - \sigma$ relation, particularly for values of σ between 90 and 220 km s^{-1} without showing any systematic trend or offset as a function of the galaxy Hubble type, or with respect to the presence of a bar. To have a more precise understanding of the contribution of the different components, careful decompositions of the central structures of a larger sample of pseudobulges and/or barred galaxies is needed. In this context Hartmann et al. (2013) studied the consequences of angular momentum redistribution driven by bars on the evolution of the velocity dispersion of the bulge using simulations and comparing the results with the observations. They showed that if the SBH does not grow during the formation and evolution of bars, then the higher value of the dispersion leads to an offset below the $M_\bullet$-σ relation of 0.2 dex. Recently, Pota et al. (2013) have studied the relation between $M_\bullet$ and globular-cluster system velocity dispersion $\sigma_{\rm GC}$. They found that $M_\bullet$ correlates with the velocity dispersion, independently from the presence of a bar.

Kormendy & Richstone (1995) and Magorrian et al. (1998) found that the SBH mass scales with the bulge luminosity $L_{\rm bul}$, showing that the presence of the bulge might be essential for SBH formation. In fact, there is no detection of a SBH in the bulgeless spiral M33 (Häring & Rix 2004), where Gebhardt et al. (2001) found an upper limit of $M_\bullet < 1500$ M$_\odot$. According to the distinction firstly proposed by Graham et al. (2003), galaxies with a Sérsic surface brightness profile show a near-quadratic relation for $M_\bullet$-$L_{\rm bul}$, whereas core-Sérsic galaxies show an almost linear $M_\bullet$-$L_{\rm bul}$ relation. Studying a sample of 75 nearby galaxies with *Two Micron All Sky Survey (2MASS)* K_s-band pho-

tometry, Scott & Graham (2013) found similar results. For core-Sérsic galaxies the $M_\bullet$-L_{bul} relation is consistent with literature findings, while the slope is steeper for the Sérsic galaxies. The SBH growth was faster than that of the spheroid, resulting in a not constant fraction $M_\bullet/M_{\rm bul}$ which increases with $M_{\rm bul}$.

The disc galaxies NGC 4486B and NGC 1277 are remarkable outliers of the $M_\bullet$-$M_{\rm bul}$ relation. Indeed, 11% and 59% of their mass resides in the central SBH, respectively (Reines et al. 2011; van den Bosch et al. 2012). It is not yet known whether these galaxies represent the tail of the SBH distribution, or whether disc-dominated galaxies fail to follow the normal SBH mass scaling relations (van den Bosch et al. 2012). But, according to Emsellem (2013), we have to be prudent with these claims because he found that also a model without SBH provides a surprisingly good fit of the observed kinematics of NGC 1277 outside the unresolved central region. Therefore, he strongly recommends a more conservative approach using 3σ confidence levels for the derived $M_\bullet$ instead of the usually adopted 1σ level.

There are many other scaling relations that link SBHs with the properties of the host galaxies, most of these are discussed in Beifiori et al. (2012). The SBH mass correlates with the central light concentration (Graham et al. 2001), the Sérsic index (Graham & Driver 2007), the virial mass of the galaxy (Ferrarese et al. 2006a), the gravitational binding energy (Aller & Richstone 2007), the kinetic energy of random motions of the bulge (Feoli & Mancini 2009), and the stellar light and mass deficit associated to the core ellipticals (Lauer et al. 2007; Kormendy & Bender 2011). Furthermore, $M_\bullet$ correlates with the inner core radius (Franceschini et al. 1998; Lauer et al. 2007) in nearby weakly active galaxies. It also weakly scales with the total luminosity of the galaxy, especially for late-type spirals (Kormendy & Gebhardt 2001; Kormendy 2001). A link between $M_\bullet$ and the circular velocity V_c (or equivalently the mass of the dark matter halo) was also proposed considering the $M_\bullet$-σ and σ-V_c relations (Ferrarese 2002; Pizzella et al. 2005). More recently, Kormendy & Bender (2011) have studied a sample of bulgeless galaxies and concluded that there is no correlation between the $M_\bullet$ and dark matter halo. Along these lines, Beifiori et al. (2012) showed the large scatter of the $M_\bullet$-V_c relation suggesting that $M_\bullet$ is more coupled to the baryonic rather than the dark matter.

Hopkins et al. (2007a,b) suggested the possibility of a linear combination between galaxy properties to reduce the scatter of the relations, introducing the idea of a black holes fundamental plane (BHFP), where some of the SBH scaling relations are projections of the BHFP (Aller & Richstone 2007; Barway & Kembhavi 2007), as done for the fundamental plane of early-type galaxies. Beifiori et al. (2012) performed both a residual analysis and third-parameter fits

considering different linear combinations of bulge or galaxy parameters with $M_\bullet$. They stated that the strongest correlations always include σ as a fundamental structural parameter. The tightest relation is found between $M_\bullet$, σ, and the effective radius of the bulge, but its scatter is slightly similar to that of the $M_\bullet - \sigma$ relation. This implies that the velocity dispersion of the spheroidal component is the fundamental parameter which drives also the BHFP.

In a general view, the existence and tightness of most of such relations suggest a connection between the evolution of SBHs and that of their host galaxies, and provide constraints on theoretical models (e.g., Hopkins et al. 2006; De Lucia et al. 2006; Marulli et al. 2008). In particular, since the merger rate was higher and major mergers were more frequent in the past than today, such connection should be established earlier in massive elliptical galaxies than in lower mass galaxies, suggesting a self regulated accretion process (Volonteri & Natarajan 2009). Studying the demographics of SBHs, especially for a wide range of Hubble types and redshift, hints to better understand the formation of the SBH seeds in the early universe (McLure & Dunlop 2002; Corbett et al. 2003; Shields et al. 2003).

A number of possible mechanisms of self regulation has been suggested. For example, during a merger event the accretion of gas onto a SBH can be regulated by star formation (Burkert & Silk 2001; Kazantzidis et al. 2005; Zheng et al. 2009) or by the accretion of matter from a nuclear disc, originated from the accretion of stars (Miralda-Escudé & Kollmeier 2005). On the other hand, the available energy of an accreting SBH can influence the properties of the hosting bulge. Feedback from AGN activity is believed to play a fundamental role in the evolution of galaxies, and, in fact, analytical models and numerical simulations show that a feedback-regulated process of SBH growth could reproduce the observed scaling relations (e.g., Younger et al. 2008; Hopkins et al. 2009; Booth & Schaye 2009), and the existence of the BHFP (Hopkins et al. 2007a,b, 2009).

1.2.3 Formation

SBHs must have formed from the same material from which galaxies and the rest of the universe is composed, but their formation in galaxy nuclei is not well understood. While core-collapse supernovae provide a natural explanation of stellar BH, dissipation on a much larger scale is required to build up SBHs. The discovery of AGN activity at redshifts $z > 6$ and the corresponding short timescale for gas accretion in SBHs may implicate that the growth mechanism is rapid (e.g., Willott et al. 2003; Barth et al. 2003; Shields et al. 2008). These considerations have prompted interest in mechanisms for producing "seeds" BH of intermediate mass ($10^2 - 10^6$ $M_\odot$) that later emerge as the drivers of luminous

AGNs (e.g., Shapiro 2004; van der Marel 2004).

Madau & Rees (2001) suggested that in the high density environments of the early universe, relic BHs with $M_\bullet > 150$ $M_\odot$ form in the cores of more massive dark matter halos, being the remnants of the so-called Population III stars. There are the first stars, formed out of primordial gas in dark matter halos of $10^6 - 10^8$ $M_\odot$ at redshifts $z \approx 20 - 50$ (Tegmark et al. 1997). These stars are supposed to be very massive as shown in simulations of the collapse of primordial gas clouds (e.g., Abel et al. 2000; Bromm et al. 2002; Yoshida et al. 2006; Gao et al. 2007) and the most massive ones (> 260 $M_\odot$) can form BHs with masses of about 100 $M_\odot$ (Bond et al. 1984; Fryer & Kalogera 2001).

Another possibility to form SBHs could be the collapse of massive objects directly out of dense gas (e.g., Begelman et al. 2006; Lodato & Natarajan 2006; Johnson et al. 2012). At the very beginning, the cooling of gas in the proto-galaxies is less efficient and therefore, fragmentation and star formation are inhibited (Bromm & Loeb 2003; Santoro & Shull 2006), leading to efficient gas collapse resulting in the formation of a supermassive star. If nuclear fusion processes may be present, this infall leads to further contraction of the core into a BH, which then grows via the accretion of the envelope up to a mass of $10^4 - 10^5$ $M_\odot$ (Begelman et al. 2006, 2008). In a study of proto-galaxies Devecchi & Volonteri (2009) found that about 20% of proto-galaxies at z $\approx$ $10 - 20$ form BH seeds with masses $M_\bullet \approx 10^3 M_\odot$.

As a further alternative, in the process of hierarchical structure assembly, dense star clusters provide one possible vehicle for generating intermediate-mass BHs (e.g., Rasio et al. 2004). Interest in star clusters as possible precursors for SBHs has grown when surveys demonstrated that massive star clusters are commonly found in the centres of both elliptical (e.g., Côté et al. 2006) and disc galaxies (e.g., Carollo et al. 1997; Böker et al. 2002; Seth et al. 2006). They can be contracted on dynamical timescales because of the nearly free-fall inflow of self-gravitating gas with a mass comparable to or larger than that of the clusters itself. The cluster core can reach a central density high enough for fast mergers of stellar BHs and hence the rapid production of a black hole seed that could have a mass of 10^5 $M_\odot$ or larger (Quinlan & Shapiro 1987, 1989, 1990). There are some theoretical works showing that SBHs could form from stellar mergers in a young, dense cluster environment (e.g., Miller et al. 2004; Portegies Zwart et al. 2004), and thus a direct link between NSC and SBH formation may therefore exist.

These scenarios are not mutually exclusive, and we currently have no direct observations that can probe specific SBH formation scenarios (Volonteri & Begelman 2010; Haiman 2013).

1.3 Nuclear star clusters

The excellent resolution of the images obtained with *HST* has shown that the majority of low- and intermediate-luminosity galaxies are found to contain in their centre a compact and barely resolved source, whose structural properties and spectral features indicate a stellar nature. For this reason, these structures are called nuclear star clusters. The fraction of galaxies hosting a NSC depends on the galaxy magnitude, morphology and adopted criteria to identify the stellar nucleus, ranging from about 70% for early-type galaxies (Côté et al. 2006), to 50% for early-type spirals (Carollo et al. 1997), and 75% for late-type spirals (Böker et al. 2002).

Unlike SBHs, the formation history of NSCs is recorded in their morphology, kinematics, and stellar populations, making them an excellent tool to study how mass accumulates into the centre of galaxies. Their photometric and kinematic properties resemble those of massive compact star clusters, but while the effective radii (≈ 5 pc) are comparable to globular clusters independently of the galaxy type (Geha et al. 2002; Böker et al. 2004; Côté et al. 2006), the luminosities exceed those of the most luminous Galactic globular clusters by up to 2 orders of magnitude (Harris 1996). Indeed, NSCs have an absolute magnitude between -14 and -10 in I-band (Böker et al. 2002; Côté et al. 2006). NSCs are very massive, with a typical dynamical mass of $10^5 - 10^8$ $M_\odot$ (Walcher et al. 2005), and populate the high-mass end of the globular cluster mass function. They are among the objects with the highest mean surface density ($> 10^5$ $M_\odot$ pc^{-2}), as shown by Walcher et al. (2005) due to their small size. NSCs in early-type spiral galaxies seem to be more massive than those in late-type spirals (Seth et al. 2006). This is in agreement with the fact that their luminosity is, on average, brighter than those in late-type spiral as shown by Carollo et al. (2002). Such distinction is also clear in the sample of van der Marel et al. (2007), where NSCs in early-type spiral galaxies tend to have younger ages than those in late-type spirals. However, NSCs in late-type spirals can have multiple stellar populations, having both a spheroidal component and an elongated ring or disc component with a scalelength of a few parsecs, as shown also by Seth et al. (2006, 2008b).

In some cases, NSCs could reside near but not exactly in the photometric centres of their host galaxies. The small offset (0.5 arcsec) may be caused by the merging of globular clusters through dynamical friction, or after the ejection of a SBH from the nucleus (Côté et al. 2006).

M33 is the nearest Sc galaxy hosting a NSC, and its nucleus has been extensively studied in the past decade (e.g., Davidge 2000; Long et al. 2002; Stephens & Frogel 2002). It shows a population younger than 0.5 Gyr, but

the star formation has varied significantly over the past several Gyr. Gordon et al. (1999) estimated a mass of 5×10^5 $M_\odot$, consistent with the upper limit of 2×10^6 $M_\odot$ derived from the velocity dispersion by Kormendy & McClure (1993).

1.3.1 Search and properties

NSCs were studied in a number of surveys performed with different instruments. Böker et al. (2002) presented a study of I-band images of 77 nearby late-type spiral galaxies using the *Wide-Field Planetary Camera 2 (WFPC2)* on board the *HST*. From an isophotal analysis of the images, they showed that about 75% of the sample galaxies host a NSC, which resides at (or very close to) the photometric centre. Fitting a Nuker-law profile to the surface-brightness profile Lauer et al. (1995) disentangled the contribution of the NSC from the total flux of the galaxy. The distribution of the absolute magnitude of the NSCs in the sample has a FWHM of 4 mag and a median value of $M_I = -11.5$, comparable to young super star clusters in starburst galaxies. They suggested that NSCs in spiral galaxies of the latest Hubble types are an homogeneous class of objects.

Using *WFPC2*, Scarlata et al. (2004) analysed optical images of the central regions of 48 nearby star forming galaxies of late-type morphology. The central surface-brightness profiles were modelled with a Nuker law. They fitted an exponential or Sérsic profile to obtain the bulge properties. The 55% of the sample galaxies has a nuclear component and about half of them is resolved. They considered only the resolved objects as NSCs. Their absolute magnitudes range from -10.0 to -14.5 in the R band.

Lauer et al. (2005) presented *WFPC2* observations of 77 early-type galaxies. To classify the central structure into "core" or "power-law" forms, they fitted Nuker-law profiles to the surface-brightness distribution of the sample galaxies. NSCs were found in 29% of the core galaxies and 60% of the power-law galaxies. NSCs were bluer than the surrounding galaxy and they are often associated to AGNs. They also found that the location of the peak in the surface-brightness profile of the NSCs is coincident with the photometric centre of the core within a physical scale < 1 pc. However, they identified 5 galaxies whose centres are significantly displaced from their surrounding cores, suggesting that these may be unresolved asymmetric double nuclei. The sample NSCs have a total luminosity in the range from 7.0×10^4 to 1.0×10^8 $L_\odot$ in the V band, and a colour $V - I$ in the range from 0.57 to 1.37 mag.

Walcher et al. (2005) presented a spectroscopic and photometric study with the *Ultraviolet and Visual Echelle Spectrograph* at the *VLT* and *WFPC2* of 9 NSCs which are very bright ($10^6 - 10^8$ $L_\odot$ in I band), compact ($r_e \approx 5$ pc), and

with velocity dispersions in the range from 13 to 34 km s^{-1}. Using spherical dynamical models, they measured masses between 8×10^5 and 6×10^7 $M_\odot$ and M/L ratios range from 0.2 to 1.5 $M_\odot/L_\odot$ in the I band. The results suggest that the sample NCSs are mostly young.

Using *STIS* and *ACS* images, De Propris et al. (2005) derived the surface-brightness profiles for ultracompact dwarfs in the Fornax Cluster and for the NSCs of dwarf elliptical galaxies in the Virgo Cluster. Ultracompact dwarfs are more extended and have higher surface brightnesses than typical NSCs, while the luminosities, colours, and sizes of the NSCs are closer to those of Galactic globular clusters. They subtracted the best fit of the Sérsic profile from the galaxy surface brightness in order to obtain the nuclear profile of the NSCs. Their absolute magnitude in g and z band are in the range from -8 to -11.5 mag.

From the sample of Carollo et al. (1998) and Böker et al. (2002, 2004), Rossa et al. (2006) collected 40 spiral galaxies whose *STIS* spectra were present in the archive. A detailed stellar population analysis was performed for half of the spectra, while the measure of the continuum slope, as quantified by the $B-V$ colour, was measured for the other half sample. They fitted single stellar populations models with different ages on NSCs to infer the star formation history, metallicity, and dust extinction. The luminosity-weighted ages range from 10 Myr to 10 Gyr and 50% of the sample clusters contain a population younger than 1 Gyr. The stellar populations of NSCs are generally best fitted with a combination of populations of different ages, meaning that NSCs do not form in a single event, but they show subsequent star formation episodes. The M/L ratio span in the range from 0.12 to 2.72 $M_\odot/L_\odot$ in the B band, with some outlayers of about 8 $M_\odot/L_\odot$. The sample late-type spirals host younger and less massive NSCs ($\log M[M_\odot] = 6.25 \pm 0.21$) than those in early-type spirals ($\log M.[M_\odot] = 7.63 \pm 0.24$). Their results are consistent with those found by Walcher et al. (2005), but in contrast with the study of Sarzi et al. (2005). In fact, Sarzi et al. (2005) presented *HST* blue nuclear spectra of intermediate resolution for 23 nearby disc galaxies, selected to have nebular emission in their nuclei. Modelling the continuum spectral energy distribution within the central 0.13 arcsec with linear combinations of single-age stellar population synthesis models, they found that the 80% of the sample nuclei have features consistent with a predominantly old stellar population ($\geq 5 \times 10^9$ Gyr): the majority of stars within the central few tens of parsecs in their sample are several Gyr old.

The largest sample of NSCs was studied using the *HST ACS* Virgo Cluster Survey (Côté et al. 2004; Ferrarese et al. 2006b): the NSCs were searched in about 100 early-type galaxies were identified using the direct inspection of the images, looking for changes in the $g-z$ colour images, and fitting with a

King profile the light excess in the nuclear surface-brightness profiles above the inward extrapolation of the best-fit galaxy model. Only a few NSCs appeared unresolved. The resolved NSCs have affective radii in the range from 2 pc to 62 pc, with a median of $r_e = 4.2$ pc (Côté et al. 2006). Their masses are between 6×10^5 and 7×10^8 $M_\odot$ (Ferrarese et al. 2006a).

Furthermore, to shed light on the properties of the stellar populations of NSCs, Seth et al. (2006) studied 14 nearby, edge-on late-type galaxies with *HST*. They found that the NSCs show multiple stellar populations: the young structure (often younger than 100 Myr) dominates the light and indicates that NSCs experience frequent star formation episodes. Otherwise, the old population has many Gyr, being sometimes only few Gyr younger than the body of the host galaxies and contains most of the mass of the NSC. Butler & Martínez-Delgado (2005), Chilingarian et al. (2007), Koleva et al. (2009), and Paudel et al. (2010) found the same results. Taking into account these properties, Seth et al. (2006) proposed a "rejuvenation" mechanism for NSCs that occurs in gas-rich disc galaxies. On the other side, NSCs in gas-poor spheroids, may evolve passively for a few Gyr and acquire stellar mass only through the merging of globular clusters onto the existing NSC. The balance between feedback from star formation and fuelling efficiency seems to regulate the rate of NSC formation and could explain star formation episodes seen in some NSCs (Walcher et al. 2006; Rossa et al. 2006), as part of the rejuvenation process.

Balcells et al. (2007) measured the near-infrared central structural properties of a sample of S0−Sbc galaxies down to scales of 10 pc using *HST Near Infrared Camera and Multi-Object Spectrometer (NICMOS)* images, finding that about the 58% of the sample galaxies host a NSC, unresolved by NICMOS. They are most likely globular clusters, but with $10 - 20$ times higher luminosities. Balcells et al. (2007) fitted a point source profile to the unresolved objects, finding K-band absolute magnitude in the range from -13 to -17 mag. For the resolved sources, they fitted a nuclear exponential profile and found NSCs with K-band absolute magnitudes in the range from -16 to -20 mag.

1.3.2 Scaling relations

NSCs are almost ubiquitous within bulges. This raises the question whether they are related. Several authors investigated whether scaling relations between NSCs and the host bulge/galaxy exist.

An important finding of the study of Carollo et al. (1998) was that the NSC luminosity correlates with the host galaxy luminosity for early-type spirals. Then, Böker et al. (2004) found a similar correlation for NSCs in late-type spirals. Both studies found that more luminous galaxies tend to have more

luminous NSCs. However, the relations between these quantities are not the same: at a fixed galaxy luminosity, NSCs in early-type spirals tend to be more luminous than those in late-type spirals (Rossa et al. 2006). This dependence on Hubble type was seen also in the study of Carollo et al. (2002), who concluded that NSCs in early-type spirals can be significantly more luminous than those in late-type spirals. Rossa et al. (2006) stated that NSC luminosities and masses appear to depend strongly on both galaxy luminosity and Hubble type.

Wehner & Harris (2006), Ferrarese et al. (2006a), and Rossa et al. (2006) also found that the mass of NSCs, $M_{\rm NSC}$, in elliptical and spiral galaxies correlate with the velocity dispersion σ.

Furthermore Ferrarese et al. (2006a) showed that there is a strong correlation between $M_{\rm NSC}$ and the total mass of the host galaxy. Erwin & Gadotti (2012) and Leigh et al. (2012) showed that $M_{\rm NSC}$-$M_{\rm gal}$ is the primary correlation for NSCs and may due to momentum feedback from stellar and supernovae winds in NSCs (McLaughlin et al. 2006). Alternatively, the $M_{\rm NSC}$-$M_{\rm gal}$ relation can be the result of the cluster formation: NSCs could be simply formed from gas accretion onto the nucleus in proportion to the galaxy masses (Li et al. 2007). The $M_{\rm NSC}$ correlates also with the galaxy magnitude in I - and K -band, the Sérsic index n, the mass and luminosity of the spheroid $L_{\rm bul}$ and $M_{\rm bul}$ (Ferrarese et al. 2006a; Wehner & Harris 2006; Rossa et al. 2006; Graham & Driver 2007). Côté et al. (2006) found that the half-light radius of NSCs scales with their total luminosity according to the relation $r_{\rm h} \propto L^{0.5\pm0.03}$. From the analysis of the population synthesis models, they found that the colours of NSCs correlate with the total luminosity of the NSC. The colour-magnitude relation observed for NSCs of their sample suggested that their chemical enrichment was governed by local or internal factors. Their Monte Carlo simulations showed that mergers of globular clusters through dynamical friction are unable to explain the observed colour-magnitude relation.

A recent and debated development in this research field is understanding whether there is a common formation scenario between SBHs and NSCs and whether they follow the same scaling relations. Ferrarese et al. (2006a) found that for a given velocity dispersion, NSCs tend to be 10 times less massive than SBHs. NSCs seem to extend the $M_\bullet - \sigma$ relation to lower masses. This suggests that the formation of a CMO is a part of galaxy evolution. Furthermore, they showed that SBHs obey the same relation between $M_{\rm NSC}$ and $M_{\rm gal}$, in the sense that low- and intermediate-luminosity galaxies tend to form NSCs and bright galaxies contain SBHs instead. The change from high-mass SBHs to lower-mass NSCs happens at a CMO mass of $\sim 10^{7.5}$ $\rm M_\odot$ (Kormendy & Ho 2013a). Thus the challenge is to understand why different types of objects are favoured in different regimes of galaxy mass. Furthermore, Rossa et al.

(2006), Ferrarese et al. (2006a) and Wehner & Harris (2006) showed that the correlation between $M_{\rm NSC}$ and the luminosity of the bulge has the same slope as the well-known correlation between $M_\bullet$ and bulge luminosity: the properties of CMOs are therefore intimately connected to the properties of the host galaxy, and in particular its bulge component. Finally, Graham & Driver (2007) found a continuous correlation between mass of the CMO and the Sèrsic index of the host galaxy, leading that SBHs and NSCs form by similar processes that favour SBHs in large galaxies and NSCs in small ones.

In an opposite view, some authors argued in favour of an absence of any universal CMO correlation and thus against a common formation and growth scenario. For example, Scott & Graham (2013) found a different correlation comparing the $M_{\rm NSC} - M_{\rm bul}$ relation to the corresponding $M_\bullet$-$M_{\rm bul}$ relation. A strong effort to this view is the fact that some galaxies contain both a SBH and a NSC, weakening the paradigm of Ferrarese et al. (2006a) because CMOs are not mutually exclusive. Furthermore, AGNs in late-type bulgeless galaxies show that SBHs exist even at the absolute magnitudes of dwarf galaxies that usually have NSC (Ho 2008). NSCs are also observed in bulgeless galaxies at high luminosities at which SBHs dominate when galaxies have bulges (e.g., M101 and NGC 6946, Kormendy & Ho 2013a).

Other works claimed that there is no correlation between these NSCs and SBHs (Balcells et al. 2007), or at least it must not be log-linear and suggest that the $M_{\rm NSC} - \sigma$ scaling relation is shallower than the corresponding $M_\bullet - \sigma$ one (Graham & Li 2009; Graham 2012; Scott et al. 2013; Leigh et al. 2012).

1.3.3 Formation

Most of the suggested scenarios explaining the formation of NSCs require a dissipation process that occurs with different mechanisms: the *in-situ* formation that contemplates also some episodes of gas infall and subsequent star formation within a few parsecs from the galaxy centre (e.g., Shlosman & Begelman 1989; Maciejewski et al. 2002; Maciejewski 2004), and the migration of dense clusters formed elsewhere in the galaxy and then falling into the centre through dynamical friction or other mechanisms such as the presence of an external tidal field (e.g., Tremaine et al. 1975; Capuzzo-Dolcetta 1993). Other formation scenarios account for accretion of intragalactic medium (e.g., Silk et al. 1987), two-body relaxation processes around a central SBH (e.g., Weedman 1983; Mihos & Hernquist 1994), and fading of star clusters in evolving dwarf irregular or blue compact dwarf galaxies (Davies & Phillipps 1988).

Numerical simulations of gas dynamics, star formation, and chemical evolution show that elliptical galaxies are able to produce dense stellar systems,

but they can not provide a clear explanation of the correlations between the dynamical properties of NSCs and their host galaxy (Bekki et al. 2006). According to Milosavljević (2004) the magneto-rotational instability within the galactic gas disc can transport gas towards the nucleus in the inner 100 pc and can support star formation there. Moreover, Emsellem & van de Ven (2008) pointed out that the tidal field becomes compressive in shallow density profiles, and gas can collapse onto the centre of both early- and late-type disc galaxies, and there forms stars. If correct, then NSC formation should be the natural consequence of galaxy formation. For barred galaxies Shlosman & Begelman (1989) suggested that the main mechanism to transport the gas into the centre is the bar-driven inflow. There it accumulates, dissipates, and forms stars, providing a natural explanation for the presence of NSCs. This happened for IC 342, where high resolution interferometric observations of the nuclear region show that mechanical feedback from recent star formation activity affects the gas inflow caused by the large stellar bar (Schinnerer et al. 2003, 2008).

Bassino et al. (1994) and Bekki et al. (2001) proposed that NSCs are the surviving nuclei of dwarf galaxies that have been extensively stripped by gravitational tidal fields in the host cluster. In fact, the dwarf galaxies have luminosities that coincide with the peak of the luminosity function of NSC (Côté et al. 2006).

Walcher et al. (2005) proposed a scenario where NSCs are protobulges that grow by accretion of gas and subsequent star formation. The difference between a NSC and a small bulge is the rate of the growth and the resulting size of the central component.

In the migration scenario some star clusters (like globular clusters of the halo and star clusters of the main disc and bulge) lose the kinetic energy of their orbital motion due to dynamical friction and merge into the centre (Tremaine et al. 1975). Indeed, Andersen et al. (2008) and Kornei & McCrady (2009) found a candidate star cluster in the inner few hundred parsecs of NGC 2139 and NGC 253 respectively, showing that off-centre star clusters exist in the inner region of galaxies. Capuzzo-Dolcetta (1993) studied the evolution of globular clusters in a triaxial galaxy in the presence of dynamical friction due to field stars. He claimed that some galactic nuclei could be formed by frictionally decayed globular clusters. The mass of the resulting nucleus is determined by the mutual feedback between the falling clusters and the tidal disruption induced by the nucleus itself. As a proof, Lotz et al. (2001, 2004), studying dwarf elliptical galaxies in the Virgo and Fornax Cluster, found a lack of the most massive globular clusters radial distribution compared to the total globular cluster distribution, suggesting that they could be merged in the centre of the galaxy because of their smaller infall timescale. Also Agarwal & Milosavljević

(2011) used analytic modelling to show that infalling star clusters from an empirical star cluster population produce NSCs of the right mass in isolated spheroidal and late-type galaxies. A number of other simulations have found that mergers occurring within the bulge component can build NSCs with the structural parameters consistent with those observed in real galaxies (Bekki et al. 2004; Miocchi et al. 2006; Capuzzo-Dolcetta & Miocchi 2008a,b). In contrast, Milosavljević (2004) found that in late-type spiral galaxies globular clusters have to be more massive than 10^6 $M_\odot$ and within 1 kpc, otherwise the timescale for spiralling into the inner region of the galaxy would be too long (> 3 Gyr). Indeed, in a study of bulgeless spiral galaxies, Neumayer et al. (2011) found that for star clusters with masses $M_{\rm NSC} > 2 \times 10^5$ $M_\odot$, the dynamical friction timescales are shorter than 2 Gyr within 500 pc.

However, the migration scenario accounts for only a part of the formation history. In fact, Hartmann et al. (2011) and De Lorenzi et al. (2013) showed that cluster infall alone cannot explain the dynamical properties of the NSC in the nearby edge-on galaxy NGC 4244, concluding that at least 50% of its mass must have been produced by an *in-situ* star formation. This means that the formation of NSCs and their subsequent growth do not necessarily have to be governed by the same mechanism, and that more than one mechanism can contribute to the evolution of an NSC after its formation. Therefore, a combined scenario could explain the formation of NSCs in late-type spiral galaxies where stars younger than 100 Myr are present and star formation is prolonged and possibly constant (Rossa et al. 2006; Walcher et al. 2006). Thus, the accretion of young star clusters formed near the centres of galaxies can rejuvenate the NSC, as observed in the Milky Way by Figer et al. (1999, 2002). Indeed Antonini (2013) studied massive globular clusters merging into the centre of the Milky Way. He found that the luminosity function is consistent with the hypothesis that half of the mass comes from old ($\approx$10 Gyr) stars and half from star of subsequent formation. He concluded that a model in which a large fraction of the mass of the Milky Way NSC is due to infalling globular clusters is consistent with existing observational constraints, only when dissipation is taken into account. Recently, Turner et al. (2012) have shown that the dominant mechanism to form the nucleus in low mass early-type galaxies is probably the infall of star clusters through dynamical friction, while at higher masses, gas accretion resulting from mergers and torques becomes dominant.

In parallel to the migration scenario, NSCs can evolve through an out-migration process. In fact, some theories suggest that when the first gas-rich protogalaxies experienced rapid nucleation (Cen 2001) they formed a dense cluster in their centre. In merging episodes, the cluster survives and lives within the halo of the merger product, because of the compactness and high stellar

density, as the Galactic globular cluster M54 that is believed to be the nucleus of the Sagittarius dwarf galaxy (Layden & Sarajedini 2000), or as ω Cen, thought to be the remnant nucleus of an accreted dwarf galaxy because of its extreme mass and multiple stellar populations (Freeman 1993). In fact, the multiple stellar populations observed in a number of globular clusters of the Galaxy can be explained assuming that globular clusters spend part of their history at the bottom of the potential well (Böker et al. 2008). This is also consistent with the roughly constant specific frequency of globular clusters and the observed universal mass fraction of globular cluster systems in the local Universe (McLaughlin 1999).

1.4 Nuclear stellar discs

NSDs are small-scale discs that reside in the nuclei of galaxies. They are smaller ($h \sim 10 - 50$ pc) and brighter ($\mu^0_{0,V} \sim 16 - 19$ mag arcsec^{-2}) than embedded discs in early-type galaxies (van den Bosch 1998), but they never dominate the light distribution of the galactic nuclei, and locally contribute at most half the galaxy surface brightness.

They have received attention primarily as probes of the mass distribution since they permit measurement of the mass of central SBHs through the observation of their stellar kinematics (e.g., van den Bosch & de Zeeuw 1996; Magorrian 1999; Cretton & van den Bosch 1999). Furthermore, the study of NSDs can also advance our understanding of galaxy formation and evolution since their formation and destruction reflects the assembly history of their host galaxies. For example, being dynamically cold systems, NSDs are fragile and do not survive a major merger. Especially in the presence of a SBH, a NSD would be significantly affected by the interaction with a second SBH of comparable mass carried by the merging galaxy (Ledo et al. 2010). Therefore, the age of a NSD could constrain the epoch of the last major merger of the host galaxy.

1.4.1 Search and properties

Several *HST* surveys were carried out to investigate the nuclei structure on scales of 10-100 pc over a wide range of morphological types. They showed that about 20% of elliptical (Ledo et al. 2010) and spiral galaxies (Pizzella et al. 2002) host a NSD.

Indeed, nuclear discs of gas, dust, and stars were clearly detected in a large number of early-type galaxies (e.g., Lauer et al. 1995; Kormendy & Gebhardt 2001; Trujillo et al. 2004), but the photometric parameters of such discs have

been derived only for a few. Furthermore, near-infrared *HST* imaging provided indirect signatures of the presence of NSDs as discy isophotes in the nuclei of early-type galaxies (Ravindranath et al. 2001) or photometrically-distinct exponential components in bulges (Balcells et al. 2003).

The stellar populations in NSDs were studied in detail in only a few objects (Table 1.1). Spectroscopic absorption line-strength indices were measured in galactic nuclei constraining the stellar population age, metallicity and α-element overabundance of the NSD by comparison with evolutionary population synthesis models (e.g., Worthey 1994; Vazdekis 1999; Thomas et al. 2003; Bruzual & Charlot 2003). In NGC 4478 the NSD is younger, more metal-rich and less over-abundant than the rest of the galaxy (Morelli et al. 2004). In contrast the NSD of NGC 5308 is made of a younger and more metal-poor stellar population than the host galaxy (Krajnović & Jaffe 2004). Both the NSD and bulge of NGC 4570 show an intermediate-age stellar population although the NSD is more metal rich (Krajnović & Jaffe 2004).

Examples of on-going star formation via dissipation include the NSDs in NGC 5845 (Kormendy et al. 1994) and in NGC 4486A (Kormendy et al. 2005). However, other NSDs are as old as the main body of the host galaxy (NGC 4128, Krajnović & Jaffe 2004, NGC 4342, van den Bosch et al. 1998, NGC 4458, Morelli et al. 2004, NGC 4621, Krajnović & Jaffe 2004, NGC 4698, Corsini et al. 2012).

1.4.2 Scaling relations

The existence of NSDs suggests that the continuity of the disc properties, with a smooth variation of scale parameters from spirals to discy ellipticals along a sequence of decreasing disc-to-bulge ratio (Kormendy & Bender 1996), can be extended to nuclear scales (van den Bosch 1998).

In fact, independently of the Hubble type of their host galaxy, NSDs seem to follow the same relation between the central face-on surface-brightness μ_0^0 in V band and scalelength h, as the main discs of lenticular and spiral galaxies and as the embedded discs of early-type galaxies However, an observative bias has to be taken into account, such as the fact that selection effects can play an important role in the lower part of the $\mu_0^0 - h$ diagram, where an object characterised by small scalelength and low central surface brightness would be difficult to detect. On the other hand, in the upper part of the diagram the discs would be characterised by high surface brightnesses and large scalelengths, making them easy to identify. Thus, this lack is real and seems to be related to the formation and evolution of the discs, that make them dynamically unstable (van den Bosch 1998).

Searching for NSCs, Balcells et al. (2007) found a number of galaxies that contains a NSD and pointed out that it is important to distinguish between these NSCs and NSDs when examining the scaling relations of CMOs. Indeed, they seem to follow quite different relations. Recently, Scott & Graham (2013) have found that the exclusion of NSDs and the inclusion of massive NSCs in the investigation of common scaling relations between NSCs and SBHs give rise to different conclusions from those by Ferrarese et al. (2006a). Indeed, no correlations were found when possible relations between photometric parameters of the nuclear disc and global properties of the host galaxies were investigated (Scott & Graham 2013).

1.4.3 Formation

Different mechanisms have been proposed to explain how NSDs form. Most of them requires the dissipation of a certain amount of gas that can be either of internal or external origin. The measurements of stellar population ages, metallicity and α-element overabundance can distinguish between the merging scenario and the formation with dissipation by constraining the metallicity gradients, dating the latest episode of star formation and measuring the timescale over which the bulk of the star formation has taken place.

Mayer et al. (2010) show via hydrodynamical simulations of mergers between galaxies with SBHs that strong gas inflows are able to build nuclear discs of a few billion solar masses, which funnel more than 10^8 $M_\odot$ of gas at the centres of merger remnants. Their properties depend on the details of gas thermodynamics. The capture of external gas accounts for the origin of the counter-rotating NSD in NGC 4458 (Morelli et al. 2004, 2010). Indeed, kinematic decoupled components are interpreted as the signature of gas accretion or merging of satellite galaxies (see Bertola & Corsini 1999, for a review). An external origin is also invoked for the gas which formed the stars of the nuclear disc in the early-type spiral NGC 4698. This is a very interesting galaxy, where the nuclear disc of gas and stars is rotating perpendicularly with respect to the main galactic disc (Bertola et al. 1999; Pizzella et al. 2002; Corsini et al. 1999, 2012). Its complexity is also showed by the fact that the bulge and the main disc are characterised by a remarkable geometrical decoupling. Indeed they appear elongated orthogonally to each other. Because the size, orientation, and location of its NSD do not depend on the observed passband, a plausible scenario is one in which the NSD is the end result of the acquisition of external gas by the pre-existing triaxial bulge on the principal plane perpendicular to its shortest axis and perpendicular to the galaxy main disc. The subsequent star formation either occurred homogeneously all over the extension of the NSD or

through a process that ended more than 5 Gyr ago.

The secular infall of gas, perhaps due to a barred potential, is an alternative way to funnel pre-enriched material into the galactic centre where it accumulates, dissipates, and forms stars. This scenario provides a natural explanation for the presence of NSDs in barred galaxies (i.e. NGC 7332, Seifert & Scorza 1996; Falcón-Barroso et al. 2004). In some cases a bar may even be destroyed in the process, as has been proposed for NGC 4570, (Scorza & van den Bosch 1998; van den Bosch & Emsellem 1998) and NGC 4621 (Sil'chenko 1997)). In this picture it is interesting to notice that many disc galaxies have double-disc structures, harbouring both an outer disc and a NSD. It raises the question whether there is a common origin of this multi-component disc structure. For example, the Sombrero galaxy (NGC 4594) is the prototype of a galaxy with a double disc structure. Emsellem et al. (1996) found that its multi-disc structure is shaped by secular evolution induced by a small bar. A similar conclusion was reached by Scorza & van den Bosch (1998) who studied the inner photometric structure of NGC 4342 and NGC 4570, two power-law early-type galaxies in the Virgo cluster with a double-disc structure. Thus, the secular evolution driven by a nuclear bar could be responsible for the formation of some NSDs. Therefore, each of the above scenarios is found to be likely for some but not for all the objects. As a matter of fact, any model for the formation of NSDs has to account for the presence of SBHs, which reside in every massive galaxy and whose gravitational influence may extend to the scale of the NSD.

Because of their stellar nature and their similar structural properties, the formation scenarios of NSDs are similar to those suggested for NSCs. In fact, one can think about a common formation mechanism. Furthermore, some authors do not make any distinction between these two classes of CMOs. This is the case of Balcells et al. (2007) who referred to structures that resemble NSDs as "discy NSCs". In fact, they found nuclear objects with discy isophotes. Fitting exponential profiles to the surface brightness of their galaxy sample, they obtained discs with sizes of a few hundred parsecs which resemble NSDs. Lauer et al. (2005) fitted Nuker-law to the surface-brightness profiles of 77 early-type galaxies to classify the central structure into core or power-law forms. Core galaxies are typically rounder than power-law galaxies. Nearly all power-law galaxies with central ellipticities $\epsilon > 0.3$ have stellar discs, implying that discs are also present in power-law galaxies with $\epsilon < 0.3$ but are not visible because of unfavourable geometry. A few low-luminosity flattened core galaxies also have discs. These may be transition forms from power-law galaxies to more luminous core galaxies which lack discs. Discy NSCs, i.e. NSDs, are present also in the Virgo Cluster sample (Côté et al. 2006; Ferrarese et al. 2006a). Agarwal & Milosavljević (2011), using analytic modelling, showed that infalling star clus-

ters from an empirical star cluster population produce NSCs of the right mass in isolated spheroidal and late-type galaxies. Such star clusters must form quite close to the galaxy centres (≈1 kpc), and the rate at which the NSC grows by accreting young star clusters depends on their formation rate, migration time, and dissolution time. The resulting compact NSC is embedded in a more extended and diffuse component resembling a small pseudobulge. The size of such a disc-like structure in models including the prompt dissolution of star clusters matches that of the observed NSDs. This opens the possibility that NSDs can be formed via star clusters accretions.

Table 1.1: Stellar population properties of NSDs.

Galaxy	Morph. Type	D [Mpc]	Age [Gyr]	Comment	[Fe/H]	[α/Fe]	Reference
(1)	(2)	(3)	(4)	(5)	(6)	(7)	(8)
NGC 4128	S0	36.3	14	as old as the galaxy	$[-0.38, -0]$	...	Krajnović & Jaffe (2004)
NGC 4342	S0	15	8	as old as the galaxy	0.25	...	van den Bosch et al. (1998)
NGC 4458	E0-1	12.6	$\sim$15	as old as the galaxy	0.2	0.3	Morelli et al. (2004)
NGC 4478	E2	12.6	6	younger than the galaxy	0.35	0.2	Morelli et al. (2004)
NGC 4486A	E2	16	$>$2	younger than the galaxy, star formation		...	Kormendy et al. (2005)
NGC 4570		15	8	as old as the bulge	0.35	...	van den Bosch et al. (1998)
	S0	25.2	...	as old as the bulge	...	...	Krajnović & Jaffe (2004)
NGC 4621	E5	7.3	10-14	as old as as the galaxy	> 0	...	Krajnović & Jaffe (2004)
NGC 4698	Sab	17	10	as old as as the galaxy	1-2.5	...	Corsini et al. (2012)
NGC 5308	E/S0	31.9	14	younger than the galaxy	> 0	...	Krajnović & Jaffe (2004)
NGC 5845	E3	20.1	...	on going star formation	...	...	Kormendy et al. (1994)

Notes. — Col.(1): Galaxy name. Col.(2): Hubble type. Col.(3): Distance. Col.(4): Age of the NSD. Col.(5): Comments about the ages of the NSD with respect to that of the host galaxy. Col.(6): Metallicity of the NSD. Col.(7): α-enhancement of the NSD. Col.(8): Reference of all the data.

1.5 Coexistence

Different types of CMOs have been observed in some galaxies, providing us the chance of understanding the assembling history of the nucleus and characterising the structural components of the host galaxy. Although CMOs usually indicate SBHs or NSCs, we also consider NSDs. Within this framework, the coexistence of CMOs in galactic nuclei covers the following cases:

- the SBH coexists with a NSC,
- the SBH coexists with a NSD,
- the NSC coexists with a NSD,
- the SBH coexists with both a NSC and a NSD.

1.5.1 Supermassive black holes and nuclear star clusters

A number of galaxies are known to host both a SBH and a NSC, but to date the masses of both the coexisting objects have been measured only in a few objects (Seth et al. 2010).

As far as quiescent galaxies concerns, the Milky Way is the most prominent example. The Galactic SBH has a mass of 4.3×10^6 $M_\odot$ (Ghez et al. 2008; Gillessen et al. 2009). The Galactic NSC was first described by Becklin & Neugebauer (1968) using IR observations, while recent studies used both star counts and kinematics, to measure the mass enclosed within the central 10 pc. The mass of the Galactic NSC is 3×10^7 $M_\odot$ (Genzel 1996; Schödel et al. 2007). Ghez et al. (2005) proved the existence of a SBH, surrounded by a cluster of young massive stars, using adaptive optics imaging and spectroscopy with large ground-based telescopes. Detections of intermediate BHs in the centres of two massive globular clusters are very interesting because they can be NSCs of stripped dwarf galaxies (Meylan et al. 2001; Bedin et al. 2004). Studying the properties of the central regions of a sample of 77 galaxies, Lauer et al. (2005) detected a NSC in 7 galaxies that host a SBH. In their sample we recognised the ellipticals IC 1459 (Cappellari 2002), NGC 1316 (Nowak et al. 2008), NGC 1399 (Gebhardt et al. 2007), and NGC 2778 (Schulze & Wisotzki 2011), the lenticular galaxy NGC 7457 (Rusli et al. 2013), and the spiral NGC 3945 (Gültekin et al. 2009) which have measured masses as results from the review of (Kormendy & Ho 2013a).

Seth et al. (2008a) studied galaxies that host both NSCs and AGNs, implying the presence of a SBH. From this sample, the elliptical galaxy NGC 3384

and the lenticular galaxy NGC 7457 have a measured SBH mass (Tremaine et al. 2002) and host a NSC (Graham & Driver 2007). Although the NSCs in both cases are unresolved in *HST* observations presented by Ravindranath et al. (2001), Seth et al. (2008b) estimated a stellar mass of 2.1×10^7 and 2.7×10^7 $M_\odot$, respectively. The study of AGNs and NSCs provides further evidence of the coexistence of SBHs and NSCs (Seth et al. 2008a; Graham et al. 2011). A NSC and intermediate-mass black hole are found to coexist in NGC 4395, a late-type spiral galaxy (Filippenko & Sargent 1989) at a distance of 4.3 Mpc (Thim et al. 2004). The galaxy is active and its AGN is one of the nearest and least luminous Seyfert 1 nuclei. The black hole mass is 3.6×10^5 $M_\odot$ (Peterson et al. 2005), while the mass of the NSC is 1.1×10^6 $M_\odot$ (Seth et al. 2008a). Shields et al. (2008) studied the NSC of the bulgeless galaxy NGC 1042. The emission-line properties of its nucleus show the evidence of an accretion power indicative of a central black hole with $M_\bullet = 3 \times 10^6$ $M_\odot$. Other examples of active galaxies hosting a NSC are ESO 205-G7 (Rossa et al. 2006), NGC 4321, NGC 5921, NGC 6384, and NGC 6951 (Scarlata et al. 2004).

González Delgado et al. (2008) analysed the *HST/ WFPC2* archival data of the AGNs of the Palomar survey (Ho et al. 1997). They identified several candidates that may host both an AGN and a NSC. But the largest search of the coexistence of SBHs and NSCs was done by Seth et al. (2008b). They selected AGNs from a sample of 176 galaxies ranging from ellipticals to late-type spirals with mass between $10^9 - 10^{11}$ $M_\odot$ and with previously detected NSCs. They found that 10% of the sample galaxies are AGNs and an additional 15% are characterised by both AGN and star formation. The masses of the coexisting CMOs are similar, although $M_{\rm NSC} < M_\bullet$. The fraction of nucleated galaxies with AGNs increases strongly as a function of the galaxy mass and $M_{\rm NSC}$. In particular, galaxies that host both a NSC and an AGN/SBH have magnitudes $M_B < -16$ and masses $M_{\rm gal} > 10^9$ $M_\odot$. For galaxies of the same mass, NSCs in late-type spiral galaxies are typically an order of magnitude less massive than those in elliptical galaxies.

Collecting information about galaxies hosting both a SBH and a NSC is crucial to understand whether a trend exists, if they share common characteristics and a common formation scenario (Ferrarese et al. 2006a). Graham & Spitler (2009) identified all galaxies with reliable measurements of both SBH and NSC mass and analysed the ratio $\frac{M_\bullet}{M_\bullet + M_{\rm NSC}}$ as a function of bulge mass. SBHs are hosted in massive bulges, whereas NSCs usually reside in pure disc galaxies. Graham & Spitler (2009) observed a transition region $10^8 < M_{*,\rm sph}/M_\odot < 10^{10}$ where both types of CMOs coexist. But, Böker et al. (2008) proposed the possibility that the presence of a NSC is necessary (but not sufficient) for the formation of a SBH.

NSCs are usually not observed in galaxies hosting SBHs with masses above 10^{10} $M_{\odot}$ (Graham & Spitler 2009). This suggests that the most massive SBHs destroyed their host NSCs. Such a phenomenon is explained by Antonini (2013). He suggested that globular clusters are tidally disrupted when a SBH is included at the centre of a galaxy. The resulting NSC has a lower density than that of NSCs formed in galaxies with no SBHs. He also stated that the formation of NSCs is inhibited because the time for globular clusters to reach the centre of the galaxy is much longer than the Hubble time. Some scaling relations appear to be in agreement with the predictions of the cluster merger model. But the size and luminosity of the NSCs are not well reproduced when a SBH is included because of its tidal field influence. Therefore, the dynamical influence of a SBH should be considered when modelling NSCs. In this sense, simulations could give us interesting results in the understanding of the formation of such structures.

Taking into account the detections of coexisting SBHs and NSCs, Nayakshin et al. (2009); Nayakshin & Power (2010) proposed the competitive accretion to describe the mutual feedback between these two objects and the mass ratio between SBH and NSC. In this paradigm, the bulge mass dictates the choice between the SBH and the NSC: if $\sigma < 150$ km s^{-1}, NSCs reach their maximum mass because the star formation occurs more rapidly than the SBH growth and drives the gas away before the SBH can accrete it. However, a number of physical processes take also place, like the evaporation of the NSC due to the SBH (Ebisuzaki et al. 2001; O'Leary et al. 2006), or the fact that binary SBHs may heat and erode the NSC (Bekki & Graham 2010).

1.5.2 Supermassive black holes and nuclear stellar discs

NSDs can be used to measure the mass of central SBHs through observations of their stellar kinematics (e.g., van den Bosch & de Zeeuw 1996; Magorrian 1999).

Galaxies with SBHs hosting NSDs are not exceptions: NGC 3115, NGC 4342, NGC 4594, and NGC 5845 are known to harbour both these objects (Kormendy et al. 1996a; Cretton & van den Bosch 1999; Lauer et al. 2005; Ledo et al. 2010). Kormendy et al. (1996b) and Emsellem et al. (1999) studied the central disc of stars and dust of NGC 3115 as it was a discy NSC. They found that the SBH of NGC 3115 is substantially more massive than the NSC.

A very interesting case is M31 where Lauer et al. (1993) found a double nucleus. They speculated that the majority, if not all, of these systems may be cases in which BHs were crucial to either create or preserve the unusual structures over long times. This is also the case of NGC 4486B (Lauer et al.

1996), one of the lowest-luminosity elliptical galaxies known. Tremaine (1995) explains the double nucleus in M31 (and also in NGC 4486B) as a deprojected eccentric disc of star stabilised by a SBH. Lauer et al. (2002) advanced two different explanations for such coexistence. The first is that a diffuse torus of star was added to a preexisting core, probably during the final stages of merger in which the tidal field of the SBH in the more massive galaxy disrupts the dense centre of a galaxy (Holley-Bockelmann & Richstone 2000). A second, more exotic idea is that stars were actually ejected from the galaxy centre by the decay of a binary SBH created in a merger and formed the disc. By modelling the orbits of the nucleus of M31, Brown & Magorrian (2013) were able to reproduce the observed *WFPC2* photometry and the line-of-sight velocity distributions of *STIS* observations. The galaxy is well described with an inclined NSD within $0''.15$ that surrounds a SBH of $M_\bullet = 1.0 \times 10^8 \mathrm{M}_\odot$.

In the sample of Lauer et al. (2005), there are some galaxies that host a NSD and have measured masses of their SBHs. They are the elliptical galaxies NGC 3377 and NGC 4473 (Schulze & Wisotzki 2011) and the lenticular galaxies NGC 821 (Schulze & Wisotzki 2011) and NGC 3585 (Gültekin et al. 2009).

1.5.3 Nuclear star clusters and nuclear stellar discs

There are only few objects where NSCs and NSDs are detected together. In particular, some galaxies of the census of NSDs by Ledo (2010) overlap those studied by Ferrarese et al. (2006a) who looked for the presence of NSCs. This is the case of NGC 4458 and NGC 4478 that are known to host a kinematically decoupled core (Halliday et al. 2001). They are classified as E0-1 (de Vaucouleurs et al. 1991) and E2 (Sandage & Tammann 1981), respectively, and are both low-luminosity ellipticals. Usually NSDs have a larger radius and are less massive that NSCs. Côté et al. (2006) fitted a King law to the surface-brightness profile of NGC 4458 and found an half-light radius of 0.78 arcsec and a total magnitude of $M_B = -18.26$ for the NSC. This corresponds to a total luminosity of $L_{B,T} = 3.1 \times 10^9$ $\mathrm{L}_\odot$. Lauer et al. (2005) fitted a Nuker law to the surface-brightness profiles of NGC 4478 and found a total magnitude of $M_V = -11.6$, corresponding to a total luminosity of $L_{V,T} = 4 \times 10^6$ $\mathrm{L}_\odot$. Morelli et al. (2004, 2010) measured the photometric parameters of the NSDs of some galaxies in several bands using the Scorza-Bender method (Scorza & Bender 1995). They found half-light radii of 0.24 and 0.63 arcsec and total luminosities of 2.7×10^6 and 10.5×10^6 $\mathrm{L}_\odot$ for NGC 4458 (B band) and NGC 4478 (V band), respectively

Moreover, Balcells et al. (2007) found 4 galaxies (NGC 5475, NGC 5707, NGC 5838, NGC 7457) that contain both an extended resolved component, well

fitted with an exponential profile and thus resembling NSDs, and an unresolved component which resembles a NSC. They revealed that the discs and clusters follow quite different relations, for example, between the nuclear disc luminosity and the galaxy luminosity. In fact, in the understanding of scaling relations, distinguishing between NSDs and NSCs plays a key role, as pointed out by Scott & Graham (2013).

Studying the central regions of 77 galaxies, Lauer et al. (2005) found that the elliptical galaxy NGC 1427 hosts a NSC surrounded by an inner disc. They recovered the photometric parameters of the CMO by subtracting the Nuker-law fitted to the pixels beyond the nucleus and found $L_{\rm CMO} = 6 \times 10^6$ L$_\odot$ in the I band. They also deconvolved the *HST* images of the galaxy sample, and from the visual inspection they found that about 20% of the sample galaxy hosts a NSC.

The coexistence of NSCs and NSDs can be detected with the analysis of the disciness of the surface brightness of the galaxy. In fact, many galaxies hosting both the objects show a double peak of the fourth Fourier coefficient A_4, because of the change of the isophotal shape due to the presence of the NSC and NSD. The double-peak feature is also visible in the simulations of Hartmann et al. (2011), who studied how the mergers of star clusters into the nucleus of a galaxy alter the structure and kinematics of NSCs. In their simulated galaxies we were able to detect the presence of a NSD, as shown in the Chapter 2 of the thesis.

1.5.4 Supermassive black holes, nuclear star clusters, and nuclear stellar discs

There are only few objects where SBHs, NSCs, and NSDs are detected together.

The nucleus of NGC 4206, an Sbc galaxy, is interesting because it represents a case where the three incarnations of such CMOs coexist. The NSC of NGC 4206 looks like a miniature S0 galaxy, possessing both an elongated disc and a spheroidal component, with physical dimensions of tens of parsecs or less (Seth et al. 2006). They refer to such kind of structures as multi-component clusters. They fitted a King profile to the surface brightness of NGC 4206 and found a magnitude of $M_I = -14.17$ for the NSC. After the subtraction of the King profile to the total light of the galaxy, the residuals clearly show evidence for a flat disc component. Therefore, they showed that the NSC of NGC 4206 is surrounded by a compact NSD of $h = 31$ pc and a central surface brightness of $\mu_0^0 = 16.61$ in I band. The NSD seems to have formed stars recently and his light dominates the central light of the galaxy with respect to the contribution

of the NSC. Seth et al. (2006) also presented evidence that NGC 4206 may contain an AGN component. In fact, they modelled the stellar continuum with a 3 Gyr single stellar population and measured the line ratio of the diagnostic emission lines finding that the source is a mixed starburst/AGN source. Based on their observational results, they proposed an *in-situ* formation mechanism for NSCs in which stars form episodically in compact NSDs and then they lose angular momentum or heat vertically to form an older spheroidal structure.

A recent work by Lyubenova et al. (2013) has presented the analysis of the NSC in NGC 1428, a nucleated elliptical galaxy in the Fornax Cluster. They found a NSC with an effective radius of 0.08 arcsec by modelling the surface-brightness profile with a Sérsic law. Using SINFONI observations, they measured the stellar kinematics and found that the NSC does not rotate within their detection limit of 6 km s^{-1}. The outer kinematics shows a clear cut rotation with a maximum at 0.6 arcsec from the galaxy centre, which overlaps the peak of the disciness of the fitted isophotes. Therefore, a dynamically cold rotating structure which has the characteristics of a NSD is present in NGC 1428. Thus, the NSC seems to be embedded in the NSD which is younger and more metal rich than the main body of the galaxy. Due to the large uncertainties on the central kinematics, they put an upper limit for a possible SBH of 10^7 $M_\odot$. The complex structure of the CMO of NGC 1428 indicates a complex formation history. Most likely gas dissipation and merging played an important role in shaping the nucleus of this galaxy.

Furthermore, there are found some interesting cases of coexistence between SBHs, NSCs, and NSDs matching the sample galaxies of several works. For example, Lauer et al. (2005) identified 4 galaxies where the NSC is surrounded by an inner stellar disc: the lenticular galaxies NGC 1023, NGC 3115, NGC 4026, and the spiral NGC 3384. The total luminosities of the NSCs are 3×10^6, 8×10^6, 4×10^6, and 4×10^6 in the I band, respectively. For these galaxies there are dynamical studies which led to SBH masses of $M_\bullet$=4.1×10^7, 9.0×10^8, 1.8×10^8, and 1.1×10^7 $M_\odot$, respectively (Bower et al. 2001; Emsellem et al. 1999; Gültekin et al. 2009; Schulze & Wisotzki 2011). Chapter 3 of the thesis is focused on the study of the NSD of NGC 1023.

1.6 Aim of the thesis

The aim of the thesis is to shed light on the physics of the central regions of the galaxies. Studying the properties of CMOs gives us the chance of understanding the assembling history of the galactic nuclei and characterising the structural components of the galaxies. We want to explore whether a continuity between

the properties of SBHs, NSCs, and NSDs exists and how they are connected with those of the hosting galaxy. In fact, understanding the formation scenarios and searching for the scaling relations between the CMOs is fundamental to provide clues about the physical properties of the formation and evolution of galaxies.

The detailed structure of this thesis is as follows.

CHAPTER 1: Introduction.

One of the key questions of the extragalactic research in the last years is how galaxies formed and evolved and how the physics of the central region of galaxies is related to these processes. Indeed, the nuclei of galaxies occupy a privileged position at the bottom of the galactic potential well and their morphology, dynamics, star formation, and chemical enrichment provide important insight into the evolutionary history of galaxies. In this picture, the study of central massive objects (CMOs), namely supermassive black holes (SBHs), nuclear star clusters (NSCs), and nuclear stellar discs (NSDs) is particularly relevant.

SBHs can be detected with high-resolution observations and are believed to be the cause of the past or present activity of the galaxies. The masses of the SBHs range between 10^6 $M_\odot \lesssim M_\bullet \lesssim 10^{10}$ $M_\odot$ and can be measured with several methods. Stellar and/or gas dynamical models, spectro-astrometry, and analysis of water megamasers are adopted for quiescent galaxies. Reverberation mapping is used for active galaxies and allows to measure the mass of SBHs at high redshift. SBHs are found to correlate with several properties of their host galaxy. The formation of such kind of objects is still unclear. They can form from massive primordial stars, or due to the collapse or merging of massive objects, such as star clusters.

NSCs are commonly found in the centres of both elliptical and disc galaxies. They are very massive ($M_{\rm NSC} \sim 10^5 - 10^8$ $M_\odot$), very compact ($r_{\rm e} \sim 5$ pc), and very bright ($-14 < M_I < -10$). They can have multiple stellar populations, possessing both an old spheroidal component and a younger elongated disc or ring component. The mass of NSCs tightly correlates with the total mass of the galaxy, but several other correlations have been proposed to link the properties of the NSCs with those of the host galaxy. A combined scenario where star formation occurs in the centre of galaxies after dissipation processes and accretes mass via the mergers of globular clusters seems the more plausible way to form NSCs.

NSDs are small ($h \sim 10 - 50$ pc) and bright ($\mu^0_{0,V} \sim 16 - 19$ mag arcsec^{-2}) discs. They never dominate the light distribution of the galactic nuclei, and locally contribute at most half the galaxy surface brightness. They are fragile systems and do not survive a major merger. Therefore, their age could constrain the epoch of the last major merger of the host galaxy. About 20% of elliptical and spiral galaxies hosts a NSD. Their stellar population has been studied in

details in only a few objects, showing a variety of phenomena. NSDs follow the same relation between the central face-on surface-brightness and the scalelength as the main discs of lenticular and spiral galaxies and embedded discs of early-type galaxies. No other relations were found with the properties of the host galaxy. The external capture or the secular infall of gas into the centre where it accumulates, dissipates and forms stars are the most studied scenarios to form NSDs.

SBHs, NSCs, and NSDs have been observed to coexist in some galaxies. The most investigated case is the coexistence of SBHs with NSCs, rising the question whether they are two incarnations of a same object and share a common formation scenario. In galaxies where a SBH coexists with a NSD, such a disc can be used to measure the SBH mass. NSCs are found to be surrounded by central discs of stars, i.e. NSDs. The three types of CMOs are found to coexist only in a very few galaxies. But a full statistics is still missing and detailed studies of objects with SBHs, NSCs, and NSDs are required.

CHAPTER 2: Searching for nuclear stellar discs in simulations of star cluster mergers.

To investigate the formation and growth of NSDs we look for their presence in a set of $N-$body simulations studying the dissipationless merging of multiple star clusters in galactic nuclei. A few tens of star clusters with sizes and masses comparable to those of globular clusters observed in the Milky Way are accreted onto a pre-existing nuclear stellar component: either a massive super star cluster or a rapidly rotating, compact disc with a scalelength of a few parsecs, mimicing the variety of observed nuclear structures.

Images and kinematic maps of the simulation time-steps are then built and analysed as if they were real and at the distance of the Virgo cluster. No NSD-like object results from the accretion of star clusters onto a pre-existing super star cluster. Instead the merger remnant has all the observed properties of a NSD when the star clusters are accreted onto a pre-existing smaller disc, even when the accreted mass is $10\times$ larger than the mass of the original disc. The photometric and kinematic properties of the NSD in the simulated galaxy are remarkably similar to those of NSDs observed in real galaxies.

This shows that, although the pre-existing disc structure possibly indicates that some gas dissipation is needed at early stages for the formation of NSD, most of its mass can be assembled from already formed stars through the migration and accretion of star clusters into the galactic centre.

CHAPTER 3: The young nuclear stellar disc in the SB0 galaxy NGC 1023.

Small kinematically-decoupled stellar discs with scalelengths of a few tens of parsec are known to reside in the centre of galaxies. Different mechanisms have been proposed to explain how they form including gas dissipation and

merging of globular clusters. Using archival *Hubble Space Telescope* imaging and ground-based integral-field spectroscopy, we investigated the structure and stellar populations of the nuclear stellar disc hosted in the interacting SB0 galaxy NGC 1023. The stars of the nuclear disc are remarkably younger and more metal-rich with respect to the host bulge. These findings support a scenario in which the nuclear disc is the end result of star formation in gas piled up in the galaxy centre. The gas can be of either internal or external origin, i.e. from either the main disc of NGC 1023 or the nearby interacting satellite NGC 1023A. The dissipationless formation from already formed stars through the migration and accretion of star clusters into the galactic centre is rejected.

CHAPTER 4: The supermassive black hole and the nuclear star cluster of NGC 383.

We present archival *Hubble Space Telescope* imaging and spectroscopic observations of the S0 galaxy NGC 383 obtained with the *Wide Field and Planetary Camera 2* mounting the F814W filter and the *Space Telescope Imaging Spectrograph* using the G570M grism, respectively. The data provide detailed information on the structure and mass profile of the stellar component, the dust optical depth, and the spatial distribution and kinematics of the ionised gas within the innermost region of the galaxy. Dynamical models, which account for the observed stellar mass profile and include the contribution of a nuclear star cluster (NSC) and a central supermassive black hole (SBH), are constructed to reproduce the kinematics derived from the [N II]λ6583 emission line along three slit positions crossing the nucleus and parallel to the galaxy major axis. A secure SBH detection with $M_\bullet = 8.5^{+1.8}_{-1.3} \times 10^8$ M$_\odot$ is obtained when a single massive central object (CMO) is considered. If we account for the presence of the NSC, then the masses of the SBH and NSC are $M_\bullet = 6.0^{+1.8}_{-1.2} \times 10^8$ M$_\odot$ and $M_{\rm NSC} = 8.9^{+5.0}_{-3.9} \times 10^7$ M$_\odot$, respectively. Both are consistent with the scaling relations linking the mass of CMOs with the properties of their host galaxy. These measurements prove that SBHs can coexist with NSCs and represent an important step forward in the characterisation of CMOs.

CHAPTER 5: Conclusions. The aim of this thesis was to investigate the physics of the central regions of galaxies. This was done by characterising some aspects of the central massive objects (CMOs) found to live in the galactic nuclei, such as studying the possible formation scenarios, stellar properties and scaling relations.

We highlighted the importance of understanding the physical properties of CMOs in galaxies by exploring their possible connection with the host galaxies. So far a few studies have been devoted to explore the coexistence of the different CMOs in the same galaxy. After reviewing the previous works on the properties,

formations scenarios, and scaling relations of supermassive black holes (SBHs), nuclear star clusters (NSCs), and nuclear stellar discs (NSDs), we presented our new results. They are based on a variety of methods aimed to understand the connection between NSDs and NSCs, and between SBHs and NSCs, ranging from N-body simulations, photometric and spectroscopic analyses of archival *HST* imaging and ground-based integral-field spectroscopy up to dynamical models, used to investigate stellar populations, and estimate the masses of CMOs.

The main conclusions and developments of this thesis can be summarised as follows.

1. NSDs can form via accretion events, but a certain amount of gas is necessary. As a future work we plan to analyse simulations of merging events which take into account the role of gas;

2. The young stellar population of the NSD of NGC 1023 suggests a formation via gas dissipation. Our proposed technique can be applied to galaxies with *SAURON* or *ATLAS3D* data to have more statistics about stellar populations of NSDs without the contamination of the bulge and to constrain the formation scenarios of such objects;

3. A SBH and a NSD coexist in NGC 383 and follow different scaling relations with the host galaxy. For the first time we were able to disentangle simultaneously the mass of both the CMOs of NGC 383 using dynamical modelling. More statistics of galaxies which host different types of CMOs is needed to understand the relations between these objects and the host galaxy.

Chapter 2

Searching for nuclear stellar discs in simulations of star cluster mergers

Abstract

The nuclei of galaxies often host small stellar discs with scalelengths of a few tens of parsecs and luminosities up to 10^7 $L_\odot$ in V band. To investigate the formation and properties of nuclear stellar discs (NSDs), we look for their presence in a set of $N-$body simulations studying the dissipationless merging of multiple star clusters in galactic nuclei. A few tens of star clusters with sizes and masses comparable to those of globular clusters observed in the Milky Way are accreted onto a pre-existing nuclear stellar component: either a massive super star cluster or a rapidly rotating, compact disc with a scalelength of a few parsecs, mimicking the variety of observed nuclear structures. Images and kinematic maps of the simulation time-steps are then built and analysed as if they were real and at the distance of the Virgo cluster. We use the Scorza-Bender method to search for the presence of disc structures via photometric decomposition. In one case the merger remnant has all the observed photometric and kinematic properties of NSDs observed in real galaxies. This shows that current observations are consistent with most of the NSD mass being assembled from the migration and accretion of star clusters into the galactic centre. In the other simulation instead, we detect an elongated structure from the unsharp masked image, that does not develop the photometric or kinematic signature of an NSD. Thus, in the context of searches for a disc structure, the Scorza-Bender method is a robust and necessary tool.

2.1 Introduction

The nuclei of galaxies occupy a privileged position at the bottom of the galactic potential well. Thus the morphology, dynamics, star formation, and chemical enrichment provide important insight into the evolutionary history of galaxies. Indeed galactic nuclei record the history of the material, whether coming from neighbouring galactic regions or accreted through mergers, that has sunk to the dynamical centre over the lifetime of the parent system.

Due to its superb spatial resolution, the *Hubble Space Telescope (HST)* has been used extensively to image the nuclei of nearby galaxies. Numerous surveys have been carried out to investigate their structure on scales of 10-100 pc over a wide range of morphological types. *HST* imaging has shown that about 20 per cent of elliptical (Ledo et al. 2010) and spiral galaxies (Pizzella et al. 2002) host a nuclear stellar disc (NSD). NSDs are smaller (scalelength $h \sim 10 - 50$ pc) and brighter (central surface brightness $\mu^0_{0,V} \sim 16 - 19$ mag arcsec^{-2}) than embedded discs in early-type galaxies (Scorza & Bender 1995), but they never dominate the light distribution of the galactic nuclei, and locally contribute at most half the galaxy surface brightness. Interestingly, independent of the Hubble type of their host galaxy, NSDs seem to follow the same relation between the central surface brightness and scalelength as the main discs of lenticular and spiral galaxies and as the embedded discs of early-type galaxies (van den Bosch 1998).

Various methods have been used to detect NSDs. The simplest, and therefore traditional, method is the unsharp-mask technique to recover non-circular structures in an image (Pizzella et al. 2002). Alternatively, the Scorza-Bender method (Scorza & Bender 1995) recovers the basic structural properties of an NSD (central surface brightness, scalelength, inclination, and major-axis position angle) by subtracting from the image the best exponential disc model, which is generally assumed to be perfectly thin.

NSDs have received attention primarily as probes of the mass distribution since they permit measurement of the mass of central supermassive black holes (SBHs) through observation of their stellar kinematics (e.g., van den Bosch & de Zeeuw 1996; Magorrian 1999; Cretton & van den Bosch 1999). However, the study of NSDs can also advance our understanding of galaxy formation and evolution since their formation and destruction reflect the assembly history of their host galaxies. For example, being dynamically cold systems, NSDs are fragile and do not survive a major merger. Especially in the presence of SBHs of comparable mass, they would be significantly affected by the interaction with a second SBH carried by the merging galaxy (Ledo et al. 2010). Therefore, the age of an NSD constrains the epoch of the last major merger of the host galaxy.

Different mechanisms have been proposed to explain how NSDs form. The capture of external gas accounts for the origin of the counter-rotating NSD in NGC 4458 (Morelli et al. 2004, 2010). Indeed, the presence of a kinematically decoupled component is usually interpreted as the signature of gas accretion or merging of satellite galaxies (Bertola & Corsini 1999). An external origin is also invoked for the gas which formed the stars of the nuclear disc in the early-type spiral NGC 4698, which is rotating perpendicularly with respect to the main galactic disc (Bertola et al. 1999; Pizzella et al. 2002; Corsini et al. 1999, 2012). The secular infall of gas, perhaps via a barred potential, is an alternative way to funnel pre-enriched material into the galactic centre where it accumulates, dissipates, and forms stars. This scenario provides a natural explanation for the presence of NSDs in barred galaxies (e.g., NGC 7332, Seifert & Scorza 1996; Falcón-Barroso et al. 2004). In some cases a bar may even be destroyed in the process, as has been proposed for NGC 4570 (Scorza & van den Bosch 1998; van den Bosch & Emsellem 1998; van den Bosch et al. 1998; Krajnović & Jaffe 2004; Morelli et al. 2010) and NGC 4621 (Sil'chenko 1997).

Examples of on-going formation via dissipation include the NSDs in NGC 5845 (Kormendy et al. 1994) and in NGC 4486A (Kormendy et al. 2005). However, other NSDs are as old as the main body of the host galaxy (NGC 4128, Krajnović & Jaffe 2004; NGC 4342, van den Bosch et al. 1998; NGC 4458, Morelli et al. 2004; NGC 4621, Krajnović & Jaffe 2004; NGC 4698, Corsini et al. 2012). The stellar populations in NSDs have been studied in detail in only a few more objects. In NGC 4478 the NSD is younger, more metal-rich and less over-abundant than the rest of the galaxy (Morelli et al. 2004). In contrast the NSD of NGC 5308 is made of a younger and more metal-poor stellar population than the host galaxy (Krajnović & Jaffe 2004). Both the NSD and bulge of NGC 4570 show an intermediate-age stellar population although the NSD is more metal rich (Krajnović & Jaffe 2004).

In some cases an NSD co-exists with a massive and dense nuclear star cluster with typical $L_V \sim 10^6 - 10^7$ $L_\odot$ and effective radius of a few parsecs. These objects are observed in the centre of both early- (e.g., NGC 4458, NGC 4478, and NGC 4570, Ferrarese et al. 2006a; Ledo et al. 2010) and late-type galaxies (e.g., NGC 4206, Seth et al. 2006).

Despite recent progress, no satisfying explanation has been provided for the deposition of the high gas densities that are needed to enable an *in situ* formation of nuclear star clusters (Shlosman & Begelman 1989; Milosavljević 2004; Bekki 2007; Emsellem & van de Ven 2008). An alternative scenario for the build-up of nuclear star clusters is the dissipationless coalescence of star clusters sinking to the bottom of the potential well by dynamical friction (Tremaine et al. 1975; Capuzzo-Dolcetta 1993; Lotz et al. 2001; Capuzzo-Dolcetta & Mioc-

chi 2008a,b; Antonini et al. 2012; Antonini 2013). Agarwal & Milosavljević (2011) showed that the rate at which the nuclear star cluster grows by accreting young star clusters depends on their formation rate, migration time, and dissolution time. The resulting compact nuclear star cluster is embedded in a more extended and diffuse component resembling a small pseudo-bulge. The size of such a disc-like structure in models including the prompt dissolution of star clusters matches that of the observed NSDs. This opens the possibility that NSDs may be forming via star cluster accretion. In addition, the observed scaling relations between the nuclear star cluster masses and the velocity dispersion of their host spheroids and between the sizes of nuclear star clusters and their luminosities can be explained by a dissipationless scenario (Antonini 2013).

Some nuclear star clusters have a complex structure possessing both a spheroidal component and an elongated ring or disc component with a scale-length of a few parsecs (Seth et al. 2006, 2008b). Hartmann et al. (2011, hereafter H11) and De Lorenzi et al. (2013) found that no more than half the mass of the multi-component nuclear star cluster in NGC 4244 could have been assembled in star clusters that migrated and merged at the centre of the galaxy. They concluded that the rest of the nuclear star cluster mass must have been produced by *in situ* star formation. In this paper we analyse some of the $N-$body simulations of H11 to look for the presence of an NSD and to test whether the dissipationless merger of star clusters is a viable scenario for the formation and growth of NSDs (as opposed to nuclear star clusters).

The details of the simulations are given in Section 2.2, and the pseudo-surface photometry and stellar kinematics are discussed in Section 2.3. Section 2.4 describes the search for NSDs, the measurement of their structural properties using the Scorza-Bender method, the estimate of the expected luminosity and mass of the NSD, the analysis of the evolution of the galaxy components, and the computation of the rotation parameter. Results and conclusions are discussed in Section 3.4 and 2.6, respectively.

2.2 Simulations

The simulations used in this thesis have been described in H11: in this section we provide a full description of these, also referring the reader to H11 for more details. They presented an extensive set of simulations testing the importance of purely stellar dynamical mergers on the formation and growth of nuclear star clusters, setting up 6 models with different initial conditions and properties (Table 2.1). After letting them to evolve, they fitted the mass surface density

profiles of the remnants, using Sérsic (1968) and King (1962) profiles, finding the structural properties of the simulated nuclear star clusters. Such properties were then compared with the ones obtained from observations and dynamical models of the nuclear star clusters at the centres of the late-types, bulge-less galaxies NGC 4244 and M33. They concluded that mergers of star clusters are able to produce a wide variety of observed properties, e.g., densities, structural scaling relations, shapes (including the presence of young discs) and even rapid rotation. Besides they were not able to reproduce the kinematics, suggesting that purely stellar dynamical mergers can not form nuclear star clusters, and that gas dissipation is a necessary ingredient for at least $\approx 50\%$ of the mass of a nuclear star cluster.

Aimed at the search of the presence of NSDs, we selected models A1 and A2 because they presented discy isophotes, as shown in the Figures 12 and 15 of H11 for edge-on projections. Models M1, M2, and M3 showed boxy isophotes, therefore they were rejected. Model A3 has the same physical conditions such as model A2, varying only for the kinematics. Therefore, we planned to study models A1 and A2 from H11 and we continue to refer to them as such here.

2.2.1 Bulge model

Both of the models live at the centre of a Hernquist (1990) bulge, with a mass density given by

$$\rho(r) = \frac{aM_{\rm b}}{2\pi r\,(r+a)^3}, \tag{2.1}$$

where $M_{\rm b}$ is the bulge mass and a is the scale radius. H11 use $M_{\rm b} = 5 \times 10^9$ $\mathrm{M}_\odot$ and $a = 1.7$ kpc. The bulge is populated by 3.5×10^6 particles with masses selected by the weighting function $w(L) \propto 3 + 5000L^2$, with L the specific angular momentum, which ensures a high resolution within the inner 160 pc (Sellwood 2008). In the case of equal mass particles for the galactic bulge, their mass is of 1500 $\mathrm{M}_\odot$. Such high mass particles would inhibit dynamical friction on objects of mass $\sim 10^4$ $\mathrm{M}_\odot$, and lead to excessive heating of any infalling clusters. Using multi-mass particles ranging from 40 $\mathrm{M}_\odot$ at the centre to 3.9×10^5 $\mathrm{M}_\odot$ further out reduces such effects. Their softening is related to their mass via $\varepsilon_p \propto m_p^{1/3}$, as shown in Figure 8 of H11. The bulge is truncated at $r > 15a$ by eliminating all particles with an energy to reach this distance. Thus at this radius the density drops gently to zero (Sellwood & Debattista 2009). Although accretion delivers higher mass particles into the central region, the distribution of particles does not change substantially.

2.2.2 Star cluster models

H11 set up model star clusters, ranging in mass from 2×10^5 $M_\odot$ to 2×10^6 $M_\odot$, using the isotropic distribution function of a lowered polytrope with index $n = 2$

$$f(x, v) \propto [-2E(x, v)]^{1/2} - [-2E_{\max}]^{1/2} \tag{2.2}$$

where (x, v) are the phase space coordinates, and E is the energy. This distribution function reproduces well the core profile of observed star clusters, as shown in Figure 9 of H11. They set up three models in equilibrium via the iterative procedure described in Debattista & Sellwood (2000). Using the naming scheme of H11, we refer to them as C3-C5. Star cluster models have all particles (4×10^5 for C3 model and 4×10^4 for C4-C5) of equal mass (5.0 $M_\odot$ for C3-C4 and 15 $M_\odot$ for C5) and equal softening ($\varepsilon = 0.13$ pc). No black holes have been included in the star cluster models. Table 2.2 lists the properties of the star cluster models. The concentration c is defined as $c \equiv \log(R_{\rm e}/R_{\rm c})$ where $R_{\rm e}$ is the half mass radius and $R_{\rm c}$ is the core radius, where the surface-density drops to half of the central. The masses and sizes of the star clusters are comparable to young massive star clusters in the Milky Way (Figer et al. 1999, 2002), in the Large Magellanic Cloud (Mackey & Gilmore 2003), in the Fornax Cluster (McLaughlin & van der Marel 2005), in irregular galaxies (Larsen et al. 2004), and in interacting galaxies (Bastian et al. 2006).

2.2.3 Numerical parameters

All the simulations were evolved with PKDGRAV (Stadel 2001), an efficient, parallel tree-code. PKDGRAV is a multi-stepping code, with timesteps refined such that $\delta t = \Delta t/2^n < \eta(\varepsilon/a)^{1/2}$, where ε is the softening and a is the acceleration at a current position of particles. H11 used an opening angle $\theta = 0.7$ in all models, setting $\eta = 0.1$, and a base timestep $\Delta t = 10^5$ years.

The relaxation time for those regions of galaxies is $\sim$ 10 Gyr. Galaxies in the Virgo Cluster have relaxation times ranging from $1 - 10$ Gyr (Merritt 2009). Therefore, it is reasonable to approximate NSDs as collisionless systems on timescales of $\lesssim$ 1 Gyr, allowing them to use standard collisionless codes to simulate their evolution. We neglect the dark matter halo since we are interested in the evolution in the inner $\sim$ 100 pc of galaxies.

2.2.4 Properties of models A1 and A2

The models A1 and A2 were originally aimed at the investigation of the photometric, kinematic, and dynamic properties of the nucleus of the Sc spiral galaxy

NGC 4244 which hosts a massive stellar cluster in rapid rotation (Seth et al. 2006, 2008b).

In model A1 H11 studied how the accretion of further star clusters can alter the structure and kinematics of a nuclear star cluster and how much mass needs to be accreted to appreciably alter the isotropic distribution of globular clusters (as Gebhardt et al. 1995 observed in the Milky Way). Moreover, the complex star formation history of observed nuclear star clusters indicate that the formation is caused by periodic star formation episodes, which can be produced by the multiple accretion of young star clusters formed in the proximity. The initial seed is a massive star cluster formed in the central region, which has fallen to the centre of the galaxy. This is the case of NGC 253 as found by Kornei & McCrady (2009) where a super star cluster is falling into the centre of the galaxy forming the basis of a nuclear star cluster. The simulation is evolved within the bulge model. In details, the initial model in run A1 consists of the bulge hosting a nuclear cluster spheroid (NCS), produced by letting star cluster C3 to fall to the centre starting from a circular orbit at 127 pc on allowing it to settle at the centre over 65 Myr, before the accretion of the star clusters start. They used model C5 for the accreted star clusters, starting them on circular orbits at a distance of 32 pc from the centre. Each accretion is allowed to finish before a new star cluster is inserted. A single accretion on average requires ~ 20 Myr. In total 27 star clusters, corresponding to $8.1\times$ the initial mass of NCS, are accreted in 810 Myr. Table 2.3 gives further details of this model and Figure 2.1 shows a screen-shot of the final timestep of the simulated model A1 using the colour codes of TIPSY[1].

Some nuclear star clusters have a complex structure possessing both a spheroidal component and an elongated ring or a small disc component with a scalelength of a few parsecs (Seth et al. 2006, 2008b). The model A2 was built in H11 to understand if the direct formation of a such small disc (called nuclear cluster disc, NCD) via gas inflows precedes the full formation of a nuclear star cluster and how the accretion of star clusters alters the properties of the initial seed. Because of the simulations do not include smooth particles hydrodynamics, but only pure $N-$body systems, in order to mimic the dissipative formation, H11 generated a bare NCD model as a seed by adiabatically growing an exponential disc at the centre of the bulge model over a period of 500 Myr. The mass density of the NCD is

$$\rho(R,z) = \frac{M_{\rm d}}{2\pi R_{\rm d}^2} e^{-R/R_{\rm d}} \frac{1}{\sqrt{2\pi} z_{\rm d}} e^{-z^2/2z_{\rm d}^2}, \tag{2.3}$$

[1]TIPSY, a theoretical image processing system, is distributed by the N-body shop at Department of Astronomy at the University of Washington, see `hpcc.astro.washington.edu`.

with a scalelength $R_{\rm d}$ = 9.5 pc, scale-height $z_{\rm d} = 0.1R_{\rm d}$ and mass of 1 × 10^6 $M_\odot$. They set Toomre-Q = 1.2, as described in Debattista & Sellwood (2000). In this model they accreted 50 copies of model C4 sequentially in 1.8 Gyr, each starting 63 pc from the centre. This corresponds to 10× the initial mass of NCD. The disc, truncated at a radius of $5R_{\rm d}$, consists of 2 × 10^5 particles each with softening ε = 0.13 pc. The final total mass is 1 × 10^6 $M_\odot$. Table 2.3 gives further details of this model and Figure 2.1 shows a screen-shot of the final timestep of the simulated model A2 using Tipsy colour codes. Also the model A2 is evolved within the bulge model.

Table 2.1: The merger models.

Model (1)	$N_{\rm SC}$ (2)	Host (3)	Comment (4)
M1	8	Disc	Star clusters at mid-plane of main disc
M2	8	Disc	Six star clusters offset from main disc mid-plane
M3	8	Disc	Star clusters at mid-plane of main disc
A1	10	Bulge	Multiple accretion of star clusters onto NCS
A2	20	Bulge	Accretion of star clusters onto a NCD
A3	20	Bulge	Like A2 with 50% retrograde orbits

Note. Col.(1): Name of the model. Col.(2): Number of accreted star clusters. Col. (3): Host galaxy model. Col.(4): Short description of the model.

Table 2.2: Models of star clusters used in the simulations.

Model	$N_{\rm p}$	$M_{\rm p}$ [$M_\odot$]	M_* [$M_\odot$]	$R_{\rm e}$ [pc]	c	ε [pc]	SBH
(1)	(2)	(3)	(4)	(5)	(6)	(7)	(8)
C3	399996	5.00882	2.0×10^6	2.18	0.12	0.13	No
C4	39996	15.0001	2.0×10^5	1.11	0.12	0.13	No
C5	39996	15.0001	6.0×10^5	1.11	0.16	0.13	No

Note. Col.(1): Name of the star cluster model. Col.(2): Number of particles for each model. Col. (3): Mass of each particle. Col.(4): Total stellar mass of the model. Col.(5): Half-mass radius. Col.(6): Concentration parameter. Col.(7): Softening parameter. Col.(8): Presence of a central SBH.

Table 2.3: Properties of models A1 and A2.

Code	Model	Seed	Host	T [Gyr]	$N_{\rm SC}$	Star cluster model	$N_{\rm Nucl}$	$M_{\rm Nucl}$ [10^6 M$_\odot$]	$\frac{M_{\rm SC}}{M_{\rm seed}}$	$N_{\rm Host}$	$M_{\rm Host}$ [10^9 M$_\odot$]
(1)	(2)	(3)	(4)	(5)	(6)	(7)	(8)	(9)	(10)	(11)	(12)
A1_10	A1	NCS	Bulge	0.31	10	C5	799956	8.00	3	3500000	5.00
A1_20	A1	NCS	Bulge	0.60	20	C5	1199916	14.00	6	3500000	5.00
A1_27	A1	NCS	Bulge	0.81	27	C5	11479888	18.20	8.1	3500000	5.00
A2_10	A2	NCD	Bulge	0.26	10	C4	599958	3.00	2	3500000	5.00
A2_20	A2	NCD	Bulge	0.60	20	C4	999918	5.00	4	3500000	5.00
A2_30	A2	NCD	Bulge	1.00	30	C4	1399878	7.00	6	3500000	5.00
A2_40	A2	NCD	Bulge	1.40	40	C4	1799838	9.00	8	3500000	5.00
A2_50	A2	NCD	Bulge	1.82	50	C4	2199798	11.00	10	3500000	5.00

NOTE. Col.(1): Name of the model timestep. Col.(2): Name of the model. Col.(3): Initial seed model. Col.(4): Galaxy model. Col.(5): Elapsed time in Gyr. Col.(6): Number of accreted star clusters. Col.(7): Name of the star clusters model. Col.(8): Number of particles in the nucleus (star cluster + seed). Col.(9): Total stellar mass in the nucleus (star cluster + seed). Col.(10): Ratio of the accreted-to-seed mass. Col.(11): Number of particles of the host. Col.(12): Total stellar mass of the host.

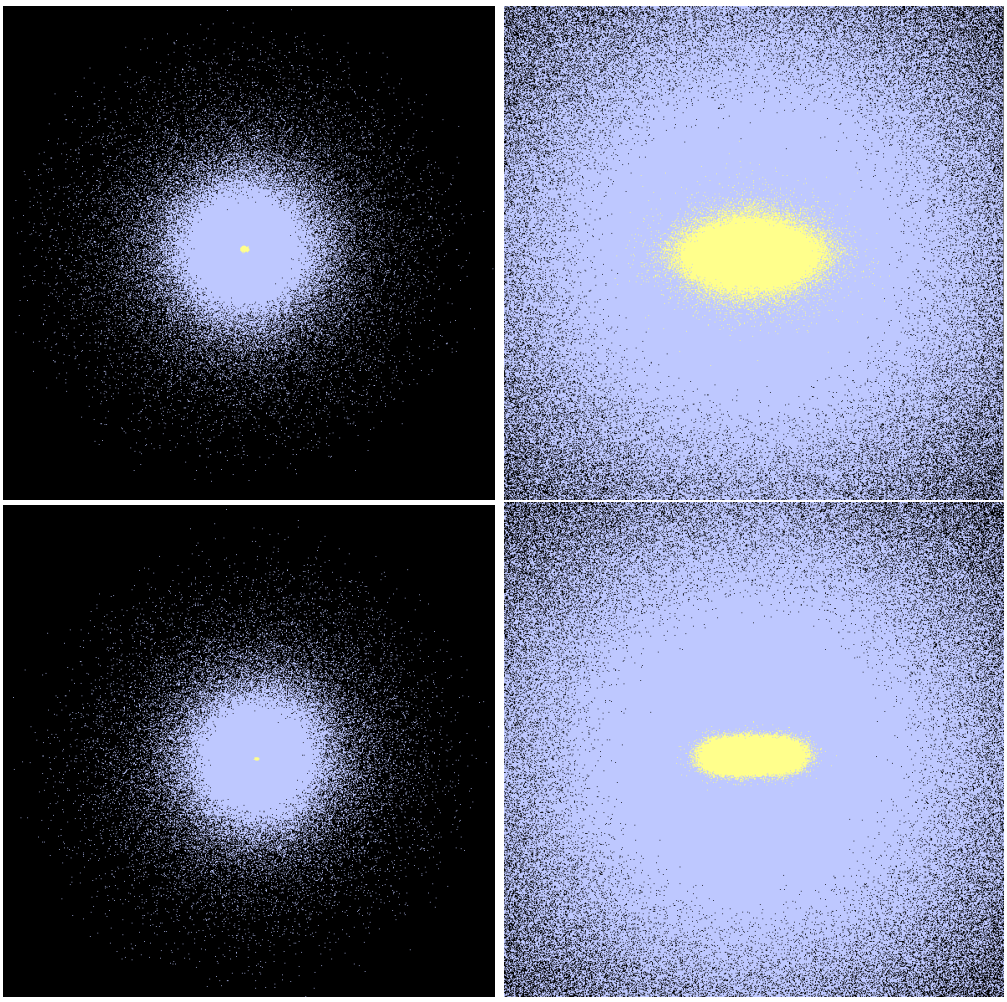

Figure 2.1: TIPSY screen-shots of the last timestep of the studied simulations for model A1 (top panel) and A2 (bottom panel). The fields of view are 50×50 kpc (left-hand panels) and 1.7×1.7 kpc (right-hand panels). The yellow points represent the star particles (i.e., the initial seed of the nuclear star cluster and the accreted star clusters), while blue points represent the surrounding particles (i.e., the bulge).

2.3 Pseudo surface photometry and stellar kinematics

2.3.1 Luminosity weighted images

H11 studied model A1 after the accretion of 10 star clusters and model A2 after the accretion of 20 star clusters. Likewise, we decided to consider 3 outputs from each run. We analysed model A1 after the accretion of 10, 20, and 27 star clusters and model A2 after the accretion of 10, 30, and 50 star clusters. To analyse the simulations as they were real galaxies, we started by building B- and I-band mock images for each timestep, choosing the appropriate distance, instrumental set-up, stellar populations, and galaxy inclination as explained in the following sections.

Galaxy distance and instrumental set-up

All the simulations of H11 were built to match the photometric and kinematic properties of the two nearby galaxies NGC 4244 and M33, that host well resolved nuclei for which integral field data are available. M33 is a late-type spiral, with an inclination $i = 49°$ and a distance $D = 0.8$ Mpc (Lauer et al. 1998). NGC 4244 is an edge-on Sc galaxy at 4.4 Mpc (Seth et al. 2005). Furthermore, because the aim of this work is trying to detect NSDs in ordinary galaxies, we decided to adopt the distance of the simulated galaxies by looking in the literature how far are the galaxies known to host a nuclear stellar disc.

Ledo et al. (2010) compiled the most comprehensive census of NSDs in nearby early-type galaxies by searching for nuclear discs in objects within 100 Mpc with available *HST* images. In order to study their physical properties, they separated the light contribution of 12 NSDs from that of their hosting spheroid. The mean distance of such NSDs is 40.3 Mpc, but most of them are in Virgo Cluster galaxies. This is also the case of the majority of previous detections: NGC 4458, NGC 4478, and NGC 4570 (Morelli et al. 2010), NGC 4486A (Kormendy et al. 2005), and NGC 4698 (Corsini et al. 2012). Therefore, we consider 16 and 40 Mpc as possible distances to be adopted for our analysis.

Most of the photometric analysis aimed at the study of the galactic nuclei is done using the *HST* instrumentation, because of the crucial importance of a subarcsec resolution. To select the final distance to be adopted for the simulated galaxies, we investigated the cameras of the main instruments on board the *HST*: the *Wide Field Planetary Camera 2 (WFPC2)*, the *Advanced Camera for Surveys (ACS)* and the *Wide Field Camera 3 (WFC3)*.

WFPC2 was mounted on *HST* during the first servicing mission. It is composed by four cameras that cover the spectral range between 1150 Å and 10500 Å. Each camera operates with different settings:

- the three *Wide Field Cameras (WFC)* have a field of view of 80 arcsec $\times$80 arcsec with an image scale of 0.1 arcsec pixel^{-1} and give rise to an "L"-shaped field of view.
- the *Planetary Camera (PC)* has a field of view of 36 arcsec $\times$ 36 arcsec and a plate scale of 0.046 arcsec pixel^{-1}.

ACS is a third-generation *HST* instrument for accurate photometry, which was repaired after an electronic malfunction during the Servicing Mission 4. It includes three channels:

- the *Wide Field Channel (WFC)*, with a field of view of 202 arcsec $\times$ 202 arcsec, a plate scale of 0.05 arcsec pixel^{-1} and covering the range from 3500 Å to 11000 Å;
- the *High Resolution Channel (HRC)*, with a field of view of 29 arcsec $\times$ 26 arcsec, a plate scale of 0.027 arcsec pixel^{-1} and covering the range from 1700 Å to 11000 Å;
- the *Solar Blind Channel (SBC)*, with a field of view of 34.6 arcsec $\times$ 30.5 arcsec, a plate scale of 0.032 arcsec pixel^{-1} and spanning the range from 1150 Å to 1700 Å.

WFC3 is a fourth-generation camera that operates in two spectral ranges, using two channels. It was mounted during the Servicing Mission 4:

- the *Ultraviolet and visible (UVIS)* channel, with a field of view of 162 arcsec $\times$ 162 arcsec, a plate scale of 0.04 arcsec pixel^{-1}, and spans the range from 2000 Å to 10000 Å;
- the *Infrared (IR*) channel, with a field of view of 123 arcsec $\times$ 136 arcsec, a plate scale of 0.13 arcsec pixel^{-1}, and covers the range from 9000 Å to 17000 Å.

The smallest NSD in the sample of Ledo et al. (2010) is in the galaxy ESO 352-057 and has a scalelength $h = 44.7$ pc. We decided to choose the instrument providing us the highest performance in observing such size. Table 2.4 shows the pixel size of the NSD of ESO 352-057 on the detector and the physical extension of the fields of view assuming $D_1 = 16$ Mpc and $D_2 = 40$ Mpc. All the

Table 2.4: Selection of the *HST* instrument.

Instrument/Camera	Plate scale [arcsec pixel^{-1}]	FoV [arcsec^2]	h_1 [pixel]	FoV$_1$ [kpc^2]	h_2 [pixel]	FoV$_2$ [kpc^2]
(1)	(2)	(3)	(4)	(5)	(6)	(7)
ACS/HRC	0.027	29×26	22.8	2.3×2.0	9.6	5.6×5.0
ACS/SBC	0.032	35×31	18.9	2.7×2.4	7.9	6.8×6.0
ACS/WFC	0.05	202×202	11.0	15.7×15.7	5.2	39.2×39.2
WFPC2/PC	0.046	36×36	14.3	2.8×2.8	5.6	7.1× 7.1
WFPC2/WF	0.1	80×80	6.8	6.2×6.2	2.6	15.5 ×15.5
WFC3/UVIS	0.04	162×162	16.3	12.6×12.6	6.5	31.4×31.4
WFC3/IR	0.13	123×136	20.5	9.5×10.6	8.2	23.9×26.4

Note. Col.(1): *HST* instrument and camera. Col.(2): Pixel size. Col.(3): Nominal field of view of the camera. Col.(4): Scalelength of an NSD with $h = 44.7$ pc at a distance of $D_1 = 16$ Mpc. Col.(5): Physical field of view of the camera assuming a distance D_1. Col.(6): scalelength of an NSD with $h = 44.7$ pc at a distance of $D_2 = 40$ Mpc. Col.(7): Physical field of view of the camera assuming a distance D_2.

cameras cover a wide physical range, which is good enough to map both the nucleus and the host spheroid. The scalelengths of the simulated NSD at 16 Mpc are more extended, and thus, easier to recover and analyse with respect to 40 Mpc. The instrument *ACS/HRC* is not operational and *WFPC2* was replaced by *WFC3* during the Servicing Mission 4. We also rejected *WFC3/IR* because it is an IR channel. Therefore, we had to select between *WFC3/UVIS*, *ACS/SBC* and *ACS/WFC*. Using *WFC3* is generally preferable where the higher angular resolution has higher priority than the larger field of view, because of its finer pixel size (Dressler 2011).

We generated the mock images of the simulated galaxies assuming the Virgo Cluster distance ($D = 16$ Mpc). Therefore, the angular size of 1 arcsec corresponds to 77.6 pc. Images of the different timesteps are trimmed to match the field of view and resolution of *WFC3/UVIS*. Gain and readout noise were set to 1.5 e^- count^{-1} and 3.0 e^- rms, respectively (Dressler 2011). Finally, a background level and photon noise are added to the resulting images to yield a signal-to-noise ratio similar to that of the *HST* images of galaxy nuclei hosting a NSD.

Stellar populations

We modelled the luminosity distribution of each galaxy component from its mass distribution by adopting the mass-to-light (M/L) ratios from Maraston (1998, 2005):

- for the NCS of model A1 we assumed two different stellar components with the same mass:

  1. a young stellar population with an age of 1 Gyr, a metallicity [Fe/H] $= -0.4$ dex, and mass-to-light ratios $(M/L)_B = 0.49$ $M_\odot/L_\odot$ and $(M/L)_I = 0.52$ $M_\odot/L_\odot$;
  2. an old stellar population with an age of 10 Gyr, a metallicity [Fe/H] $= -1.4$ dex, and mass-to-light ratios $(M/L)_B = 3.32$ $M_\odot/L_\odot$ and $(M/L)_I = 2.70$ $M_\odot/L_\odot$;

- for the initial NCD of model A2 we adopted a stellar population with mass-to-light ratios $(M/L)_B = 0.09$ $M_\odot/L_\odot$ and $(M/L)_I = 0.20$ $M_\odot/L_\odot$ corresponding to an age of 70 Myr and a metallicity of [Fe/H] $= -0.4$ dex;

- for the host bulge in both models A1 and A2 we considered the same population as the old part of the NCS;

- in each timestep of both models A1 and A2 we considered the same mixed population of the NCS for all the star clusters except for the last accreted one, for which we adopt the same young population as the NCD.

These ages and metallicities were chosen to match the properties of the stellar components observed in the nucleus of NGC 4244 (Seth et al. 2006) as in H11. During the evolution time, we considered that all the components become older, reaching the same mixed population as the NCS, except for the last accreted star cluster, for which we adopted the M/L ratio described above. In order to increase the resolution at the centre of the model, particles in the bulge model have different masses depending on their total angular momentum; at larger radii particles have masses as large as $3.9 \times 10^5 M_\odot$. Since these project onto the nucleus, in our analysis of projected quantities we excluded all bulge particles beyond 200 pc from the galaxy centre.

Figure 2.2 shows the two-dimensional nuclear colour map $B-I$ for model A1 and model A2. Except for the bulge particles, the maximum colour difference is $B - I < 1.5$ for both the models, and only the very central regions show fluctuations. So far, to compare our results with previous studies, we decided to do the analysis using the $I-$band images. Thus, if not specified, hereafter all the following analysis, plots and tables, are referred to the mock images of the galaxy built in the $I-$band filter of the Johnson-Cousin system.

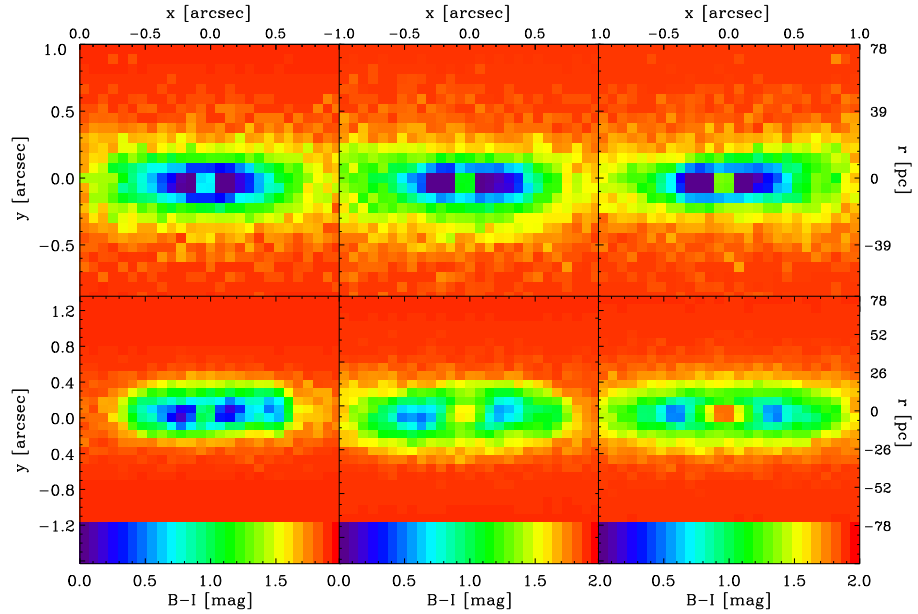

Figure 2.2: Top panels: $B-I$ colour map obtained for model A1 after the accretion of 10 (left-hand panel), 20 (central panel) and 27 (right-hand panel) star clusters. Bottom panels: same but for model A2 after the accretion of 10 (left-hand panel), 30 (central panel) and 50 (right-hand panel) star clusters.

Galaxy inclination

We planned to apply the Scorza & Bender method (Scorza & Bender 1995) to obtain the structural parameters of the NSDs. This is based on the assumption that isophotal discyness is the result, with few exceptions, of the superimposition of a spheroidal component (which is either an elliptical galaxy or a bulge) and an inclined disc. The two components are assumed to have both perfectly elliptical isophotes with constant but different ellipticities (Figure 2.3).

NSDs are easier to detect when their luminosity is high and they are nearly edge-on. Thus we generated mock images by adopting a galaxy inclination of 75° which takes into account the detection limit of embedded discs as a function of their luminosity and inclination (Rix & White 1990).

2.3.2 Kinematic maps

The luminosity-weighted kinematics of the stars was derived for each simulated galaxy as seen edge-on after excluding the contribution of the bulge to avoid

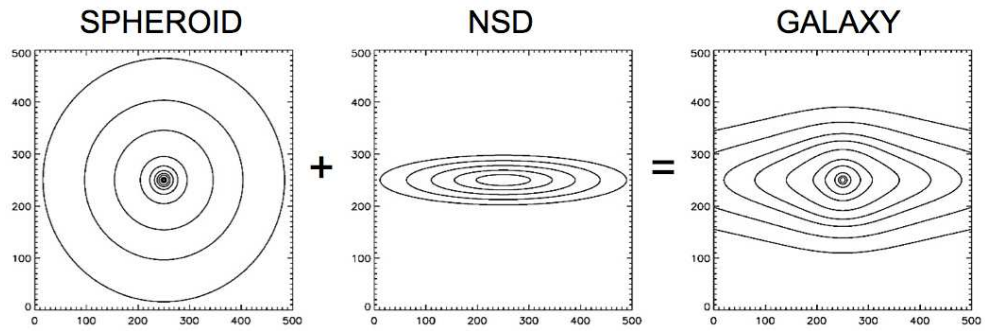

Figure 2.3: Left-hand panel: surface-brightness isophotes of a spheroid with ellipticity $\epsilon = 0$. Central panel: surface-brightness isophotes of a inclined disc with ellipticity $\epsilon = 0.8$. Right-hand panel: the superposition of the two galactic components generates discy isophotes.

its contamination. The resulting maps of the line-of-sight velocity and velocity dispersion are shown in Figures 2.4 and 2.5 for model A1 and A2, respectively. As pointed out by H11, the measured kinematics is dominated by the nuclear star cluster out to 15 pc from the centre. At larger radii ($r \simeq 30$ pc) the amplitude of the stellar rotation ($10 \lesssim V_{\rm max} \lesssim 40$ km s^{-1}) is consistent with kinematic measurements of actual NSDs (e.g., van den Bosch et al. 1998; Bertola et al. 1999; Halliday et al. 2001).

We also decided to rotate the models of 90° with respect to the $z-$ axis, which is perpendicular to the galaxy plane. Then we projected the galaxy and we measured the I-band luminosity-weighted kinematic of the stars as seen edge-on, neglecting the contribution of the bulge. This is consistent with the one we showed in Figures 2.4 and 2.5. This means that the galaxy has a symmetric distribution and we can consider only one line of sight.

2.4 Analysis

2.4.1 Detection of the nuclear stellar disc

Various methods have been used to detect NSDs. The simplest method is the unsharp-mask technique to recover non-circular structures in an image (Pizzella et al. 2002). The alternative is interpolating the isophotes with ellipses extracting the radial profiles of many parameters that describe the light distribution of the galaxy. The Fourier coefficients, A_n and B_n (with $n > 3$) parametrise the deviations of the isophotal shape from a perfect ellipse. In particular, positive

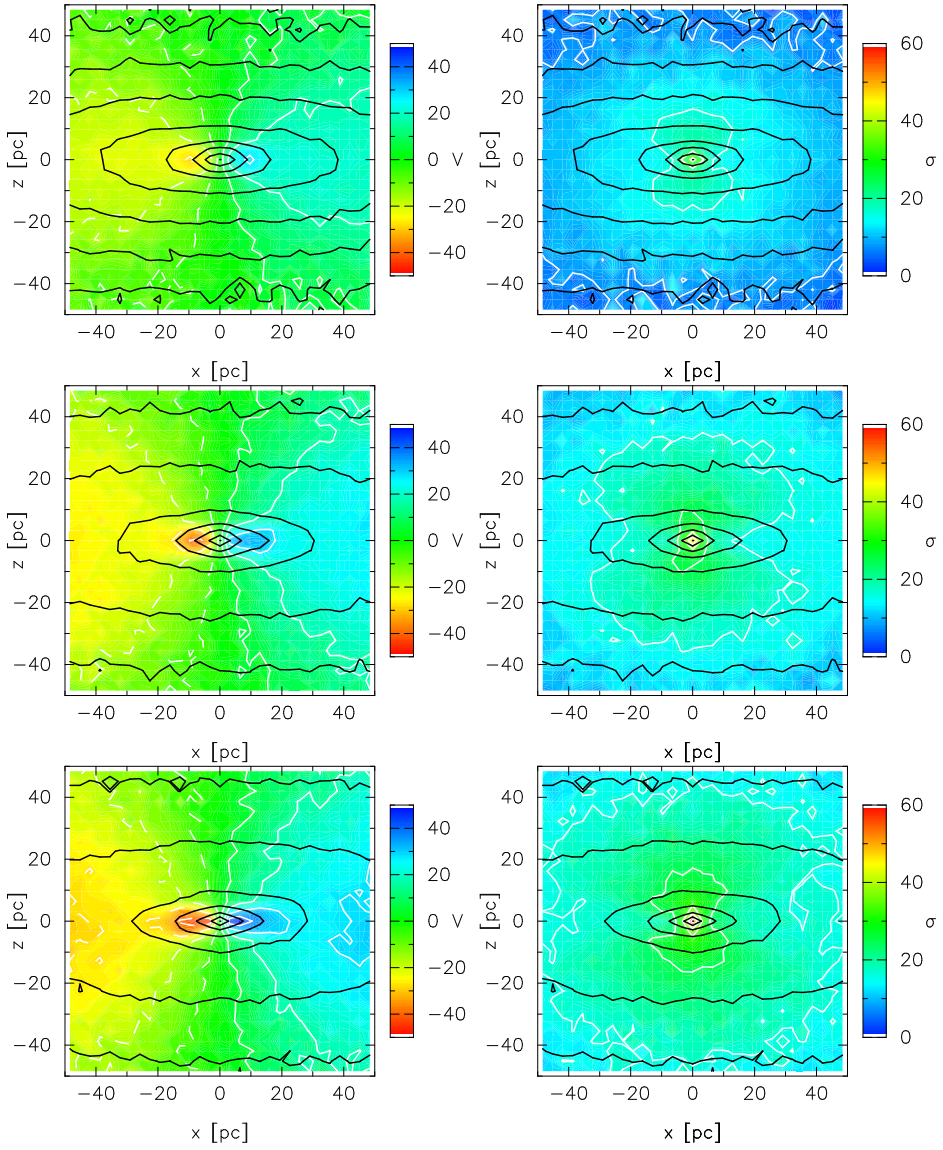

Figure 2.4: Line-of-sight stellar velocity (left-hand panels) and velocity dispersion (right-hand panel) maps for the simulated galaxy in model A1 after the accretion of 10 (top row), 20 (central row), and 27 star clusters (bottom row). The colour code is at the right of each panel. The black contours show the galaxy isophotes at a level of $90, 80, \ldots, 10$ per cent of the central surface brightness. The white lines show kinematic contours appropriate to each panel. The field of view is 0.65×0.65 arcsec^2 (corresponding to 50×50 pc^2 at the assumed distance).

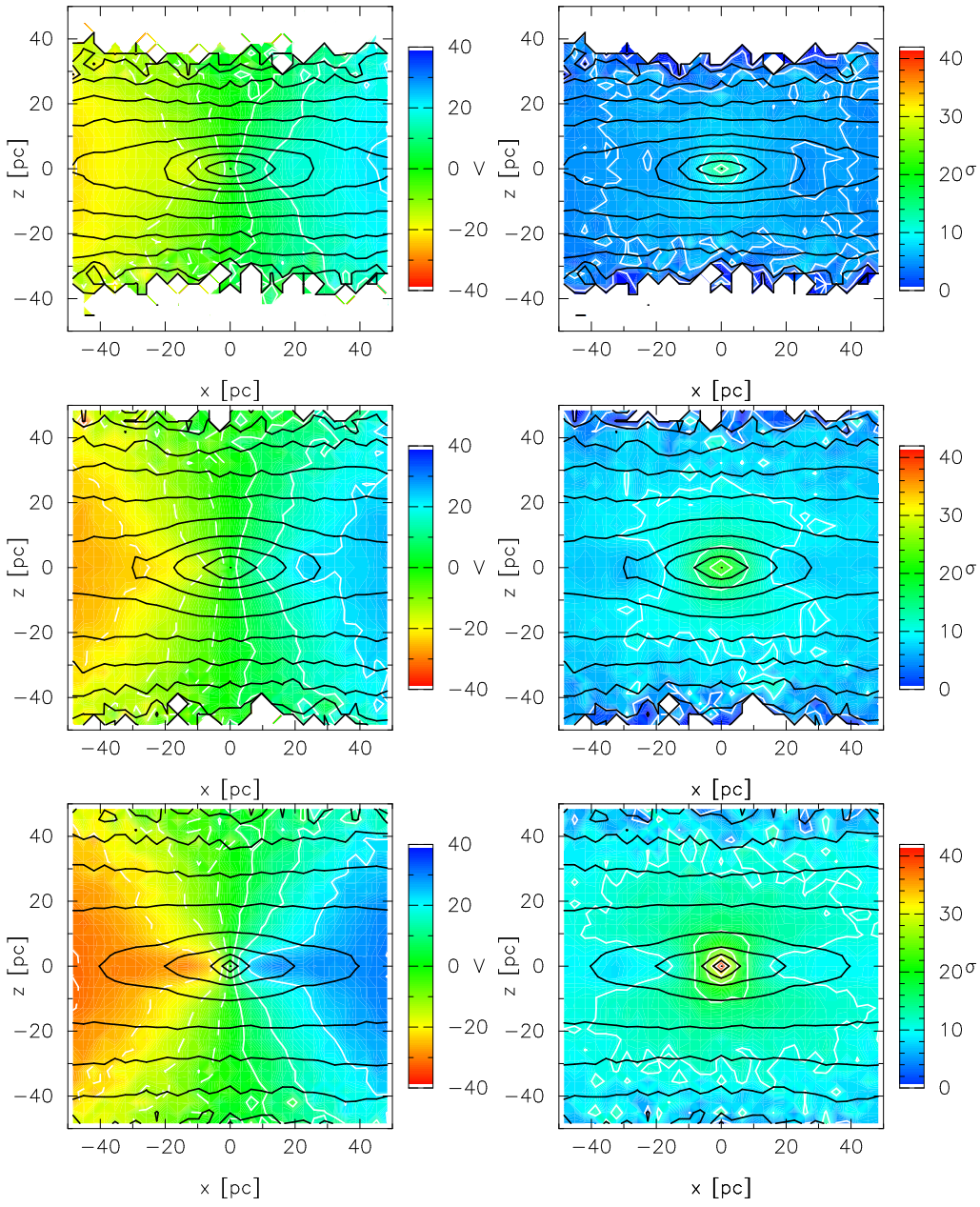

Figure 2.5: As in Figure 2.4, but for the simulated galaxy in model A2 after the accretion of 10 (top row), 30 (central row), and 50 star clusters (bottom row).

values of the fourth term A_4 are characteristic of discy isophotes (Bender et al. 1988).

Unsharp masking technique

The unsharp masking technique is useful to have a first guess of the possible presence of the nuclear disc. Such method consists in dividing the original image, pixel by pixel by itself convolved with a circular Gaussian of *a priori* standard deviation

$$I_{\rm unsharp}(x,y) = \frac{I(x,y)}{I(x,y) * G(x,y)} \tag{2.4}$$

where $I(x,y)$ is the intensity of the pixel with coordinates (x,y) of the original image, while $I_{\rm unsharp}(x,y)$ is the one of the corresponding pixel of the unsharped-masked image and $G(x,y)$ is the intensity of the circular Gaussian function

$$G(x,y) = N \exp\left[-\left(\frac{x^2+y^2}{2\sigma^2}\right)\right] \tag{2.5}$$

where N is the normalisation factor and σ is the standard deviation.

To test for the presence of an NSD in the mock *WFC3/UVIS* images of the simulated galaxies, we constructed the unsharp-masked image of the frames as in Pizzella et al. (2002). Each image was divided by itself after convolution with a circular Gaussian of width $\sigma = 2, 6, 10$, or 20 pixels corresponding to $0.08, 0.2, 0.4$, or 0.8 arcsec, respectively. The results for models A1 and A2 are given in Figures 2.6 and 2.7, respectively. This procedure enhances any non-circular structure extending over a spatial scale comparable to the smoothing scale. Different values of σ were adopted to identify structures of different sizes. For each model, the location, orientation, and size of the elongated nuclear component remain similar in all the timesteps.

Morelli et al. (2004) demonstrated that bright, elongated nuclear structures in unsharp-masked images are not an artifact of the image processing. Such structures are always observed in galactic nuclei if an inclined NSD is present. However, the same feature in the unsharp-masked images of bulges can also be caused by isophotes of increasing ellipticity inwards. Therefore, to unveil an NSD it is necessary to perform also a detailed measurement of the surface-brightness distribution in the nuclear regions.

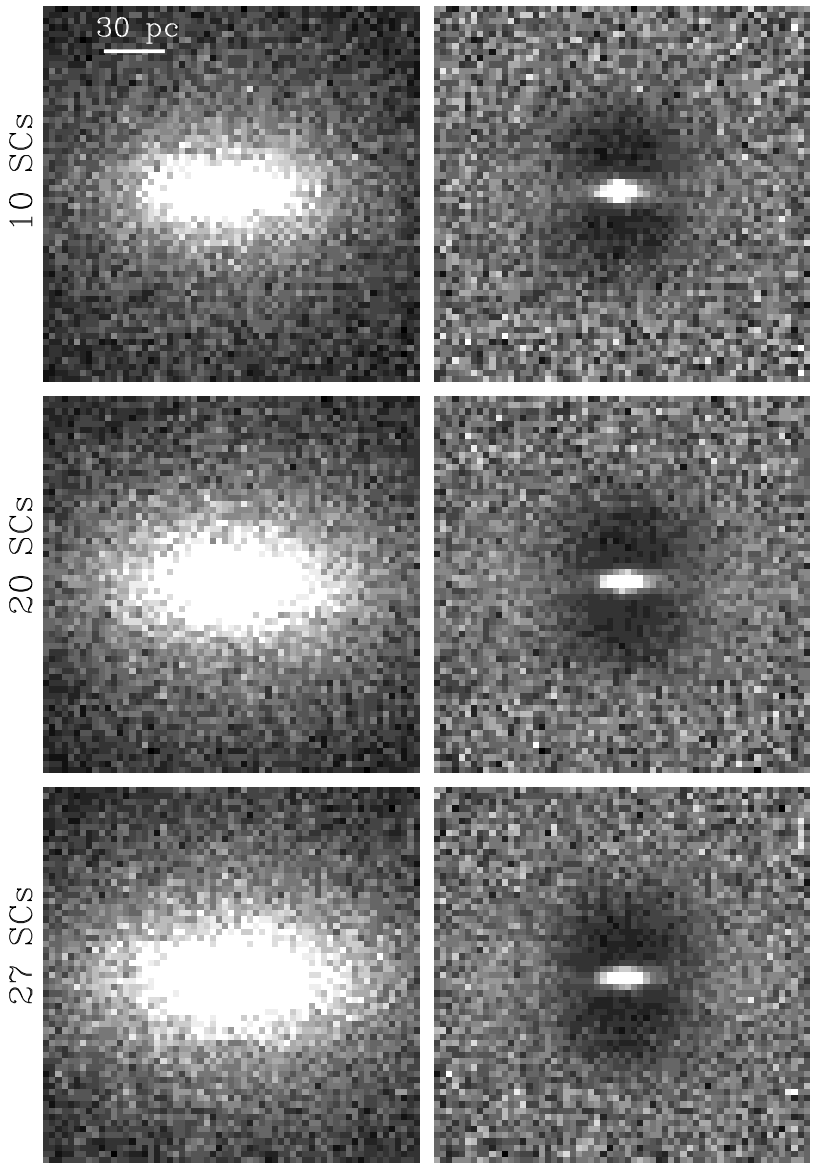

Figure 2.6: Mock *WFC3/UVIS I*-band (left-hand panels) and unsharp-masked images (right-hand panels) of model A1 after the accretion of 10 (top panels), 20 (middle panels), and 27 star clusters (bottom panels). The field of view is 2.4 × 2.4 arcsec^2 (corresponding to 186 × 186 pc^2) and the image scale is given in the upper left corner of the first panel. The unsharp-masked images were obtained by adopting a smoothing Gaussian of $\sigma = 10$ pixel corresponding to 0.4 arcsec. These images have been obtained with an inclination of 75°.

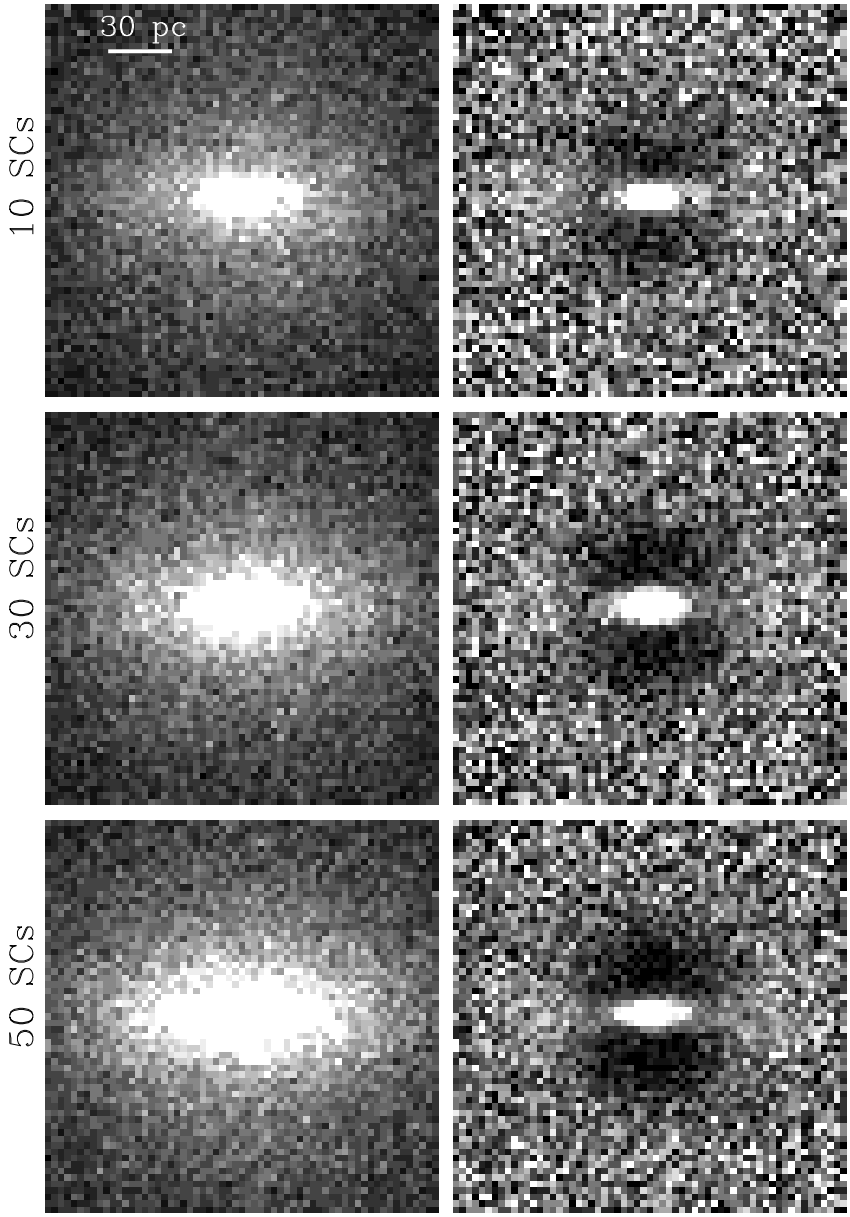

Figure 2.7: As in Figure 2.6, but for model A2 after the accretion of 10 (top panels), 30 (middle panels), and 50 star clusters (bottom panels).

Analysis of the surface-brightness distribution

The isophotes of a galaxy connect points characterised by the same surface brightness. To describe in a quantitative way the light distribution of a galaxy we usually interpolate the isophotes with ellipses. This technique allows us to extract the radial profiles that describe the behaviour of the surface brightness, μ, ellipticity, ϵ, major-axis position angle, PA, and Fourier coefficients, A_n and B_n (with $n > 3$), that parametrise the deviations of the isophotal shape from a perfect ellipse.

Assuming elliptical isophotes, the galaxy surface brightness in each point (x, y) is given by

$$\mu = \mu(s) \quad \text{with} \quad s^2 = \widehat{x}^2 + \frac{\widehat{y}^2}{(1-\epsilon)}\,, \tag{2.6}$$

where

$$\begin{aligned} \widehat{x} &= (x - x_c)\cos\theta_0 + (y - y_c)\sin\theta_0 \\ \widehat{y} &= (y - y_c)\cos\theta_0 + (x - x_c)\sin\theta_0. \end{aligned} \tag{2.7}$$

(x_c, y_c) are the coordinates of the centre of the ellipse, θ_0 is the position angle of the major axis of the ellipse, a_0, and $\epsilon = (1 - b/a)$ is the ellipticity. In the coordinate system centred in (x_c, y_c) and aligned with the major axis of the ellipse, the coordinates (x_c, y_c) can be written as a function of the eccentric anomaly ϕ, which is the position angle measured from the major axis of the ellipse

$$\begin{aligned} x &= a_0 \cos\phi \\ y &= a_0(1-\epsilon)\sin\phi. \end{aligned} \tag{2.8}$$

Hence, the surface brightness of an isophote along the ellipse can be written as:

$$\mu(\phi) = \mu_0 + \sum_{n=1}^{\infty} A_n \cos(n\phi) + \sum_{n=1}^{\infty} B_n \sin(n\phi) \tag{2.9}$$

where μ_0 is the average surface brightness of the isophote along the ellipse and

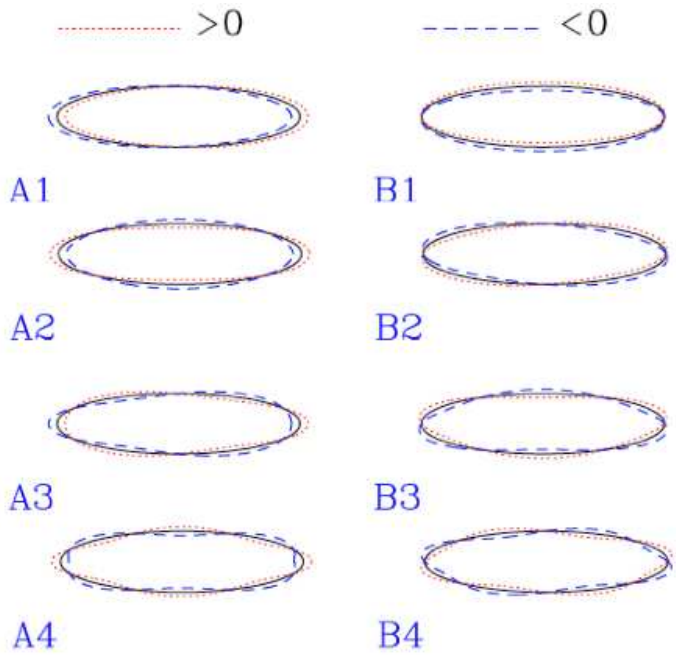

Figure 2.8: Graphic description of distortion on the isophotes parametrised by the Fourier coefficients. In each panel the shape of an isophote with a positive (red line) and negative value (blue line) of the corresponding coefficient is compared with that of a perfect ellipse (black line).

the A_n and B_n Fourier coefficients are respectively

$$\begin{aligned} A_n &= \frac{1}{\pi}\int_0^{2\pi} R(\phi)\cos(n\phi)\mathrm{d}\phi \\ B_n &= \frac{1}{\pi}\int_0^{2\pi} R(\phi)\sin(n\phi)\mathrm{d}\phi. \end{aligned} \tag{2.10}$$

Usually, the isophotes of a bulge are expected to be nearly elliptical, even if the ellipticity changes with radius. Instead, the presence of an inclined NSD will result in isophotes with a discy shape (Figure 2.16), due to the superposition of the light contribution of the rounder bulge with the one from the more elongated disc (Scorza & Bender 1995). A sharp increase of the disciness of the innermost isophotes of a galaxy is usually associated with a strong increase of their ellipticity. The peak of both ellipticity and disciness in the same radial range is therefore the full photometric signature of the presence of a disc

embedded in the bulge.

We fitted isophotes to the model images using the IRAF[2] task ELLIPSE (Jedrzejewski 1987). They are fitted with ellipses, allowing their centres to vary in order to look for asymmetries in the light distribution. Within the errors of the fits we found no evidence of variations in the fitted centres. The ellipse fitting was then repeated with the ellipse centres fixed. The resulting azimuthally-averaged surface brightness, μ, ellipticity, ϵ, position angle, PA, and fourth cosine Fourier coefficient, A_4, profiles are presented in Figures 2.9 and 2.10 for models A1 and A2, respectively. Positive values of the A_4 Fourier coefficient are characteristic of discy isophotes (Bender et al. 1988).

The radial profile of ellipticity peaks at about 0.2 arcsec from the centre ($\epsilon_{\rm max} \simeq 0.6$) in all the mock images of model A1. Round isophotes ($\epsilon \simeq 0$) are observed for radii larger than 2 arcsec. Within the innermost 2 arcsec there is no change in the A_4 Fourier coefficient, which is nearly constant and slightly positive ($A_4 \simeq 0.01$ after the accretion of 10 and 20 star clusters, increasing to $A_4 \simeq 0.02$ after the accretion of 27 star clusters). Thus model A1 never develops the photometric signature of observed NSDs.

In model A2, instead, both the ellipticity and the A_4 Fourier coefficient show a sharp increase within 1.5 arcsec from the centre in all the timesteps. The maximum observed values of ellipticity and disciness are $\epsilon_{\rm max} \simeq 0.6$ and $A_{4,\rm max} \simeq 0.05$, respectively. We interpret these photometric features as the signature of an embedded NSD in the bulge of model A2. Indeed the same photometric features are observed in galactic nuclei hosting a NSD (e.g., Scorza & van den Bosch 1998; Krajnović & Jaffe 2004; Morelli et al. 2010).

2.4.2 Photometric decomposition

The Scorza-Bender decomposition method (Scorza & Bender 1995) recovers the structural properties of an NSD (central surface brightness, I_0, and the scalelength, h, inclination, i, and major-axis position angle, PA) by subtracting from the image the best exponential disc model, which is generally assumed to be perfectly thin.

Analysis of the position angle

We first measured the PA of the major axis of the elongated structures found in models A1 and A2 in order to check whether we could successfully recover the

[2]Imaging Reduction and Analysis Facilities (IRAF) is distributed by the National Optical Astronomy Observatories which are operated by the Association of Universities for Research in Astronomy (AURA) under cooperative agreement with the National Science Foundation.

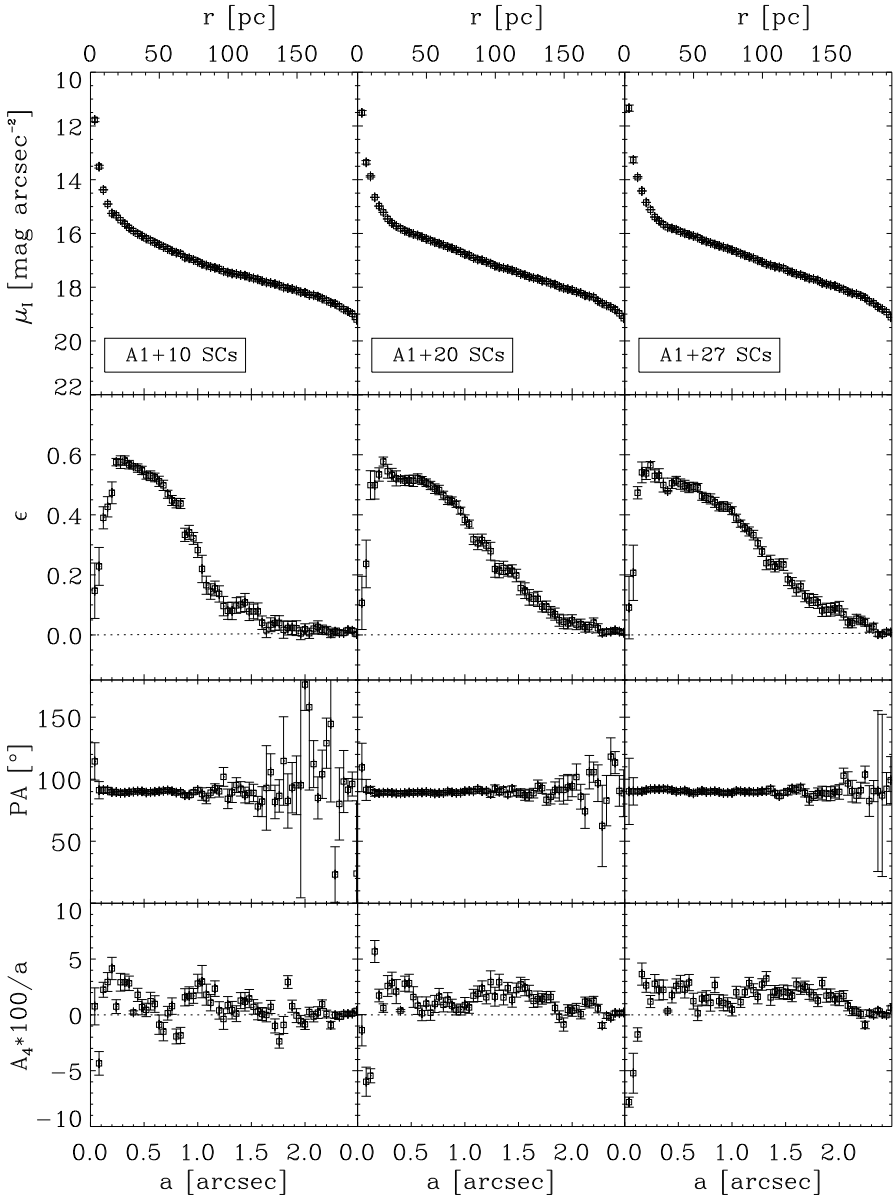

Figure 2.9: Isophotal parameters of the nuclear region of model A1 as a function of the isophotal semi-major axis based on the analysis of the surface-brightness distribution after the accretion of 10 (left-hand panels), 20 (central panels), and 27 (right-hand panels) star clusters. From top to bottom: Radial profiles of the surface brightness, ellipticity, position angle, and fourth cosine Fourier coefficient.

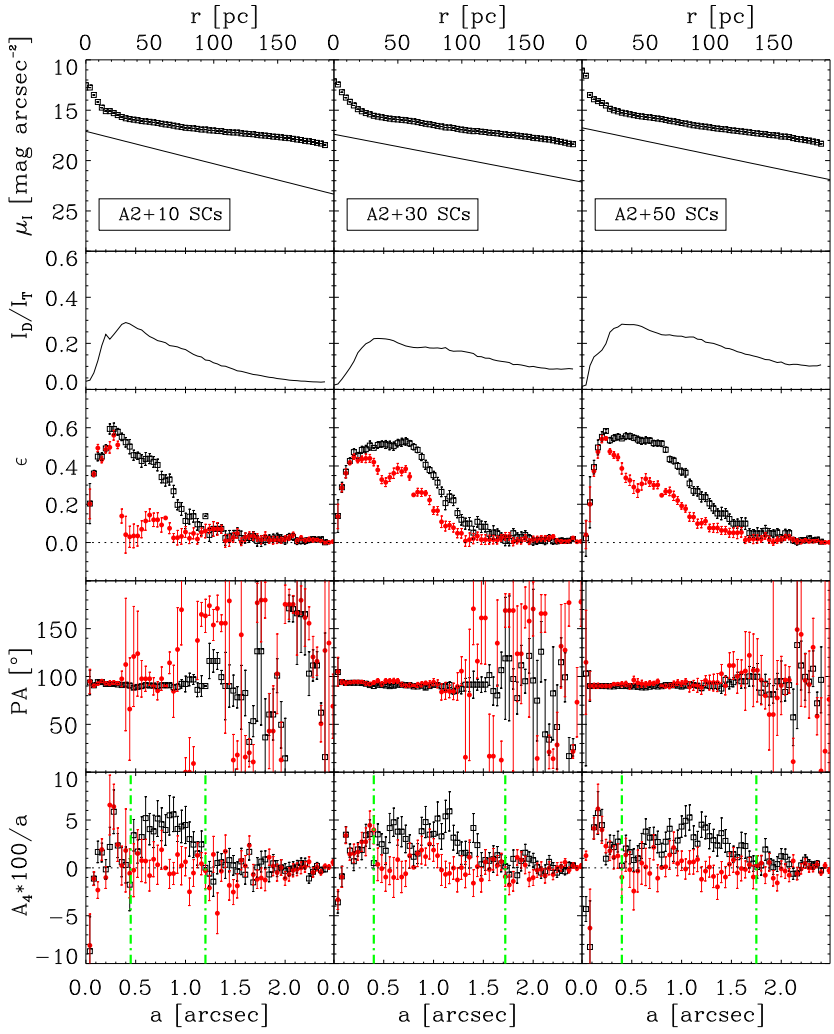

Figure 2.10: Isophotal parameters of the nuclear region of model A2 as a function of the isophotal semi-major axis based on the analysis of the surface-brightness distribution measured in the mock images obtained after the accretion of 10 (left-hand panels), 30 (central panels), and 50 (right-hand panels) star clusters. From top to bottom: surface-brightness radial profiles of the galaxy (open black squares) and NSD (solid line), radial profiles of the NSD-to-total surface-brightness ratio, radial profiles of the galaxy ellipticity, position angle and fourth cosine Fourier coefficient before (open black squares) and after (filled red circles) the subtraction of the best-fitting model for the NSD. The vertical (green) dot-dashed lines mark the radial range within which the light distribution is characterised by discy isophotes ($A_4 > 0$) due to the presence of the NSD.

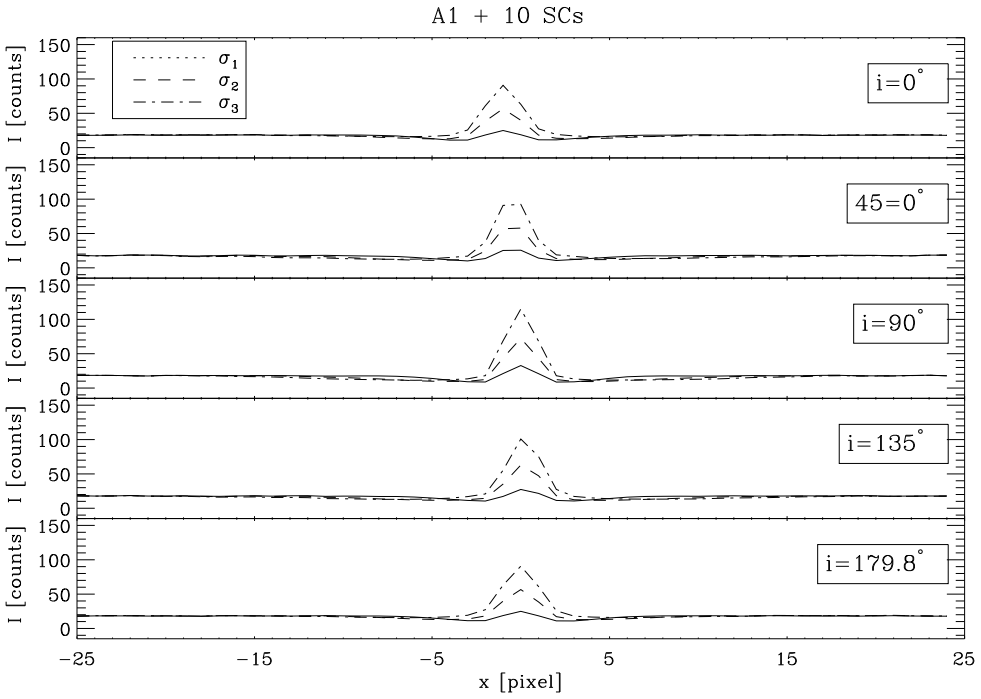

Figure 2.11: Analysis of the position angle for the model A1 after 10 star cluster accretions. From top to bottom: I-band flux of the unsharped-masked images obtained with $\sigma_i = 2, 6$ and 10 pixels, as given in the legend, after the rotation of the images of 0°, 45°, 90°, 135°, and 179.8°. The flux is measured within a box of 51×9 pixels^2 after the rotation of the images.

orientation of the possible NSD. We assumed the images are oriented with the North up and East left and analyse them after unsharp masking. The images were rotated from 0° to 179.°8 in steps of 0.°2 and we measured the flux within a horizontal strip of 51×9 pixels crossing the galaxy centre. The maximum flux is measured when the strip is aligned with the NSD major axis. In this way we find PA $= 90° \pm 2°$, consistent with the input line-of-nodes of the system.

Limits of the photometric decomposition method

Deviations of the isophotes from perfect ellipse are described by the Fourier coefficients. The fourth term A_4 is linked to the shape of the ellipses, being positive values of A_4 characteristic of discy isophotes (Bender et al. 1988).

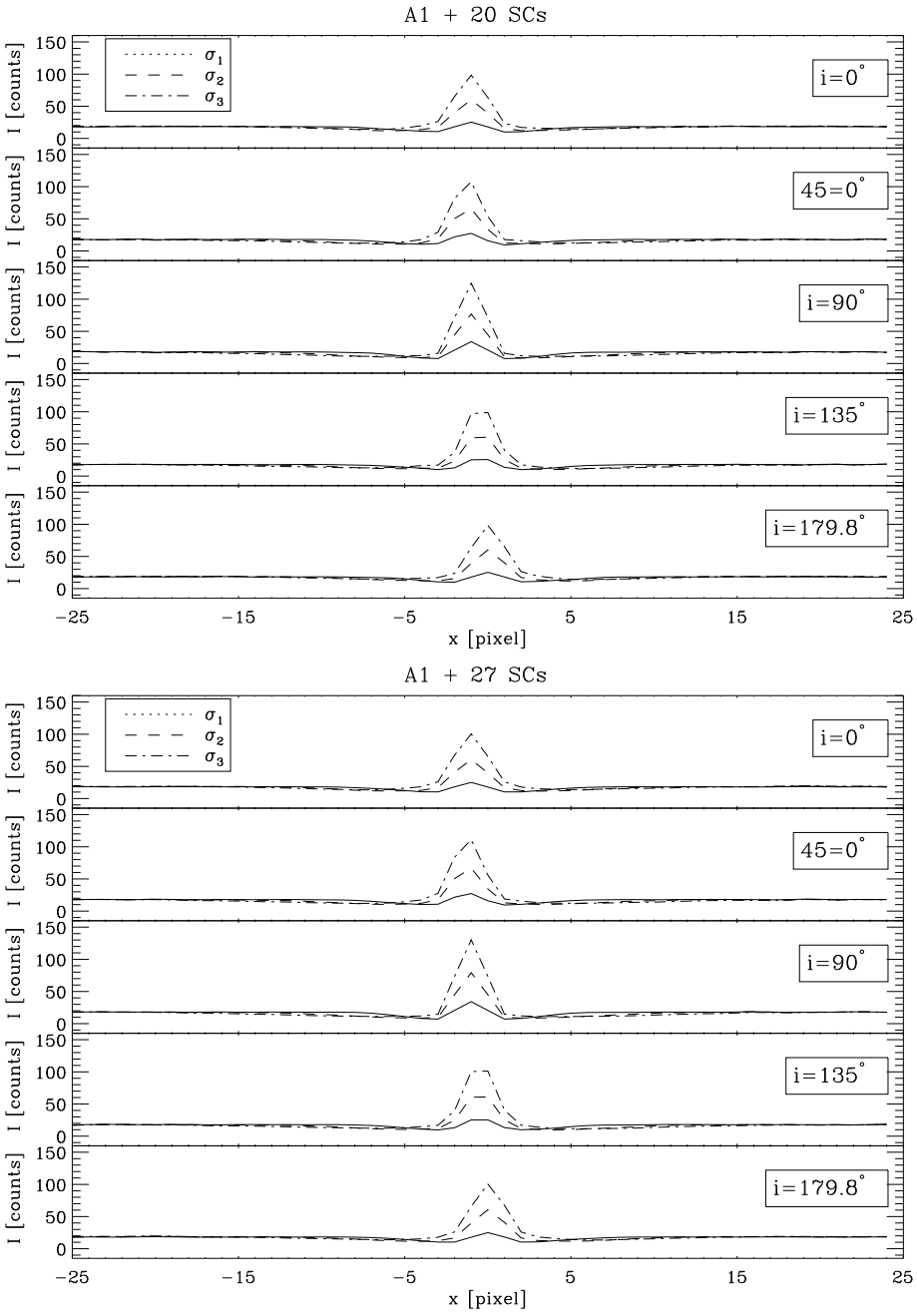

Figure 2.12: As in Figure 2.11, but after the accretion of 20 (top panel) and 27 (bottom panel) star clusters of model A1.

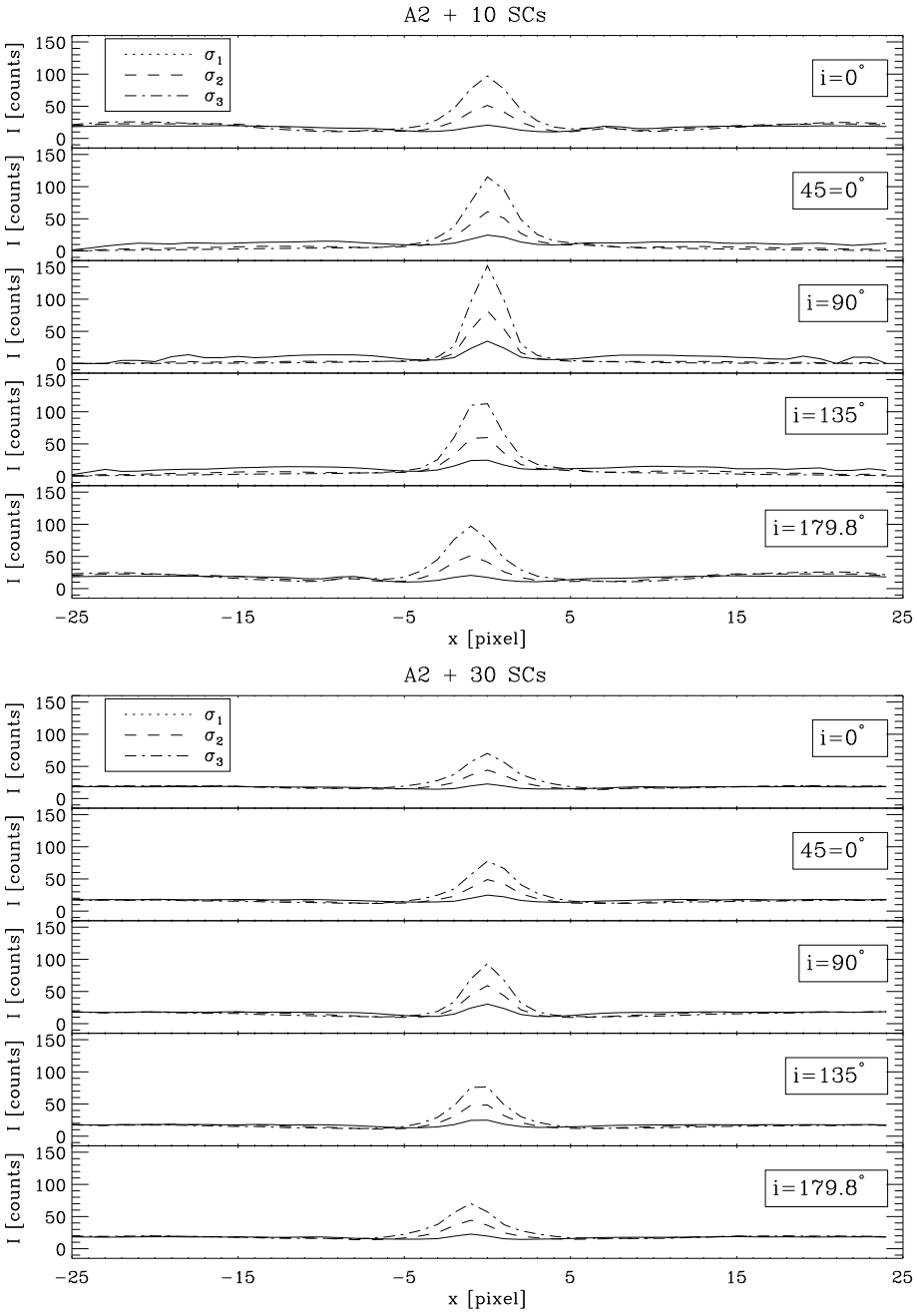

Figure 2.13: As in Figure 2.11 but after the accretion of 10 (top panel) and 30 (bottom panel) star clusters of model A2.

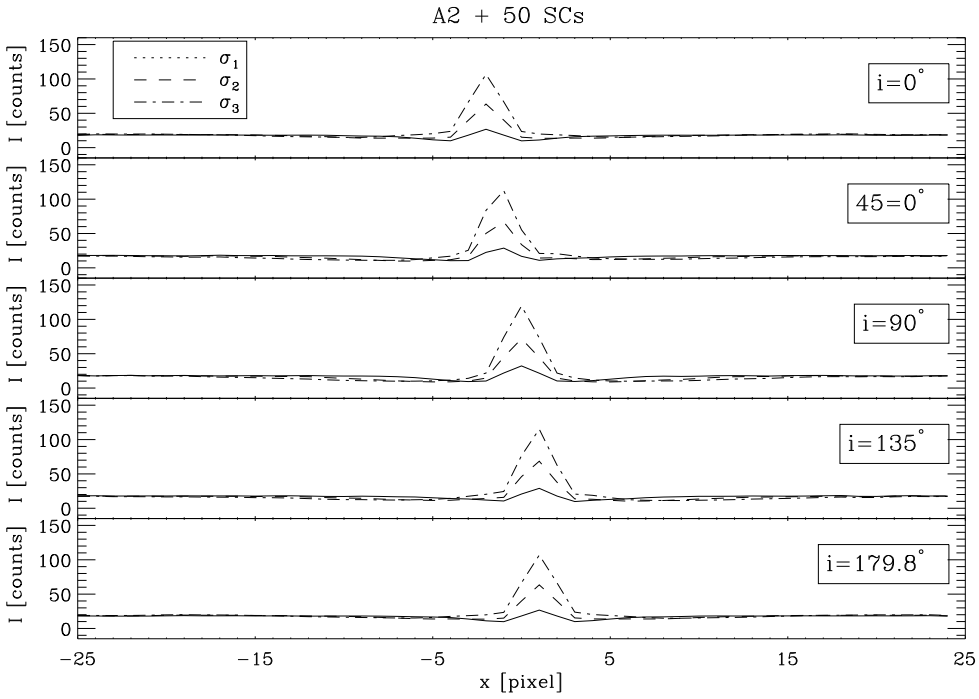

Figure 2.14: As in Figure 2.11, but after the accretion of 50 star clusters of model A2.

Rix & White (1990) investigated the frequency and the luminosity of disc components in elliptical galaxies by studying the photometric properties of models containing a spheroidal component and a faint exponential disc. They tested the sensitivity of the detection by means of the A_4 Fourier coefficient and they found that the fourth cosine is quite sensitive to the presence of a weak (20% of the total light) disc only when it is nearly edge-on. Deviations of the isophotes from perfect ellipses, as characterised by the parameter A_4, depend predominantly on the disc-to-spheroid ratio and galaxy inclination. Similar A_4 profiles can be produced by a wide range of combinations of disc-to-spheroid ratios ($L_{\rm D}/L_{\rm B}$) and inclinations. The sixth Fourier coefficient A_6 provides a good diagnostic for nearly edge-on galaxies. For many parameter combinations, the discs are practically undetectable. Therefore, they found that the Scorza-Bender method is very efficient for inclinations $\cos(i) < 0.4$ (i.e., $i > 66°$) but very inefficient for inclinations $\cos(i) > 0.6$ (i.e., $i < 53°$) for any spheroid-to-disc ratio. On the opposite hand, deviations from perfect ellipses are also difficult to detect for most galaxies with $L_{\rm D}/L_{\rm B} < 0.25$ (Figure 2.15).

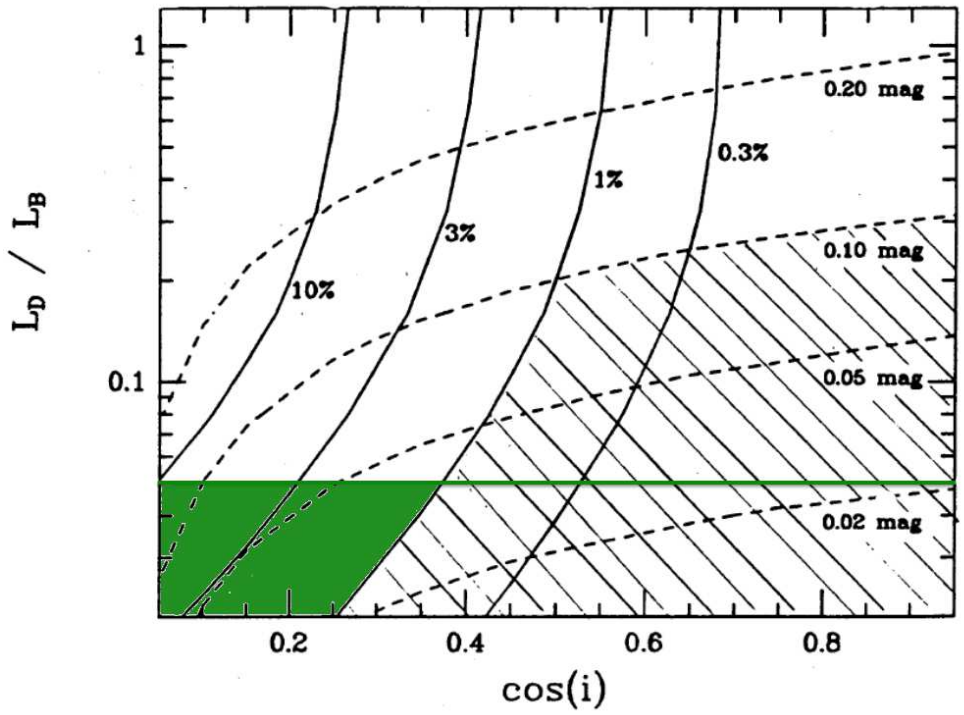

Figure 2.15: Impact of a disc component on the isophote shape and radial profiles in the $(L_{\rm D}/L_{\rm B}, \cos(i))$ plane. Loci of constant A_4 (solid lines) and constant rms deviation from an $r^{1/4}$ law (dashed lines) are shown. From Rix & White (1990).

Scorza-Bender photometric decomposition of model A2

We then applied the photometric decomposition of the surface brightness based on the Scorza-Bender method (Scorza & Bender 1995), as implemented by Morelli et al. (2004), to the images of model A2. The photometric decomposition, which is performed independently for each timestep, is based on the assumption that both the host bulge and the inclined NSD are each characterised by elliptical isophotes with constant ellipticity (Figure 2.16). The method consists of an iterative subtraction of different models of an infinitesimally thin exponential disc. The disc has the observed central surface brightness I_0, scale-length h, and apparent axial ratio q.

Therefore, its surface-brightness radial profile is given by

$$I(r) = I_0 \exp\left[-\left(\frac{r}{h}\right)\right] = I_0^0 \exp\left[-\left(\frac{r}{h}\right)\right] \cos i \qquad (2.11)$$

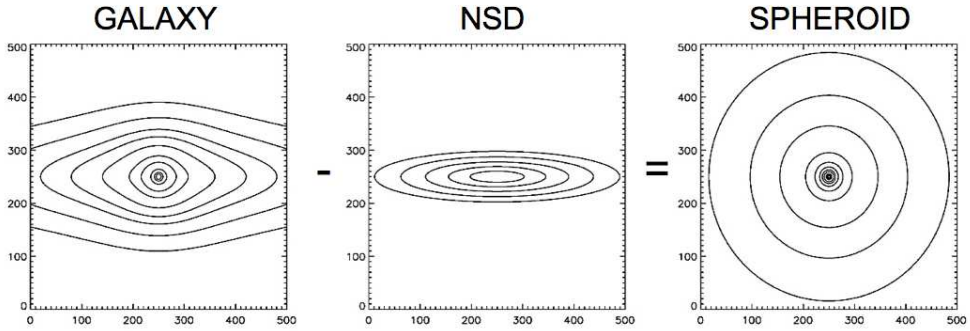

Figure 2.16: The subtraction from a galaxy with discy isophotes (left-hand panel) of a disc (central panel) gives rise to perfect elliptical isophotes (right-hand panel).

where I_0^0 and I_0 are the central surface brightness of the disc as observed and seen face on, respectively, and $\cos i = q$, with i the disc inclination.

For real images it is crucial to first deconvolve the surface-brightness distribution from the effects of the *HST* point spread function (PSF) in order to properly derive the photometric parameters of the NSDs (e.g., van den Bosch & Emsellem 1998; Pizzella et al. 2002; Krajnović & Jaffe 2004; Morelli et al. 2010). We did not apply any deconvolution to our mock *WFC3/UVIS* images since they have not been convolved with any PSF to begin with.

The remaining NSD parameters were adjusted until the departures from perfect ellipses are minimised (i.e., $A_4 \simeq 0$ over all the observed radial range, Figures 2.10). For each disc model, first we obtained the disc-free image of the galaxy by subtracting the disc model from the galaxy image. Then, we performed an isophotal analysis of the disc-free image using ELLIPSE. We calculated

$$\chi^2 = \sum_{i=1}^{N} \frac{A^2_{4,\mathrm{disc-free}}(i)}{\sigma^2(i)} \tag{2.12}$$

where $A_{4,\mathrm{disc-free}}(i)$ is the value of the A_4 Fourier coefficient measured for the $i-$th isophote in the disc-free image, and N is the total number of fitted isophotes. We assumed $\sigma(i) = 0.01$ as a typical error on $A_{4,\mathrm{disc-free}}$ for all the isophotes in the region of the NSD. The NSD region is bracketed by two vertical lines in Figure 2.10. The minimum value of χ^2 corresponds to the best-fitting model of the NSD. We determined $\Delta\chi^2 \equiv \chi^2 - \chi^2_{\mathrm{min}}$ and derive its confidence levels under the assumption that the errors are normally distributed (Figure 2.17). The inclination is calculated as $i = \arccos q$. The resulting values of the observed central surface brightness, scalelength, inclination, and total lu-

minosity of the NSD in the I-band for the different timesteps of model A2 are listed in Table 2.5. The total luminosity of the disc is given by

$$L = 2\pi I_0 h^2 q. \tag{2.13}$$

We also tested our decompositions by an independent analysis of images of model A2 built with the same assumptions as in Section 2.3.1, but changing the stellar population of the last star cluster, which has a strongly different M/L ratio with respect to the others. We considered four different cases for such stellar population:

- young (Y) star cluster: with an age of 1 Myr and a metallicity of [Fe/H] $= -0.4$ dex which gives $(M/L)_I = 0.15$ $M_\odot/L_\odot$;
- young and metal-rich (Y+M) star cluster: with an age of 1 Myr and a metallicity of [Fe/H] $= 0.35$ dex which gives $(M/L)_I = 0.09$ $M_\odot/L_\odot$;
- old (O) star cluster as the galaxy: with the same stellar population of the NCS of model A1;
- very old star cluster (VO): with an age of 15 Gyr and a metallicity of [Fe/H] $= -1.35$ dex which gives $(M/L)_I = 3.60$ $M_\odot/L_\odot$;

Such cases have not a real counterpart, but allowed us to test the robustness of the assumptions we made in Section 2.3.1. Figure 2.18 shows the resulting I-band surface-brightness distribution. The shape of the surface-brightness profile did not change, except for the very inner part of the galaxy where the nuclear star cluster dominates the total light. Thus, when we applied the Scorza-Bender decomposition on such images, we found photometric parameters that are in agreement with those already discussed.

Scorza-Bender decomposition for model A1

We also applied the Scorza-Bender method to model A1. In this case it failed to find a reasonable NSD, with the best model having a scalelength $h = 0$ pc. In fact, as already pointed out, within the innermost 2 arcsec of model A1 there is no change in the A_4 Fourier coefficient, which is nearly constant, even being slightly positive ($A_4 \simeq 0.01$ after the accretion of 10 and 20 star clusters, increasing to $A_4 \simeq 0.02$ after the accretion of 27 star clusters). This confirms that we do not detect a NSD in model A1.

But, to exclude the possibility that the detection is inhibited by the fact that the NSD is faint and not enough inclined, we repeated the photometric

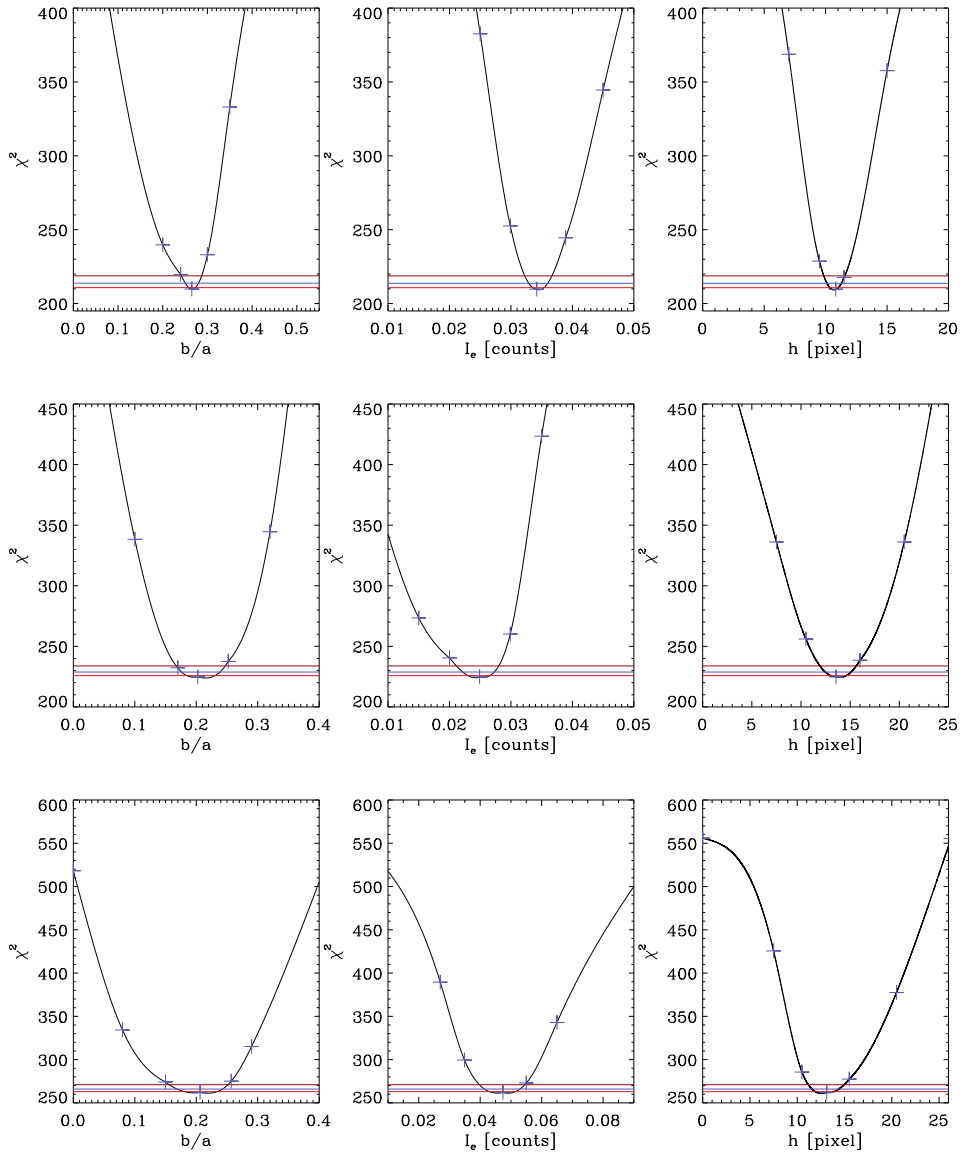

Figure 2.17: χ^2 distribution of the photometric decomposition of the NSD for model A2 after 10 (top panels), 20 (middle panels) and 50 (bottom panels) star clusters as a function of the axial ratio, b/a (left-hand panels), central surface brightness, I_0 (central panels), and scalelength, h (right hand panels). The horizontal lines indicate the 1σ, 2σ, and 3σ confidence levels on best-fitting values after marginalising over all the parameters.

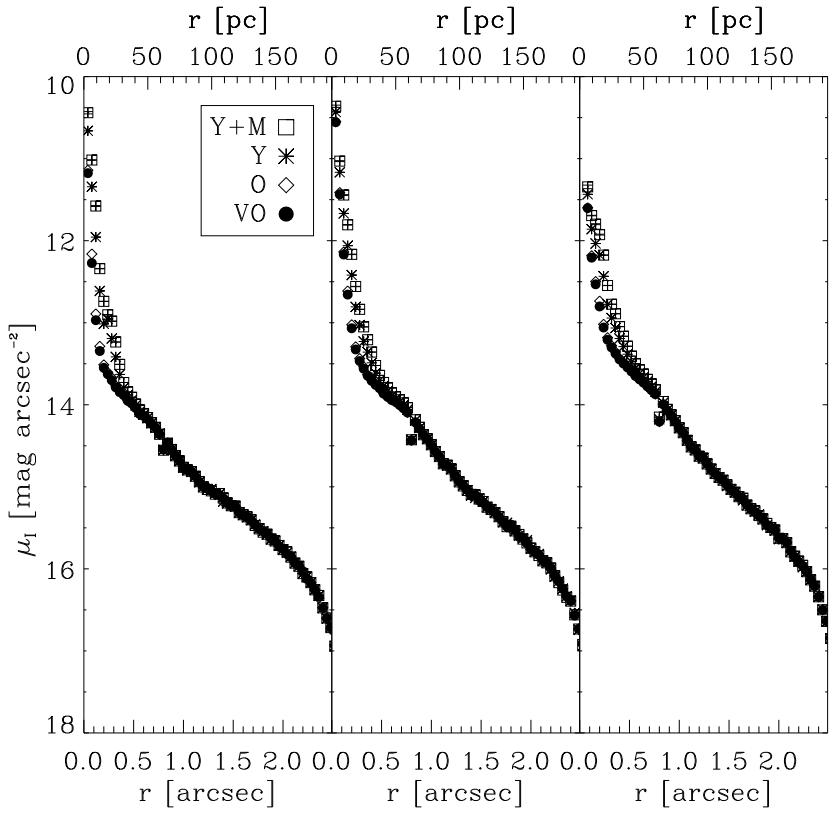

Figure 2.18: Surface-brightness distribution of the nuclear region of model A2 as a function of the isophotal semi-major axis, after the accretion of 10 (left-hand panels), 30 (central panels), and 50 (right-hand panels) star clusters. The profiles are obtained varying the M/L ratio of the last star cluster to match a young (asterisks), young and metal-rich (squares), old (diamonds), and very old (circles) stellar population.

analysis of the surface-brightness distribution on the I-band images of each timestep of model A1. We made the same assumptions as in Section 2.3.1, but we adopted an inclination of $i = 90°$. We also included the analysis of the radial profiles, the B_3 Fourier coefficient to look for any asymmetric deviation due to the possible NSD. The resulting azimuthally-averaged surface brightness, μ, ellipticity, ϵ, position angle, PA, third sine, B_3, and fourth cosine A_4 Fourier coefficient profiles are presented in Figure 2.19.

The radial profile of ellipticity peaks at about 0.3 arcsec from the centre ($\epsilon_{\rm max} \simeq 0.7$) in all the mock images of model A1 seen edge-on. Round isophotes ($\epsilon \simeq 0$) are observed for radii larger than 2 arcsec. Within the innermost 2

arcsec there is no change in the A_4 Fourier coefficient, which is nearly constant and slightly positive, and confined in the range $0.01 < A_4 < 0.02$. Therefore, we concluded that also inclining the galaxy of model A1 by $i = 90°$, it never develops the photometric signature of observed NSDs.

We made another test by flatting the distribution of the star cluster particles of 30%, to explore if a "compressed" distribution gives rise to a nuclear disc. Thus, we performed the photometric analysis of the surface-brightness distribution on an I-band image of each timestep of model A1 with the same assumptions as in Section 2.3.1, but assuming that the distribution of the accreted star clusters particles on the z-axis was $z' = 0.7z$. The resulting azimuthally-averaged surface-brightness, μ, ellipticity, ϵ, position angle, PA, and fourth cosine Fourier coefficient, A_4 profiles are presented in Figure 2.20.

The radial profile of A_4 Fourier coefficient of the model after the accretion of 10 star clusters is confusing. It shows a peak at $a = 1.0$ arcsec, reaching $A_4 \approx 0.05$, but it is spatially limited. Instead, the ellipticity and the A_4 Fourier coefficient show a sharp increase within 1.9 arcsec from the centre after the accretion of 20 star clusters and up to 2.2 arcsec after the accretion of 27 star clusters. The maximum observed values of ellipticity and disciness are $\epsilon_{\rm max} \simeq 0.6$ and $A_{4,\rm max} \simeq 0.04$, respectively. Therefore, we applied a photometric decomposition of the surface brightness based on the Scorza-Bender method to the images of model A1, finding successful results for the galaxy after the accretion of 20 and 27 star clusters (Figure 2.20). The resulting values of the observed central surface brightness, scalelength, inclination, and total luminosity of the NSD in the I-band for the different timesteps of model A2 are listed in Table 2.6. Thus, if the star clusters were able to flat of at least 30% their distribution, an NSD could have been formed.

Finally, we can state that a dry merging could be a viable way for forming NSDs at least if there is a pre-existing disc. The photometric and kinematic properties we found are similar to those of the observed NSDs. The same mechanism can form an NSD in a pre-existing spheroidal structure only if the accreted star clusters are able to flat their distribution of at least 30%. This result is not an observational bias. This is confirmed by the fact that also changing the inclination of the galaxy, the A_4 profile never develops a peak. Having recovered the photometric parameters of the NSD of model A2, we tested the robustness of our decompositions by doing statistical evaluation and by applying different methods as described in the following sections.

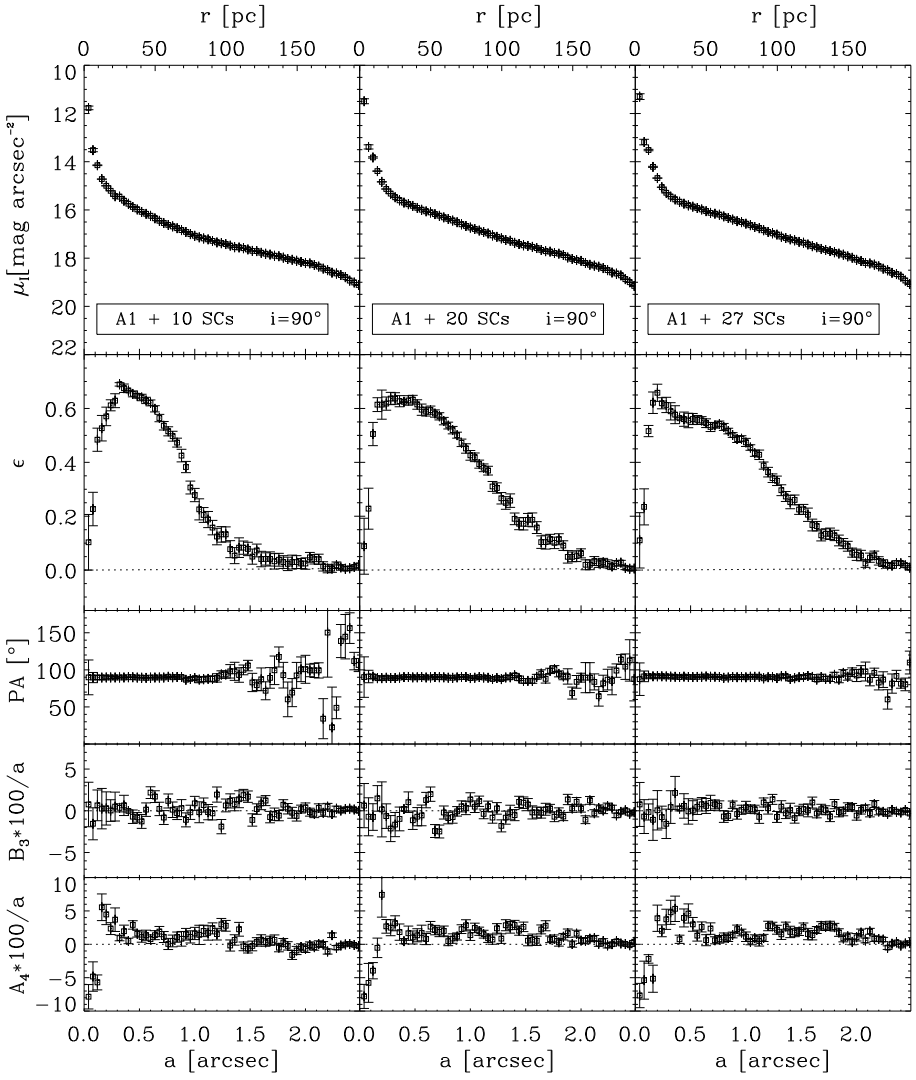

Figure 2.19: Isophotal parameters of the nuclear region of model A1 with an inclination of $i = 90°$ as a function of the isophotal semi-major axis based on the analysis of the surface-brightness distribution after the accretion of 10 (left-hand panels), 20 (central panels), and 27 (right-hand panels) star clusters. From top to bottom: Radial profiles of the surface brightness, ellipticity, position angle, third sine and fourth cosine Fourier coefficient.

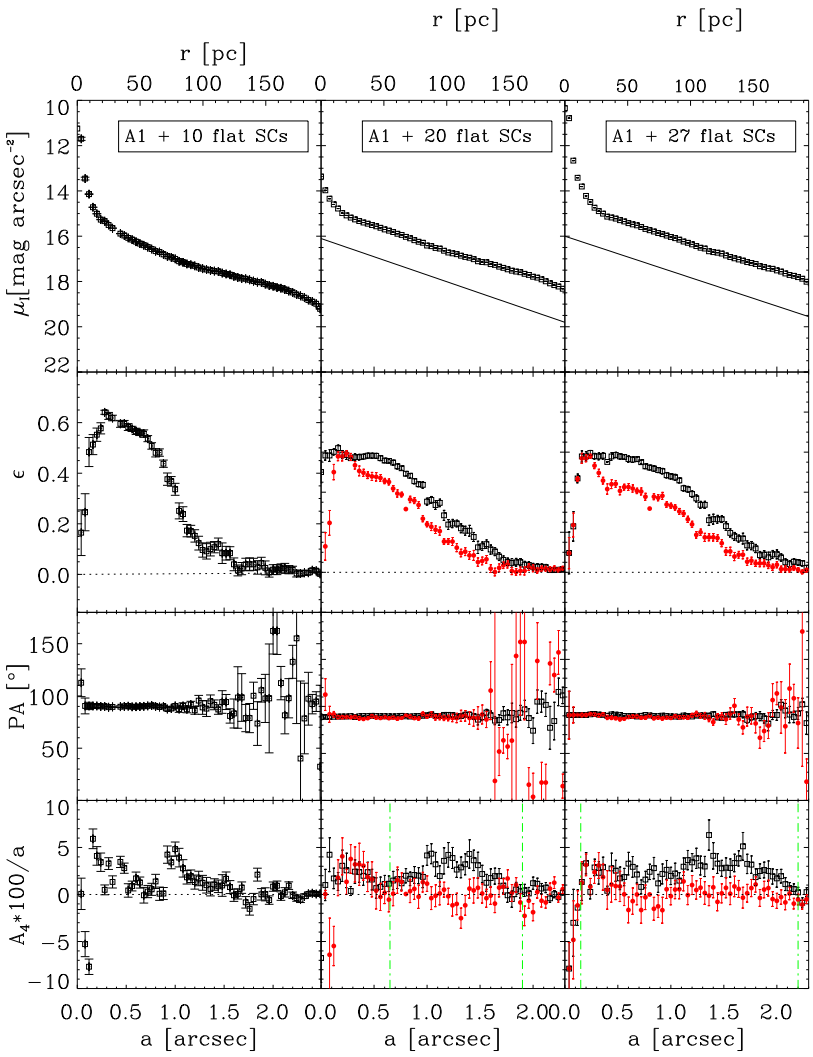

Figure 2.20: Isophotal parameters of the nuclear region of model A1 obtained flattening the star cluster particles distribution of 30% on the z-axis as a function of the isophotal semi-major axis based on the analysis of the surface-brightness distribution measured in the mock images obtained after the accretion of 10 (left-hand panels), 20 (central panels) and 27 (right-hand panels) star clusters. From top to bottom: surface-brightness radial profiles of the galaxy (open black squares) and NSD (solid line) where present, radial profiles of the galaxy ellipticity, position angle and fourth cosine Fourier coefficient before (open black squares) and after (filled red circles) the subtraction of the best-fitting model for the NSD if it was performed. The vertical (green) dot-dashed lines mark the radial range within which the light distribution is characterised by discy isophotes ($A_4 > 0$) due to the presence of the NSD.

Table 2.5: Photometric parameters of the nuclear stellar discs derived from the photometric decomposition of the mock images of model A2.

Model	$N_{\rm SC}$	Fit	$\mu_{0,I}$ [mag arcsec^{-2}]	h [arcsec]	i [°]	$L_{{\rm T},I}$ [10^6 L$_\odot$]
(1)	(2)	(3)	(4)	(5)	(6)	(7)
A2	10	SB	$17.09^{+0.03}_{-0.11}$	$0.43^{+0.02}_{-0.04}$	$75.5^{+1.5}_{-1.9}$	$4.7^{+0.1}_{-0.5}$
A2	10	EF	16.92 ± 0.20	0.40 ± 0.04	77.9 ± 1.4	$3.8^{+0.5}_{-1.0}$
A2	30	SB	$17.39^{+0.31}_{-0.14}$	$0.54^{+0.08}_{-0.12}$	$78.3^{+2.3}_{-3.3}$	$4.6^{+1.2}_{-0.6}$
A2	30	EF	17.11 ± 0.20	0.52 ± 0.04	76.7 ± 0.8	$6.8^{+1.3}_{-1.2}$
A2	50	SB	$16.94^{+0.19}_{-0.15}$	$0.52^{+0.07}_{-0.08}$	$78.1^{+3.1}_{-2.8}$	6.5 ± 1.0
A2	50	EF	16.85 ± 0.10	0.54 ± 0.04	77.3 ± 0.6	7.6 ± 0.7

Note. Col.(1): Name of the model. Col.(2): Number of accreted star clusters. Col.(3): Photometric decomposition method: SB = Scorza-Bender method on the mock images including the light contribution of the bulge, EF = exponential fit on the mock images excluding the light contribution of the bulge. Col.(4): Observed central surface brightness. Col.(5): Scalelength. Col.(6): Inclination. Col.(7): Total I-band luminosity.

Table 2.6: Photometric parameters of the nuclear stellar discs derived from the photometric decomposition of the mock images of model A1 for a flattened distribution of star cluster particles.

Model	$N_{\rm SC}$	$\mu_{0,I}$ [mag arcsec^{-2}]	h [arcsec]	i [°]	$L_{{\rm T},I}$ [10^6 L$_\odot$]
(1)	(2)	(3)	(4)	(5)	(6)
A1_Flat	20	$16.41^{+0.04}_{-0.03}$	$0.68^{+0.04}_{-0.05}$	$77.0^{+0.7}_{-0.9}$	$19.2^{+0.1}_{-0.1}$
A1_Flat	27	$16.31^{+0.04}_{-0.04}$	$0.70^{+0.02}_{-0.04}$	$80.6^{+0.8}_{-1.9}$	$16.7^{+0.1}_{-0.1}$

Note. Col.(1): Name of the model. Col.(2): Number of accreted star clusters. Col.(3): Observed central surface brightness. Col.(4): Scalelength. Col.(5): Inclination. Col.(6): Total I-band luminosity.

2.4.3 Estimate of expected total luminosity and mass of the nuclear stellar disc in model A2

To test the robustness of our decompositions of timesteps of model A2, we can predict the range of the expected total luminosity of the NSD by doing some considerations. Indeed, we can establish the lower limit of the total luminosity of the NSD by assuming that it is formed only by the particles of the initial NCD that grown in size during the merging episodes. Applying the M/L ratio for an evolved NCD as described in Section 2.3.1, we obtained

$$L_{\mathrm{T,I}}^{\mathrm{lower}} = \frac{M_{\mathrm{NCD}}}{(M/L)_{\mathrm{NCD}}} = \frac{1 \times 10^6}{1.6} = 6.3 \times 10^5 \, \mathrm{L}_\odot. \tag{2.14}$$

Instead, assuming that all the particles of the accreted star clusters contributed to the formation and growth of the NSD we obtained the upper limit of its total luminosity as

$$\begin{aligned} L_{\mathrm{T,I}}^{\mathrm{upper}} = \frac{M_{\mathrm{NCD}}}{(M/L)_{\mathrm{NCD}}} + \frac{M_{\mathrm{49SCs}}}{(M/L)_{\mathrm{49SCs}}} + \frac{M_{\mathrm{lastSC}}}{(M/L)_{\mathrm{lastSC}}} = \\ \frac{1 \times 10^6}{1.6} + \frac{9.8 \times 10^6}{1.6} + \frac{2 \times 10^5}{0.2} = 7.8 \times 10^6 \, \mathrm{L}_\odot. \end{aligned} \tag{2.15}$$

The total luminosities resulting from the Scorza-Bender method are in agreement with such ranges of values.

We can also have a rough estimate of the total mass of the NSD. We adopted the M/L ratio to find the range of mass corresponding to the measured total luminosity, assuming a completely old and a completely young population to obtain the upper and the lower limit of the mass, respectively

$$\begin{aligned} M_{\mathrm{T}}^{\mathrm{min}} &= L_{\mathrm{T,I}} \cdot (M/L)_{\mathrm{young}} \\ M_{\mathrm{T}}^{\mathrm{max}} &= L_{\mathrm{T,I}} \cdot (M/L)_{\mathrm{old}} \end{aligned} \tag{2.16}$$

obtaining the values shown in Table 2.7.

The mass of the NSD ($\sim 1 \times 10^7$ $\mathrm{M}_\odot$) is close to that of the few NSDs for which it has been measured (Morelli et al. 2004).

Table 2.7: Lower and upper limits of the mass of the measured nuclear stellar discs of model A2.

Model	SC	$L_{\rm T,I}$	$(M/L)_{\rm young}$	$(M/L)_{\rm old}$	$M_{\rm T}^{\rm min}$	$M_{\rm T}^{\rm max}$
		$[10^6$ L$_\odot]$	[M$_\odot$/L$_\odot$]	[M$_\odot$/L$_\odot$]	$[10^6$ M$_\odot]$	$[10^7$ M$_\odot]$
(1)	(2)	(3)	(4)	(5)	(6)	(7)
A2	10	4.7	0.2	2.7	1.0	1.3
A2	30	4.6	0.2	2.7	0.9	1.2
A2	50	7.8	0.2	2.7	1.6	2.1

Note. Col.(1): Name of the model. Col.(2): Number of accreted star clusters. Col.(3): Total I-band luminosity of the nuclear stellar disc. Col.(4): I-band mass-to-light ratio for a young stellar population. Col.(5): I-band mass-to-light ratio for an old stellar population. Col.(6): Lower limit of the mass of the NSD. Col.(7): Upper limit of the mass of the NSD.

2.4.4 The evolution of galaxy components

Because our galaxies result from simulations, we have the opportunity of separating the different galactic components to see how they evolve and how they contribute to the evolution of the galaxy. Therefore, we generated $I-$band images for each timestep of both the models, modelling the luminosity distribution of each galaxy component by adopting the same M/L ratio as in Section 2.3.1, and assuming $(M/L)_I = 0$ M$_\odot$/L$_\odot$ for the remaining components. Figure 2.21 shows the evolution of the initial NCS, bulge, and accreted star clusters of model A1 for all the timesteps. Figure 2.22 shows the evolution of the initial NCD, bulge, and accreted star clusters for all the timesteps of model A2.

In both the models, the light is dominated by the accreted star clusters in the central regions and by the bulge outward. The bulges, that initially have a spherical distribution, are altered in the central region, reaching an ellipticity $\epsilon = 0.2$. The position angles do not change for the different galaxy components, showing that they are all aligned along the major axis of the galaxy. This is also an expected feature because the accretion of the star clusters starts in the plane of the galaxy. The A_4 coefficients show a positive peak only when more components are superimposed, being such evidence a good proof of the assumptions of the Scorza-Bender method. The most relevant difference we found comparing both the models is that the particles of the star clusters in model A1 tend to mimic the same distribution of the particles of the NCD, e.g., reaching the same flattening and evolving together. So far, the growth of the initial NCD can be a possible issue of the formation of the NSD. Indeed,

except for the first timestep, the NCS and the accreted star clusters in model A1 do not merge in one single component, leading to structures that we can not clearly identify.

Therefore, the discriminating factor is the distribution of the particles of the star clusters with respect to the galactic plane. They are able to merge with the NCD and stay in a flat distribution in model A2. On the contrary, they are more scattered in model A1. This is also confirmed by the fact that when they are able to flat of at least 30%, then a NSD forms, as shown is Section 2.4.2. To have a robust proof of this result, we built I-band images of models A1 and A2 with the same assumptions about instrumental set-up and stellar population as in Section 2.3.1, but excluding the contribution of bulge and adopting an arbitrary distance and different galaxy inclinations. Figure 2.23 shows mock images of the galaxies with a physical scale of 0.25 pc pixel^{-1}. Model A2 shows a flatter structure with respect to model A1.

2.4.5 Two-dimensional photometric decomposition

We also tested our Scorza-Bender decompositions by an independent analysis of an image which excludes all bulge particles. We analysed the I-band image of each timestep with the same assumptions as in Section 2.3.1 including only the light contribution of the bare NCD and accreted star clusters, which are expected to be the building blocks of the NSD. The resulting surface-brightness distribution is modelled with a Sérsic component and an exponential disc by applying the two-dimensional fitting algorithm GALFIT (Peng et al. 2002), as shown in Figure 2.26. The Sérsic component accounts for the central bright structure which dominates the light distribution in the innermost 0.2 arcsec (Figure 2.10), and is given by

$$I(r) = I_{\rm e} \exp\left[-k\left(\left(\frac{r}{r_{\rm e}}\right)^{\frac{1}{n}} - 1\right)\right] \tag{2.17}$$

where n is the concentration parameter, and $I_{\rm e}$ is the surface brightness at the effective radius $r_{\rm e}$, which is the radius where half of the total flux is within.

The best-fitting parameters of the exponential disc are in agreement within errors with the NSD parameters we derived with the Scorza-Bender method, as shown in Table 2.5. Figure 2.27 shows the two-dimensional best-fitting models and the residual maps obtained from the subtraction of such model from the image of the galaxy. The residuals are low, except from the very inner part of the galaxies, where the NCS dominates and where H11 fitted a King profile.

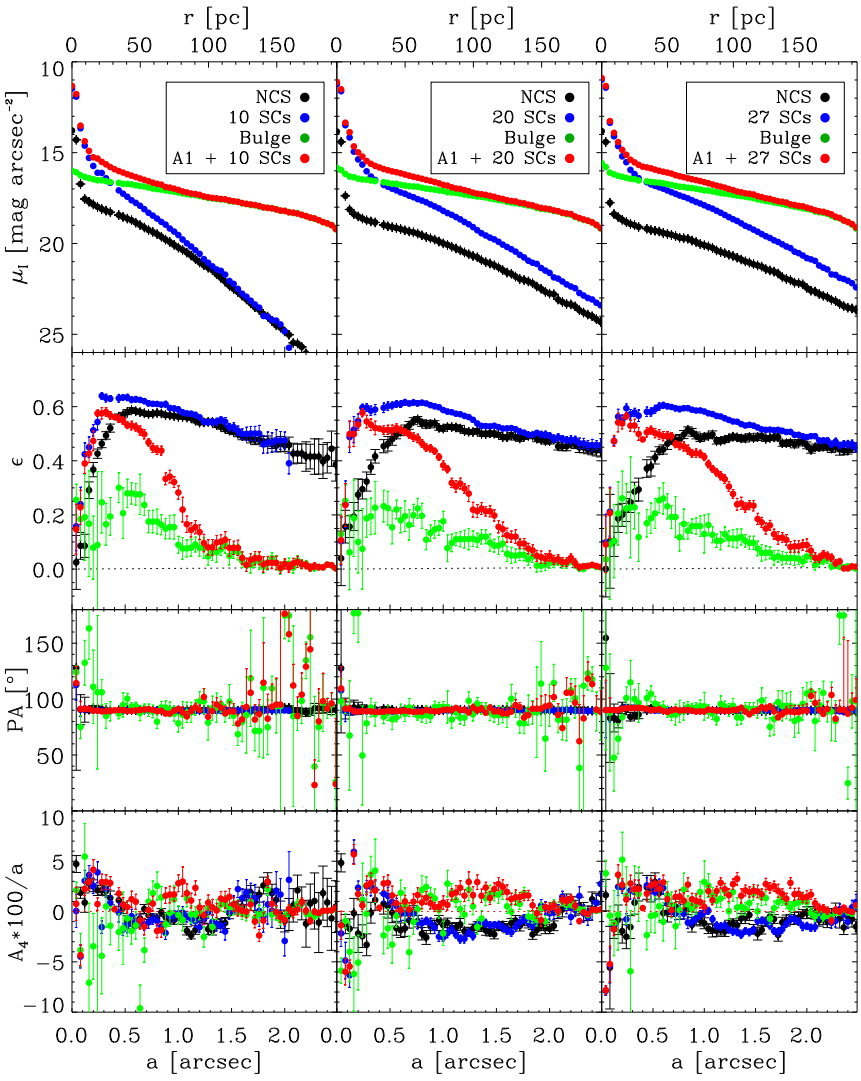

Figure 2.21: Isophotal parameters of the nuclear region of model A1 as a function of the isophotal semi-major axis based on the analysis of the surface-brightness distribution after the accretion of 10 (left-hand panels), 20 (central panels), and 27 (right-hand panels) star clusters, disentangling the different contribution of the galaxy components: the initial seed (black), accreted star clusters (blue), bulge (green), and total (red). From top to bottom: Radial profiles of the surface brightness, ellipticity, position angle, and fourth cosine Fourier coefficient.

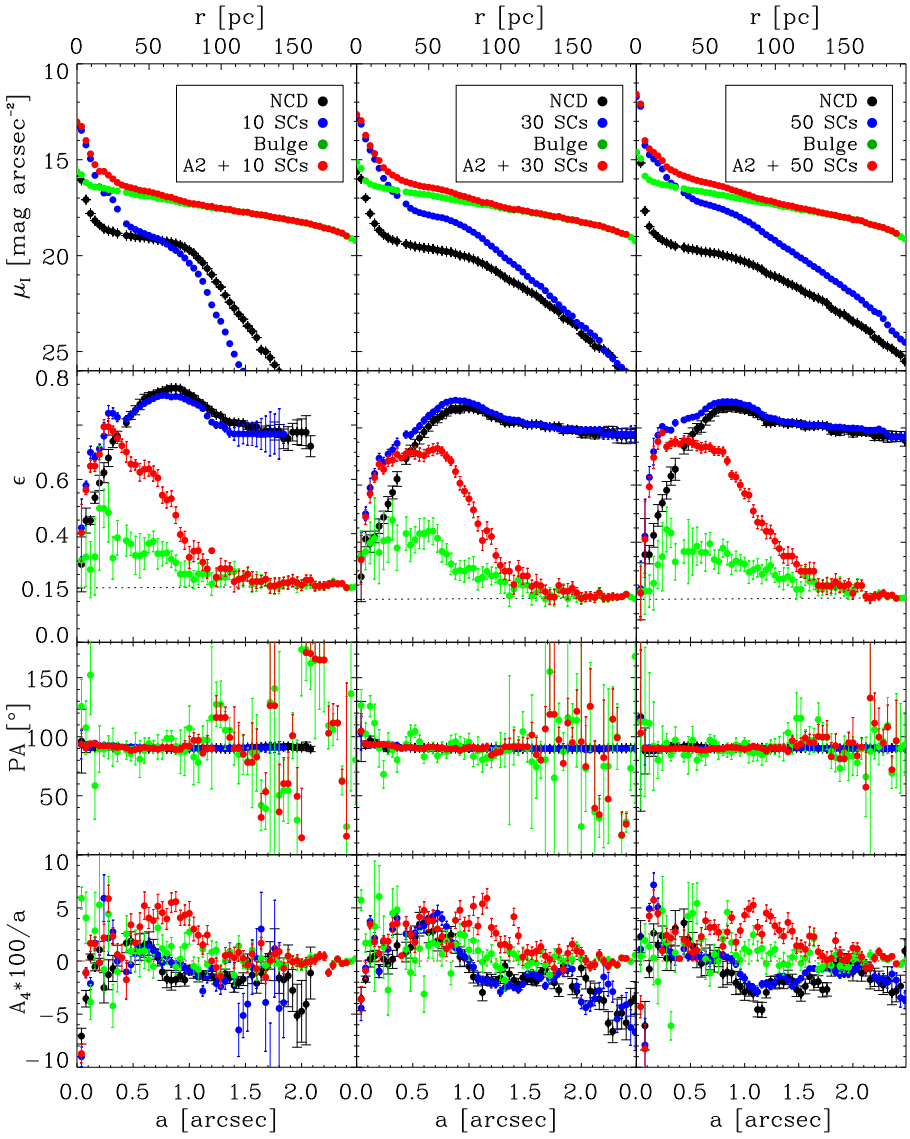

Figure 2.22: As in Figure 2.21, but for model A2 after the accretion of 10 (left-hand panels), 30 (central panels), and 50 (right-hand panels) star clusters.

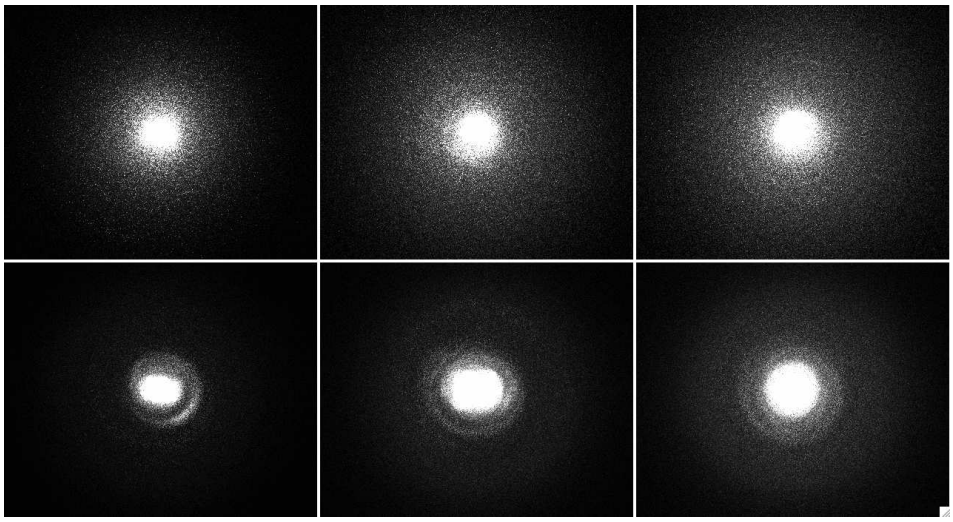

Figure 2.23: Top panels: mock image of the galaxy of models A1 after the accretion of 10 (left-hand panel), 20 (central panel), and 27 (right-hand panel) star clusters, as seen face on. Bottom panels: the same, but for model A2 after the accretion of 10 (left-hand panel), 30 (central panel) and 50 (right-hand panel) star clusters. The field of view is 105 pc $\times$ 85 pc.

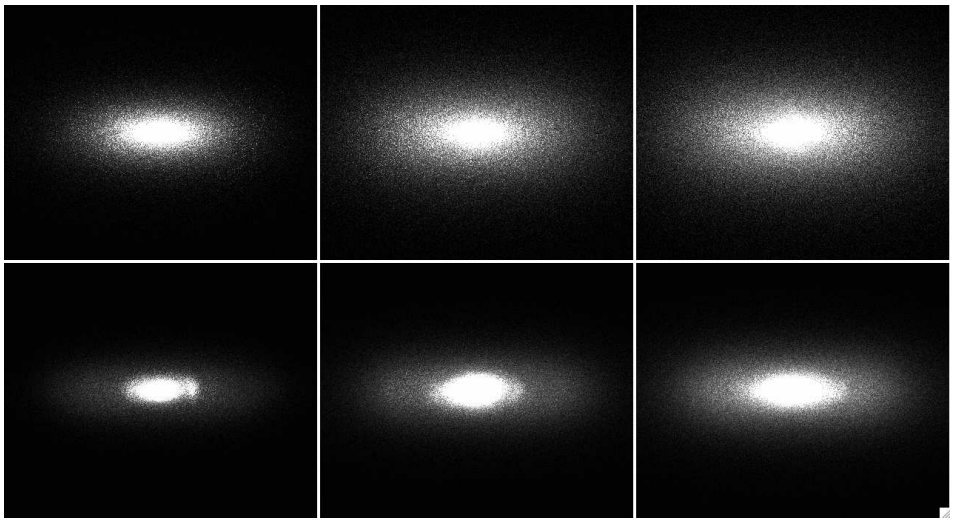

Figure 2.24: As in Figure 2.23, but adopting a galaxy inclination of 75°.

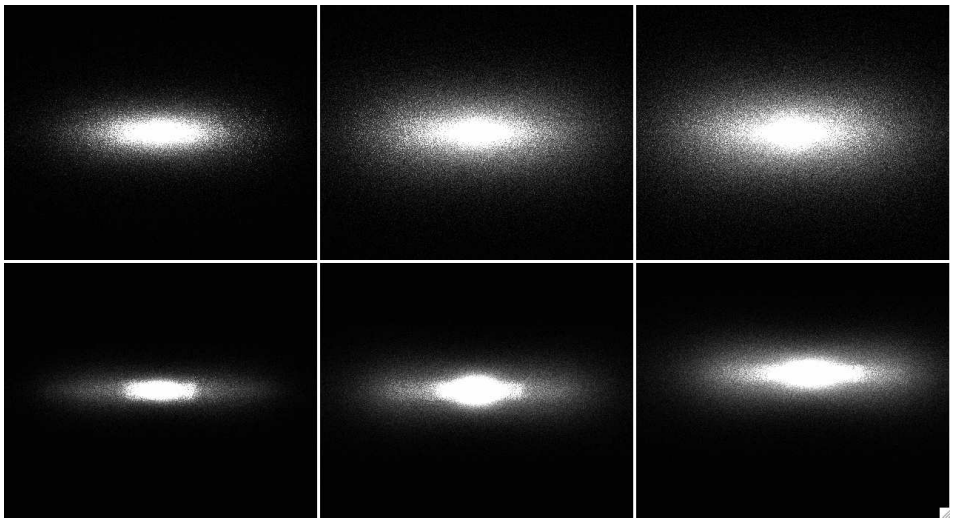

Figure 2.25: As in Figure 2.23, but adopting a galaxy inclination of 90°.

2.4.6 Rotation parameter

We computed the rotation parameter as:

$$\frac{V}{\sigma} = \sqrt{\frac{\langle V^2 \rangle}{\langle \sigma^2 \rangle}} = \sqrt{\frac{\Sigma_{n=1}^{N} F_n V_n^2}{\Sigma_{n=1}^{N} F_n \sigma_n^2}}, \tag{2.18}$$

and the mean ellipticity as:

$$\epsilon = 1 - q = 1 - \sqrt{\frac{\langle y^2 \rangle}{\langle x^2 \rangle}} = 1 - \sqrt{\frac{\Sigma_{n=1}^{N} F_n y_n^2}{\Sigma_{n=1}^{N} F_n x_n^2}}, \tag{2.19}$$

where q is the axis ratio and, following H11, V_n, σ_n, and F_n are the line-of-sight velocity, velocity dispersion, and flux of the pixel at (x_n, y_n), respectively. The origin of the Cartesian coordinates (x, y) is at the centre of the galaxy, with the x-axis aligned with the line-of-nodes. We considered only the N pixels between 15 and 40 pc from the galaxy centre to calculate the luminosity-weighted values of $\langle V^2 \rangle$, $\langle \sigma^2 \rangle$, $\langle x^2 \rangle$ and $\langle y^2 \rangle$ in order to exclude the contribution of the pre-existing nuclear structure (i.e., the NCS in model A1 and the NCD in model A2). There is no need to correct for inclination, since the kinematic maps are built with the simulated galaxies edge-on. We also derived the ratio, $(V/\sigma)^*$, of the measured (V/σ) to the value $(V/\sigma)_{\rm ISO}$ predicted for an edge-on, isotropic

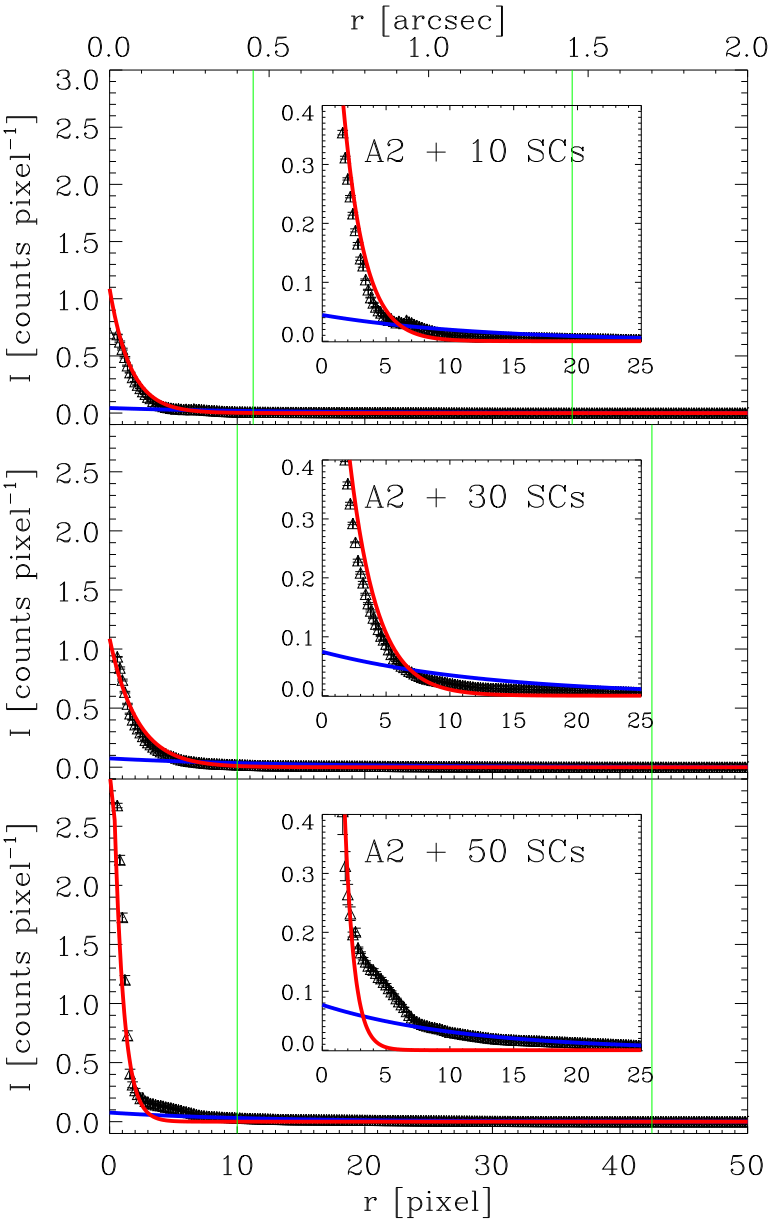

Figure 2.26: Surface-brightness radial profiles of the galaxy of the model A2 (black triangles) after the accretion of 10 (top panel), 30 (middle panel), and 50 (bottom panel) star clusters. Red and blue lines show the best-fitting Sérsic and exponential profiles, respectively. The vertical green lines mark the radial range within which we performed the Scorza-Bender decomposition.

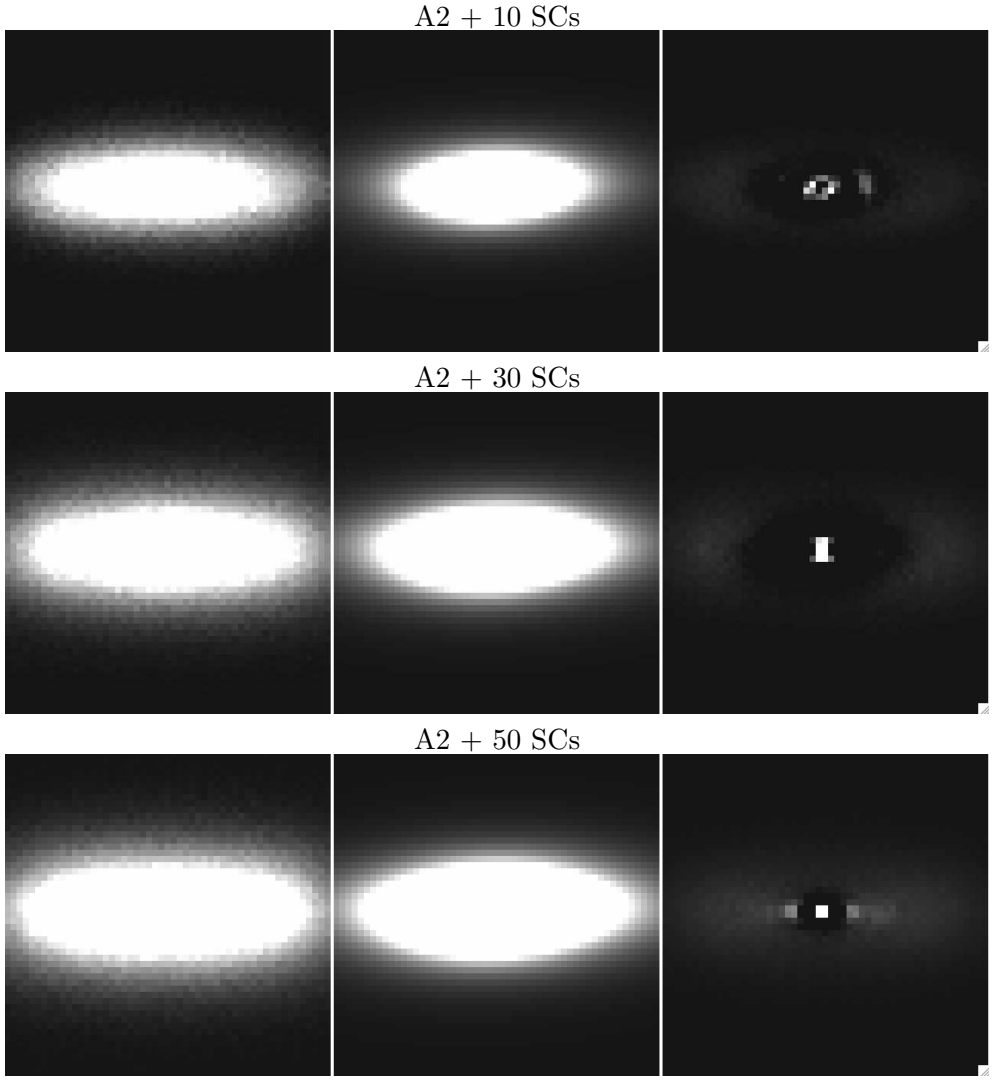

Figure 2.27: The image of the simulated galaxy (left-hand panels), two-dimensional best-fitting model obtained using a Sérsic and an exponential profile (central panels), and residual map (right-hand panels) for model A2 after the accretion of 10 (top panels), 30 (middle panels), and 50 (bottom panels) star clusters, as obtained using GALFIT algorithm. The grey-scale used is kept the same.

oblate system flatten by rotation with the same intrinsic ellipticity ϵ as the

elongated structure, following Kormendy & Illingworth (1982):

$$\left(\frac{V}{\sigma}\right)^{*} = \frac{\left(\frac{V}{\sigma}\right)}{\left(\frac{V}{\sigma}\right)_{\rm ISO}} \simeq \left(\frac{\epsilon}{1-\epsilon}\right)^{\frac{1}{2}}. \tag{2.20}$$

The resulting values of the luminosity-weighted velocity, velocity dispersion, and ellipticity together with the rotation parameter (V/σ) and $(V/\sigma)^*$ for all timesteps are listed in Table 2.8. The axis ratio of the elongated structure measured in the nucleus of model A1 is $q \simeq 0.4$. The stellar kinematics and ellipticity are therefore consistent with an anisotropic rotator with $(V/\sigma)^* \simeq 0.6$. The elongated structure of model A2 ($q \simeq 0.3$) instead rotates almost as fast as an isotropic oblate system, $(V/\sigma)^* \simeq 0.8$. In both models, V and σ increase with the number of accreted star clusters, although the difference between the values measured in the first and last timestep is smaller than the typical 1σ error ($5 - 10$ km s^{-1}) on the stellar kinematics measured in galactic nuclei (e.g., Emsellem et al. 2004).

Figure 2.28 shows the resulting profiles of the velocity, velocity dispersion, and V/σ for both the models taking into account all the simulated galaxy components. These profiles show similar shapes in all the timesteps of model A1. The highest values are reached during the last accretion, where the velocity is equal to 27 km s^{-1} at 0.1 arcsec, and decreases to 5 km s^{-1} in the external regions. Likewise, the central velocity dispersion reaches 70 km s^{-1} and decreases to 40 km s^{-1}. The maximum of (V/σ) is about 0.5. The velocity profiles of model A2 show different behaviours during all the timesteps. After the accretion of 10 and 30 star clusters the velocity profile has a central narrow peak, while after the accretion of 50 star cluster the profile is smoothed and the peak is reached at 0.1 arcsec. Moreover, the velocity dispersion profile of model A2 after the accretion of 50 star clusters differs from the ones of the others timesteps, showing a central peak instead of a central lack. Therefore, this is imprinted in the different shapes of (V/σ) and indicates the presence of an initial inner component that is rotating faster. After the accretion of 50 star clusters, such component has reduced the velocity and incremented the dispersion. However, in all the cases, model A1 shows higher values of velocity and velocity dispersion with respect to model A2. Such profile is dominated by the nuclear star cluster for both the models.

Figure 2.29 shows the profiles of the velocity, velocity dispersion, and V/σ for both the models A1 and A2 excluding the contribution of the bulge. In both the models, the profiles show similar shapes between all the timesteps. Indeed, without the bulge, the kinematics of model A2 is regular with respect to the

Table 2.8: Kinematic parameters of the nuclear elongated structure observed in models A1 and A2.

Model	$N_{\rm SC}$	$\frac{M_{\rm SC}}{M_{\rm in}}$	V [km s^{-1}]	σ [km s^{-1}]	$\frac{V}{\sigma}$	ϵ	$\left(\frac{V}{\sigma}\right)^*$
(1)	(2)	(3)	(4)	(5)	(6)	(7)	(8)
A1	10	3	15.1	15.7	0.95	0.65	0.70
A1	20	6	15.7	19.4	0.80	0.62	0.63
A1	27	8.1	16.7	21.8	0.77	0.60	0.63
A2	10	2	12.6	7.6	1.66	0.75	0.96
A2	30	6	14.2	11.0	1.29	0.68	0.82
A2	50	10	18.5	13.8	1.34	0.72	0.84

Note. Col. (1): Model number. Col. (2): Number of accreted star clusters. Col. (3): Ratio of the accreted mass to initial mass of the nuclear star cluster. Cols. (4) and (5): Luminosity-weighted velocity and velocity dispersion excluding the contribution of the central pre-existing structure. Col. (6): Rotation parameter. Col. (7): Luminosity-weighted ellipticity. Col. (8): Ratio of V/σ to the value predicted for an edge-on oblate isotropic rotator with an intrinsic ellipticity given in Col. (7) and flattened by rotation.

previous case. The last accretion is characterised by the highest velocity and velocity dispersion: model A1 has $V = 29$ km s^{-1} and $\sigma = 70$ km s^{-1}, while model A2 has $V = 10$ km s^{-1} and $\sigma = 50$ km s^{-1}. The (V/σ) profile is almost constant ($\simeq 0.6$) in model A1, while it ranges from 0.6 to 1.1 in model A2.

Figure 2.30 shows the resulting profiles of the velocity, velocity dispersion, and V/σ for both the model excluding the contamination of both the nuclear star cluster and bulge. The inner drop is due to the exclusion of the particles of the nuclear star cluster. As in the previous cases, the last accretion is characterised by the highest velocity and velocity dispersion: in model A1 the velocity and velocity dispersion reach 18 km s^{-1} and 23 km s^{-1} respectively, while in model A2 they reach 21 km s^{-1} and 14 km s^{-1}. The (V/σ) profile is almost similar between the timesteps of model A1, while it shows the highest values during the first timestep of model A2, reaching 2.0.

Comparing the three cases of kinematic profiles, the rotational parameter (V/σ) is lower when we consider all the components of the galaxy and reaches the peak when the bulge and the nuclear star cluster are excluded from the analysis.

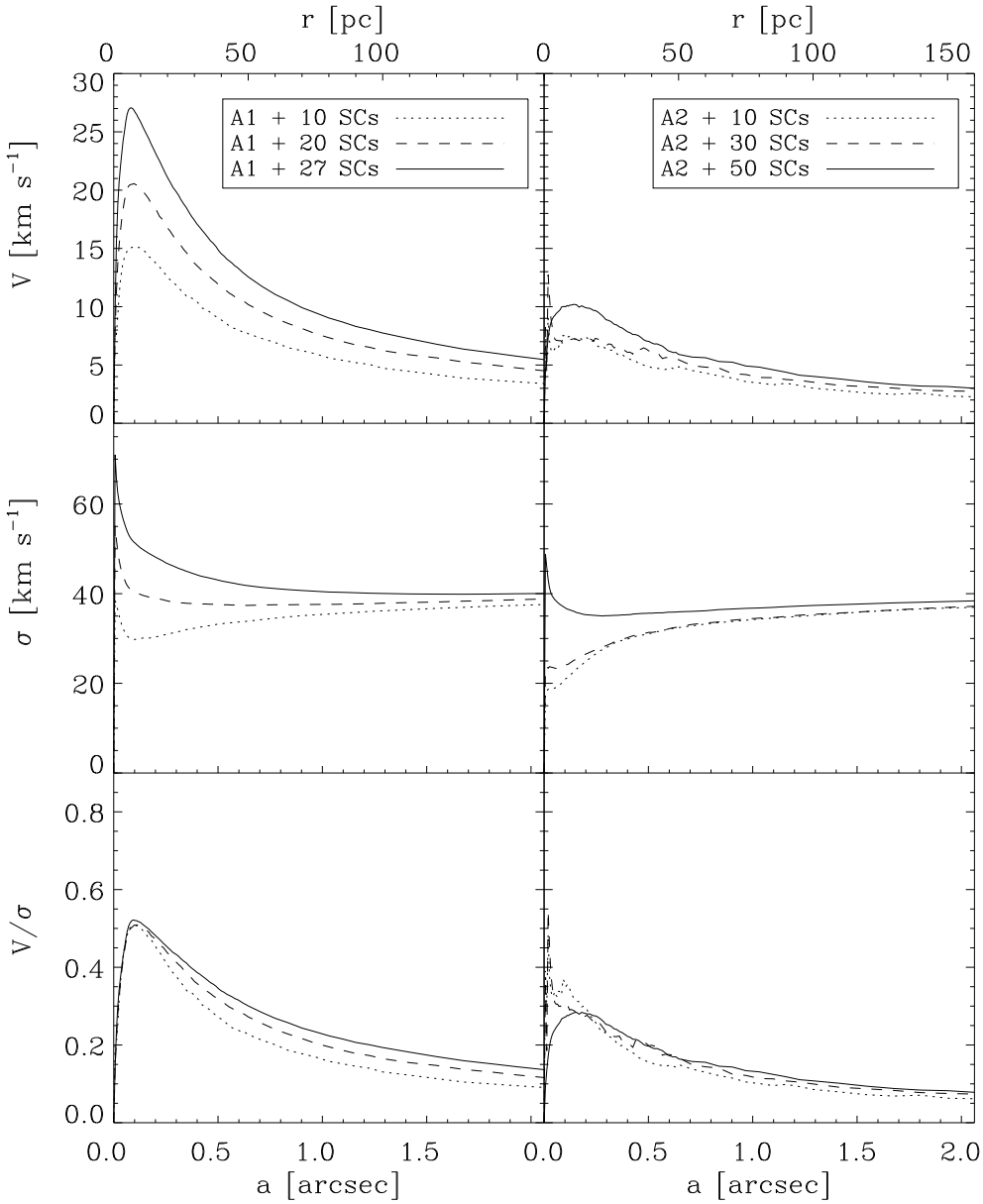

Figure 2.28: Radial profiles of the velocity (top panels), velocity dispersion (middle panels), and V/σ (bottom panels) considering all the galaxy components of models A1 (left-hand panels) and A2 (right-hand panels) for all the three timesteps, as given in the legend.

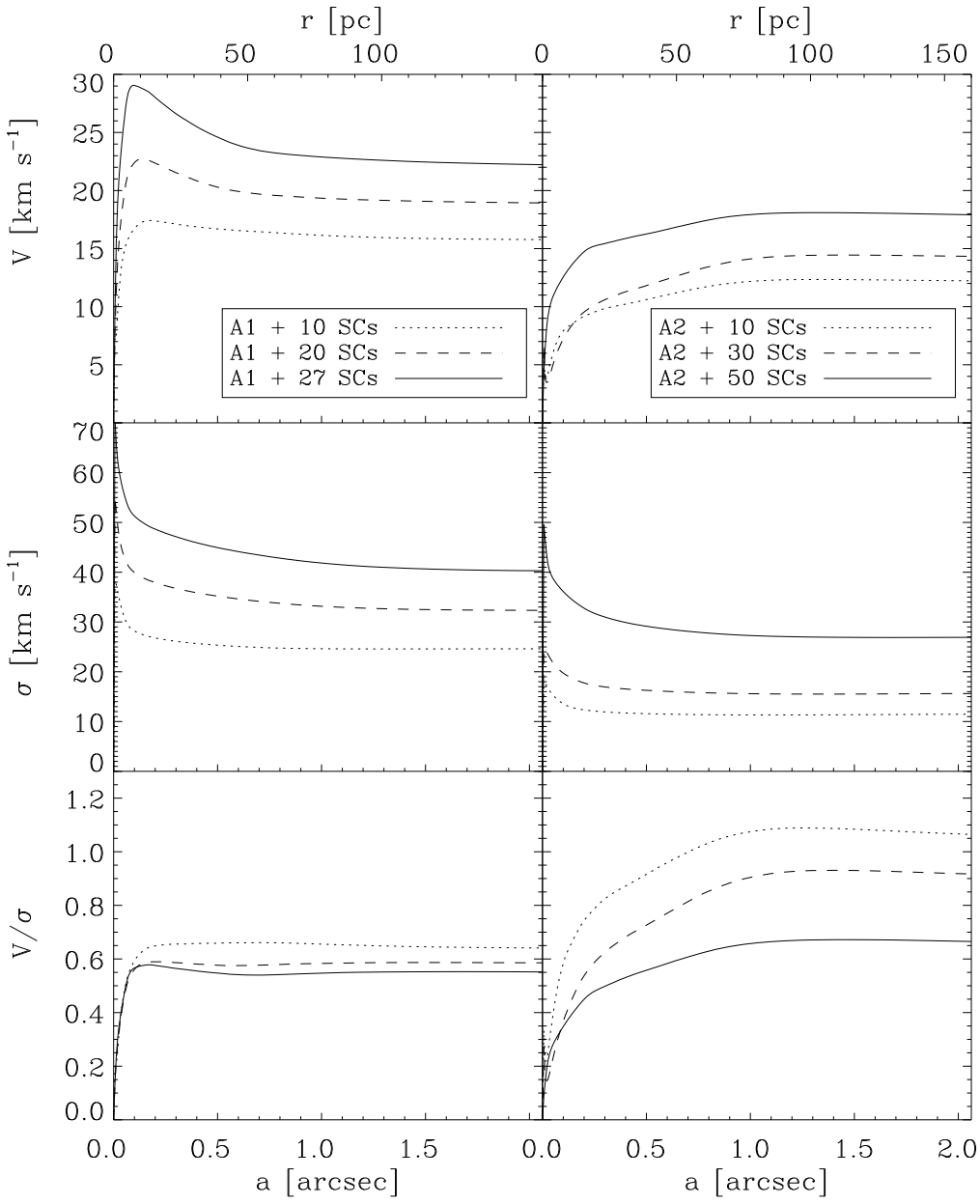

Figure 2.29: As in Figure 2.28, but excluding the contribution of the bulge.

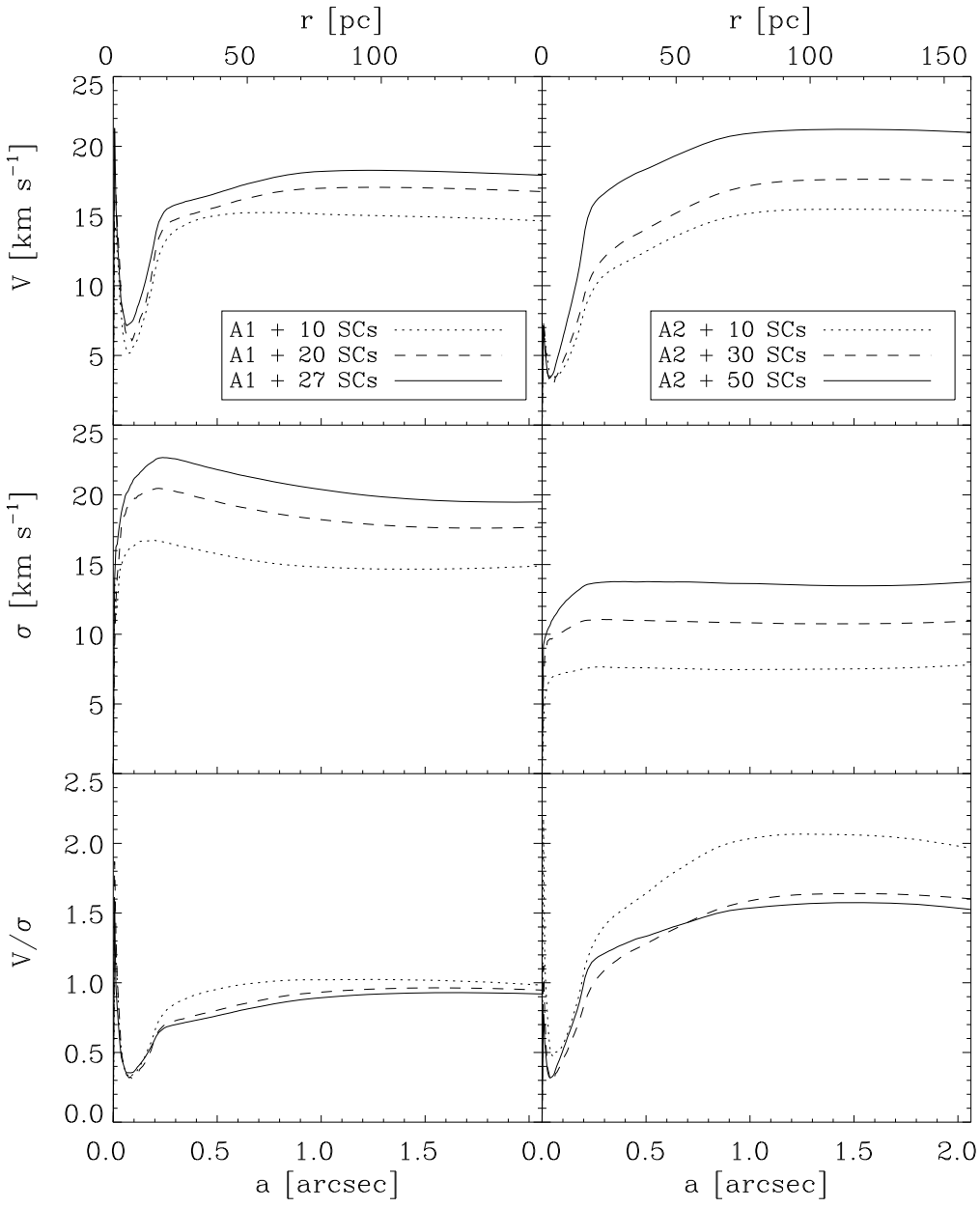

Figure 2.30: As in Figure 2.28, but excluding the contribution of the bulge and of the particles within the central 15 pc, where the nuclear star cluster resides.

2.5 Discussion

From the analysis of the unsharp masked image, the nucleus in model A1 shows an elongated structure (Figure 2.6). Its radial extent increases with the number of accreted star clusters as seen from the increase of the radial range where significantly elongated isophotes are measured (Figure 2.9). Indeed, $\epsilon > 0$ out to 1.1, 2.1, and 2.4 arcsec from the centre after the accretion of 10, 20, and 27 star clusters. In all the timesteps the ellipticity peaks at $\epsilon_{\rm max} \simeq 0.6$ at about 0.2 arcsec (15 pc), where the NCS dominates, as shown in the analysis of H11, and it gently decreases outwards. The absence of a sharp peak in the A_4 radial profile at the location where NSDs reside is the main photometric reason for concluding that no NSD is present, even if the unsharp-mask technique shows an elongated structure. Such feature can also be caused by isophotes of increasing ellipticity inwards. Therefore unveiling an NSD requires performing a detailed measurement of the surface-brightness distribution in the nuclear regions. In addition, the rotation parameter and ellipticity measured from the stellar kinematics are consistent with an anisotropic rotation (Table 2.8). Therefore, we conclude that the elongated nuclear structure observed in model A1 is not a NSD, in spite of the fact that the total accreted mass, 1.6×10^7 $\mathrm{M}_\odot$, is comparable to that of observed NSDs (e.g., Morelli et al. 2004).

On the other hand, the photometric and kinematic properties of the nuclear structure seen in model A2 (Figure 2.7) are reminiscent of an NSD. The rising ellipticity is associated with discy isophotes over a radial range which steadily increases with the number of accreted star clusters (Figure 2.10). The ellipticity peaks at a similar value as model A1 ($\epsilon_{\rm max} \simeq 0.6$) although it is $\epsilon \simeq 0.5$ over a wider radial range ($0.2 - 0.8$ arcsec). At larger radii, the isophotes quickly become round. The elongated structure rotates as fast as an oblate isotropic spheroid (Table 2.8). Its surface-brightness distribution can be modelled as an inclined exponential disc with a maximum local light contribution to the total surface brightness of about 30% at 0.4 arcsec from the centre. The NSD parameters measured in the three timesteps are consistent with each other within the errors. Their mean values from the Scorza-Bender method are $\mu_{0,I} = 17.14$ mag arcsec^{-2}, $h = 0.50$ arcsec (38.8 pc), and $i = 77\overset{\circ}{.}3$ corresponding to $L_{\mathrm{T},I} = 5.3 \times 10^6$ $\mathrm{L}_\odot$. The inclination and PA of the line-of-nodes of the NSD and its host bulge are the same within the errors. The total accreted mass is 1.0×10^7 $\mathrm{M}_\odot$ and it is consistent with that of observed NSDs.

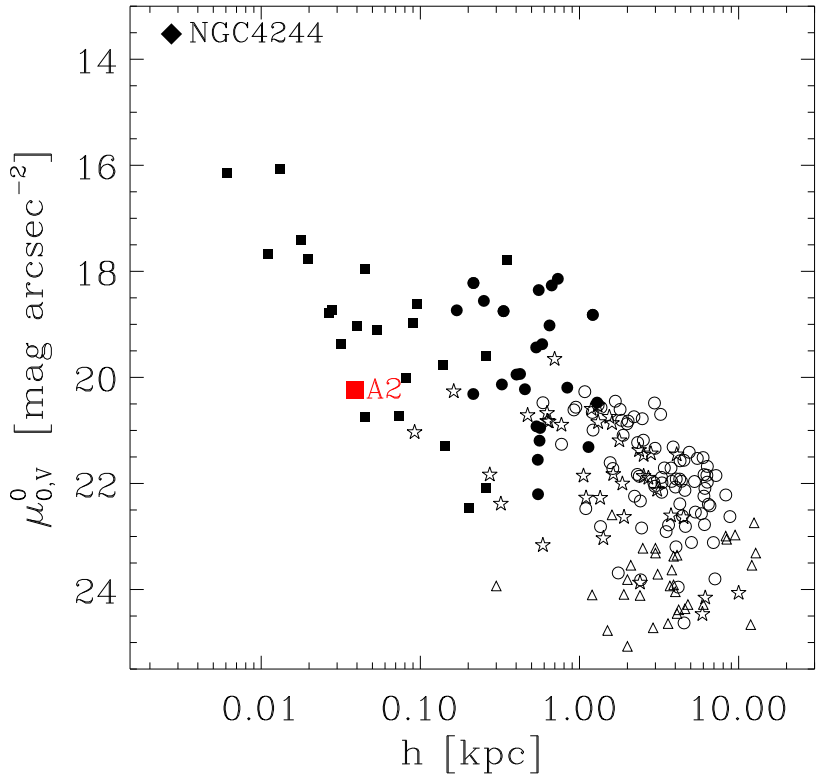

Figure 2.31: The face-on central surface brightness as a function of disc scalelength adapted from Ledo et al. (2010) and including the NSD of NGC 4698 (Corsini et al. 2012). The large red square marks the NSD of model A2. Open circles indicate high surface-brightness spirals, triangles low surface-brightness spirals, stars show S0s, and filled circles discy ellipticals. Small squares represent observed NSDs. The filled diamond represents the NCD of NGC 4244.

2.5.1 The $\mu_0 - h$ relation for nuclear stellar discs

We compared the structural properties of the NSD of model A2 to those of the known NSDs (Ledo et al. 2010; Corsini et al. 2012). We derived the Johnson V-band central surface brightness of the model NSD from the mean I-band value using the IRAF task SYNPHOT. Because this correction depends on the galaxy spectral energy distribution, it is calculated using the spectral template for an Sc spiral galaxy by Kinney et al. (1996) to match the late morphological type of NGC 4244. The resulting shift is $V - I = 1.46$ mag. The mean observed

Table 2.9: Photometric parameters of nuclear stellar discs for the $\mu^0_{0,V} - h$ diagram.

Galaxy	Type	D	$\mu^0_{0,\mathrm{I}}$	h	i	Reference	$\mu^0_{0,\mathrm{I,resc}}$
		[Mpc]	[mag arcsec^{-2}]	[pc]	[°]		[mag arcsec^{-2}]
(1)	(2)	(3)	(4)	(5)	(6)	(7)	(8)
ESO352-057	S0	76.11	20.74	44.74	76.26	Ledo et al. (2010)	20.74
ESO378-020	S0	39.87	19.10	53.39	65.98	Ledo et al. (2010)	19.10
ESO507-027	S0	43.27	18.61	94.87	68.28	Ledo et al. (2010)	18.61
IC 0875	S0	42.32	22.08	259.67	84.84	Ledo et al. (2010)	22.08
NGC 0584	E	24.49	18.97	90.18	73.86	Ledo et al. (2010)	18.97
NGC 1425	SAb(s)	13.1	18.07	26.5	70	Pizzella et al. (2002)	18.78
NGC 3115	E-S0	9.2	15.36	13	81.60	van den Bosch (1998)	16.08
NGC 3385	S0	108.67	17.78	351.19	61.71	Ledo et al. (2010)	17.78
NGC 3610	E	26.99	19.60	260.38	81.81	Ledo et al. (2010)	19.60
NGC 3898	SAab(s)	16.4	16.69	17.9	73	Pizzella et al. (2002)	17.40
NGC 4128	S0	36.3	19.77	138.01	85.76	Ledo et al. (2010)	19.77
NGC 4342	S0	11.26	15.42	6	83	van den Bosch (1998)	16.13
NGC 4458	E	12.6	16.95	11.03	83	Morelli et al. (2004)	17.66
NGC 4474	S0	18.0	21.29	143.5	86.49	Ledo et al. (2010)	21.29
NGC 4478	E	12.6	18.31	40.05	80	Morelli et al. (2004)	19.02
NGC 4570	S0	12.6	17.05	20	81	van den Bosch (1998)	17.77
NGC 4621	E	18.0	20.72	73.87	83.97	Ledo et al. (2010)	20.72
NGC 4623	SB0	12.6	18.00	28	90	van den Bosch (1998)	18.72
NGC 4660	E	18.0	20.02	81.19	78.92	Ledo et al. (2010)	20.02
NGC 4698	SAab(s)	17.0	17.24	45.2	75.5	Corsini et al. (2012)	17.95
NGC 5308a	S0	25.46	22.46	201.59	89.89	Ledo et al. (2010)	22.46

Note. Col. (1): Galaxy name. Col. (2): Morphological type from RC3. Col. (3): Distance, as assumed in Col (7). Col. (4): $I-$band observed central surface brightness corrected for mean inclination of the NSD. Col. (5): Scalelength of the NSD. Col. (6): Inclination of the NSD. Col. (7): Reference for the photometric parameters and distances. Col. (8): $I-$band observed central surface brightness corrected for mean inclination of the NSD rescaled using an Hubble constant of $H_0 = 72$ km s^{-1} Mpc^{-1}.

central surface brightness is corrected for mean inclination as

$$\mu^0_{0,V} \;=\; \mu_{0,V} - \; 2.5\log(\cos i) \;=\; 20.24 \text{ mag arcsec}^{-2}. \qquad (2.21)$$

The scalelength and face-on central surface brightness are close to those of the larger observed NSDs and fit on the $\mu^0_{0,V} - h$ relation for galaxy discs, as we show in Figure. 2.31. Table 2.9 lists the photometric parameters of the NSDs for which the photometric decompositions are available so far. They are rescaled using an Hubble constant of $H_0 = 72$ km s^{-1} Mpc^{-1}. The photometric properties of the NSD in the simulated galaxy are remarkably similar to those of NSDs observed in the nuclei of real galaxies. Indeed, the scalelength and face-on central surface brightness fit on the $\mu^0_{0,V} - h$ relation for galaxy discs.

2.5.2 The Tully-Fisher relation for nuclear stellar discs

We also compare the total luminosity of the NSD with that predicted by extrapolating the I-band Tully-Fisher relation (Masters et al. 2006, Figure 2.32)

to discs of similar rotational velocity (~ 20 km s^{-1})

$$M - 5\log h = -20.85 - 7.85\,(\log W - 2.5) \tag{2.22}$$

with scatter $\epsilon = 0.41 - 0.44\,(\log W - 2.5)$ where $h = H_0/100$, with an Hubble constant $H_0 = 72$ km s^{-1} Mpc^{-1}. The relation is consistent with the Cepheids-calibrated one using the Masters et al. (2006) sample

$$M = -20.485 \pm 0.05 \pm 0.06 - (7.85 \pm 0.1)(\log W - 2.5) \tag{2.23}$$

where the first error is statistical and the second is due to the total uncertainty and H_0.

We assumed the rotation width of the NSD of model A2 to be $W = 2\,\langle V_{\rm rms}\rangle$ where the luminosity-weighted second-order kinematic moment

$$\langle V_{\rm rms}\rangle = \sqrt{\langle V^2\rangle + \langle\sigma^2\rangle} \tag{2.24}$$

is measured from the kinematic maps of the simulated galaxy excluding the light contribution of the bulge (Table 2.10). We found that the rotation width and luminosity of the NSD of model A2 are consistent with the Tully-Fisher relation. Similarly we measure the rotational width for the NSDs for which both the stellar kinematics and photometric decomposition are available so far. As we knew the total luminosity and central surface brightness of the decomposed NSDs from literature, we recovered the absolute magnitude using the Pogson formula

$$M_{\rm T,I} = -2.5\log(L_{\rm T,I}) + M_{\odot,\rm I} \tag{2.25}$$

where

$$M_{\odot,\rm I} = 4.08\,{\rm mag}. \tag{2.26}$$

In measuring such parameter, we derived I-band total magnitude from the instrumental $F814W$-band value using the IRAF task SYNPHOT, matching the morphological type of the sample galaxies with spectral templates by Kinney et al. (1996). Moreover, we rescaled all the distances using the value $H_0 = 72$ km s^{-1} Mpc^{-1}. The adopted rotational widths are luminosity weighted and also corrected for the inclination using the formula

$$\langle V_{\rm rms,I}\rangle = \sqrt{\left(\frac{V_I^2}{\sin i}\right) + \sigma_I^2} \tag{2.27}$$

where i is the inclination of the galaxy, and

$$V_{\rm I} = \frac{\sum_{i=1}^{n} I_{\rm I}(i) \cdot V(i)}{\sum_{i=1}^{n} I_{\rm I}(i)} \tag{2.28}$$

and

$$\sigma_{\rm I} = \frac{\sum_{i=1}^{n} I_{\rm I}(i) \cdot \sigma(i)}{\sum_{i=1}^{n} I_{\rm I}(i)} \tag{2.29}$$

are the velocity and the velocity dispersion measured within the n radii between $r = 0$ and $r = r_{\rm max}$ where $V(i) = V_{\rm max}$ of the NSD. Table 2.10 lists the photometric and kinematic parameters we recovered from literature for NSDs for which both the stellar kinematics and photometric decomposition are available. We decided to exclude NGC 4342 from the sample because its kinematics is totally dominated by the central SBH. The luminosities of the sample galaxies are offset below the Tully-Fisher relation in agreement with the earlier findings of Morelli et al. (2004).

The NSDs in real and simulated galaxies show a different behaviour in the Tully-Fisher relation in spite of having similar luminosities and similar maximum light contributions (Figure 2.32). We explain the discrepancy as due to the fact that for real galaxies observations miss a proper decomposition of the line-of-sight velocity distribution. The rotation widths of NSDs in real galaxies are over-estimated due to the contribution of the host spheroid to the kinematics (in particular to the velocity dispersion) measured in the nuclear regions. This is not the case of the NSD of model A2 where we have the actual kinematics of the nuclear disc, making the comparison with the Tully-Fisher prediction straightforward. Its rotational width increases and the NSD drops below the Tully-Fisher relation if the measured stellar kinematics includes the bulge contribution. However, the rotational width ($\simeq$ 80 km s^{-1}) is not as large as in the observed NSDs ($\simeq$ 230 km s^{-1}) since its bulge has a lower velocity dispersion compared to the larger spheroidal component of the early-type galaxies hosting the NSDs shown in Figure 2.32.

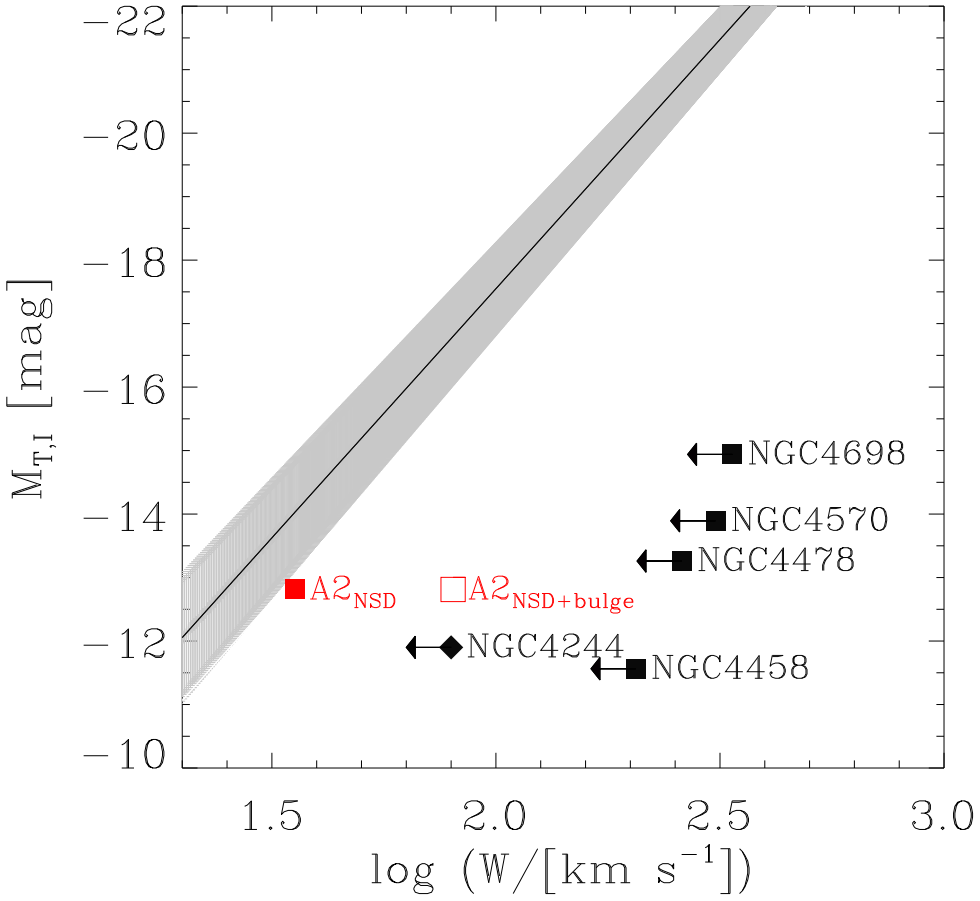

Figure 2.32: The total magnitude as a function of the rotation width for the NSDs observed in real galaxies (black squares) and in the nucleus of model A2 (red squares). Only observed NSDs with both measured kinematics and photometric decomposition are shown. The two values for model A2 are derived by excluding (filled red square) and including (open red square) the bulge contribution. The filled diamond represents the NCD of NGC 4244. The solid line and the grey region correspond to the Tully-Fisher relation in the I band by Masters et al. (2006) and its scatter, respectively.

Table 2.10: Photometric and kinematic parameters of nuclear stellar discs for the Tully-Fisher relation.

Galaxy	D [Mpc]	i [°]	$L_{\mathrm{T,I}}$ 10^6 $\mathrm{L}_\odot$	Reference	$M_{\mathrm{T,I}}$ [mag]	V_{I} [km s^{-1}]	σ_{I} [km s^{-1}]	Reference [km s^{-1}]	$V_{\mathrm{rms,I}}$	$\log(W)$
(1)	(2)	(3)	(4)	(5)	(6)	(7)	(8)	(9)	(10)	(11)
A2	16.0	77.3	5.3	this work	−12.8	15.	10.7	this work	18.6	1.5
A2 + bulge	16.0	77.3	5.3	this work	−12.8	15.8	36.8	this work	40.1	1.9
NGC 4342	7.1	83	2.4	Scorza & van den Bosch (1998)	−11.8	220.0	420.0	van den Bosch et al. (1998)	474.5	2.9
NGC 4458	12.6	83	3.2	Morelli et al. (2010)	−11.6	18.7	100.9	Halliday et al. (2001)	102.6	2.3
NGC 4478	12.6	80	15.2	Morelli et al. (2010)	−13.3	31.9	126.0	Halliday et al. (2001)	130.1	2.4
NGC 4570	12.6	81	27.1	Morelli et al. (2010)	−13.9	52.0	145.4	Krajnović & Jaffe (2004)	154.5	2.5
NGC 4698	17.0	75.5	40.7	Corsini et al. (2012)	−14.9	18.3	167.4	Bertola et al. (1999)	168.6	2.5

Note. Col. (1): Name of the galaxy or model. Col. (2): Distance in Mpc. Col. (3): Inclination of the galaxy or model. Col. (4): $I-$band total luminosity of the NSD, rescaled using $H_0 = 72$ km s^{-1} Mpc^{-1}. Col. (5): Reference from photometric data. Col. (6): Absolute magnitude of the NSD. Col. (7): Luminosity-weighted mean velocity of the NSD. Col. (8): Luminosity-weighted mean velocity dispersion of the NSD. Col. (9): Reference from kinematic data. Col. (10): Luminosity-weighted second-order kinematic moment, measured using Equation 2.27. Col. (11): Logarithm of the rotation width $W = 2\langle V_{\mathrm{rms}}\rangle$.

2.5.3 Nuclear cluster discs and nuclear stellar discs

To study whether there is a link between NSDs and NCDs, we plotted the NCD of NGC 4244 in the $\mu^0_{0,V} - h$ relation.

We used the photometric data from Seth et al. (2006), where the $F814W$ surface brightness of the disc is fitted by an exponential thick disc (with scale-length h=2.73 pc, central scale-height z_0 =1.42 pc, L_0=13.18 mag arcsec $^{-2}$), and assuming that $L_0 = I_0/2h$ is the face-on central surface brightness at coordinates $(x, y) = (0, 0)$

$$I(r) = I_0 \exp\left[-\left(\frac{r}{h}\right)\right] = 2z_0 L_0 \exp\left[-\left(\frac{r}{h}\right)\right]. \tag{2.30}$$

We calculated

$$\mu^0_{0,\mathrm{V}} = -2.5 \log I_0 + 1.46 + \mu_{\odot,\mathrm{I}} = 13.52\,\mathrm{mag\,arcsec}^{-2} \tag{2.31}$$

where the solar surface brightness in $I-$band is $\mu_{\odot,\mathrm{I}} = 25.65$ mag arcsec^{-2}. The NCD of NGC 4244 would be located in the upper-left corner of the $\mu^0_{0,V} - h$ diagram (Figure 2.31), where the discs have the higher surface brightness and smaller radius, determining a continuity in the relation, and therefore a link between NCDs and NSDs.

We also measured the Tully-Fisher relation for the NCD of NGC 4244. We used the photometric data from Seth et al. (2006). Following the Equation 8 of van der Kruit & Searle (1981), the total luminosity of such thick disc in NGC 4244 is

$$L_\mathrm{T} = 4\pi h^2 z_0 L_0 = 2\pi h z_0 I_0 \tag{2.32}$$

leading to $M_{\mathrm{T,I}} = -11.9$ mag using the Equation 2.25. Extrapolating the second-order kinematic moment of the NCD from H11, we found $\log(W) = 1.9$. Therefore, the NCD of NGC 4244 rotates faster with respect to the NSD we found in model A2 (Figure 2.32). Moreover despite its high surface brightness, the NCD of NGC 4244 is radially limited with respect to the scales of NSDs, as shown in Figure 2.31. Therefore, it is less bright than the NSD of model A2.

Understanding whether there is a link between NSDs and NCDs is a very interesting and open topic. It deserves more attention for future investigation: studying the properties of such objects will allow us to know if a continuity exists and if they are causally connected.

2.6 Conclusions

We have analysed two $N-$body simulations from H11 exploring the dissipationless merging of multiple star clusters into the centre of a galaxy. The simulations were originally aimed at investigating the photometric, kinematic, and dynamic properties of the nucleus of NGC 4244 which hosts a massive stellar cluster in rapid rotation (Seth et al. 2006, 2008b). In this thesis we have investigated the images and kinematic maps built from the simulation as if they were real, assuming the galaxy to be at the distance of the Virgo cluster. We have tested the importance of purely stellar dynamical mergers for the formation and growth of NSDs by looking for their presence in the nucleus of the simulated galaxies. Our main conclusions can be summarised as follows.

- A flattened merger remnant ($q \simeq 0.3 - 0.4$) with a radius of about 100 pc is observed in the nucleus of the simulated galaxy when a few tens of star clusters with sizes and masses comparable to those of globular clusters observed in the Milky Way are accreted onto a pre-existing stellar component at the centre. This flattened structure forms regardless of whether the pre-existing component is a massive spherical cluster (as is the NCS of model A1) or a rapidly rotating disc (as is the NCD of model A2) and regardless of the amount of accreted mass ($2-10\times$) with respect to the mass of the pre-existing component ($\sim 10^6$ $M_\odot$).

- The merger remnant passes all observational constraints to be an NSD when the star clusters are accreted onto a pre-existing NCD. The structural parameters of the NSD were obtained by applying the same photometric decomposition adopted for real galaxies based on the analysis of isophotal shapes. The photometric and kinematic properties of the NSD in the simulated galaxy are remarkably similar to those of NSDs observed in the nuclei of real galaxies. In particular, the scalelength (38.8 pc) and face-on central surface brightness (20.24 V-mag arcsec^{-2}) fit on the $\mu^0_{0,V} - h$ relation for galaxy discs. The total luminosity (5.3×10^6 $L_\odot$) is consistent with that predicted by extrapolating the I-band Tully-Fisher relation to discs of similar rotational width (~ 40 km s^{-1}) and it is consistent with lower and upper limits we found assuming reasonable $M_\odot/L_\odot$ ratios. The mass of the NSD ($\sim 1 \times 10^7$ $M_\odot$) is close to that of the few NSDs for which it has been measured.

- The same mechanism can form an NSD in a pre-existing spheroidal structure only if the accreted star clusters are able to flat their distribution of

at least 30%. Otherwise the merger remnant never develops photometric nor kinematic properties similar to those observed for NSDs.

- The independent analysis performed on model A2 by fitting an exponential disc to the surface-brightness distribution after excluding the light from the bulge finds best-fitting disc parameters in agreement with those derived with the Scorza-Bender method, showing that the latter is robust. The elongated structures found in the unsharp images are not sufficient proof of the presence of an NSD: the same feature can also be caused by isophotes of increasing inwards ellipticity at small radii. Therefore, to unveil an NSD, performing a detailed measurement of the surface-brightness distribution in the nuclear regions is necessary and the Scorza-Bender decomposition method is a robust way of doing this.

- The $\mu^0_{0,V} - h$ relation for galaxy discs shows a continuity between the properties of NSDs and NCDs, as done for the galaxy NGC 4244. Considering the Tully-Fisher relation, the NCD of NGC 4244 is located close to the position of NSDs, sharing similar rotational width and total luminosity. The link between such nuclear discs of different scales is a very interesting and still open topic, which deserves further investigation.

- The purely stellar dynamical merger of star clusters onto the centre of a galaxy is a viable mechanism for growing an NSD. This shows that most of its mass (up to $70-90$ per cent) can be assembled from already formed stars through the migration and accretion of star clusters onto the galactic centre.

Chapter 3

The young nuclear stellar disc in the SB0 galaxy NGC 1023

Abstract

Small kinematically-decoupled stellar discs with scalelengths of a few tens of parsec are known to reside in the centre of galaxies. Different mechanisms have been proposed to explain how they form including gas dissipation and merging of globular clusters. Using archival *Hubble Space Telescope* imaging and ground-based integral-field spectroscopy, we investigated the structure and stellar populations of the nuclear stellar disc hosted in the interacting SB0 galaxy NGC 1023. The stars of the nuclear disc are remarkably younger and more metal-rich with respect to the host bulge. These findings support a scenario in which the nuclear disc is the end result of star formation in gas piled up in the galaxy centre. The gas can be of either internal or external origin, i.e. from either the main disc of NGC 1023 or the nearby interacting satellite NGC 1023A. The dissipationless formation from already formed stars through the migration and accretion of star clusters into the galactic centre is rejected.

3.1 Introduction

Small discs of stars with scalelengths of a few tens of parcsecs and luminosities up to 10^7 $L_\odot$ in the I band are known to reside in the nuclei of galaxies (Pizzella et al. 2002; Ledo et al. 2010).

Different mechanisms have been proposed to explain how NSDs assembled. Most of them are believed to be formed from gas funnelled into the nucleus, as a consequence of either the secular infall driven by a bar (Sil'chenko 1997; Scorza & van den Bosch 1998; Krajnović & Jaffe 2004) or an external accretion (Pizzella et al. 2002; Morelli et al. 2004; Corsini et al. 2012). In both scenarios, the gas is efficiently directed toward the galaxy centre, where first it settles as it dissipates and then turns into stars as density rises. Ionised gas and dust are actually observed in a few nuclear discs (Kormendy et al. 1994, 2005). In this picture, the age of NSDs may constitute a useful proxy to trace the epoch since it occurred the last major merging of the host galaxy. NSDs are indeed fragile structures that should not survive such an event (Ledo et al. 2010). This would make NSDs a powerful tool to constrain the assembling history of galaxies. This picture has been recently challenged by the results of Portaluri et al. (2013). They found that although some gas dissipation is needed in the early stages of the formation of a NSD, most of its mass can be assembled from already formed stars through the migration and accretion of star clusters into the galactic centre. If this is the case the stars of a nuclear disc could be formed earlier than the disc itself.

A crucial piece of information to help us to understand the processes of formation of NSDs is imprinted in their stellar populations. To date only a number of galaxies hosting a NSD have been studied in some detail. The age, metallicity, and abundance ratio of the stars in the circumnuclear regions were derived via stellar population models using colour-colour diagrams (van den Bosch et al. 1998), line-strength indices (Sil'chenko 1999; Morelli et al. 2004; Krajnović & Jaffe 2004), and population synthesis (Sarzi et al. 2005). But all these results refer to the integrated stellar population without properly separating the contribution of the NSD from that of the host galaxy. Therefore, it is necessary to perform a detailed measurement of the surface-brightness distribution of NSDs since they never dominate the light distribution of the galactic nuclei, and locally contribute at most half the galaxy surface brightness (Pizzella et al. 2002; Morelli et al. 2004, 2010; Corsini et al. 2012).

We decided to revisit the case of NGC 1023 since such a galaxy represents an excellent test case to derive the actual properties of the stellar population of its NSD. NGC 1023 is a highly-inclined disc galaxy classified as $SB0_1(5)$ by Sandage & Tammann (1981) and $SB0^-$(rs) by de Vaucouleurs et al. (1991, hereafter RC3). Its total B-band magnitude is $B_T = 10.35$ (RC3), which, after correcting for inclination and extinction, corresponds to $M^0_{B_T} = -20.11$ for an adopted distance of 10.9 Mpc (Faber et al. 1997, $H_0 = 75$ km s Mpc^{-1}). NGC 1023 is the brightest member of the LGG 70 group (Garcia 1993). Its

closest companion, NGC 1023A, is a Magellanic irregular dwarf galaxy of low surface brightness (Sandage & Bedke 1994) which is located near the eastern end of NGC 1023. The two galaxies are separated by an angular distance of 2.7 arcmin (RC3), corresponding to a projected linear distance of about 8 kpc. They are connected by a bridge of neutral hydrogen which suggests an ongoing interaction (Sancisi et al. 1984). The broad-band images of the centre of NGC 1023 obtained by *Hubble Space Telescope (HST)* show a NSD seen close to edge on (Faber et al. 1997; Sil'chenko 1999; Sarzi et al. 2006; Ledo et al. 2010). The stellar dynamics confirms the presence of a nuclear flattened component, as it results from the tangentially anisotropic distribution of the innermost stellar orbits (Bower et al. 2001). Finally, the stellar population of the nucleus has significantly different chemical properties with respect to the rest of the galaxy. Indeed, the nucleus is younger, more metal-rich and has an higher magnesium overabundance than the surrounding bulge (Sil'chenko 1999; McDermid et al. 2006).

In this work, we improve the previous results by quantitatively constraining the stellar age and metallicity of the NSD of NGC 1023. The photometric decomposition of archival multiband optical images of the galaxy nucleus obtained with *HST* allows us to get the basic structural parameters of the NSD (central surface brightness, I_0, scalelength radius, h, inclination, i, and major-axis position angle, PA) in Section 3.2. Previous studies limited to detect the NSD from the inspection of structure maps built by unsharp-masking the galaxy images, from the residual maps obtained by subtracting a purely elliptical surface-brightness distribution, or from the analysis of the shape of galaxy isophotes. The relative contribution of the NSD to the total surface-brightness distribution is adopted in Section 3.3 to derive at last the actual properties of its stellar population from the line-strength indices measured in the galaxy nucleus using stellar population models. Our findings about the formation process of the NSD are discussed in Section 3.4.

3.2 Structural properties of the nuclear stellar disc

3.2.1 Broad-band imaging

We retrieved from the *HST* Science Data Archive the images of NGC 1023 obtained with the *Advanced Camera for Survey* (*ACS*) and filter F475W (Prop. Id. 12202, PI: G. Sivakoff) and with the *Wide Field Planetary Camera 2* (*WFPC2*) and filters F555W and F814W (Prop. Id. 6099, PI: S. M. Faber). These three datasets were selected as a compromise to analyse the deepest and unsatu-

rated broad-band images of the galaxy nucleus obtained at the highest spatial resolution.

The *ACS* images were taken with the *Wide Field Channel* (*WFC*), which consists of two SITe CCDs with 2048 × 4096 pixels each of size 15 × 15 μm^2. The image scale is 0.049 arcsec pixel^{-1} and the field of view of the combined detectors covers an approximately square area of about 202 × 202 arcsec^2. The gain and readout noise of the four WFC amplifiers are about 2.0 e^- count^{-1} and 4.2 e^- (rms), respectively. All the *WFPC2* exposures were taken by centring the galaxy nucleus on the *Planetary Camera* (*PC*). The *PC* detector is Loral CCD with 800 × 800 pixels and a pixel size of 15 × 15 μm^2. The image scale of 0.046 arcsec pixel^{-1} yields a field of view of about 36 × 36 arcsec^2. The gain and readout noise are 14.0 e^- count^{-1} and 7.0 e^- (rms), respectively. To help in identifying and correcting cosmic ray events, different exposures were taken with each filter. The total exposure times was 1552 s for the F4755W filter, 1620 s for the F555W filter, and 1880 s for the F814W filter. For both *ACS* and *WFPC2* images the telescope was always guided in fine lock, giving a typical rms tracking error per exposure of 0.005 arcsec.

The *ACS* images were calibrated using the CALACS reduction pipeline in IRAF[1]. Reduction steps include bias subtraction, dark current subtraction, flat-fielding correction, and correction for geometric distortion with IRAF task MULTIDRIZZLE (Fruchter et al. 2009) as described in detail in *ACS* instrument and data handbooks (Pavlovsky et al. 2004, 2006). The images obtained in the same filter were aligned by comparing the centroids of stars in the field of view and then combined, rejecting cosmic rays in the process. Residual cosmic ray events and hot pixels were removed using the LACOS_IMA procedure (van Dokkum 2001). The sky level was determined from regions free of sources at the edge of the field of view and then subtracted. The *WFPC2* images were reduced using the CALWFPC reduction pipeline in IRAF. Reduction steps include bias subtraction, dark current subtraction, and flat-fielding, as described in detail in the *WFPC2* instrument and data handbooks (Baggett et al. 2002; Mc Master & Biretta 2008). Subsequent analysis including alignment and combination of images and rejection of cosmic rays was performed using MULTIDRIZZLE and LACOS_IMA. The sky level was determined from regions free of sources in the Wide Field (WF) chips and subtracted from the combined PC frames after appropriate scaling.

The ACS/F475W, *WFPC2*/F555W, and *WFPC2*/F814W passbands are

[1]The Imaging Reduction and Analysis Facility (IRAF) is distributed by the National Optical Astronomy Observatory, which is operated by the Association of Universities for Research in Astronomy (AURA), Inc., under cooperative agreement with the National Science Foundation.

similar to Johnson-Cousins B, V, and I bands, respectively. The flux calibration to the Vega magnitude system in the three observed *HST* passbands was performed following Holtzman et al. (1995).

3.2.2 Photometric model

The surface-brightness distribution of the NSD was derived in the different passbands using the method of Scorza & Bender (1995) as implemented by Morelli et al. (2004). But, we adopted a different best-fitting algorithm to perform the photometric decomposition and followed the prescriptions of Morelli et al. (2010) and Corsini et al. (2012) for the treatment of the isophotal shape of the spheroidal component and to account for the point-spread function (PSF), respectively. The photometric decomposition was performed independently for each bandpass. It is based on the assumption that the isophotal disciness, which is quantified by the positive value of the fourth cosine Fourier coefficient A_4 (Jedrzejewski 1987; Bender et al. 1988), is the result of the superimposition of the light contribution of a rounder host spheroid and a more elongated nuclear disc. We assumed that the nuclear disc has perfectly elliptical isophotes ($A_{4,\mathrm{disc}} = 0$) with constant ellipticity ϵ_{disc} whereas the spheroidal component has elliptical isophotes with constant $A_{4,\mathrm{spheroid}}$ and constant ellipticity $\epsilon_{\mathrm{spheroid}}$. The isophotes of the spheroid can be either perfectly elliptical ($A_{4,\mathrm{spheroid}} = 0$) or be characterised by a constant discy ($A_{4,\mathrm{spheroid}} > 0$) or a constant boxy shape ($A_{4,\mathrm{spheroid}} < 0$). The original Scorza & Bender (1995) method adopted perfectly elliptical isophotes for the spheroidal component (see also Pizzella et al. 2002; Ledo et al. 2010; Corsini et al. 2012).

Let (x, y) be the Cartesian coordinates in sky plane with the origin in the galaxy centre, the $x-$axis parallel to the direction of right ascension and pointing westward, the $y-$axis parallel to the direction of declination and pointing northward. We assumed the surface brightness of the nuclear disc to follow the exponential law (Freeman 1970) and have elliptical isophotes centred on $(x_0,\, y_0)$ with constant position angle PA and constant ellipticity $\epsilon = 1 - q$ where q is the minor-to-major axis ratio. The disc surface-brightness distribution is given by:

$$I(x, y) = I_0 \, \exp\left[-\frac{r(x, y)}{h}\right], \tag{3.1}$$

where I_0 and h are the central surface brightness and scalelength of the disc, respectively, and r is:

$$r(x,y) = \left[(-(x-x_0)\sin\mathrm{PA} + (y-y_0)\cos\mathrm{PA})^2 - ((x-x_0)\cos\mathrm{PA} - (y-y_0)\sin\mathrm{PA})^2/q^2\right]^{1/2}. \quad (3.2)$$

The isophote fitting with ellipses was carried out on the galaxy image using the IRAF task ELLIPSE (Jedrzejewski 1987). First isophotes were fitted by ellipses allowing their centres to vary. Within the errors, no variation in the ellipse centres was found. Therefore, we assumed the disc centre to be coincident with the galaxy centre. The final ellipse fits were done at fixed ellipse centres out to a distance of 3.6 arcsec. The ellipse-averaged profiles of the surface brightness, position angle, ellipticity, and fourth cosine Fourier coefficient are plotted in Figure 3.1.

We derived the photometric parameters of the nuclear disc (I_0, h, q, and PA) by iterative subtraction of the model surface brightness given by Eq. 3.1 from the observed surface-brightness distribution of the galaxy. The nuclear disc parameters were adjusted until the isophotes in the disc-free image have the same shape of the isophotes of the host spheroid, which we measured in the galaxy image outside the region where the inner peak of A_4 is observed. Indeed we expect to measure $A_{4,\mathrm{disc-free}} = A_{4,\mathrm{spheroid}}$ out to the very centre after subtracting the best-fitting model of the nuclear disc.

For each nuclear disc model, the disc-free image of the galaxy was obtained from the galaxy image by subtracting the nuclear disc model after convolving with the *HST* PSF. The adopted PSF model was calculated with the TINYTIM package (Krist & Hook 1999) taking into account the instrumental set-up and position of the NSD on the given image. Then, we performed an isophotal analysis of the disc-free image using ELLIPSE. We calculated:

$$\chi^2 = \sum_{i=1}^{N} \left(\frac{A_{4,\mathrm{disc-free}}(i) - A_{4,\mathrm{spheroid}}}{\sigma(i)} \right)^2 \quad (3.3)$$

where $A_{4,\mathrm{disc-free}}(i)$ is the value of the A_4 Fourier coefficient measured for the i-th isophote in the disc-free image and N is the total number of fitted isophotes. We assumed $\sigma(i) = 0.01$ as a typical error on $A_{4,\mathrm{disc-free}}$ for all the isophotes in the region of the NSD. The χ^2 was computed in the radial range between 0.3 and 2.3 arcsec. For the spheroidal component of NGC 1023, we adopted $A_{4,\mathrm{spheroid}} = -0.013$, which we measured in the galaxy images as the average value of A_4 at radii between 2 and 3 arcsec. The disc models resulting in $|\langle A_{4,\mathrm{disc-free}}\rangle - A_{4,\mathrm{spheroid}}| > 0.002$ were rejected to avoid not realistic solutions.

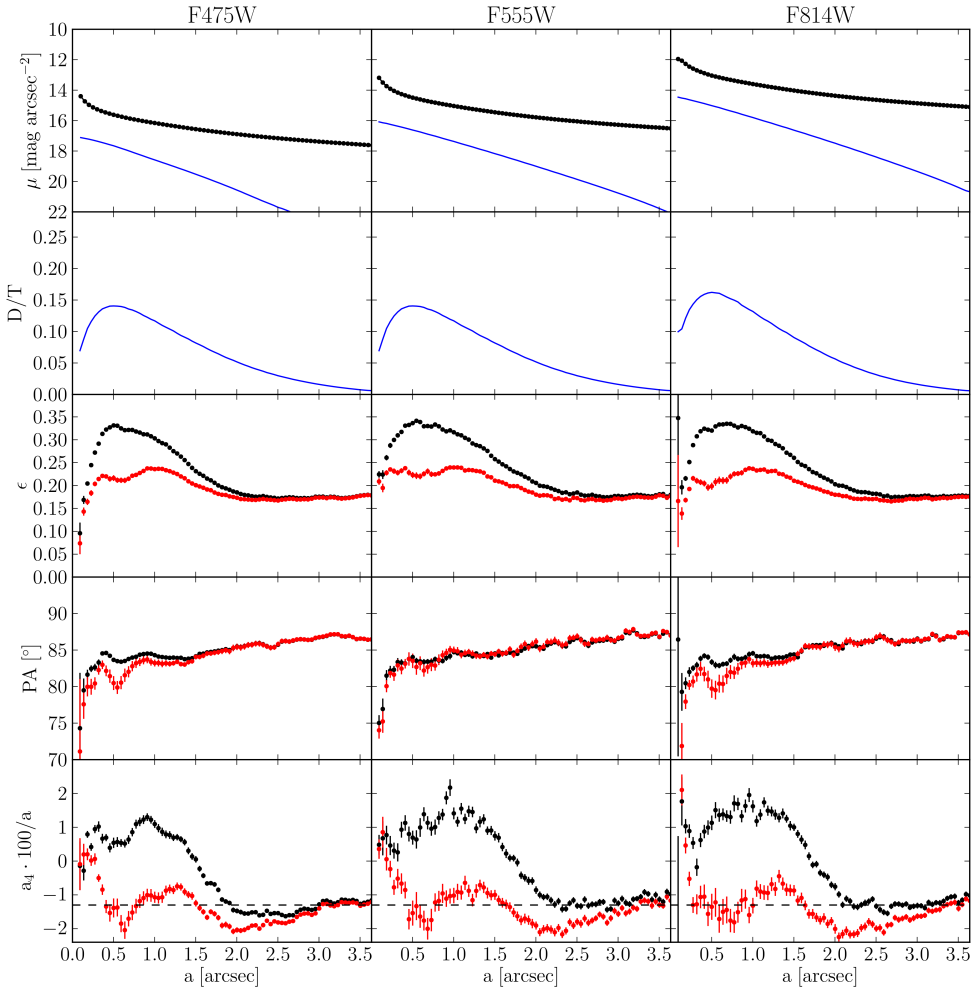

Figure 3.1: Isophotal parameters of the nuclear region of NGC 1023 as a function of the isophotal semi-major axis based on the analysis of the surface-brightness distribution measured in the *ACS*/F475W (left-hand panels), *WFPC2*/F555W (central panels), and *WFPC2*/F814W (right-hand panels) images, respectively. From top to bottom: surface-brightness radial profiles of the galaxy (open black squares) and NSD (after convolution with the *HST* PSF, solid blue line); radial profile of the NSD-to-total luminosity ratio; radial profiles of the galaxy ellipticity, position angle, and fourth cosine Fourier coefficient before (filled black circles) and after (filled red circles) the subtraction of the best-fitting model for the NSD.

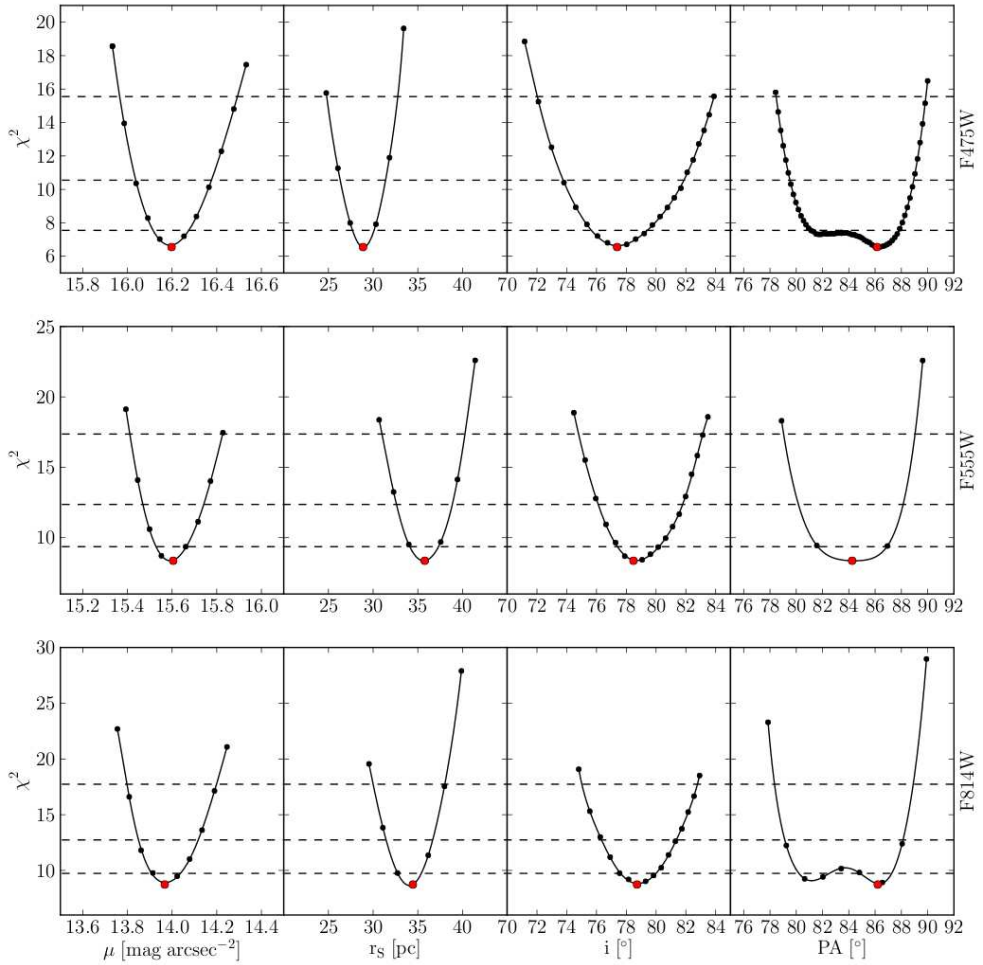

Figure 3.2: χ^2 distribution for the photometric decomposition of the ACS/F475W (top panels), *WFPC2*/F555W (middle panels), and *WFPC2*/F814W (bottom panels) images of NGC 1023 as a function of I_0, h, i, and PA (from left to right), respectively. The dotted horizontal lines indicate the confidence levels of 1 σ, 2 σ, and 3 σ on the best-fitting values, marginalising over all other parameters.

Table 3.1: Photometric parameters of the nuclear stellar disc.

Filter	μ_0	h	i	PA	$L_{\mathrm{T,NSD}}$	
	[mag arcsec^{-2}]	[pc]	[°]	[°]	[10^6 L$_\odot$]	
(1)	(2)	(3)	(4)	(5)	(6)	(7)
F475W	$16.20^{+0.29}_{-0.23}$	$28.9^{+3.8}_{-4.1}$	$77.4^{+5.4}_{-6.7}$	$86.1^{+3.8}_{-7.7}$	$7.4^{+1.8}_{-1.7}$	
F555W	$15.61^{+0.22}_{-0.19}$	$35.8^{+4.6}_{-4.8}$	$78.5^{+3.7}_{-4.8}$	$84.3^{+4.8}_{-5.2}$	$16.0^{+3.1}_{-2.9}$	
F814W	$13.97^{+0.23}_{-0.17}$	$34.5^{+3.6}_{-4.4}$	$78.7^{+3.7}_{-4.1}$	$86.2^{+3.3}_{-7.7}$	$22.3^{+3.8}_{-4.3}$	

Note. Col. (1): Passband. Col. (2): Observed central surface brightness. Col. (3): Scalelength. Col. (4): Inclination derived as $i = \arccos(q)$. Col. (5): Major-axis position angle. Col. (6): Total luminosity derived as $L_{\mathrm{T,NSD}} = 2\pi I_0 h^2 q$.

We explored the parameter space in a twofold process by running a PyRAF[2] code. First, we built a set of NSD models covering the central surface brightnesses $15.7 \leq \mu_{0,\mathrm{F475W}} \leq 17.8$ mag arcsec^{-2}, $14.1 \leq \mu_{0,\mathrm{F555W}} \leq 16.2$ mag arcsec^{-2}, $13.0 \leq \mu_{0,\mathrm{F814W}} \leq 15.1$ mag arcsec^{-2}, scalelengths $8 \leq h \leq 65$ pc, axial ratios $0.04 \leq q \leq 0.35$, and position angles $80° \leq \mathrm{PA} \leq 88°$. The model corresponding to the minimum value of χ^2 was adopted as the starting guess for a further χ^2 minimisation based on the downhill simplex method (Nelder & Mead 1965). The resulting χ^2 minimum χ^2_{min} corresponds to the best-fitting model of the nuclear disc. We determined $\Delta\chi^2 = \chi^2 - \chi^2_{\mathrm{min}}$ and derived its confidence levels under the assumption that the errors are normally distributed. The best-fitting values and confidence levels of I_0, h, q, and PA alone, marginalising over all other parameters are shown in Figure 3.2. The photometric parameters of the NSD and their 3σ errors are listed in Table 3.1. We considered the disc to be infinitesimally thin and derived its inclination as $i = \arccos(q)$. The comparison between the isophotal parameters of NGC 1023 measured before and after the subtraction of the best-fitting model of the NSD is shown in Figure 3.1.

The structural parameters of the NSD (i.e., scalelength, inclination, and position angle) are constant within the errors in all the available images. Therefore, the location, orientation, and size of the NSD do not depend on the observed passband. This also implies the absence of colour gradients in the NSD, an important constraint on the star formation process. The mean values of the

[2]PyRAF is a product of the Science Software Branch at the Space Telescope Science Institute.

NSD parameters are $\langle h \rangle = 33.1$ pc, $\langle i \rangle = 78\overset{\circ}{.}2$, and $\langle \mathrm{PA} \rangle = 85\overset{\circ}{.}5$. The size and luminosity of the NSD of NGC 1023 are consistent with those of the other NSDs detected so far (see Ledo et al. 2010, for a census).

3.3 Properties of the stellar populations of the NSD

3.3.1 Integral-field spectroscopy

The integral-field spectroscopic observations of the nucleus of NGC 1023 were carried out with the 6-m telescope of the Special Astrophysical Observatory by Sil'chenko (1999). The Multi-Pupil Field Spectrograph (MPFS) mapped a field of view of 11×21 arcsec^2 at PA $= 122^\circ$ with 8×16 spectra. The spectral range between 4600 and 5450 Å was covered with an instrumental resolution of 5 Å (FWHM) corresponding to $\sigma_{\mathrm{inst}} = 131$ km s^{-1} at Hβ. The exposure time on the galaxy was 60 min with an average seeing FWHM = 1.6 arcsec. Further details about the observations and data reduction are given in Sil'chenko (1999).

The resulting spectra were summed to obtain azimuthally-averaged spectra within concentric circular rings centred onto the galaxy nucleus. This allowed to increase the signal-to-noise ratio and derive more precisely the values of the Mgb, Fe5270, Fe5335, and Hβ line-strength indices as defined by Worthey (1994). The mean accuracy of the line-strength indices measured in the azimuthally-averaged spectra is 0.10 Å (Sil'chenko 1999).

We extracted the values of the Mgb, Fe5270, $\langle$Fe$\rangle$, and Hβ indices from Figures 4a and 5a by Sil'chenko (1999). Then, we calculated the values of the Fe5335 index and derived the magnesium-iron index

$$[\mathrm{MgFe}]' = \sqrt{\mathrm{Mg}b(0.72 \times \mathrm{Fe5270} + 0.28 \times \mathrm{Fe5335})}$$

as defined by Thomas et al. (2003). The equivalent widths of the line-strength indices measured in the azimuthally-averaged spectra and their 1σ errors are listed in Table 3.2.

Table 3.2: Line-strength indices and stellar population properties in the concentric circular rings centred on the galaxy nucleus.

Radius	Mgb	Hβ	$\langle$Fe$\rangle$	[MgFe]$'$	t	[Z/H]	[α/Fe]	$\frac{L_{\rm NSD}}{L_{\rm T}}$
[arcsec]	[Å]	[Å]	[Å]	[Å]	[Gyr]	[dex]	[dex]	
(1)	(2)	(3)	(4)	(5)	(6)	(7)	(8)	(9)
0.00-0.65	5.04 ± 0.10	1.57 ± 0.10	3.00 ± 0.07	3.99 ± 0.23	7.9 ± 3.1	0.46 ± 0.16	0.27 ± 0.03	0.06
0.65-1.95	4.53 ± 0.10	1.80 ± 0.10	3.17 ± 0.07	3.85 ± 0.21	3.7 ± 2.1	0.54 ± 0.23	0.17 ± 0.04	0.03
1.95-3.25	4.18 ± 0.10	1.46 ± 0.10	2.94 ± 0.07	3.57 ± 0.20	14.0 ± 3.5	0.09 ± 0.12	0.09 ± 0.04	0.00
3.25-4.55	4.03 ± 0.10	1.45 ± 0.10	2.83 ± 0.07	3.42 ± 0.19	15.3 ± 3.9	-0.01 ± 0.11	0.09 ± 0.04	0.00
4.55-5.85	3.95 ± 0.10	1.43 ± 0.10	2.74 ± 0.07	3.33 ± 0.18	16.5 ± 3.7	-0.06 ± 0.10	0.11 ± 0.03	0.00
5.85-7.15	3.89 ± 0.10	1.23 ± 0.10	2.51 ± 0.07	3.22 ± 0.18	...	...	...	0.00
7.15-8.45	3.50 ± 0.10	1.59 ± 0.10	2.52 ± 0.07	3.03 ± 0.17	13.5 ± 3.0	-0.14 ± 0.10	0.10 ± 0.03	0.00

Note. Col.(1): Minimum and maximum radii of the concentric circular ring. Columns (2)-(5): Equivalent widths of the line-strength indices measured in the concentric ring. Col. (6)-(8): Mean age, total metallicity, and total [α/Fe] enhancement of the stellar population. Col. (9): NSD-to-total luminosity ratio within the ring.

3.3.2 Stellar population model

From the equivalent widths of the line-strength indices measured in the azimuthally -averaged spectra, we derived the radial trend of the properties of the stellar populations using the stellar population models by Thomas et al. (2003). We considered Hβ, Mgb, $\langle$Fe$\rangle$, and [MgFe]$'$ among the measured line-strength indices because Hβ is sensitive to warm turn-off stars and thus useful as an age indicator, Mgb covers the α-element abundance, $\langle$Fe$\rangle$ gives the metal abundance as well as [MgFe]$'$ which is almost independent of the ratio [α/Fe] between the α and iron-peak elements. Because of the inclusion of element ratio effects, the models of Thomas et al. (2003) predict the values of the selected line-strength indices as function of the mean age t, total metallicity [Z/H], and total [α/Fe] enhancement of a single stellar population (SSP). The models cover the ages $1 \leq t \leq 15$ Gyr, metallicities $-2.25 \leq [Z/\mathrm{H}] \leq 0.67$ dex, and abundance ratios $-0.3 \leq [\alpha/\mathrm{Fe}] \leq 0.5$ dex.

In the left panel of Figure 3.3 the equivalent widths of Hβ and [MgFe]$'$ are compared with the model predictions for two stellar populations with solar ([α/Fe]$=$ 0.0 dex) and super-solar [α/Fe] enhancement ([α/Fe]$=$ 0.5 dex), respectively. In this parameter space, the mean age and total metallicity appear to be almost insensitive to the variations of the [α/Fe] enhancement. In the right panel of Figure 3.3, the values of Mgb and $\langle$Fe$\rangle$ are compared with the model predictions for two stellar populations with intermediate (3 Gyr) and old age (12 Gyr), respectively. In this parameter space, the total metallicity and total [α/Fe] enhancement appear to be almost insensitive to the variations of the age.

We derived the parameters of the stellar population from the line-strength indices in a iterative procedure. First, we assumed the [α/Fe] ratio and determined the age and metallicity for the index pair ([MgFe]$'$, Hβ) from the model grids shown in the left panel of Figure 3.3. Then, the age was used to derive the metallicity and [α/Fe] ratio for the index pair (Mgb, $\langle$Fe$\rangle$) from the model grids shown in the right panel of Figure 3.3. The resulting [α/Fe] ratio is used to start a new iteration. These two steps were repeated until the guess and resulting values of the [α/Fe] ratio are consistent within 1 per cent accuracy. We interpolated linearly between the points of the model grids to derive the parameter pair (t, [Z/H]) from ([MgFe]$'$, Hβ) and ([Z/H], [α/Fe]) from (Mgb, $\langle$Fe$\rangle$). We excluded the ring $5.85 < R < 7.15$ arcsec from the analysis because its values of [MgFe]$'$ and Hβ are not consistent with the model predictions of age and metallicity. The derived values of stellar-population age, metallicities, and overabundances in the remaining concentric rings centred on the nucleus of NGC 1023 are given in Table 3.2. They are consistent with

the results by McDermid et al. (2006) and Kuntschner et al. (2010) which are based on integral-field spectroscopic data obtained with OASIS and SAURON, respectively.

Figure 3.4 translates the trends observed in Figure 3.3 as follows. The central regions of NGC 1023 ($R < 1.95$ arcsec) are younger ($t \approx 5$ Gyr), more over-abundant ($[\alpha/\mathrm{Fe}] \approx 0.2$ dex), and more metal rich ($[Z/\mathrm{H}] \approx 0.5$ dex) than the outer regions. For $R > 1.95$ arcsec we measured old ages ($t \approx 15$ Gyr), low over-abundance ($[\alpha/\mathrm{Fe}] \approx 0.1$ dex) and a metallicity gradient ranging from $[Z/\mathrm{H}] \approx 0.15$ dex to -0.15 dex with increasing radius. In the following we will interpret the radial variations described above as the result of the superposition of the NSD detected photometrically in Section 3.2 and the main body of the galaxy.

We derived the light contribution of the NSD to the total luminosity of the galaxy in the concentric circular rings listed in Table 3.2. We analysed the *HST* and disc model images in the different passbands after convolving with the PSF of the spectroscopic observations. We adopted a Gaussian PSF with FWHM = 1.6 arcsec. The nuclear disc-to-total luminosity ratio $L_{\mathrm{NSD}}/L_{\mathrm{T}}$ does not depend on the observed passband. The NSD contributes a maximum of 6 per cent of the total luminosity in the innermost ring and it is negligible at radii larger than 1.95 arcsec (Table 3.2). The surface-brightness distribution is dominated by the light contribution of the bulge in this radial range, whereas the main stellar disc become more relevant at much more larger radii ($R > 70$ arcsec; Debattista et al. 2002; Noordermeer et al. 2008).

To constrain the stellar population of the NSD, we used a linear combination of two SSP synthesis templates from the spectral library of Vazdekis et al. (2010) covering the full optical spectral range at moderately high resolution (FWHM = 2.51 Å). In our analysis we adopted a Salpeter (1955) initial mass function and weighted the template spectra of the NSD and galaxy main body according to their light contribution to the total luminosity. For the galaxy we assumed a stellar population with an age $t = 14.1$ Gyr and a metallicity $[Z/\mathrm{H}] = 0.2$ dex, which are consistent with the values obtained in the two innermost rings by linearly interpolating the ages and metallicities measured in the outer rings. For the stellar population of the NSD we considered 7 different ages spanning the range between 0.1 and 5 Gyr and 4 different metallicities from -0.68 to 0.2 dex. The specific ages and metallicities employed are $t = 0.1$, 0.5, 1.0, 2.0, 3.2, 4.0, and 5.0 Gyr and $[Z/\mathrm{H}] = -0.68$, -0.38, 0.0, and 0.2 dex, respectively. We looked for the optimal combination of the template spectra of the galaxy and nuclear disc matching the line-strength indices measured in the two innermost concentric rings. The best-fitting stellar population of the NSD was chosen to have the same age and metallicity in both rings. The nuclear

disc of NGC 1023 is younger ($t = 2$ Gyr) than the main body of the galaxy and has solar metallicity ($[Z/\mathrm{H}] = 0.0$ dex).

3.4 Discussion and conclusions

The structure and properties of the stellar population of the nuclear regions of the interacting SB0 galaxy NGC 1023 were investigated through a detailed analysis of archival *HST* imaging and ground-based integral-field spectroscopy. The galaxy is known to host a highly-inclined NSD (Faber et al. 1997; Sil'chenko 1999; Sarzi et al. 2006; Ledo et al. 2010). Moreover, the stars of the galaxy nucleus have significantly different chemical properties with respect to the surrounding bulge. They are younger, more metal-rich and have an higher magnesium overabundance (Sil'chenko 1999; McDermid et al. 2006).

In this work, we derived the central surface brightness, scalelength, inclination, and position angle of the NSD of NGC 1023 in all the available *HST* images by assuming that it is an infinitesimally thin exponential disc. We applied the photometric decomposition method of Scorza & Bender (1995) and adopted the algorithm by Morelli et al. (2004, 2010), which we implemented for a better determination of the best-fitting parameters. The size, orientation, and location of the NSD do not depend on the observed passband, as already observed for the few other NSDs for which a detailed multiband photometric analysis was performed (Krajnović & Jaffe 2004; Morelli et al. 2010; Corsini et al. 2012). We measured the light contribution of the NSD to the total luminosity of the galaxy $L_{\mathrm{NSD}}/L_{\mathrm{T}}$ in the same concentric circular rings centred on the galaxy nucleus where the equivalent widths of the line-strength indices were obtained from ground-based integral-field spectroscopy by (Sil'chenko 1999). *HST* images were smeared to the resolution of the spectroscopic observations. The NSD contributes a few per cent of the galaxy light in the innermost two rings ($R < 1.95$ arcsec), whereas the luminosity of the NSD is negligible in the outer rings ($R > 1.95$ arcsec) in all the passbands.

The ratio $L_{\mathrm{NSD}}/L_{\mathrm{T}}$ was used in combination with the SSP synthesis template spectra from the spectral library of Vazdekis et al. (2010) to derive the properties of the stellar population of the NSD by matching the measured line-strength indices. For the host galaxy we assumed an old stellar population ($t = 14.1$ Gyr) with super-solar metallicity ($[Z/\mathrm{H}] = 0.2$ dex) to be consistent with the constant age and metallicity gradient which we measured in the outer rings. We found that the stellar population of the nuclear disc of NGC 1023 is younger ($t = 2$ Gyr) than the host bulge and has solar metallicity ($[Z/\mathrm{H}] = 0.0$ dex).

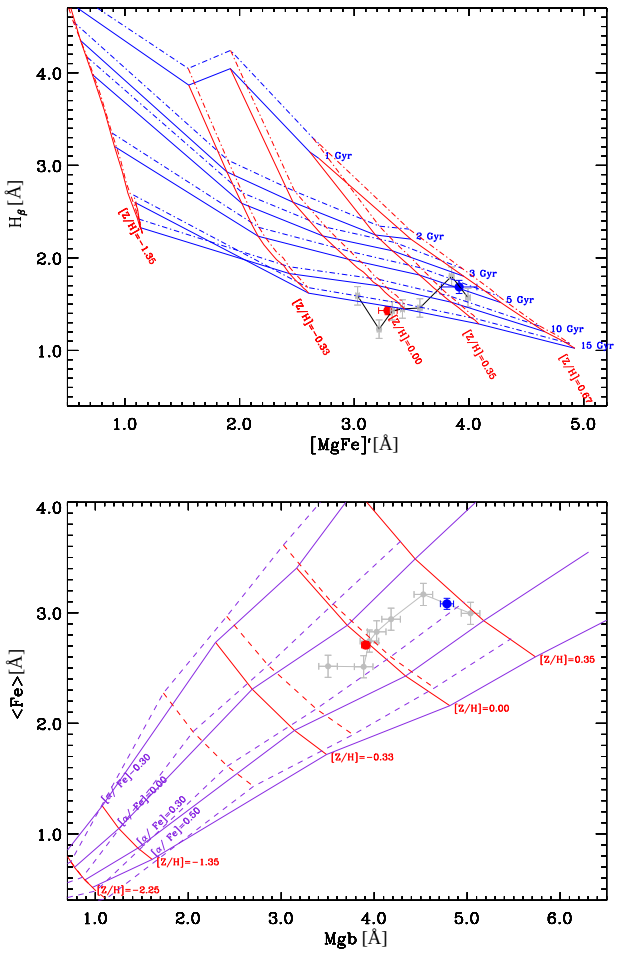

Figure 3.3: Equivalent width of the Hβ and [MgFe]$'$ (top panel) and $\langle$Fe$\rangle$ and Mgb line-strength indices (bottom panel) measured in the azimuthally-averaged spectra of NGC 1023 (grey circles) and predictions from single stellar population models by Thomas et al. (2003). The blue and red circles correspond to the weighted means of the line-strength indices in the regions where the NSD does ($0 \leq R \leq 1.95$ arcsec) and does not ($1.95 < R \leq 8.45$ arcsec) contribute to the galaxy luminosity, respectively. In the left-hand panel the age-metallicity grids are plotted with two different [α/Fe] enhancements: [α/Fe] = 0.0 dex (continuous lines) and [α/Fe] = 0.5 dex (dashed lines). In the right-hand panel the [α/Fe]-metallicity grids are plotted with two different ages: 3 Gyr (continuous lines) and 12 Gyr (dashed lines).

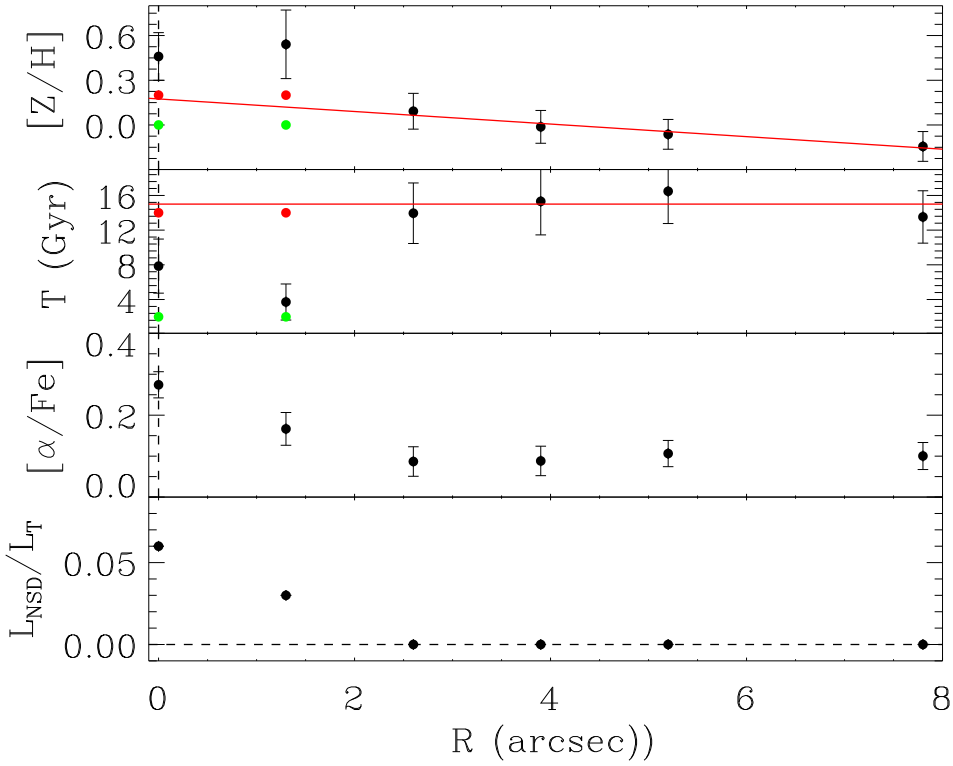

Figure 3.4: From top to bottom: the radial profiles of metallicity, age, magnesium overabundance, and nuclear disc-to-total luminosity ratio measured in the concentric circular rings centred on the galaxy nucleus (black circles). The red solid lines fit the metallicity and age in the outer rings ($R > 1.95$ arcsec). The red and green circles correspond to the values which were assumed for the spheroidal component and derived for the NSD in the two innermost rings ($R < 1.95$ arcsec), respectively.

These new results about NGC 1023 give us the opportunity to gain further insight on the formation of NSDs, because for the first time we were able to disentangle the stellar population of a NSD from that of its host galaxy. This is not the case of all the NSDs studied so far. The properties of their stellar populations were derived by assuming a negligible contamination of the host galaxy to the colours and line-strength indices measured in the nucleus. According to this assumption, some NSDs are found to be as old as the host galaxy (NGC 4128, Krajnović & Jaffe 2004; NGC 4342, van den Bosch et al. 1998; NGC 4458, Morelli et al. 2004; NGC 4621, Krajnović & Jaffe 2004; NGC 4698, Corsini et al. 2012). The NSD of NGC 4570 shows the same intermediate age but it is more metal rich than the galaxy bulge (Krajnović & Jaffe 2004). In NGC 4478 the NSD is younger, more metal-rich and less over-abundant than the main body of the galaxy (Morelli et al. 2004). In contrast, the NSD of NGC 5308 is made of a younger and more metal-poor stellar population than the host galaxy (Krajnović & Jaffe 2004). Finally, a few cases are characterised by on-going star formation (NGC 5845, Kormendy et al. 1994; NGC 4486A, Kormendy et al. 2005).

The younger age of the NSD excludes it assembled from already formed stars through the accretion of star clusters migrating from the much older bulge of NGC 1023 into its centre. This points toward a dissipational process of star formation in gas funnelled into the galaxy centre. The stars of the NSD have solar metallicity and therefore formed from processed gas which can be of either internal or external origin. Indeed, the main disc of NGC 1023 and the interacting satellite NGC 1023A are both a possible reservoir for the gas building the NSD of NGC 1023. Assessing the properties of the stellar populations of the main disc of NGC 1023 and measuring the metallicity of the gas in the stream arising from the on-going merger between NGC 1023 and NGC 1023A will allow a direct test of any role it may play in the formation of the NSD.

Chapter 4

The supermassive black hole and nuclear star cluster of NGC 383

Abstract

We present archival *Hubble Space Telescope* imaging and spectroscopic observations of the S0 galaxy NGC 383 obtained with the *Wide Field and Planetary Camera 2* mounting the F814W filter and the *Space Telescope Imaging Spectrograph* using the G570M grism, respectively. The data provide detailed information on the structure and mass profile of the stellar component, the dust optical depth, and the spatial distribution and kinematics of the ionised gas within the innermost region of the galaxy. Dynamical models, which account for the observed stellar mass profile and include the contribution of a nuclear star cluster (NSC) and a central supermassive black hole (SBH), are constructed to reproduce the kinematics derived from the [N II]λ6583 emission line along three slit positions crossing the nucleus and parallel to the galaxy major axis. A secure SBH detection with $M_\bullet = 8.5^{+1.8}_{-1.3} \times 10^8$ M$_\odot$ is obtained when a single massive central object (CMO) is considered. If we account for the presence of the NSC, then the masses of the SBH and NSC are $M_\bullet = 6.0^{+1.8}_{-1.2} \times 10^8$ M$_\odot$ and $M_{\rm NSC} = 8.9^{+5.0}_{-3.9} \times 10^7$ M$_\odot$, respectively. Both are consistent with the scaling relations linking the mass of CMOs with the properties of their host galaxy. These measurements prove that SBHs can coexist with NSCs and represent an important step forward in the characterisation of CMOs.

4.1 Introduction

The nuclei of galaxies are found to provide special physical conditions because they are located at the bottom of the potential well of their host galaxies. This unique location manifests itself in various distinctive phenomena such as active galactic nuclei (AGN), supermassive black holes (SBHs), or extreme stellar densities, such as nuclear star clusters (NSCs). Moreover, the evolution of galactic nuclei is closely linked to that of their host galaxies, as inferred from a number of scaling relations. For these reasons, a special interest has recently focused onto the compact sources found in the nuclei of many nearby galaxies, called central massive objects (CMOs). Despite the interesting connection between NSCs and SBHs, and their link to galaxy formation and evolution, very few systematic studies of the overlap between these classes of objects exist.

SBHs can be detected with high-resolution observations and are believed to be the cause of the past or present activity of the galaxies. The masses of the SBHs range between 10^6 and $\lesssim 10^{10}$ $M_\odot$ and can be measured with several methods. The demography of SBHs accounts for about 90 masses measured in quiescent galaxies (Kormendy & Ho 2013a) and about 150 masses in AGNs (Ho 2008). Stellar and/or gas dynamical models, spectro-astrometry, and analysis of water megamasers are adopted for quiescent galaxies. Reverberation mapping is used for active galaxies and allows to measure the mass of SBHs at high redshift. SBHs are found to correlate with several properties of their host galaxy. The most studied relation is between the masses of SBHs and the stellar velocity dispersion σ of their host spheroid (Ferrarese & Merritt 2000; Gebhardt et al. 2000b). In a general view, the existence and tightness of most of scaling relations suggests a connection between the evolution of SBHs and that of their host galaxies, and could provide constraints on theoretical models (e.g., Hopkins et al. 2006; De Lucia et al. 2006; Marulli et al. 2008). In particular, since the merger rate was higher and major mergers were more frequent in the past than today, such connection should be established earlier in massive elliptical galaxies than in lower mass galaxies, suggesting a self regulated accretion process (Volonteri & Natarajan 2009). Studying the demographics of SBHs, especially for a wide range of Hubble types and redshifts, hints to better understand the formation of the SBH seeds in the early universe (McLure & Dunlop 2002; Corbett et al. 2003; Shields et al. 2003). The formation of such kind of objects is still unclear. They can form from massive primordial stars, or due to the collapse or merging of massive objects, such as star clusters. While core-collapse supernovae provide a natural explanation of stellar BHs, dissipation on a much larger scale is required to build up SBHs. The discovery of AGN activity at redshifts $z > 6$ and the corresponding short timescale for gas ac-

cretion in BH may implicate that the growth mechanism is rapid (e.g., Willott et al. 2003; Barth et al. 2003; Shields et al. 2008). These considerations have prompted interest in mechanisms for producing "seeds" BHs of intermediate mass ($10^2 - 10^6$ $M_\odot$) that later emerge as the drivers of luminous AGNs (e.g., Shapiro 2004; van der Marel 2004).

NSCs are easily detectable photometrically because they are responsible for a pronounced upturn above the inward extrapolation of the galaxy profile. NSCs are commonly found in the centres of galaxies of all morphological types: 75% in late-type (Scd-Sm) spiral (Böker et al. 2002), 50% in early-type (Sa-Sc) spirals (Carollo et al. 1997), and 70% in spheroidal (E and S0) galaxies (Côté et al. 2006). They are very massive ($10^5 \leq M_{\rm NSC} \leq 10^8$ $M_\odot$, Walcher et al. 2005) and 40 times brighter than normal globular clusters ($-14 < M_I < -10$, Harris 1996). However, NSCs are as compact as Galactic globular clusters. Their half-light radius typically is 2−5 pc, independent of galaxy type (Böker et al. 2004; Geha et al. 2002; Côté et al. 2006). They can have multiple stellar populations, possessing both an old spheroidal component and a younger elongated disc or ring component (Walcher et al. 2006; Rossa et al. 2006). The youngest generation is often younger than 100 Myr which is strong evidence that NSCs experience frequent and repetitive star formation episodes (Walcher et al. 2006). The mass of NSCs tightly correlates with the total mass of the galaxy, but several other correlations have been proposed to link the properties of the NSCs with those of the host galaxy. There is a large number of suggested formation scenarios for NSCs and only a few have been ruled out so far. The migration formation scenario in which dense clusters form elsewhere in the galaxy and then fall into the centre via dynamical friction and an *in-situ* cluster build-up via (possibly episodic) gas infall and subsequent star formation within a few parsecs from the galaxy centre are the two main proposed scenarios. Simulations of the orbital decay and subsequent merging of globular clusters were investigated by Capuzzo-Dolcetta & Miocchi (2008a) and Hartmann et al. (2011), who concluded that this is indeed a viable formation scenario, at least under certain starting conditions. Analytical calculations presented in Milosavljević (2004) confirm that the expected amount of mass contributed by infalling star clusters over a Hubble time is consistent with the typical NSC masses observed today. A combined scenario where star formation occurs in the centre of galaxies after dissipation processes and accretes mass via the mergers of globular clusters seems the more plausible way to form NSCs.

It was proposed by Ferrarese et al. (2006a) that NSCs extend to lower masses the well-known scaling relation between the mass of a galaxy and that of its central SBH. This leads to speculate about a common formation mechanism of NSCs and SBHs, governed mostly by the mass of the host galaxy. The idea

is that NSCs and SBHs are two incarnations of a CMO which forms in every galaxy. In galaxies above a certain mass threshold ($M_{\rm gal} < 10^{10}$ M$_\odot$), galaxies form predominantly SBHs while lower mass galaxies form NSCs. This apparent connection opens more questions than it answers. We present the study of a galaxy with both a NSC and a SBH to better understand the relation between the two types of objects. The galaxy selection is discussed in Section 4.2, and the spectroscopic and photometric analysis are discussed in Section 4.3 and Section 4.4, respectively. Section 4.5 describes the dynamical model obtained considering a single CMO and both the SBH and NSC. Results and conclusions are discussed in Section 4.6.

4.2 Galaxy selection

Our project is aimed at measuring both the masses of the SBH and NSC in a galaxy that host both the objects. We looked for candidates which

- host a NSC with a resolved half-light radius;
- host a SBH with a resolved sphere of influence;
- are observed with *HST*stis mounting the G750M grism to measure the ionised-gas kinematics in the galaxy nucleus.

4.2.1 Sample selection

We started our analysis from the sample of galaxies of Beifiori et al. (2009). From the *HST* Science Archive they collected nuclear spectra ($0.1 - 0.3$ arcsec) of 177 galaxies spanning a wide range of Hubble types. The long-slit spectra were obtained with *STIS* using the G750M grating which gives the possibility to access to the emission lines of [N II] λ6583, Hα, and [S II] $\lambda\lambda$6716, 6731. The aim of Beifiori et al. (2009) was to derive stringent upper bounds on the mass of the SBHs for the sample galaxies by modelling the widths of the observed emission lines in terms of gas motions in a thin disc of unknown orientation but known spatial extent. They decided to consider only galaxies with velocity dispersion measurements in the literature, which were available for 137 objects out of 177. They also dropped further five objects, since upon closer inspection they revealed unrelaxed morphologies. For a number of objects with a sharp central surface-brightness profile, the two-dimensional rectification of the spectrum they performed during the data reduction produced anomalous undulations in the flux level of continuum of the very central rows, introducing also

artificial fluctuations in the emission-line flux profiles across the nucleus. This problem forced Beifiori et al. (2009) to remove a further 8 galaxies from the sample. Furthermore, 14 galaxies of the sample have too faint nebular emission and were consequently dropped from the sample. 3 further galaxies were discarded because their line profile could not be well represented as a simple sum of Gaussian components. Finally, 2 galaxies were rejected because the radial profile of the flux of the [N II] lines was strongly asymmetric and not suitable for modelling. Thus, they derived 105 upper limits of the mass of the SBHs which were compared with the $M_\bullet - \sigma_c$ relation by Ferrarese & Ford (2005) as a function of galaxy distance and morphological type (Figure 4.1). The upper and lower edges of the dotted lines correspond to $M_\bullet$ values estimated assuming an inclination of $i = 33°$ and $81°$ for the unresolved Keplerian disc, respectively. Large circles mark galaxies with $\sigma_c < 90$ km s^{-1} and found to host a NSC. The dashed lines show the 1σ (0.34 dex) scatter in $M_\bullet$.

The sample of Beifiori et al. (2009) included galaxies of all morphological types (27% classified as ellipticals, 19% lenticular galaxies and 54% spirals). It was limited in distance, including only galaxies within 100 Mpc (with a mean of 20.2 Mpc) and with measured values of the central stellar velocity dispersion (ranging between $58 \leq \sigma \leq 419$ km s^{-1}). The distances were measured from surface-brightness fluctuations (Tonry et al. 2000, 2001), from Cepheid variables (Freedman et al. 2001; Tully 1988), or were derived from the weighted mean recessional velocity corrected to the reference frame defined by the microwave background radiation from de Vaucouleurs et al. (1991) (RC3), assuming $H_0 = 75$ km s^{-1} Mpc^{-1}, $\Omega_m = 0.3$, and $\Omega_\Lambda = 0.7$. The most of these galaxies were classified as LINERS, but the sample contains also a fraction of Seyferts and transition objects.

From the sample of 105 galaxies, we selected the ones which host a NSC in their nucleus as it resulted from the analysis of the surface-brightness distribution. Using the IRAF[1] task ELLIPSE (Jedrzejewski 1987) we fitted isophotes to the surface brightness of the galaxies observed with *STIS*/F28x50LP. They are fit with ellipses, allowing their centres to vary in order to look for asymmetries in the light distribution. We masked all the features that can spoil the fit, such as foreground stars, dust lanes, and spiral arms. Within the errors of the fits we found no evidence of variations in the fitted centres. The ellipse fitting was then repeated with the ellipse centres fixed. We normalised the surface-brightness distribution of the sample galaxies to their central surface-

[1]Imaging Reduction and Analysis Facilities (IRAF) is distributed by the National Optical Astronomy Observatories which are operated by the Association of Universities for Research in Astronomy (AURA) under cooperative agreement with the National Science Foundation.

brightness. We compared it with the normalised surface-brightness distribution of the *Point Spread Function* (PSF). To match properly the observations, we assumed as PSF a star observed with the *STIS*/F28x50LP filter during the observing program GO ID 7361 (Principal Investigator: H. W. Rix) rather than a synthetic PSF build with TINYTIM. Following Böker et al. (2004), we considered

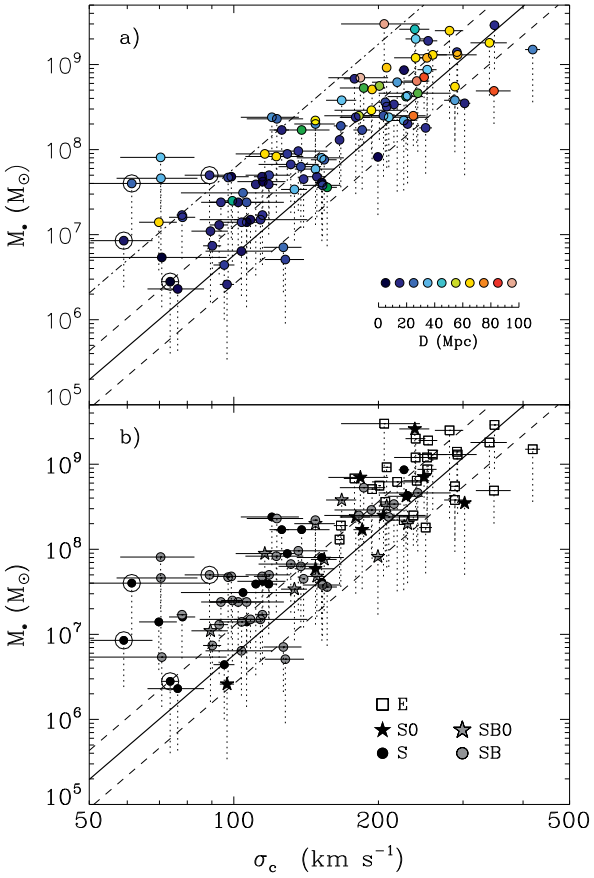

Figure 4.1: Comparison of $M_\bullet$ upper limits from Beifiori et al. (2009) with the $M_\bullet - \sigma_c$ relation by Ferrarese & Ford (2005) (black line) as a function of galaxy distance (a) and morphological type (b). The upper and lower edges of the dotted lines correspond to $M_\bullet$ values estimated assuming an inclination of $i = 33°$ and $81°$ for the unresolved Keplerian disc, respectively. Large circles mark galaxies with $\sigma_c < 90$ km s^{-1} that host a NSC. The dashed lines show the 1σ (0.34 dex) scatter in $M_\bullet$. Figure from Beifiori et al. (2009).

Table 4.1: Properties of the sample galaxies which are candidate to host a NSC.

Galaxy	Morph. T.	D [Mpc]	Ref.	M_B^0 [mag]	σ_c [km s^{-1}]	Ref.	M$_\bullet$ ($i = 33^\circ$) [M$_\odot$]	M$_\bullet$ ($i = 81^\circ$) [M$_\odot$]
(1)	(2)	(3)	(4)	(5)	(6)	(7)	(8)	(9)
IC 3639	SBbc(rs):	48.0	1	−20.70	99 ± 5	3	$2.5{\cdot}10^7$	$4.8{\cdot}10^6$
NGC 289	SBbc(rs)	18.3	1	−19.91	118 ± 12	4	$5.0{\cdot}10^7$	$1.3{\cdot}10^7$
NGC 383	SA0$^-$:	63.4	1	−21.33	259 ± 18	4	$1.3{\cdot}10^9$	$2.9{\cdot}10^8$
NGC 2110	SAB0$^-$	31.2	1	−20.62	219 ± 25	6	$6.2{\cdot}10^8$	$3.2{\cdot}10^7$
NGC 2273	SBa(r):	25.0	1	−19.97	127 ± 11	6	$7.1{\cdot}10^6$	$2.1{\cdot}10^6$
NGC 2903	SABbc(rs)	11.2	1	−21.14	102 ± 13	7	$2.4{\cdot}10^7$	$6.4{\cdot}10^6$
NGC 2911	SA0(s): pec	46.6	1	−21.09	238 ± 17	8	$2.6{\cdot}10^9$	$6.6{\cdot}10^8$
NGC 3021	SAbc(rs)	23.9	1	−19.37	61 ± 27	9	$4.0{\cdot}10^7$	$9.8{\cdot}10^6$
NGC 3078	E2-3	35.2	1	−20.79	226 ± 13	10	$2.2{\cdot}10^8$	$3.3{\cdot}10^7$
NGC 3081	(R)SAB0/a(r)	35.9	1	−20.19	134 ± 8	3	$3.4{\cdot}10^7$	$8.5{\cdot}10^6$
NGC 3245	SA0^0(r):?	20.9	2	−19.53	205 ± 18	11	$2.5{\cdot}10^8$	$4.8{\cdot}10^7$
NGC 3310	SABbc(r) pec	15.6	1	−20.01	113 ± 29	12	$1.5{\cdot}10^7$	$5.0{\cdot}10^6$
NGC 4041	SAbc(rs):	18.2	1	−19.54	95 ± 5	4	$4.4{\cdot}10^6$	$1.0{\cdot}10^6$
NGC 4088	SABbc(rs)	12.7	1	−20.00	93 ± 4	4	$1.3{\cdot}10^7$	$3.4{\cdot}10^6$
NGC 4212	SAc:	3.4	1	−16.28	74 ± 3	4	$2.8{\cdot}10^6$	$4.0{\cdot}10^5$
NGC 4245	SB0/a(r):	15.6	1	−18.96	89 ± 10	13	$5.0{\cdot}10^7$	$5.6{\cdot}10^6$
NGC 4278	E1-2	16.1	2	−20.06	251 ± 8	14	$1.8{\cdot}10^8$	$5.2{\cdot}10^7$
NGC 4501	SAb(rs)	34.6	1	−22.84	152 ± 17	7	$8.0{\cdot}10^7$	$1.5{\cdot}10^7$
NGC 4548	SBb(rs)	19.2	2	−20.63	153 ± 14	15	$3.8{\cdot}10^7$	$9.6{\cdot}10^6$
NGC 4579	SABb(rs)	24.6	1	−21.66	123 ± 16	7	$2.3{\cdot}10^8$	$4.3{\cdot}10^7$
NGC 5347	(R")SBab(rs)	34.6	1	−19.59	70 ± 13	6	$4.6{\cdot}10^7$	$6.5{\cdot}10^6$
NGC 5643	SABc(rs)	18.6	1	−21.11	97 ± 1	16	$4.7{\cdot}10^7$	$3.1{\cdot}10^6$
NGC 5728	SABa(r):	40.3	1	−21.37	210 ± 44	17	$2.4{\cdot}10^8$	$6.2{\cdot}10^7$
NGC 5879	SAbc(rs):?	11.4	1	−18.88	59 ± 9	18	$8.5{\cdot}10^6$	$2.4{\cdot}10^6$
NGC 6300	SBb(rs)	15.2	1	−20.71	94 ± 5	3	$2.4{\cdot}10^7$	$9.4{\cdot}10^6$

NOTES– Col. (1): Galaxy name. Col. (2): Morphological type from RC3. Col. (3): Distance. Col. (4): Reference for column (3). Col. (5): Absolute corrected B magnitude derived from $B_{0,T}$ (RC3) with the adopted distance. Col. (6): Central velocity dispersion of the stellar component within $r_e/8$. Col. (7): Reference for the measured stellar velocity dispersion and corresponding size of the central aperture from which was calculated the value given in column (6) by following Jorgensen et al. (1995). Col. (8): $M_\bullet$ upper limit for a Keplerian disc model assuming $i = 33^\circ$, from Beifiori et al. (2009). Col. (9): $M_\bullet$ upper limit for $i = 81^\circ$ from Beifiori et al. (2009).
REFERENCES– (1) m v_{3k} given by de Vaucouleurs et al. (1991), (2) Tonry et al. (2001), (3) Terlevich et al. (1990), (4) Garcia-Rissmann et al. (2005), (5) Batcheldor et al. (2005), (6) Simien & Prugniel (1997), (7) Nelson & Whittle (1995), (8) Héraudeau & Simien (1998), (9) di Nella et al. (1995), (10) Héraudeau et al. (1999), (11) Carollo et al. (1993), (12) Simien & Prugniel (1998), (13) Falcón-Barroso et al. (2006), (14) Barth et al. (2002), (15) Whitmore & Kirshner (1981), (16) Gu et al. (2006), (17) Wagner & Appenzeller (1988), (18) Falcón-Barroso et al. (2002).

that galaxies with surface-brightness profiles that lay systematically above the PSF surface-brightness profile (i.e. which have a central light excess) may host a NSC. We selected 25 galaxies that can host a NSC (Figure 4.2). Figure 4.3 shows two sample galaxies where the central surface-brightness profile follows the PSF. Thus, they do not show evidence of NSCs. The properties of the candidate galaxies to host a NSC and the details of their *STIS* observations are given in Table 4.1 and Table 4.2, respectively.

Then, we estimated the mass of the SBH from the central stellar velocity dispersion, according to the relation found by Gültekin et al. (2009)

$$\log\left(\frac{M_\bullet}{M}\right) = (1.66 \pm 0.24) + (4.86 \pm 0.43) \cdot \log\left(\frac{\sigma_{\rm c}}{200\,{\rm kms}^{-1}}\right), \tag{4.1}$$

where $\sigma_{\rm c}$ is the velocity dispersion measured within the effective radius. The values are shown in Table 4.1.

We estimated the radius of the sphere of influence $r_{\rm infl}$ of the SBH, defined as

$$r_{\rm infl} = \frac{GM_\bullet}{\sigma^2} \tag{4.2}$$

where σ is the rotational velocity or velocity dispersion characteristic of the inner part of the galaxy, and G is the gravitational constant. An object at a given distance D has an angular radius of influence $r_{\rm infl}$ of

$$r_{\rm infl}({\rm arcsec}) = 10.57\,{\rm arcsec}\left(\frac{M_\bullet}{10^8{\rm M}_\odot}\right)\left(\frac{\sigma_{\rm c}}{200\ {\rm km\ s}^{-1}}\right)^{-2}\left(\frac{D}{0.206265}\right)^{-1}. \tag{4.3}$$

$r_{\rm infl}$, σ, and D are key parameters, because they give information whether instruments have an angular resolution high enough to resolve the sphere of the influence of a SBH.

Figure 4.4 shows when the resolution limit of an instrument can resolve the radius of the sphere of influence of the SBH as a function of distance and velocity dispersion. SBHs at a distance of a few Mpc with masses below 10^8 $M_\odot$ require *HST* or adaptive-optics on the ground-based telescopes for resolving the sphere of influence.

Figure 4.5 shows the value of the $M_\bullet$ as a function of $r_{\rm infl}$ for galaxies which were observed with *STIS*. The dotted lines represent the lower limits for the resolution of $r_{\rm infl}$ of galaxies observed with the 0.1- and 0.2- arcsec slits. We found that only 5 candidates host a NSC with a resolved sphere of influence using *STIS*: NGC 383, NGC 2110, NGC 2911, NGC 3078, and NGC 5728.

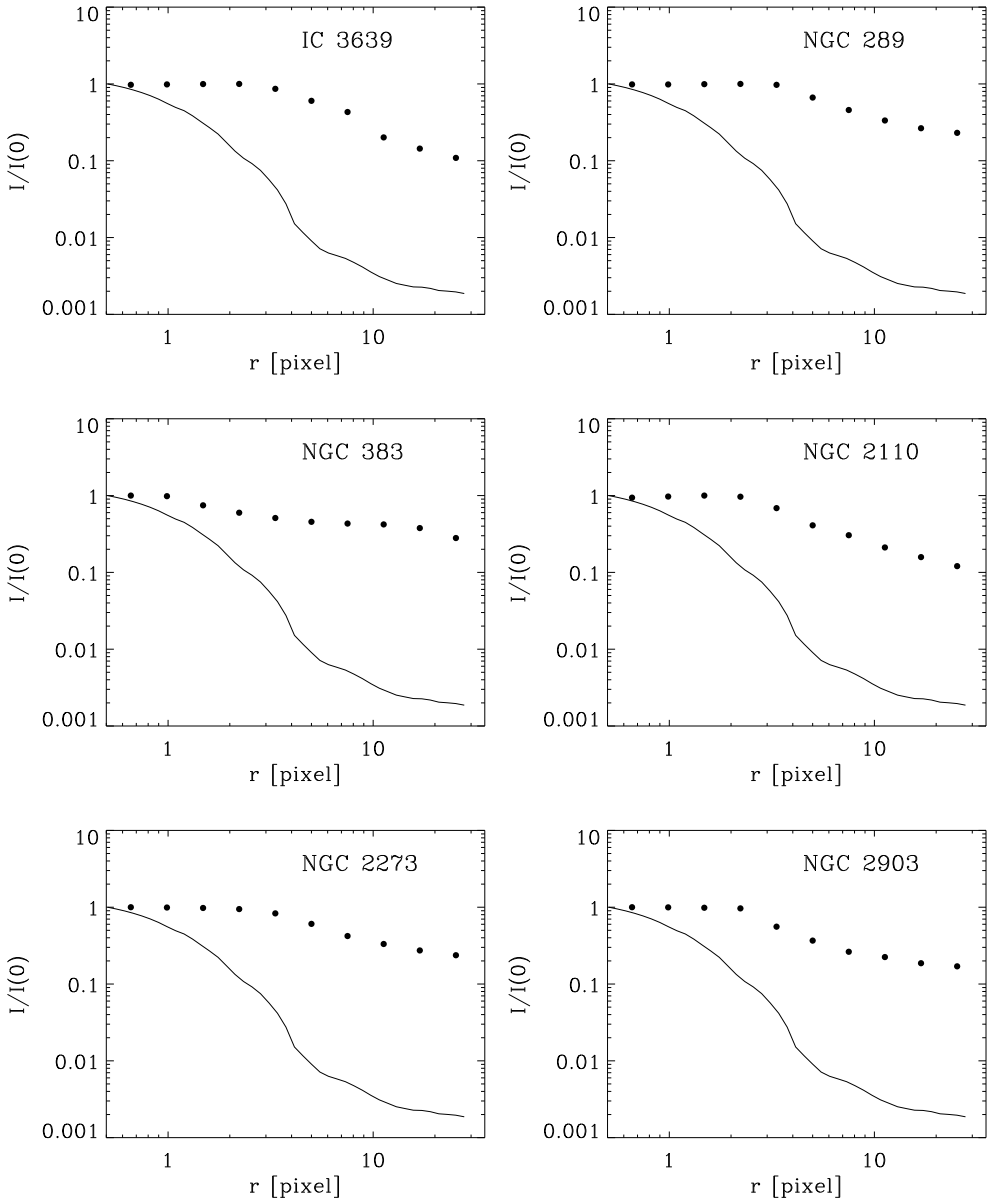

Figure 4.2: Comparison between the *STIS*/F28x50LP surface brightness profile of the sample galaxies which are candidate to host a NSC (points) and the PSF profile obtained using a star observed during the observing program GO ID 7361 (solid lines). The surface brightness of each galaxy is normalised to its central value $I(0)$.

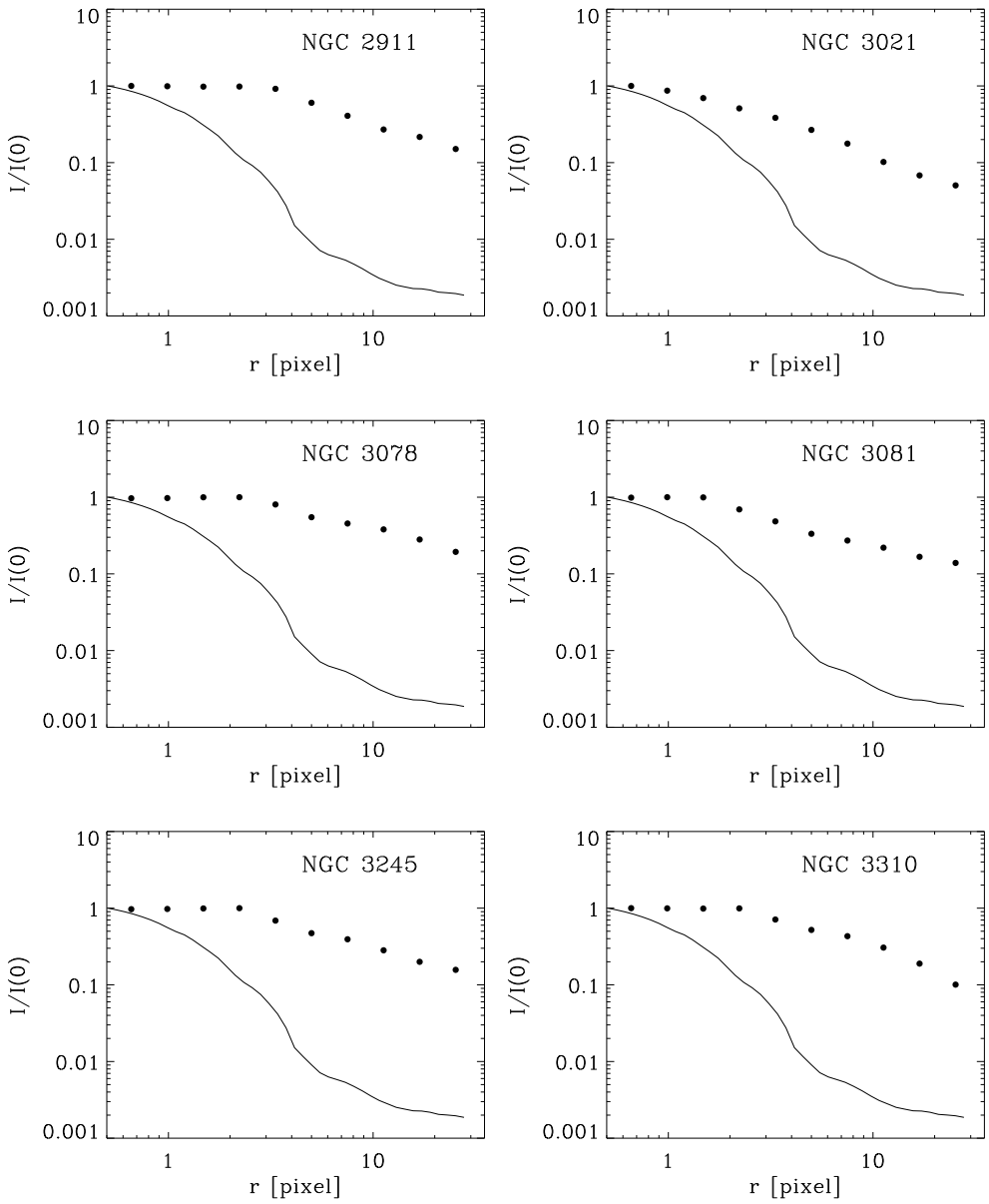

Figure 4.2: Continued.

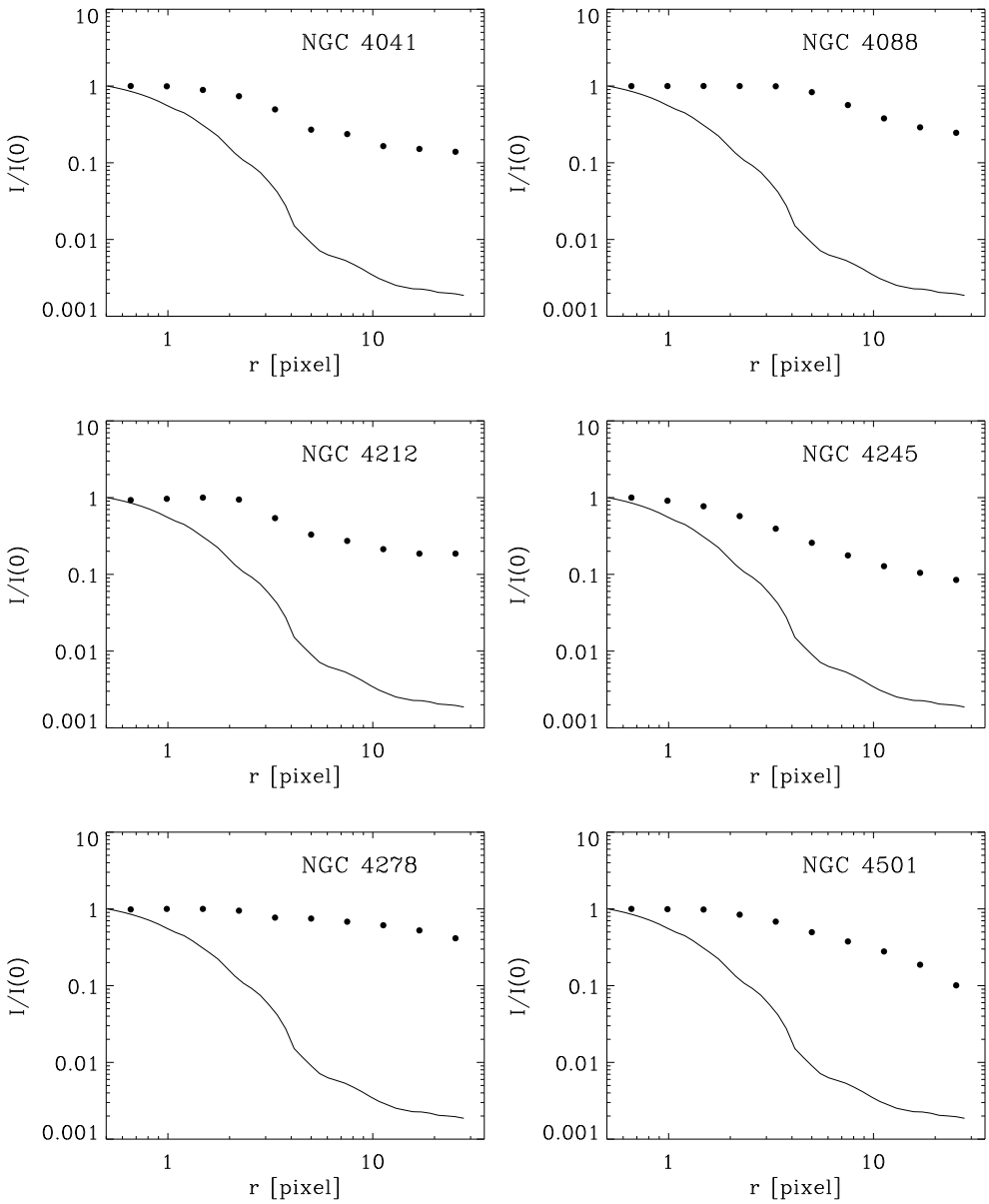

Figure 4.2: Continued.

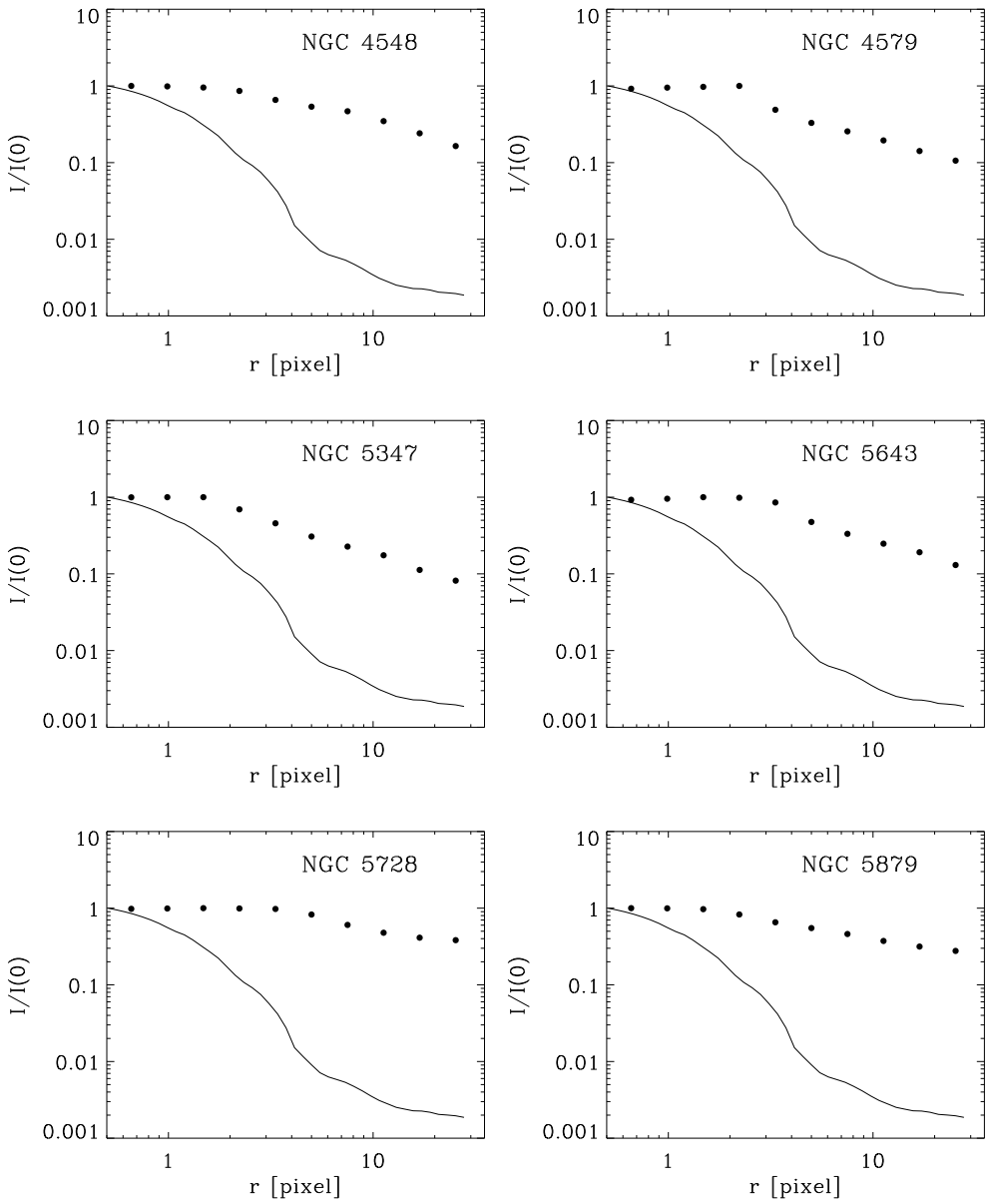

Figure 4.2: Continued.

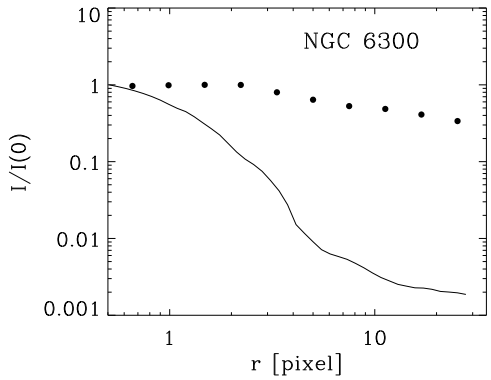

Figure 4.2: Continued.

Table 4.2: Predicted SBH parameters and details of *STIS* observations for the sample galaxies candidates to host a nuclear star cluster.

Galaxy	Program ID	Aperture [arcsec]	Aperture [pc]	Binning [arcsec]	$r_{\rm infl}$ [arcsec]	$M_\bullet$ [$M_\odot$]
(1)	(2)	(3)	(4)	(5)	(6)	(7)
IC 3639	9143	0.25×0.2	58×47	1×1	0.0102	$5.443{\cdot}10^6$
NGC 289	8228	0.25×0.2	22×18	1×1	0.1530	$1.277{\cdot}10^7$
NGC 383	8236	0.15×0.1	46×31	2×1	0.0401	$5.830{\cdot}10^8$
NGC 2110	8610	0.25×0.2	38×30	2×1	0.0445	$2.580{\cdot}10^8$
NGC 2273	9143	0.25×0.2	30×24	1×1	0.0479	$1.826{\cdot}10^7$
NGC 2903	8228	0.30×0.2	16×11	2×2	0.1299	$6.293{\cdot}10^6$
NGC 2911	7354	0.15×0.1	34×23	2×1	0.0051	$3.866{\cdot}10^8$
NGC 3021	8228	0.25×0.2	29×23	1×1	0.1484	5.173e 5
NGC 3078	9163	0.30×0.2	51×34	2×2	0.0326	$3.006{\cdot}10^8$
NGC 3081	9143	0.25×0.2	44×35	1×1	0.1891	$2.370{\cdot}10^7$
NGC 3245	7403	0.25×0.2	25×20	1×1	0.0461	$1.871{\cdot}10^8$
NGC 3310	8228	0.30×0.2	23×15	2×2	0.1216	$1.035{\cdot}10^7$
NGC 4041	8228	0.25×0.2	22×18	1×1	0.0240	$4.454{\cdot}10^6$
NGC 4088	8228	0.25×0.2	15×12	1×1	0.0324	$4.017{\cdot}10^6$
NGC 4212	8228	0.25×0.2	4×3	1×1	0.0630	$1.323{\cdot}10^6$
NGC 4245	7361	0.25×0.2	19×15	1×1	0.0233	$3.244{\cdot}10^6$
NGC 4278	7403	0.25×0.2	19×16	1×1	0.4380	$5.006{\cdot}10^8$
NGC 4501	7361	0.25×0.2	42×34	1×1	0.0485	$4.373{\cdot}10^7$
NGC 4548	7361	0.25×0.2	23×19	1×1	0.0891	$4.515{\cdot}10^7$
NGC 4579	7403	0.25×0.2	30×24	1×1	0.0372	$1.563{\cdot}10^7$
NGC 5347	9143	0.25×0.2	42×34	1×1	0.0052	$1.009{\cdot}10^6$
NGC 5643	9143	0.25×0.2	22×18	1×1	0.0249	$4.929{\cdot}10^6$
NGC 5728	8123	0.15×0.1	29×20	1×1	0.1050	$2.104{\cdot}10^8$
NGC 5879	8228	0.30×0.2	16×11	2×2	0.0098	$4.399{\cdot}10^5$
	8607	0.30×0.2	16×11	1×2		
NGC 6300	9143	0.25×0.2	18×15	1×1	0.0279	$4.231{\cdot}10^6$

NOTES. — Col.(1): Galaxy name. Col.(2): *HST* proposal number referred to the *STIS*/G750M spectrum. Col.(3): Size of the central aperture in arcsec and Col.(4): in physical units. Col.(5): x dimension of the rectangular aperture, or radius of the circular aperture if no value is given in Col.(8). Col.(6): y dimension of the rectangular aperture. Col.(7): Pixel binning.

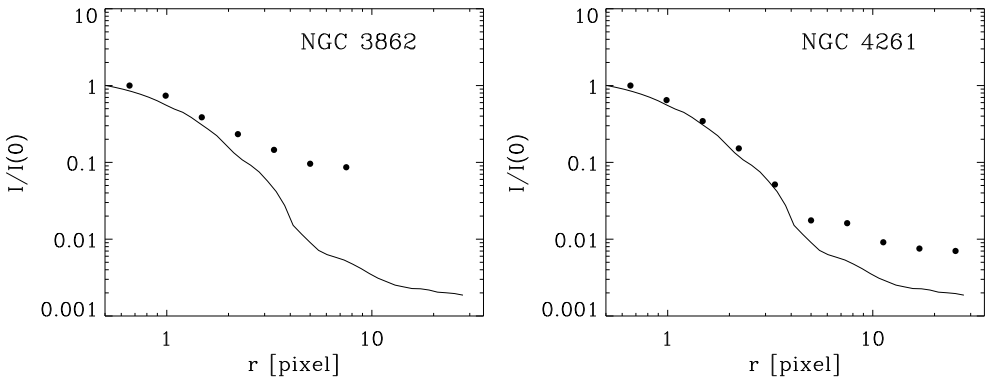

Figure 4.3: As in Figure 4.2.1 but for two sample galaxies which do not host a NSC.

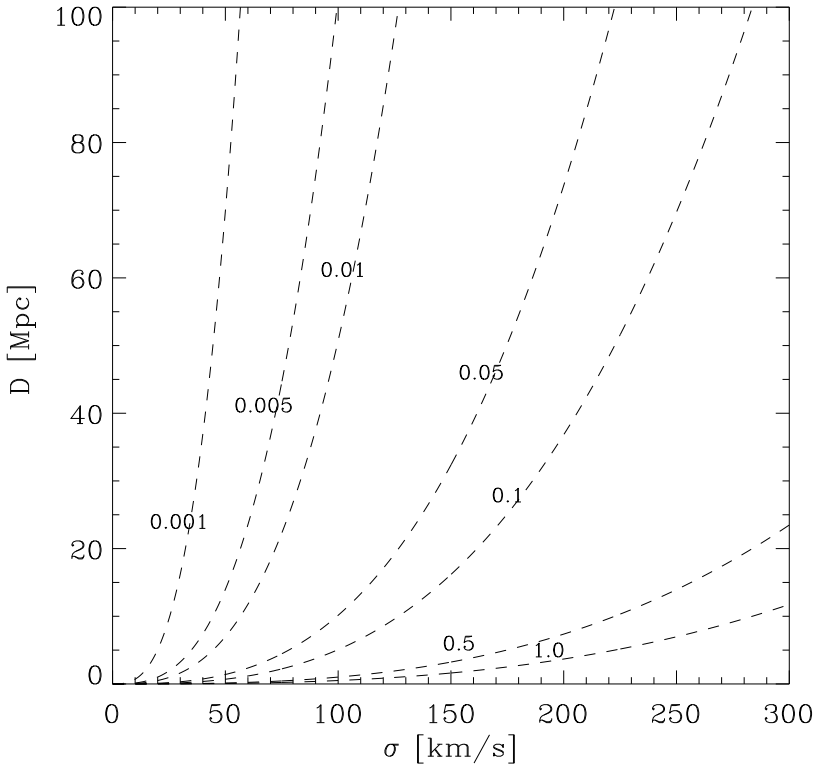

Figure 4.4: The radius of the sphere of influence of a SBH as a function of the velocity dispersion and distance of the host galaxy. The dashed lines correspond to the radii ranging from 0.001 to 1.0 arcsec.

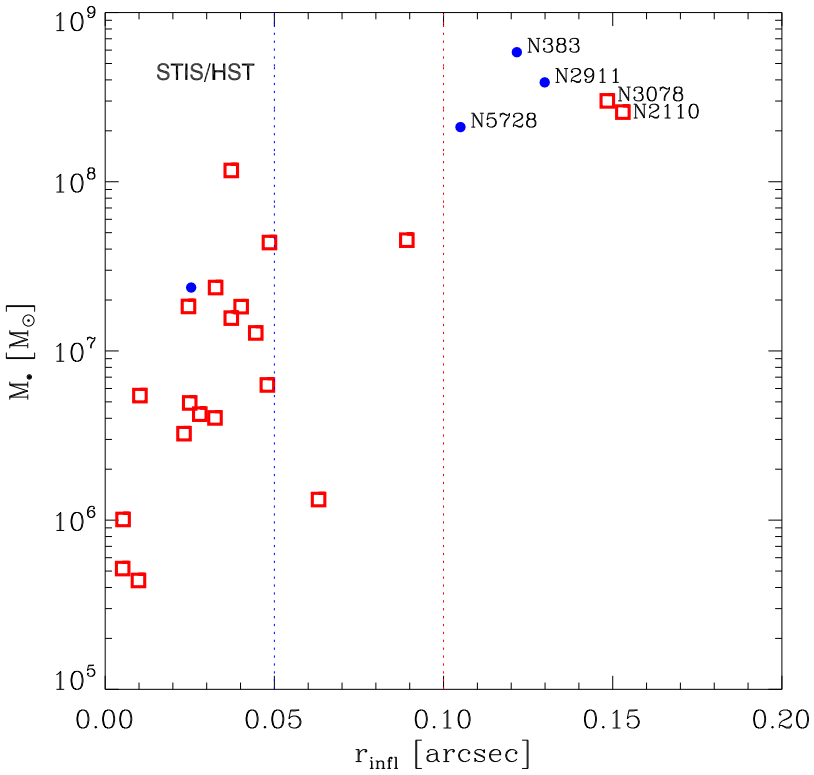

Figure 4.5: Predicted values of the SBH mass $M_\bullet$ of the sample galaxies candidates to host a NSC as a function of the radius of their sphere of influence. The blue and red line represent the lower limits for resolution of $r_{\rm infl}$ of galaxies observed with the 0.1- (blue points) and 0.2-arcsec (red squares) slit widths.

Furthermore, in order to constrain the orientation of the gaseous disc, we need spectra obtained in offset positions in addition to the nuclear one. Thus, we excluded from the study NGC 2110 because only the spectrum crossing the nucleus of the galaxy is available. The last criterion for selecting the target galaxies was to search whether the resolution limits of *HST* instruments can resolve the size of the NSC at the distance of the sample galaxies. Thus, we studied the profile of the angular size of a typical NSC as a function of the distance of the host galaxy. We adopted the values found by Böker et al. (2004) of the half-light radius of NSCs, $r_{\rm e}$, which ranges from 0.7 to 28.8 pc, with a mean of 5.1 pc. Figure 4.6 shows the value of the $r_{\rm e}$ as a function of the distance for galaxies of the sample of Böker et al. (2004). The two dashed and the solid lines represent the lower, higher, and mean values of $r_{\rm e}$ of the sample.

The two dotted lines represent the resolution limit of the Planetary Camera of *HST/WFPC2* and the *UVIS* channel of *HST/WFC3*.

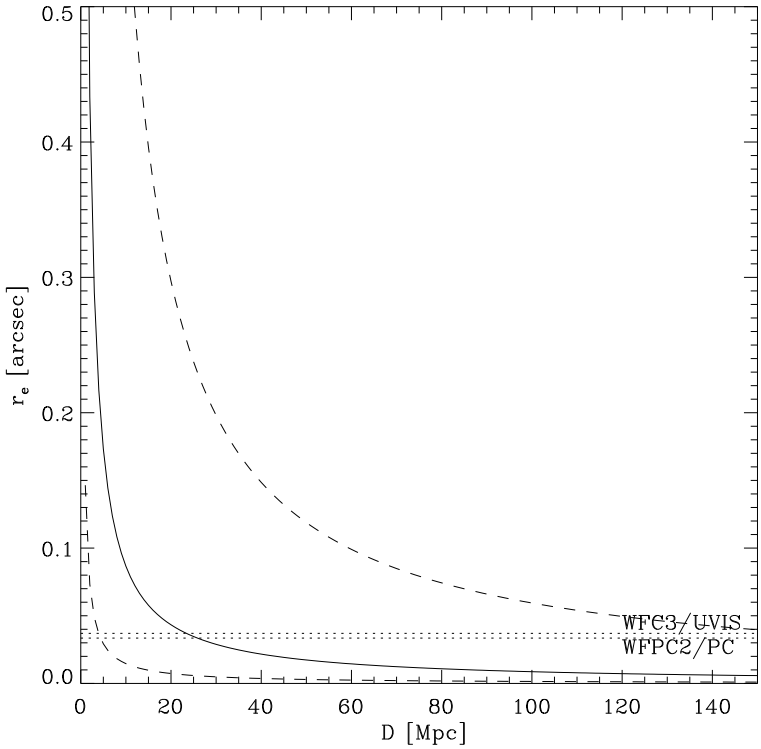

Figure 4.6: Measured values of the half-light radius for galaxies of the sample of Böker et al. (2004) as a function of the galaxy distance. The bottom and top dashed, and the solid lines represent the lower ($r_e = 0.7$ pc), higher (28.8 pc), and mean values ($r_e = 5.1$ pc) of the half-light radius of the sample, respectively. The two dotted lines represent the resolution limit of the Planetary Camera of *HST/WFPC2* and the *UVIS* channel of *HST/WFC3*.

At the distance of NGC 383, NGC 2911, NGC 3078, and NGC 5728, the size of the NSC is well resolved with both *WFPC2* and *WFC3*. Thus we have 4 candidates to host both a resolved NSC and a SBH with a resolved sphere of influence.

To map and highlight the nuclear dust structures, the *STIS* acquisition images were unsharp masked (Figure 4.7) using the same technique adopted by Pizzella et al. (2002). We divided each image by itself after the convolution by a circular Gaussian of width $\sigma = 3, 5$, and 10 pixel, corresponding to $\sigma = 0.15, 0.25$, and 0.5 arcsec, respectively. This technique enhances any

surface-brightness fluctuation and non-circular structure extending over a spatial region comparable to the σ of the smoothing Gaussian. The dust lanes appear well-defined in all the images and, therefore, are promising of a regular gas kinematics (Ho et al. 2002). We decided to focus on NGC 383 which looks the most promising target, by showing a clearly symmetric dust distribution.

4.2.2 NGC 383

NGC 383 (or UGC 0689) is a lenticular galaxy, classified as $SA0^-$: at a distance of 63.4 Mpc (de Vaucouleurs et al. 1991). It is located at $\alpha = 01^\circ\ 07'\ 24.9$ arcsec and $\delta = +32^\circ\ 24'\ 45$ arcsec and has a systemic velocity of 5098 km s^{-1}. The absolute corrected B magnitude derived from $B_{0,T}$ (de Vaucouleurs et al. 1991) is -21.33. The position angle of the galaxy major axis is 30°. The radius of the isophote with surface brightness of $\mu_B = 25$ mag arcsec^{-2}, derived from the diameter D_{25} listed in de Vaucouleurs et al. (1991) is 47.5 arcsec. The respective inclination derived from the logarithm of the ratio between the major and minor diameters of that isophote is 32°.

NGC 383 is the brightest galaxy in the Zwicky cluster $0107.5 + 3212$ (Sakai et al. 1994). NGC 383 is inside a chain of galaxies and forms a pair with NGC 382, which is at distance 11 kpc. NGC 383 has a nearly face-on central dust disc (Martel et al. 1999; Verdoes Kleijn et al. 1999, 2006a), which shows a spiral structure with a counterclockwise orientation. Martel et al. (1999) detected a dust disc in the companion NGC 382 as well. NGC 383 has a nuclear point source that is clearly bluer than its surroundings (Verdoes Kleijn et al. 1999, 2006b). Komossa & Böhringer (1999) performed an X-ray study of the NGC 383 group and found indications for a hard X-ray component that might be associated with the central AGN. The radio jet has been extensively studied (e.g., Lara et al. 1997). The radio jet shows a distorted morphology, suggesting gravitational interaction between NGC 383 and its companion NGC 382. Evidence for an optical jet was claimed by Butcher et al. (1980), but not confirmed by later studies (Keel 1988; Owen et al. 1990; Fraix-Burnet et al. 1991).

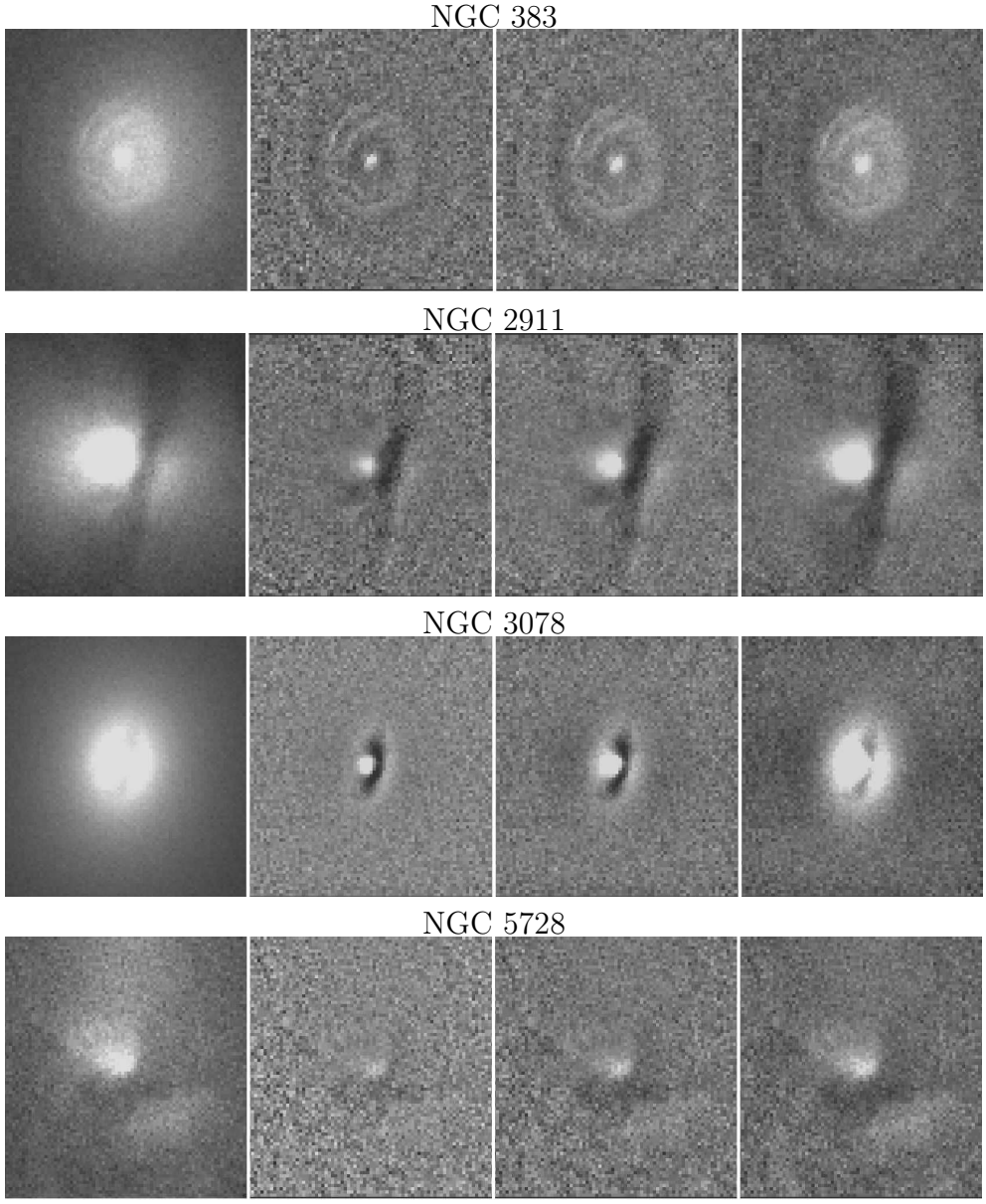

Figure 4.7: *STIS*/F28x50LP acquisition images of the sample galaxies (left-hand panels) and unsharp masked images obtained convolving the image with a circular Gaussian of width $\sigma = 2$ (left-hand panels), 4 (central panels), and 6 pixel (right-hand panels). The fields of view are 5.2×5.2 arcsec^2. The grey-scales are kept constant.

4.3 Spectroscopy: observations, data reduction, and analysis

4.3.1 HST/STIS observations

The high-resolution spectroscopic observations of NGC 383 were carried out on October, 2000 (Table 4.2) within the program GO-8236 (P.I S. Baum). The detector was the Scientific Imaging Technologies (SITe) CCD with 1024×1024 pixel^2 of 21×21 μm^2. To measure the ionised gas kinematics the G750M grating was used at prime tilt, in combination with the 0.1-arcsec slit. This configuration has a central wavelength $\lambda_{\rm cen} = 6768$ Å and covers the wavelength range between 6482 to 7054 Å, including the Hα, [N II] $\lambda\lambda 6548, 6583$, and the [S II] $\lambda\lambda 6716, 6731$ emission lines. On-chip rebinning of 2 pixels in the spectral direction was adopted to reduce the read-out noise. The resulting reciprocal dispersion is 1.108 Å pixel^{-1} , which corresponds to ≈ 50 km s^{-1} at Hα. The spatial scale is 0.0508 arcsec pixel $^{-1}$. The instrumental FWHM of the spectral line-spread function was ≈ 60 km s^{-1} for the 0.1 arcsec slit.

NGC 383 was observed in two orbits. For each orbit the target acquisition of the object was done using the acquisition image to find the position of the galaxy centre. The two acquisition images have a field of view of 5.2×5.2 arcsec^2 and a pixel scale of 0.0508 arcsec pixel^{-1}. The exposure time was 60 s each and the gain was 4 e^- DN^{-1} . The long-pass F28x50LP was centred at 7230 Å with a FWHM=2720 Å. It roughly covers the R band. The first image was obtained by adopting the galaxy coordinates from RC3 (de Vaucouleurs et al. 1991). The image was summed over a check box of 3×3 pixel to find the position of the intensity peak. The flux-weighted centre of the brightest check box was assumed to be coincident with the location of the galaxy nucleus. This was used to re-centre the nucleus and obtain the second image. The acquisition images were bias subtracted, corrected for bad pixels and cosmic rays, flat-fielded, and combined using the *STIS* reduction pipeline maintained by the Space Telescope Science Institute (STScI).

The *STIS* slits were aligned parallel to the galaxy major axis at three different positions, the first crossing the galaxy nucleus, and the two additional ones displaced by one slit width on either side perpendicular to the slit axis. Two spectra were taken at each slit position. Each exposure was about 500 s long and the second shifted by 4 pixels in the spatial direction to allow accurate bad pixel and cosmic-ray removal (Table 4.3). The analog-to-digital gain was 1 e^-DN^{-1} and the read-out noise was 4.02 e^- rms.

Table 4.3: Log of the *STIS* observations of NGC 383.

Spectrum name	UT date	Observing time	Δx [arcsec]	Δy [arcsec]	PA [° E of N]	Exp. Time [s]
(1)	(2)	(3)	(4)	(5)	(6)	(7)
O5EE03030	2000-10-15	12:06:08	−0.1	−0.1014	144.456	500
O5EE03040	2000-10-15	12:15:29	−0.1	0.1014	144.456	582
O5EE03060	2000-10-15	13:14:00	0.0	−0.1014	144.456	500
O5EE03070	2000-10-15	13:23:21	0.0	0.1014	144.456	500
O5EE03080	2000-10-15	13:33:34	0.1	−0.1014	144.456	500
O5EE03090	2000-10-15	13:42:55	0.1	0.1014	144.456	598

NOTES. — Col.(1): Spectrum name reflecting the position of the slit. Col.(2): Observation date. Col.(3): Observation time. Col.(4)-(5): Nominal offset of the slit along the x (perpendicular to the slit) and y (along the slit direction) axes with respect to the centre of the galaxy. Col.(6): Position angle of the slit in ° from East to North. Col.(7): Exposure time.

4.3.2 Data reduction

The archival spectra were reduced using IRAF[2] and the CALSTIS reduction pipeline maintained by the Space Telescope Science Institute (STScI). It performs the basic reduction steps, which include overscan subtraction, bias and dark subtraction, and flat-field correction, as described in detail in the *STIS* instrument and data handbooks (Kim Quijano et al. 2007; Dressel et al. 2007).

We aligned the two spectra obtained in the same position with IMSHIFT. Cosmic ray events and hot pixels were removed using the task LACOS_SPEC (van Dokkum 2001). Residual bad pixels were corrected by means of a linear one-dimensional interpolation using the data quality files and stacking individual spectra with OIMCOMBINE. This allowed us to increase the signal-to-noise ratio of the resulting spectra. We performed wavelength and flux calibration as well as geometrical correction for two-dimensional distortion following the standard reduction pipeline and applying X2D. This task corrects the wavelength scale to the heliocentric. The surface brightness of the flux calibrated, rectified, two-dimensional spectral images is in units of erg s $^{-1}$ cm^{-2} Å^{-1}. Figure 4.8 shows the reduced nuclear two- and one-dimensional spectra obtained by extracting a squared aperture centred on the continuum peak. The orientation of NGC 383 and the location and size of the slit placed in the galaxy centre on the acquisition image are also shown.

[2]IRAF is distributed by NOAO, which is operated by AURA Inc., under contract with the National Science Foundation

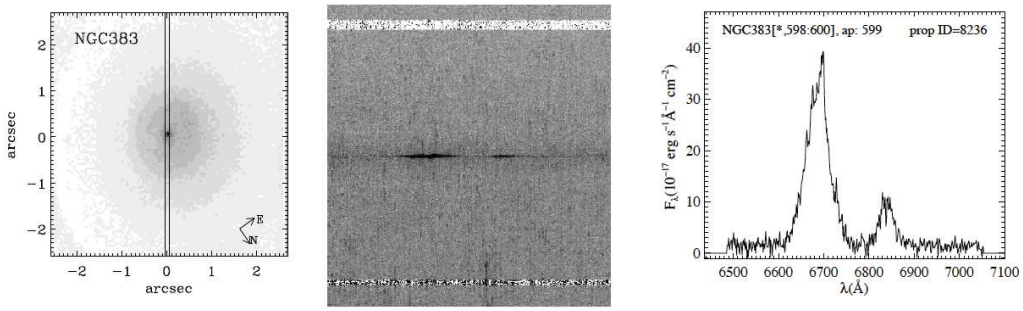

Figure 4.8: *STIS*/F28X50LP acquisition image of NGC 383 (left-hand panel) which shows the orientation of the galaxy and the location and size of the slit placed in the galaxy centre. The field of view is 5.2 × 5.2 arcsec^2. The spatial axis is horizontal and ranges between $-1''.0$ and $+1''.0$, while the wavelength axis ranges from 6482 to 7054 Å. Other spectra correspond nominally to a slit-position offset of -0.1 and $+0.1$ arcsec. The nuclear two-dimensional spectra obtained by extracting a squared aperture centred on the continuum peak and the one-dimensional spectrum extracted summing 3 central lines are shown in the central and right panels, respectively.

4.3.3 Location of the slits

In the observing strategy, the 0.1-arcsec slit was nominally centred on the galaxy nucleus and it was aligned along the direction of the columns of the acquisition image at the end of the target acquisition and peak up. The two subsequent offsets were done by applying shifts of 0.1 (i.e. westwards) and +0.1 arcsec (i.e. eastwards) in the direction of the rows of the acquisition image. Sometimes the actual position is not exactly the same of the nominal one. The difference between the nominal and actual position of the slit centre is typically 1 pixel (e.g., Coccato et al. 2006).

Following Coccato et al. (2006), we compared the light profile of the spectrum with the one extracted from the acquisition image to check the effective location of the slits relative to the galaxy centre. With this aim, we extracted a series of "synthetic" slits from the acquisition images by averaging two adjacent columns (corresponding to the width of the 0.1-arcsec slit) at the nominal slit orientation. We obtained the surface-brightness radial profile of the nuclear spectrum by collapsing the stellar continuum of the spectrum along the wavelength direction over the spectral range between 6350 and 6800 Å. The surface-brightness radial profiles obtained for each synthetic slit were then compared to the profiles obtained by the collapsed spectrum, as shown in Figure 4.9 and Figure 4.10. The best match was determined by minimising the χ^2 of the resid-

uals obtained from the difference between the light profile of the spectrum and the light profile extracted from the acquisition image.

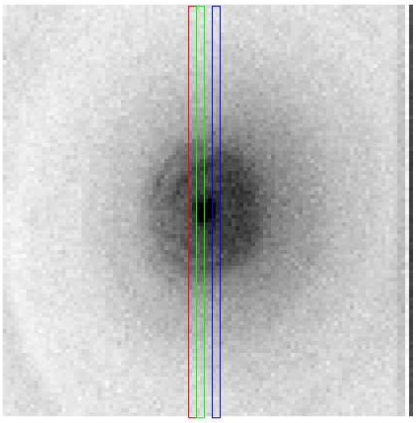

Figure 4.9: Location of the slits with respect to the *STIS*/F28x50LP acquisition images. Different colours are used to indicate the portion of the acquisition images that corresponds to the central (green), −0.1 (red) and 0.1-arcsec (blue) offset spectra.

In all cases, the slits were found to be slightly misplaced with respect to their nominal locations. The surface-brightness profile of *STIS*/G750M spectrum of NGC 383 which was nominally obtained crossing the nucleus of the galaxy is best matched with the profile extracted from the two adjacent columns placed at −0.076 arcsec from the galaxy centre (−1.5 pixel) in the acquisition image. The surface-brightness profile of the spectrum nominally obtained at −0.1 arcsec from the nucleus of the galaxy is best matched with the surface-brightness profile extracted from the two adjacent columns placed at −0.178 arcsec from the galaxy centre (−3.5 pixel) in the acquisition image. Thus, it is −0.1 arcsec (−2 pixel) far away from the actual position of the central slit. Finally, the surface-brightness profile of the spectrum nominally obtained at +0.1 arcsec from the nucleus of the galaxy is best matched with the profile extracted from the two adjacent columns placed at +0.127 arcsec from the galaxy centre (+2.5 pixel) in the acquisition image, thus at −0.203 arcsec (5 pixel) from the actual position of the central slit

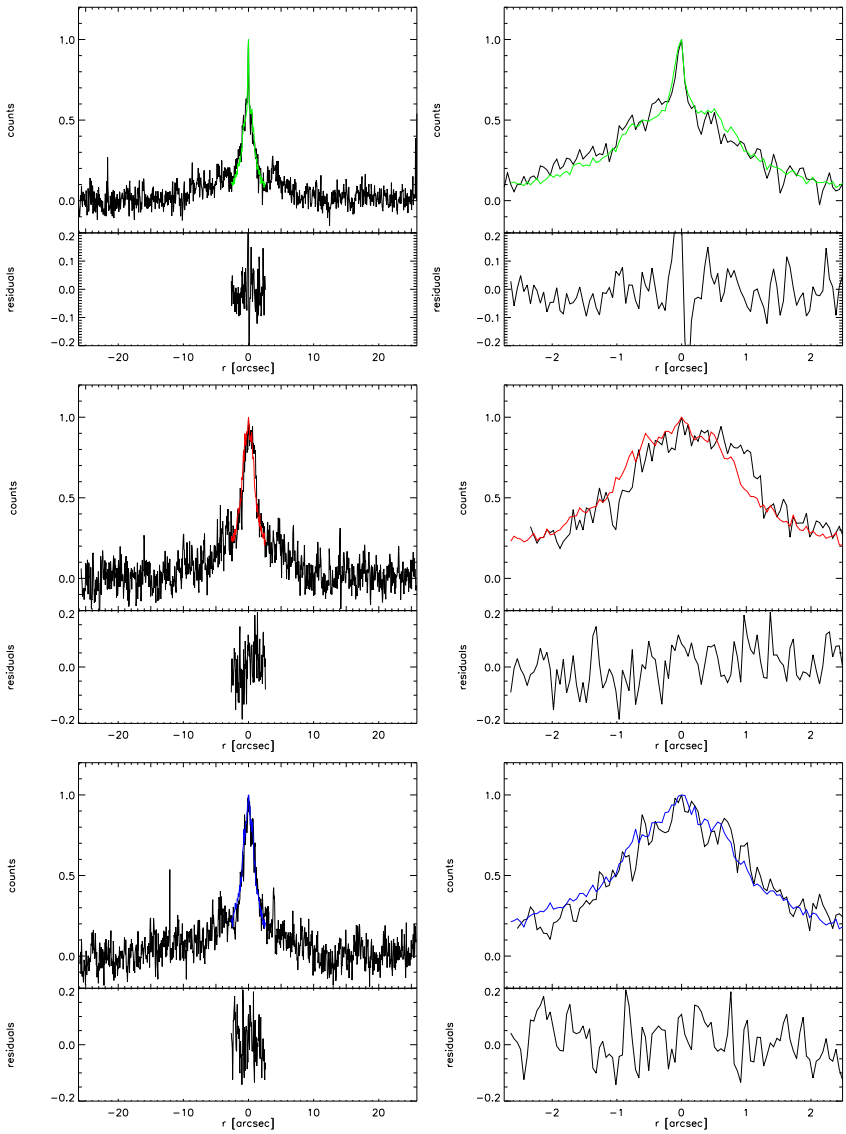

Figure 4.10: Surface-brightness profile of the *STIS*/G750M spectrum (black line) nominally obtained crossing the nucleus of the galaxy (top panels), and at −0.1 (central panels) and 0.1 (bottom panels) arcsec from the galaxy centre, compared with the best-matching profile extracted from two adjacent columns of the acquisition image. The figure shows the profile extracted from the spectrum (left-hand panels) and the profile in the region corresponding to the field of view of the acquisition image (right-hand panels). Different colours are used to indicate the portion of the acquisition images that corresponds to the central (green), −0.1 (red) and 0.1-arcsec (blue) offset spectra. The residuals are also shown.

Hereafter, we refer as major axis to the slit nominally crossing the nucleus of the galaxy, but placed at -0.076 arcsec from the galaxy centre. It was obtained combining the O5EE03060 and O5EE03070 spectra. Offset 1 refers to the nominal -0.1-arcsec slit position, but placed at -0.178 arcsec from the galaxy centre and obtained combining the O5EE03030 and O5EE03040 spectra. Offset 2 refers to the nominal $+0.1$-arcsec slit position, but placed at $+0.127$ arcsec from the galaxy centre and obtained combining the O5EE03080 and O5EE03090 spectra (Table 4.3).

4.3.4 Measurement of the emission lines

To derive the mass of the SBH, we need to measure the radial profile and kinematics of the nebular emission, so that we can gauge both the depth of the potential well and the concentration of its gaseous tracer. We focused on the emission narrow component from forbidden transitions, disregarding the broad-line emission in our spectra that could be the sign of broad and/or asymmetric emission arising from regions much smaller than our resolution limit.

In the wavelength range of our spectra, this means measuring the width and flux profile of the [N II] $\lambda\lambda 6548, 6583$ emission lines since these are usually brighter than the [S II] $\lambda\lambda 6716, 6731$ emission lines. The [N II] doublet also traces the nuclear kinematics better than Hα, given that this line could be significantly affected by emission from circumnuclear star-forming regions (e.g., Verdoes Kleijn et al. 2000; Coccato et al. 2006). To measure the width and flux profile of the narrow component of the [N II] lines, we fit our spectra with multiple Gaussians to match both the broad and narrow components of all the observed lines, while describing the stellar continuum with a low-order polynomial. The [N II] were constrained to have equal velocity widths. The widths of the [S II] lines were also required to be the same, when present, a necessary constraint due to the lower S/N of these lines in some region of the spectrum. Although the widths of the two [S II] can differ, the effect is small (Filippenko & Halpern 1984; Filippenko & Sargent 1989). The Hα line was let free to follow a different kinematics. The computation was done using the MPFIT algorithm[3] implemented under the Interactive Data Language (IDL[4]) environment (Markwardt 2009). A flux ratio of 1:2.96 was assumed for the [N II] doublet, as dictated by atomic physics (e.g., Osterbrock 1989) and both the [N II] and [S II] doublets were assumed to share a common line centroid and width.

[3]The code is available at http://cow.physics.wisc.edu/∼craigm/idl/idl.html.
[4]Interactive Data Language is distributed by Research System Inc.

We consider the possibility of adding broad components in the central pixels by comparing the reduced χ^2 of the fit. The broad components could originate either as an artifact of attempting to fit Gaussians to non-Gaussian line profiles, or from a physical source such as a broad-line region or a change in the characteristics of the gas as the inner regions of the disk are approached. This procedure allowed us to describe also lines with Voigt profiles which are produced when the spectral line is broadened by two types of mechanisms: the Doppler or terminal broadening and the Lorentzian collisional broadening. The first one is due to the moving atoms that absorb and emit radiations, while the second one by the interactions between the particles. The Voigt profile is then a convolution of the Lorentzian profile and a Gaussian profile:

$$G(x;\sigma) = \frac{\exp -x^2/(e\sigma^2)}{\sigma\sqrt{2}\pi}$$

$$L(x;\gamma) = \frac{\gamma}{\pi(x^2+y^2)}$$

$$V(x:\sigma,\gamma) = \int_{-\,\mathrm{inf}}^{+\,\mathrm{inf}} G(x';\sigma)L(x-x':\gamma)\mathrm{d}x'$$

where x is the frequency for line centre. The presence of such a Voigt profile indicates that collisions in this gas are the main mechanism of the ionisation. It is large and therefore wee see the Lorentzian part of the profile.

The central wavelength, FWHM, and flux of all the observed emission lines were measured by fitting the broad and narrow components with multiple Gaussians, while the stellar continuum was described with a low-order polynomial. The best-fitting Gaussian parameters were derived using a nonlinear least-squares minimisation based on the robust Levenberg- Marquardt method (e.g., Press et al. 1992), given the minimisation of the quantity

$$\chi^2 = \sum_i \frac{(I_{\mathrm{mod}} - I_{\mathrm{obs}})^2}{\delta I_{\mathrm{obs}}^2} \tag{4.4}$$

where I_{mod} is the flux referred to the model, while I_{obs} is referred to the observed quantity, and δI_{obs} is the measurement error. We rescaled the errors to obtain

$$\chi^2_\nu = \frac{\chi^2}{N-M} = 1 \tag{4.5}$$

where N is the number of fitted elements and M the free parameters.

The final flux of the fitted Gaussian is given by

$$F_{\rm line} = \sqrt{2\pi I_{\rm line}\sigma_{tot}} \tag{4.6}$$

where $I_{\rm line}$ is the measured intensity of the line, corresponding to the peak of the Gaussian, and $\sigma_{\rm tot}$ is the total velocity dispersion

$$\sigma_{\rm tot} = \sqrt{\sigma^2_{\rm gas} + \sigma^2_{\rm instr}} \tag{4.7}$$

where $\sigma_{\rm gas}$ represent the velocity dispersion due to the ionised gas and $\sigma_{\rm gas}$ is due to the instrumental width. Thus, in building Gaussian, the procedure takes into account the contribution to the velocity dispersion due to the instrumental width

$$\sigma_{\rm instr} = \frac{\rm FWHM_{\mathit{HST}}[\text{Å}]}{2.35482}\frac{c}{\lambda_0} \tag{4.8}$$

where λ_0 is the central wavelength and $\rm FWHM_{\mathit{HST}}$ is the instrument FWHM.

Figure 4.12 shows the results of the multi-Gaussian fitting of the spectra extracted at the nuclear and offset locations.

The fit is improved by the addition of a broad component, as showed also by Noel-Storr et al. (2003). The major axis spectrum shows a broad-line emission within the inner 0.3 arcsec, that is spatially extended compared to the typical FWHM of the *STIS* PSF (~ 0.075 arcsec). Both the offset spectra show a broad Hα component within few rows, which possibly originates in the same nebular complex that gives rise to the broad-line emission observed along the central slit.

Especially in the external regions, we were not confident with the fit of the [S II] $\lambda\lambda 6716, 6731$ emission lines, thus we preferred to exclude the doublet from the fit.

At larger radii, the intensity of the emission lines dropped off, and we therefore binned adjacent spectral rows until a good signal-to-noise was reached.

Then, the instrumental resolution was subtracted in quadrature from the observed line-width values to obtain the intrinsic gas velocity dispersion. The *STIS* Instrument Handbook provides model line spread functions for point source observations through a sample of supported slits as a function of observing wavelength. Nominally, the instrumental FWHM for CCD first-order modes of the slit 52×0.1 arcsec^2 is 1.5 Å in the range around 7000 Å. Rather than adopting this value, we decided to measure the instrumental FWHM from the arc lamp (i.e., `*wav.fits`) supplied to the observation files. The Hole in the Mirror (HITM) system which contains two Pt-Cr/Ne line lamps was used to obtain wavelength comparison exposures and to illuminate the slit during

target acquisitions in the observing strategy. Light from the HITM lamps is projected through a hole in the second correction mirror (CM2). The external shutter is closed during the HITM lamp exposures.

We recovered 6 lamps from the *HST* archive which have exposure times of 3.9 s and bin of 1 × 1. We reduced and combined the ones taken at the same slit position with the IRAF task OIMCOMBINE, obtaining 3 calibrated lamps. We identified 8 unblended emission lines. Before measuring, we re-binned the lamp in the wavelength direction with the IRAF task BLKAVG to match the properties of the spectra of NGC 383. Then, we measured the FWHM of the emission lines with the IRAF task SPLOT which fits a single Gaussian to the emission line. Figure 4.11 shows the values obtained analysing the lamps before and after the re-bin. For the Gaussian fit we adopted $\mathrm{FWHM_{instr}}$ of 1.03 Å and $\sigma_{\mathrm{instr}} = 20.0$ km s^{-1}. To obtain the intrinsic gas velocity dispersion, the instrumental resolution corresponding to the adopted aperture was subtracted in quadrature from the observed line-width values before modelling.

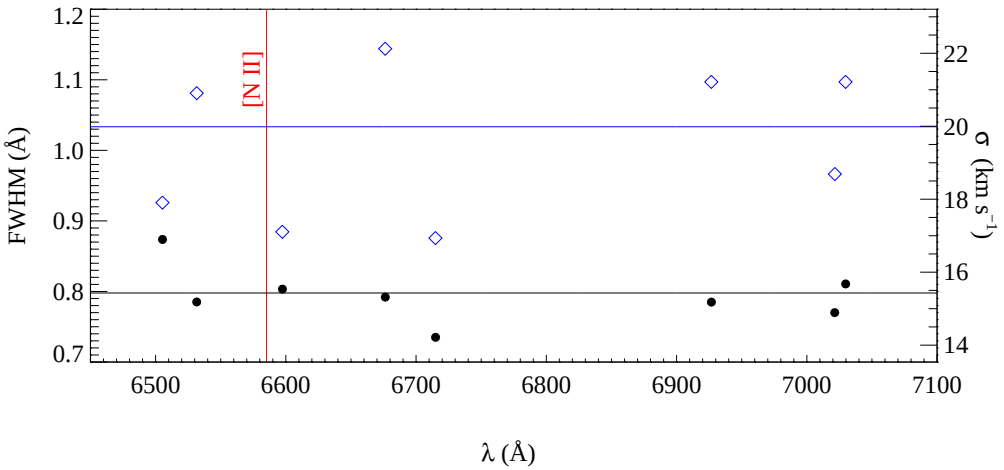

Figure 4.11: Measurement of the instrumental resolution for the adopted *STIS*/G570M set up. The mean FWHM of the emission lines measured in the spectra of the arc lamp before (black circles) and after 2×1 rebinning (diamonds) are shown. The horizontal lines correspond to the instrumental FWHM before (black line) and after re-binning (blue line). The vertical red line corresponds to the rest-frame wavelength of the [N II] λ6583 emission line.

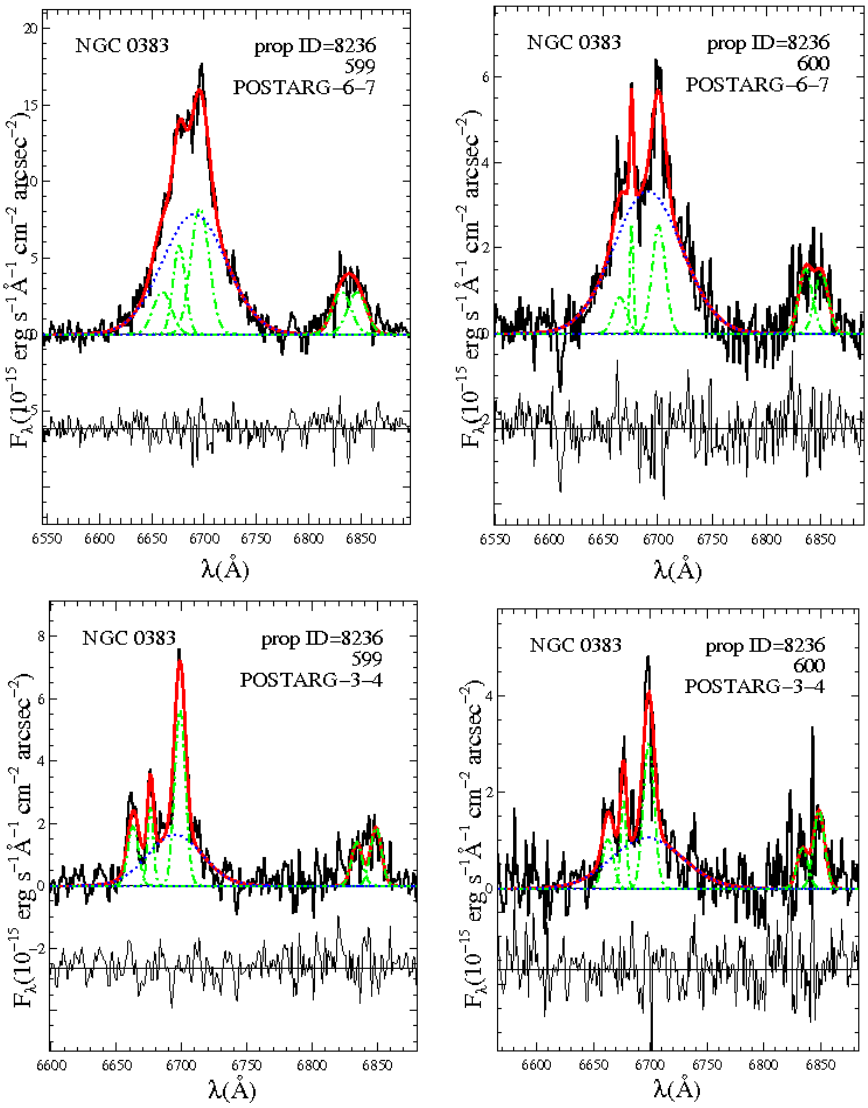

Figure 4.12: Some of continuum-subtracted G750M spectra of NGC 383 illustrating the multi Gaussian fitting procedure of the Hα, [N II] $\lambda\lambda 6548, 6583$, and [S II] $\lambda\lambda 6716, 6731$ emission lines. In each panel, the red solid line shows the overall line blend, whereas the green dashed-dotted lines and blue dashed lines show the adopted narrow and broad Gaussian components, respectively. The fit residuals, which are offset for better visibility are also shown. Each panel shows on the right the proposal ID, row number and the name of the spectrum. POSTARG3-4, POSTARG6-7, and POSTARG8-9 refer to offset 1, central, and offset 2 spectra, respectively.

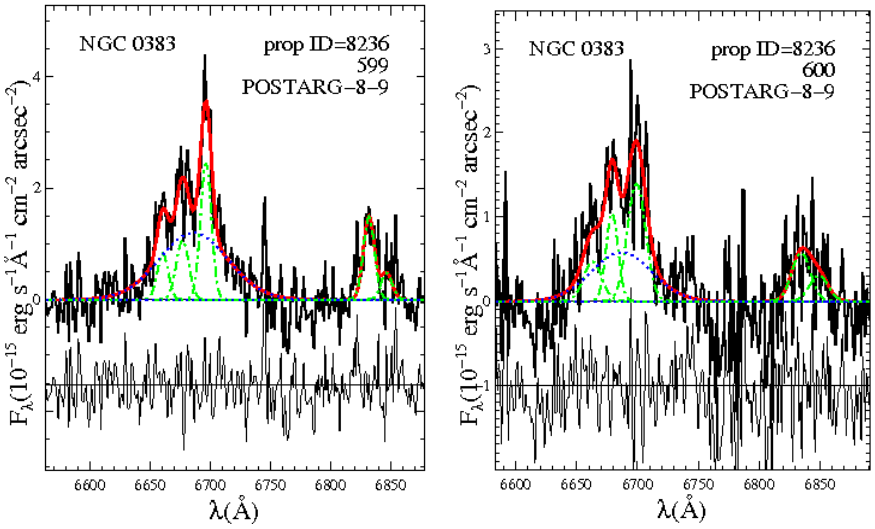

Figure 4.12: Continued.

Furthermore, we decided to adopt the relativistic regime to convert the observed wavelength into line-of-sight velocities. If $\lambda_{\rm obs}$ and λ_0 are the observed and rest-frame wavelength of the emission lines (Table 4.4), respectively, it is

$$\frac{\lambda_{\rm obs}}{\lambda_0} = \sqrt{\frac{1+v/c}{1-v/c}} \tag{4.9}$$

where V is the line-of-sight velocity of the ionised gas. Therefore

$$v[{\rm kms}^{-1}] = {\rm c}\frac{\left(\frac{\lambda_{\rm obs}}{\lambda_0}\right)^2 - 1}{\left(\frac{\lambda_{\rm obs}}{\lambda_0}\right)^2 + 1} \tag{4.10}$$

$$\sigma[{\rm km\cdot s^{-1}}] = {\rm v_1[km\cdot s^{-1}]} - {\rm v_c[km\cdot s^{-1}]} = {\rm c}\left[\frac{\left(\frac{\lambda_{1,\rm obs}}{\lambda_0}\right)^2 - 1}{\left(\frac{\lambda_{1,\rm obs}}{\lambda_0}\right)^2 + 1} - \frac{\left(\frac{\lambda_{\rm c,obs}}{\lambda_0}\right)^2 - 1}{\left(\frac{\lambda_{\rm c,obs}}{\lambda_0}\right)^2 + 1}\right]$$

where $\lambda_{\rm c,obs}$ is the wavelength at the peak of the Gaussian, while $\lambda_{1,\rm obs} = \lambda_{\rm c,obs} + 1\sigma$ is the wavelength at the right end of the Gaussian flux. The difference between non-relativistic and relativistic velocities is of about 40 km s^{-1}.

The final central velocities, central velocity dispersions and fluxes of the

Table 4.4: Properties of the spectral lines in the region of the G750M grism.

Name	Transition	$\lambda_{\rm air}$ [Å]	$\lambda_{\rm vacuum}$ [Å]	Ref
(1)	(2)	(3)	(4)	(5)
[N II]	$^3P_1 - ^1D_2$	6548.05	6549.86	1
Hα		6562.80	6564.51	2
[N II]	$^3P_2 - ^1D_2$	6583.39	6585.21	1
[S II]	$^4S_{3/2} - ^2D_{5/2}$	6716.44	6718.29	1
[S II]	$^4S_{3/2} - ^2D_{5/2}$	6730.81	6732.67	1

NOTES. — Col.(1): Ion responsible for the emission line. Col.(2): Transition configuration terms. Col.(3): Rest-frame air wavelength. Col.(4): Rest-frame vacuum wavelength. Col.(5): Reference: (1) Wallerstein et al. (2001); (2) Reader & Corliss (1998).

ionised-gas component we measured for the [N II] λ6583 emission lines are given in Table 4.5 and shown in Figure 4.14.

Table 4.5:: Measured [N II] λ6583 kinematics of NGC 383.

r [arcsec]	V [km s^{-1}]	σ [km s^{-1}]	F_λ [10^{-15} erg s^{-1} Å^{-1} cm $^{-1}$ arcsec^{-2}]
(1)	(2)	(3)	(4)
		OFFSET 1	
−0.46	4825 ± 45	138 ± 45	4± 5
−0.36	4949 ± 22	143 ± 22	9± 5
−0.25	4932 ± 21	186 ± 21	18± 4
−0.20	4968 ± 11	98 ± 11	13± 3
−0.15	4955 ± 17	183 ± 18	24± 4
−0.10	5023 ± 21	324 ± 24	53± 7
−0.05	5065 ± 9	268 ± 10	90± 6
0.00	5124 ± 8	183 ± 10	58± 6
0.05	5124 ± 17	214 ± 19	36± 7
0.10	5195 ± 36	359 ± 34	30± 5
0.15	5222 ± 65	424 ± 57	20± 5
		MAJOR AXIS	
−0.51	4773 ± 52	187 ± 53	5 ± 8
−0.36	4876 ± 32	189 ± 33	9 ± 8
−0.25	4751 ± 13	95 ± 13	12 ± 3
−0.20	4799 ± 14	169 ± 15	30 ± 5
−0.15	4831 ± 17	233 ± 19	50 ± 8
−0.10	4889 ± 14	238 ± 17	69 ± 11

Table 4.5 – Continued

r [$''$] (1)	V (km s^{-1}) (2)	σ km s^{-1}) (3)	$F_\lambda[10^{-15}]$ (erg s^{-1} Å^{-1} cm $^{-1}$ arcsec^{-2}) (4)
−0.05	4868 ± 17	425 ± 23	183 ± 25
0.00	4999 ± 21	393 ± 24	182 ± 27
0.05	5221 ± 24	275 ± 27	38 ± 8
0.10	5238 ± 22	210 ± 26	25 ± 6
0.15	5255 ± 47	244 ± 48	13 ± 9
0.30	5339 ± 40	87 ± 41	3 ± 7
		OFFSET 2	
−0.36	4832 ± 16	73 ± 16	5 ± 4
−0.20	4792 ± 11	119 ± 11	20 ± 4
−0.25	4754 ± 15	84 ± 16	9 ± 3
−0.15	4822 ± 12	149 ± 13	29 ± 5
−0.10	4895 ± 24	240 ± 22	41 ± 7
−0.05	4951 ± 11	183 ± 12	47 ± 6
−0.00	5025 ± 16	201 ± 20	28 ± 6
0.05	5146 ± 55	335 ± 73	26 ± 17
0.10	5195 ± 29	201 ± 29	16 ± 4
0.15	5152 ± 38	191 ± 38	11 ± 4
0.20	5162 ± 30	105 ± 31	4 ± 4

NOTES. — Col. (1): Galactocentric distance Col. (2): Line-of-sight heliocentric velocity (uncorrected for inclination) Col. (3): Line-of-sight velocity dispersion (corrected for instrumental velocity dispersion) Col. (4): Flux. All the parameters were obtained from the Gaussian narrow component to the [N II] λ6583 emission line.

4.3.5 Ionised-gas kinematics

The presence of a nearly face-on central dust disc with a diameter of about 7 arcsec (corresponding to 2.3 kpc) and an axis ratio b/a =0.77 was recognised by Martel et al. (1999) and Verdoes Kleijn et al. (1999). It shows a spiral symmetric structure with a counterclockwise orientation (Figure 4.7). The dust lanes are more prominent in the South-East side of the galaxy. Noel-Storr et al. (2003, 2007) studied the kinematic and photometric properties of the nucleus of NGC 383, under the assumption that the gas giving rise to the Hα and [N II] $\lambda\lambda$6548, 6583 emission lines shares the same velocity and velocity dispersion. They showed that the gas exhibits a regular rotation profile.

We measured the ionised-gas kinematics only from the narrow component of the [N II] λ6583. The radial profiles of the line-of-sight velocity, velocity dispersion, and flux of the ionised gas along the *STIS* slit positions are shown in Figure 4.14. The measurements extend from −0.56 to 0.35 arcsec along

the major axis spectrum, from -0.46 to 0.10 arcsec in the offset 1 spectrum, and from -0.35 to 0.25 arcsec in the offset 2 spectrum. The velocity curves are regular and symmetric within the errors, as previously suggested by the smoothness and regularity of the ionised-gas discs. This makes this object appealing for dynamical modelling. We found the centre of symmetry of the rotation curve of NGC 383 using the equation

$$v(r) = v_0 + \frac{2}{\pi} v_{\rm c} \arctan \frac{r - r_0}{r_t} \tag{4.11}$$

where $R = (r - r_0)/r_{\rm t}$, v_0 is the velocity centre of rotation, i.e. the systemic velocity, r_0, is the spatial centre of the galaxy, $v_{\rm c}$ is an asymptotic velocity, and $r_{\rm t}$ is a transition radius between the rising and flat part of the rotation curve (Courteau 1997). Figure 4.13 shows the best-fit model we obtained for the rotation curve of the major axis spectrum of NGC 383. The best-fit parameters are $v_0 = 5057.75$ km s^{-1}, $v_{\rm c} = 303.3$ km s^{-1}, $r_0 = 0.01$ arcsec, and $r_{\rm t} = 0.06$ arcsec. Thus, we subtracted v_0 from the velocities we measured by fitting the emission lines of [N II] $\lambda\lambda 6548, 6583$.

The rotation velocity increases very rapidly within the inner 0.1 arcsec, showing a steep gradient and reaching more than 200 km s^{-1}, and flattening right after. The rotation curve flattens further out. The velocity dispersion peaks at about 450 km s^{-1} in the galactic centre. It declines on either side of the galaxy, although not symmetrically. The off-axis kinematics shows a similar pattern, although there are some differences. Along the offset positions, we measured some values of the velocity dispersions far from the one we expected.

The fluxes we measured are in agreement within the error bars with those measured by Noel-Storr et al. (2003) by fitting simultaneously the Hα and the [N II] $\lambda\lambda 6548, 6583$ doublet, while our velocities and velocity dispersion are less spatially extended and systematically smaller than those measured by Noel-Storr et al. (2003). Measuring the kinematics by fitting Hα and [N II] together, as they did, is different than fitting only the [N II], as we did and as claimed by Coccato et al. (2006). In particular, the [N II] flux is much more concentrated towards the centre, while most of the Hα flux appear to come from the circumnuclear regions where Noel-Storr et al. (2003) found low [NII]/Hα ratios, suggesting possible star formation. Thus, the [N II] $\lambda\lambda 6548, 6583$ emission appears to probe better the nuclear regions than Hα.

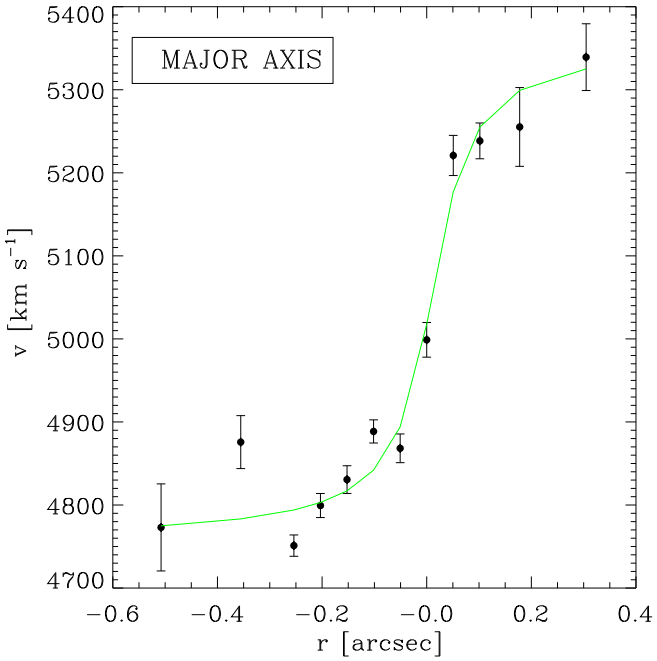

Figure 4.13: Parametric model (solid line) of the major-axis rotation curve (circles) of NGC 383 to derive the systemic velocity $v_0 = 5057.75$ km s^{-1}.

4.4 Imaging: observations, data reduction, and analysis

4.4.1 HST/WFPC2 observations

We retrieved the *WFPC2* images of NGC 383 from the *HST* Science Archive. We selected the images that were observed using the filter F555W (similar to the Johnson V band) and F814W (similar to the Kron-Cousin I band) to correct the effects of dust absorption. The F555W and F814W filters give a good sensitive coverage and their passbands do not overlap. This is an important requirement in order to apply the dust correction. The log of the photometric observations of NGC 383 are shown in Table 4.6.

The nucleus of NGC 383 is located on the Planetary Camera (*PC*) chip which consists of 800 × 800 pixel with a plate scale of 0.0455 arcsec pixel^{-1}, yielding a field of view of about 36 × 36 arcsec^2. The outer region of the galaxy is located on the Wide Field chips (*WF*), three CCDs of 800 × 800 pixel^2 with

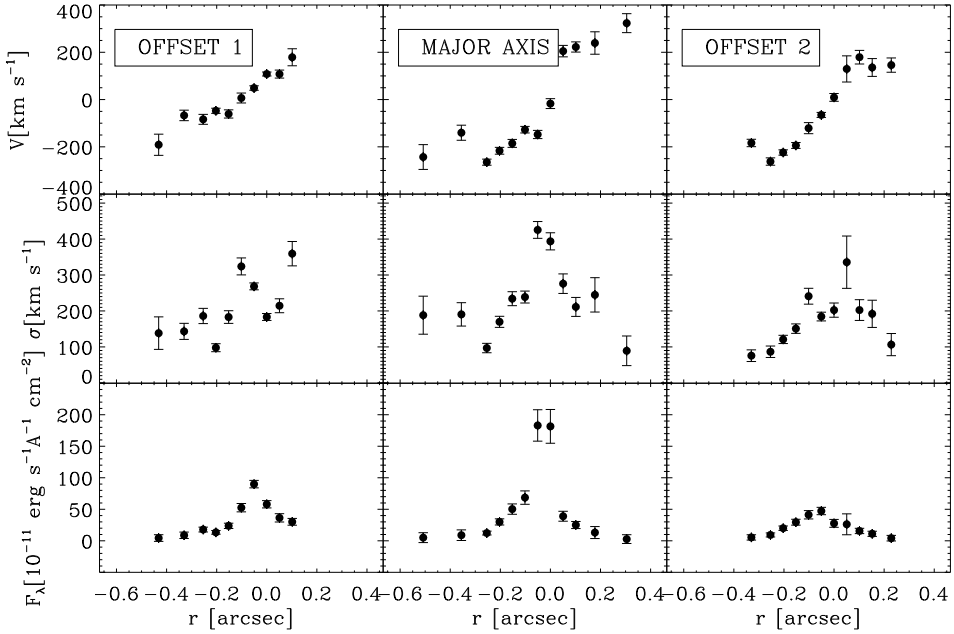

Figure 4.14: [N II] λ6583 kinematics from the spectra obtained in the major axis (central panels), OFFSET 1 (left panels) and OFFSET 2 (right panels). For each slit position the line-of-sight velocity curve (top panel), the radial profile of the line-of-sight velocity dispersion (corrected for instrumental velocity dispersion, (middle panel), and the emission line flux (bottom panel) are given.

a plate scale of 0.0996 arcsec pixel^{-1}, yielding a L-shape field of view of about 150 $\times$150 arcsec^2. The exposure times were 460 s for each filter and they were taken with a gain of 7 e^- DN^{-1} and a read-out noise of 5.24 e^- in *PC* and 5.51, 5.22, 5.19 e^- in the three chips of *WF*.

4.4.2 Data reduction

The images were calibrated using the standard *WFPC2* reduction pipeline CALWFP maintained by the STScI. Reduction steps, including bias subtraction, dark current subtraction and flat-fielding are described in detail in Holtzman et al. (1995) and in the *WFPC2* instrument and data handbooks (Baggett et al. 2002; Heyer et al. 2004). Subsequent reduction was completed using standard tasks in the STSDAS package of IRAF. Bad pixels were corrected by means of a linear one-dimensional interpolation using the data quality files. The two images of the same filter were aligned, corrected for geometric distortion and combined

Table 4.6: Log of the *WFPC2* observations of NGC 383.

Filter	Pivot λ [Å]	FWHM [Å]	Exp. Time [s]	Obs. Date	Gain [e^- DN^{-1}]
(1)	(2)	(3)	(4)	(5)	(6)
			WFPC2		
F555W	5439	1229	2×230	1998 September 23	7
F814W	8012	1539	2×230	1998 September 23	7

NOTES. — Col. (1): Filter name. Col. (2): Pivot wavelength (Heyer et al. 2004). Col. (3): Filter width (Heyer et al. 2004). Col. (4): Exposure time. Col. (5): Observation date. Col. (6): Analog to digital gain.

using MULTIDRIZZLE and TWEAKSHIFT. The alignment of images was obtained by comparing the centroids of stars in the field of view, identifying objects with proper motion not equal to zero in the Naval Observatory Merged Astrometric Datase (NOMAD) catalogue, following the procedure described in Zacharias et al. (2005) and marking other stars using the task STARFIND and GEOMAP. We calculated the local sigma of the image from the combined effect of Poisson and read-out noise. When we combined the images, pixels deviating by more than three times the local sigma were flagged as cosmic rays and were rejected. Other cosmic ray events were removed using the task CRREJ. The cosmic ray removal and bad pixel correction were checked by inspection of the residual images obtained with the cleaned and combined image and the original frames. The sky level (≈ 1 DN pixel^{-1}) was determined from regions free of sources in the *WF* chips and subtracted from the *PC* images after being properly rescaled.

The final calibrated *WFPC2*/F555W and *WFPC2*/F814W images are shown in Figure 4.15.

4.4.3 Isophotal analysis of the surface brightness

Using the IRAF task ELLIPSE (Jedrzejewski 1987), we obtained the isophotal parameters, including coordinates of the isophotal centre, surface brightness profile, ellipticity, major axis position angle, and deviations of the isophotes from pure ellipses. For each semi-major axis length, the best fitting set of parameters are those that minimise the sum of the squares of the residuals between the data and the first two moments of the Fourier series expansion of the azimuthally-sampled surface brightness:

$$I(\phi) = I_0 + \sum_k [A_k \sin(k\phi) + B_k \cos(k\phi)]. \quad (4.12)$$

Figure 4.15: *WFPC2*/F555W (left panel) and *WFPC2*/F814W (central panel) images of NGC 383. The right panel shows F555W-F814W colour obtained from the two filters. The grey-scale used for both filters is kept the same, while the scale for the combination of images is chosen to highlight the distribution of the nuclear dust. All images have been background subtracted. The field of view is 36 × 36 arcsec^2. The orientation is shown on the upper-left corner.

The third and fourth order moments (A_3, B_3, A_4 and B_4) describe deviations of the isophotes shape from pure ellipses.

The isophotal semi-major axis was increased logarithmically, with each isophote being fitted at a semi-major axis 10% longer than that of the isophote preceding it. All parameters were allowed to vary freely while fitting the isophotes. To avoid the contamination by foreground stars and bad pixels, pixels deviating by more than three times the standard deviation of the mean intensity along each trial isophote were excluded from the fit. The resulting properties of the azimuthally-averaged surface brightness, μ, ellipticity, ϵ, position angle, PA, third and fourth cosine Fourier coefficients A_3, A_4, third and fourth sine Fourier coefficients B_3, and B_4 are presented in Figure 4.17 as a function of the geometric mean radius $r_{\rm geo} = a[1-\epsilon(a)]^{1/2}$, where a is the semi-major axis length. The colour profile F555W-F814W is also shown.

We converted the flux $I(\phi)$ from DN s^{-1} to surface brightness in the AB magnitudes system (Oke 1974) using the relation found by Holtzman et al. (1995) for *WFPC2* images

$$\mu_{\rm F555W} = -2.5\ \log I_s(\phi)_{\rm F555W} + {\rm ZPT}_{\rm AB,F555W} + {\rm APT}, \qquad (4.13)$$

$$\mu_{F814W} = -2.5\ \log I_s(\phi)_{\rm F814W} + {\rm ZPT}_{\rm AB,F814W} + {\rm APT}$$

where $I_s(\phi)_{\rm F555W}$ and $I_s(\phi)_{\rm F814W}$ represent the azimuthally averaged, background subtracted intensity, normalised for the exposure time in F555W and

F814W filters, respectively, and $ZPT_{AB,F555W}$ and $ZPT_{AB,F814W}$ represent the zeropoints measured according to the *WFPC2* data handbook (Baggett et al. 2002; Heyer et al. 2004). It is

$$ZPT_{AB,\lambda} = -2.5\log(\mathrm{PHOTFLAM}) - 21.10 - 5\log(\mathrm{PHOTPLAM}) + 18.6921$$

where PHOTFLAM is the inverse sensitivity in units of erg sec^{-1} cm^{-2} Å^{-1}, while PHOTPLAM is the bandpass pivot wavelength in Å. $\mathrm{ZPT_{AB,F555W}} = 22.56$ and $\mathrm{ZPT_{AB,F814W}} = 22.08$, respectively. *APT* is the correction for an infinite aperture.

Because the galaxy completely fills the field of view of the *PC* detector, we subtracted the nominal sky background, as listed in the Instrument Handbooks (Heyer et al. 2004). We adopted $SKY_{\mathrm{F555W}} = 0.010$ e^- s^{-1} pixel^{-1}=0.0014 DN s^{-1} pixel^1; and $SKY_{\mathrm{F555W}} = 0.011$ e^- s^{-1} pixel^{-1}= 0.0016 DN s^{-1} pixel^{-1}.

4.4.4 Correction for dust obscuration

The correction for dust obscuration is necessary to recover the intrinsic stellar luminosity density and the spatial distribution of the ionised gas within the galaxy. To minimise the effects of dust absorption, we need to perform the photometric analysis in passbands which do not overlap and thus cover two different regions of the wavelength spectrum. This is the case of the adopted *WFPC2*/F555W and *WFPC2*/F814W passbands, as shown in Figure 4.16.

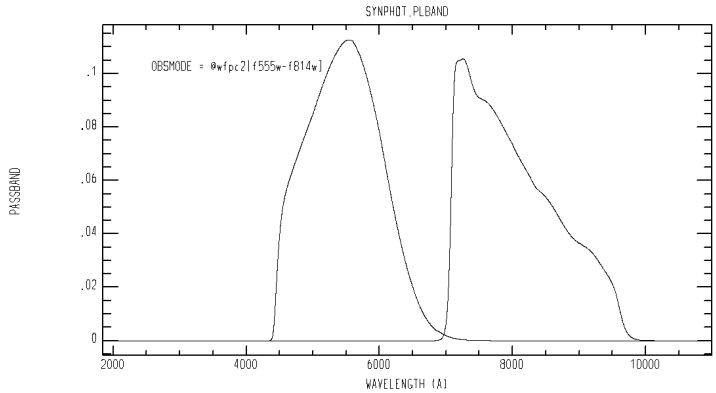

Figure 4.16: Normalised passbands including system response for *WFPC2*/F555W (on the left) and *WFPC2*/F814W (on the right) filters.

We followed the procedure described by Ferrarese et al. (2006a). They as-

sumed that the intrinsic colour of the galaxy (F555W-F814W in our case) in the regions obscured by dust can be estimated by linearly interpolating across the dust area (or extrapolating, if the dust affects the centre) the azimuthally-averaged colour, measured in the regions unaffected by dust. Using the IRAF task ELLIPSE, we derived the mean values of the isophotal parameters straight out of the dust regions. We created an artificial image making a linear interpolation of the colour in the region affected by the dust. Then, we calculated the mean absorption A_λ in the F555W band which is bluer and thereby more affected by the dust. A pixel with coordinates (x, y) is flagged as affected by dust if (1) $A_\lambda(x, y)$ is positive; (2) $A_\lambda(x, y)$ is larger than the local standard deviation in the dust extinction map; and (3) if more than two contiguous pixels are affected by dust. We re-applied ELLIPSE on the corrected-image, assuming that the dust is in front of the galaxy and that the relation between $I_{\rm in}$ and $I_{\rm out}$, the intrinsic and observed luminosity respectively, is

$$I_{\rm out} = I_{\rm in} {\rm e}^{-\tau_\lambda} \tag{4.14}$$

where τ_λ is the optical depth. In units of magnitudes, it is

$$m_{\rm out} = m_{\rm in} + A_\lambda \tag{4.15}$$

and we can obtain

$$\begin{aligned} -2.5 \log \frac{I_{\rm out}}{I_{\rm in}} &= A_\lambda \\ I_{\rm out} &= I_{\rm in} 10^{-0.4 \cdot A_\lambda}. \end{aligned} \tag{4.16}$$

Considering both the filters $F(\lambda_1)$ and $F(\lambda_2)$, it is

$$\begin{aligned} I_{\rm in}(\lambda_1) &= I_{\rm out}(\lambda_1) 10^{0.4 \cdot A_{\lambda_1}}; \\ I_{\rm in}(\lambda_2) &= I_{\rm out}(\lambda_2) 10^{0.4 \cdot A_{\lambda_2}}. \end{aligned} \tag{4.17}$$

Operating as a function of the first filter and defining $q_{ij} = \frac{A_i}{A_j}$ with $i, j = 1, 2$, we obtained

$$q_{12} = \frac{A_{\lambda_1}}{A_{\lambda_2}} \rightarrow A_{\lambda_2} = \frac{A_{\lambda_1}}{q_{12}} \tag{4.18}$$

Thus, the new equations are

$$I_{\rm in}(\lambda_1) = I_{\rm out}(\lambda_1) 10^{0.4 \cdot A_{\lambda_1}}; I_{\rm in}(\lambda_2) = I_{\rm out}(\lambda_1) 10^{0.4 \cdot \frac{A_{\lambda_1}}{q_{12}}}, \tag{4.19}$$

making A_{λ_1} the only unknown parameter

$$A_{\lambda_1} = \frac{2.5}{1 - \frac{1}{q_{12}}} \cdot \log \frac{[I(\lambda_1)/I(\lambda_2)]_{\rm in}}{[I(\lambda_1)/I(\lambda_2)]_{\rm out}} \tag{4.20}$$

$q_{12} = 1.668$ was measured from listed $\frac{A(\lambda_1)}{A(V)}$ by Schlegel et al. (1998).

$$\begin{aligned} \frac{A(\lambda_{F555W})}{A(V)} &= 0.996 \\ \frac{A(\lambda_{F814W})}{A(V)} &= 0.597. \end{aligned} \tag{4.21}$$

In this procedure, it is further assumed that the dust lies in the galaxy foreground (i.e. the so-called "screen" approximation). This makes the quoted values for the dust absorption a lower limit to the true absorption. Once the absorption in a specific passband is known, the intrinsic fluxes are easily recovered simply by correcting the measured fluxes for the derived magnitude loss due to dust obscuration. The extinction-corrected surface brightness profiles of the sample galaxies in the F555W and F814W passbands are shown in Figure 4.17.

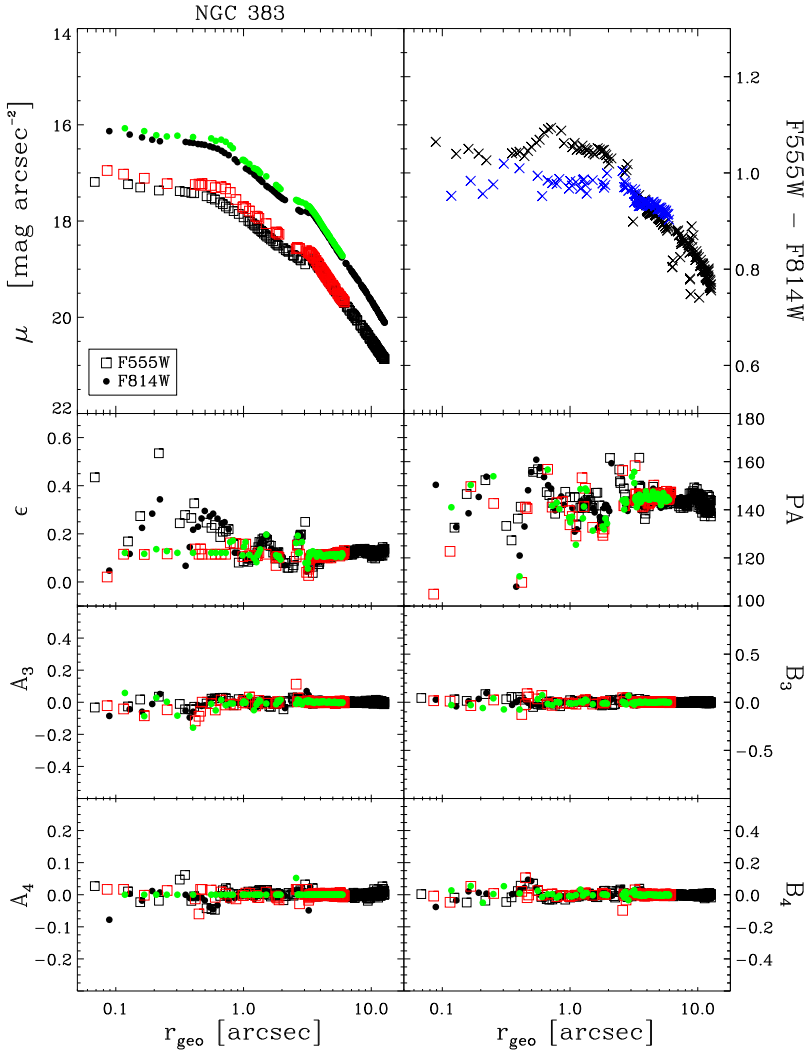

Figure 4.17: Isophotal parameters for NGC 383 plotted against the "geometric mean" radius $r_{\rm geo} = a(1-\epsilon)^{1/2}$, where a is the measured semi-major axis of the galaxy. The panels show the radial profiles of surface brightness μ (in mag arcsec^{-2}) in *WFPC2*/F555W (squares) and *WFPC2*/F814W (filled circles) passbands, F555W−F814W (asterisks) colour, ellipticity ϵ, position angle PA (in degrees, measured from North to East), and parameters A_3, A_4, B_3, and B_4, measuring deviations of the isophotes from pure ellipses (see text for details). Coloured symbols show the inner radial profile of μ and the subsequent colour F555W-F814W measured on the image corrected for dust obscuration (as described in the text) with the addition of the Galactic extinction correction by Schlegel et al. (1998).

Figure 4.18: *WFPC2*/F814W mosaic image of NGC 383. The field of view is 145 × 145 arcsec^2. The orientation is shown in the lower right corner of the mosaic.

4.4.5 Deprojected stellar density without a nuclear star cluster

To derive the contribution of the stellar component to the galaxy gravitational potential we need the deprojected luminosity density. It was recovered from the *WFPC2*/F814W image after correcting for dust obscuration, using the multi-Gaussian expansion (MGE) method (Bendinelli 1991; Monnet et al. 1992; Emsellem et al. 1994), as implemented by Cappellari (2002) [5] under the IDL[6]) environment.

The *WFPC2*/PC image is not enough extended to cover the outer part of the galaxy. Therefore, we combined the other *WFPC2* CCDs (*Wide Field 1, 2*, and *3*) to obtain a mosaic (Figure 4.18).

[5]It is available at http://www-astro.physics.ox.ac.uk/~mxc/idl/.
[6]Interactive Data Language is distributed by Research System Inc.

The intensities and radii obtained on the *WFPC2* mosaic image were then rescaled to match the scale of the *PC* CCD.

Then, we built the image of the instrumental PSF for the *WFPC2*/F814W setup, using the TINYTIM package (Krist & Hook 1999). It was parametrised by MGE as the sum of 4 circular Gaussians (Figure 4.19). The PSF best-fit parameters values were used to convolve the best-fitting MGE model of the galaxy surface brightness. Figure 4.20 shows the surface brightness-profile of the PSF along 7 sectors.

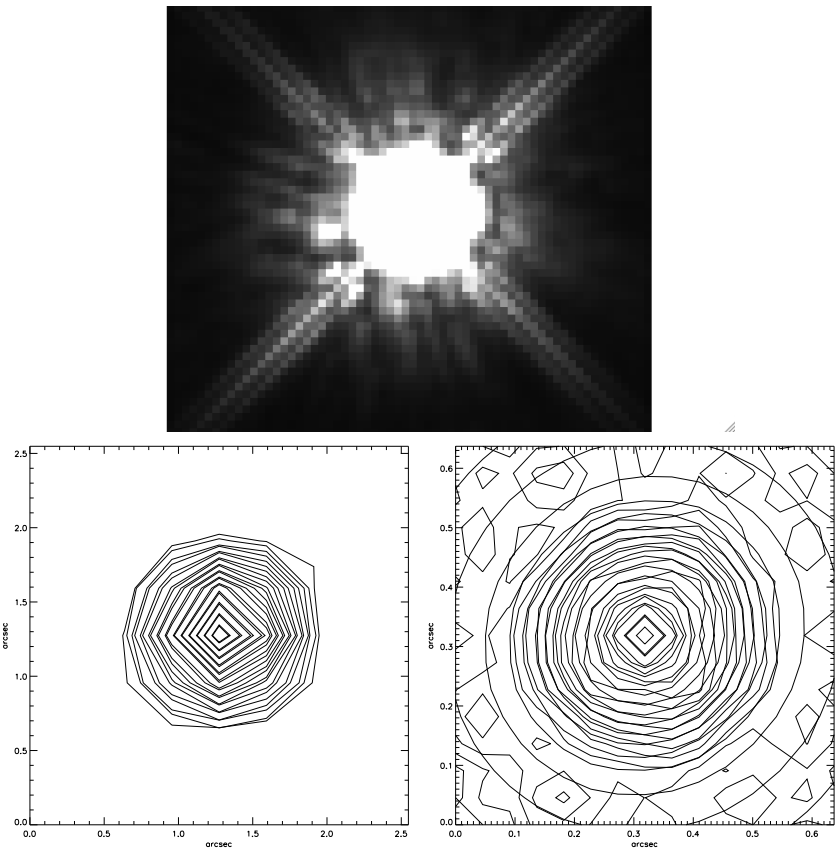

Figure 4.19: Top: *WFPC2*/F814W image of the PSF obtained with TINYTIM. Bottom: Contour plots of the whole (left-hand panel) and zoomed image (right-hand panel) of the PSF with the logarithmically-spaced contours of the MGE best-fitting model of the surface brightness of the PSF.

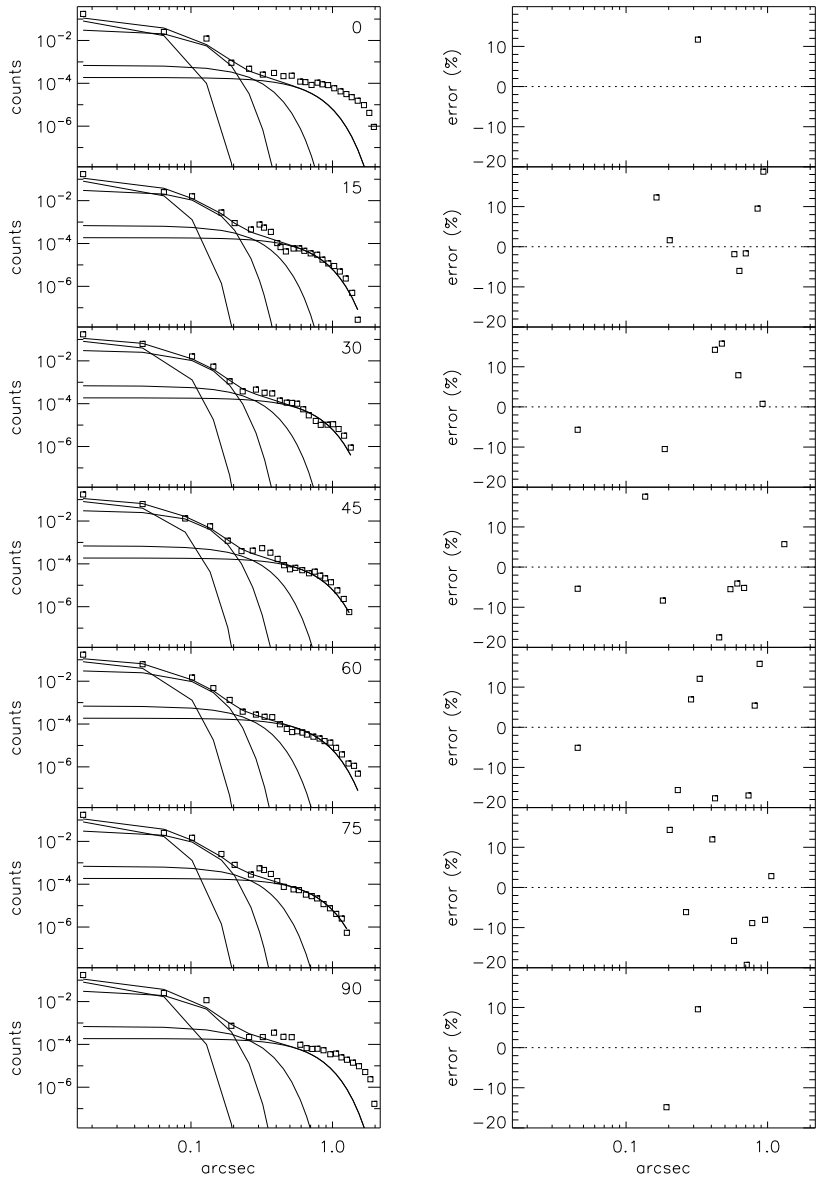

Figure 4.20: Left panels: From top to bottom the model fit of the *WFPC2*/F814W PSF measured along different sectors from the major to the minor axis are shown. Right panels: Percentage errors along the profile for different sectors.

We were able to parametrise the surface-brightness distribution of NGC 383 with MGE using 7 Gaussians (Table 4.7). We converted the MGE parameters (i.e., intensity, σ, and axial ratio of each Gaussian) adopting the *WFPC2* flux zero point and pixel scale used for the photometric calibration and then deprojected. The counts of each Gaussian were first converted into the corresponding peak of surface brightness in counts pixels^{-1}, then into the surface brightness in mag arcsec^{-2} by using the photometric zero-point, and finally into surface density in $L_\odot$ pc^{-2} assuming an I-band absolute magnitude for the Sun of $M_{I,\odot} = 4.08$ (Binney & Merrifield 1998). The luminosity of each Gaussian was calculated as $L = 2\pi I_0 \sigma_{\rm obs}^2 q_{\rm obs}$, where I_0, $\sigma_{\rm obs}$, and $q_{\rm obs}$ are the central intensity, the observed width, and the axial ratio calculated for each Gaussian. To deproject the parameters, we adopted an orientation of $i = 71°$ as found by FIND_GALAXY. Table 4.7 summarises all the parameters we obtained from the MGE analysis. Then, we derived the total I-band luminosity of the galaxy, L_I, by summing the luminosity of all the Gaussian components obtaining $L_I = 4.43 \times 10^{12}$ $L_\odot$. Figure 4.21 and Figure 4.22 show the contour plots of NGC 383 in the *WFPC2*/F814W image with the logarithmically-spaced contours of the intrinsic MGE surface brightness, convolved with the PSF. We tested the results by parametrising the one-dimensional surface brightness of NGC 383 with MPFIT. The findings are in good agreement as shown in Figure 4.23. Figure 4.24 shows the deprojected surface brightness, stellar luminosity density, and circular velocity profiles assuming $(M/L)_*$=1.

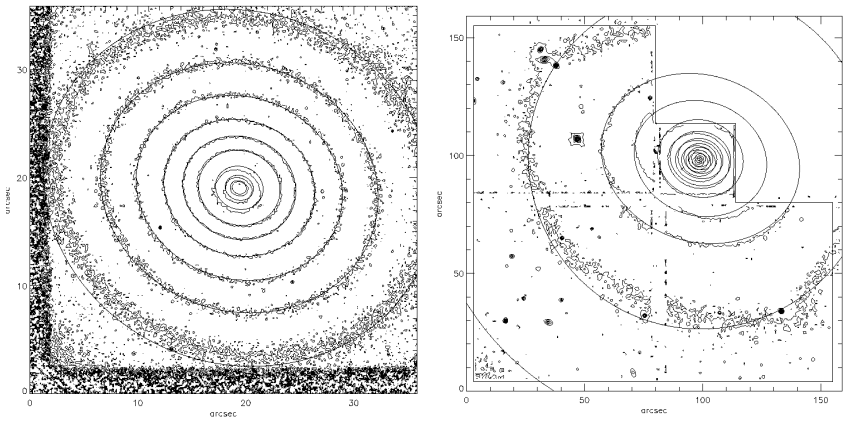

Figure 4.21: Contour plots of the *WFPC2*/F814W *PC* (left-hand panel) and mosaic image (right-hand panel) of NGC 383 with the logarithmically-spaced contours of the MGE best-fitting model of the surface brightness of the galaxy. The orientation is kept the same in the images.

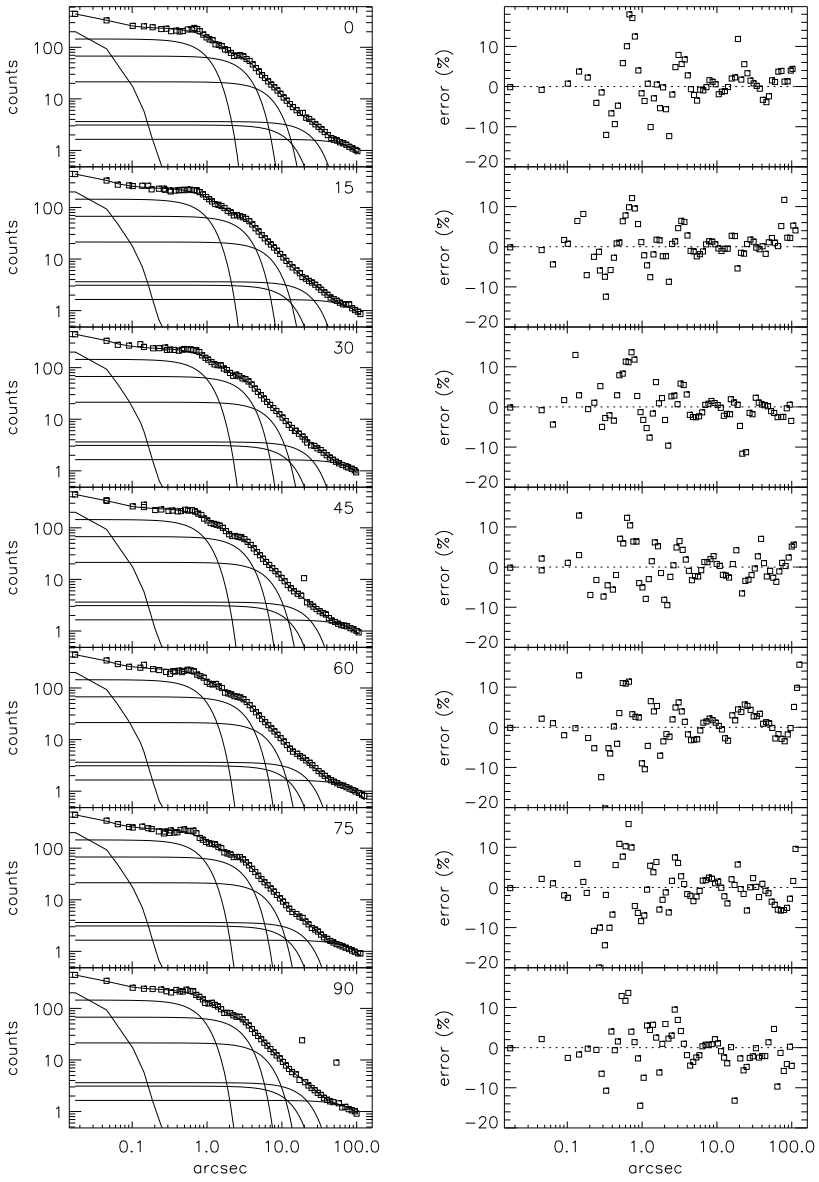

Figure 4.22: Left panels: From top to bottom the model fit of NGC 383 convolved with the *WFPC2*/F814W PSF measured along different sectors from the major to the minor axis are shown. Right panels: Percentage errors along the profile for different sectors.

Table 4.7: Parameters of the surface brightness of NGC 383 obtained from the multi-Gaussian expansion.

Gaussian	$I_{\rm G}$	$\sigma_{\rm G}$		$q_{\rm obs}$	$q_{\rm G}$	$L_{\rm G}$
	$[{\rm L}_{\odot}{\rm pc}^{-2}]$	[arcsec]	[pc]			$[{\rm L}_{\odot,F814W}]$
(1)	(2)	(3)	(4)	(5)	(6)	(7)
1	53028.80	0.019	5.91	0.880	0.865	1.03×10^{7}
2	5864.62	0.776	238.62	0.852	0.833	1.78×10^{9}
3	2672.50	2.638	810.95	0.907	0.896	1.00×10^{10}
4	845.56	5.815	1787.23	0.858	0.839	1.45×10^{10}
5	122.93	10.441	3209.16	1.000	1.000	7.95×10^{09}
6	143.44	21.133	6495.75	0.802	0.776	3.04×10^{10}
7	65.05	95.490	29351.02	1.000	1.000	3.52×10^{11}

NOTES. — Col. (1): Gaussian component. Col. (2): Central intensity of the Gaussian component. Cols. (3)-(4): Width of the Gaussian component in arcsec and in pc. Cols. (5)-(6): Observed and intrinsic axial ratio of the Gaussian component. Col. (7): I-band luminosity of the Gaussian component.

4.4.6 Photometric decomposition with a nuclear star cluster

We performed the two-dimensional photometric decomposition by using the GAlaxy Surface Photometry 2Dimensional Decomposition (GASP2D, Méndez-Abreu et al. 2008), which allows to obtain the structural parameters of the bulge and disc. Since NGC 383 is classified as a lenticular galaxy, we assumed that the surface-brightness distribution was the sum of the contributions of a bulge and a disc component. Each component is characterised by elliptical and concentric isophotes with constant ellipticities and position angles. Let (x, y, z) be Cartesian coordinates with the origin corresponding to the position of the galaxy surface-brightness peak, the x axis parallel to direction of right ascension and pointing westward, the y axis parallel to direction of declination and pointing northward, and the z axis along the line-of-sight and pointing toward the observer. The plane of the sky is confined to the (x, y) plane. Bulge isophotes are ellipses centred on (x_0, y_0), with constant position angle $PA_{\rm b}$ and constant axial ratio $q_{\rm b}$. We adopted the Sérsic law (Sérsic 1968) to describe the surface brightness of the bulge component

$$I_{\rm b}(x,y) = I_{\rm e} 10^{-b_n\left[\left(\frac{r}{r_{\rm e}}\right)^{\frac{1}{n}}-1\right]} \tag{4.22}$$

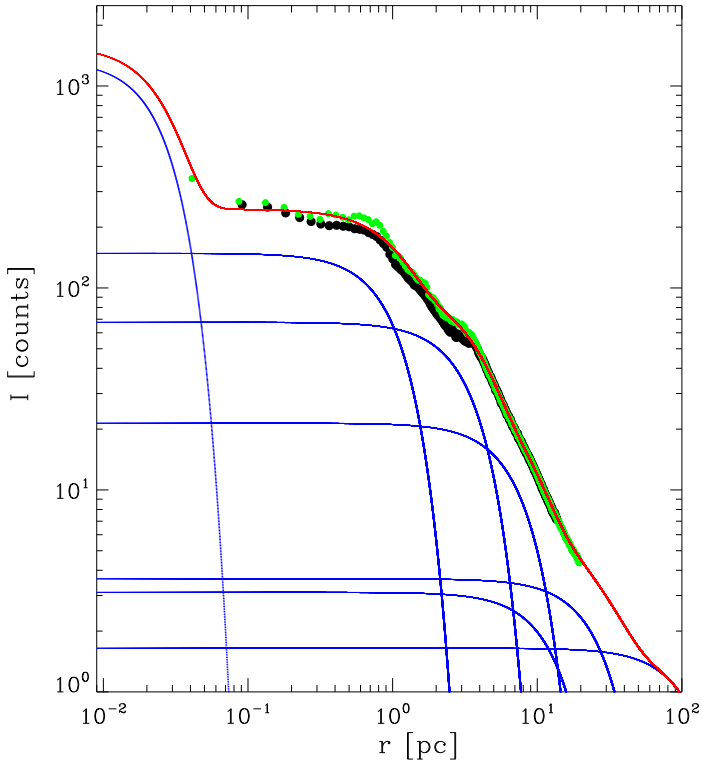

Figure 4.23: Surface brightness profiles of NGC 383 before (black points) and after (green points) the correction for dust absorption. The blue lines represent the 7 best-fitting Gaussians used to parametrise the surface brightness distribution of NGC 383. The red line shows the sum of the Gaussians.

where $r_{\rm e}$, $I_{\rm e}$, and n are respectively the effective radius, surface brightness at $r_{\rm e}$, and the shape parameter describing the curvature of the profile. The value of b_n is coupled to n so that half of the total flux is always within $r_{\rm e}$ and can be approximated as $b_{\rm n} = 0.868n{-}0.142$ (Caon et al. 1993).

Disc isophotes are ellipses centred on (x_0, y_0), with constant position angle $PA_{\rm d}$ and constant axial ratio $q_{\rm d}$, implying that the galaxy inclination is $i = \arccos q_{\rm d}$.

For the surface brightness distribution of the disc component we assumed

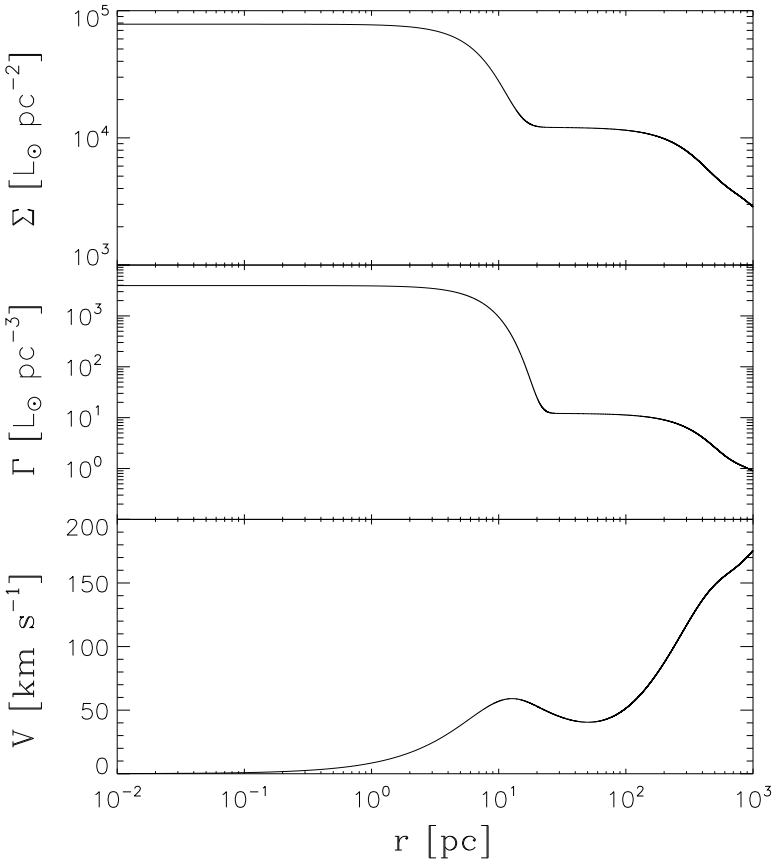

Figure 4.24: Deprojection steps for the stellar mass profile of NGC 383. Top panel: Multi-Gaussian fit to the PSF-deconvolved surface brightness profile derived from the extinction-corrected *WFPC2*/F814W image. Middle panel: Deprojected stellar luminosity density profile. Bottom panel: Circular velocity curve assuming $(M/L)_*= 1$.

the exponential law (Freeman 1970)

$$I_{\rm d}(x,y) = I_0 \exp -\frac{r}{h} \tag{4.23}$$

where h and I_0 are the scalelength and central surface brightness of the disc, respectively and h is the radius where the surface brightness is a factor of 1/e with respect to I_0. NSC isophotes are circles centred on (x_0, y_0). We adopted

the King law (King 1962) to describe the surface brightness of the NSC.

$$I_{\rm k} = I_{0,\rm k}\left[\frac{1}{\sqrt{1+\left(\frac{r_{\rm k}}{r_{\rm c}}\right)^2}} - \frac{1}{\sqrt{1+\left(\frac{r_{\rm t}}{r_{\rm c}}\right)^2}}\right] \tag{4.24}$$

where $I_{0,\rm k}$ is the central surface brightness, $r_{\rm c}$ is the core radius where the surface brightness is half of the central value, and $r_{\rm t}$ is the tidal radius after which the surface brightness drops to zero. The radius $r_{\rm k}$ is given by

$$r_{\rm k} = [(x-x_0)^2 + (y-y_0)^2]^{\frac{1}{2}}. \tag{4.25}$$

Previous choices for parametrising the NSC surface brightness include the exponential (Binggeli & Cameron 1993; Stiavelli et al. 2001), Nuker (Rest et al. 2001; Ravindranath et al. 2001; Lauer et al. 2005), and Sérsic law profiles (Durrell 1997; Stiavelli et al. 2001). Our decision to parametrise the NSC of NGC 383 with King model is motivated by high-resolution observations of the nuclei of nearby galaxies. King models are found to provide accurate representations of the central components (Butler & Martínez-Delgado 2005; Monaco et al. 2005) in nucleated Local Group galaxies such as NGC 205 and Sagittarius, or in the sample of Côté et al. (2006)

To derive the photometric parameters of the bulge ($I_{\rm e}$, $r_{\rm e}$, n, $PA_{\rm b}$, $q_{\rm b}$), disc (I_0, h, $PA_{\rm d}$, $q_{\rm d}$), and NSC (I_0,$r_{\rm c}$, $r_{\rm t}$), and the position of the galaxy centre (x_0, y_0), we fitted iteratively a model of the surface brightness $I(x,y) = I_{\rm b}(x,y)+I_{\rm d}(x,y)+I_{\rm k}(x,y)$ to the pixels of the galaxy mosaic using a non-linear least-squares minimisation based on the robust Levenberg-Marquardt method by Press et al. (1992). The actual computation has been done using the MPFIT algorithm (Markwardt 2009) under the IDL environment (Figure 4.25). Each image pixel has been weighted according to the variance of its total observed photon counts due to the contribution of both the galaxy and sky, and determined assuming photon noise limitation and taking into account the detector read-out noise. The seeing effects were taken into account by convolving the model image with a circular Gaussian PSF with the FWHM measured from the field stars in the galaxy image. The convolution was performed as a product in Fourier domain before the least-squares minimisation. We first assess all the galaxy parameters from the analysis of our image and with the calibration constant present as a keyword in the header of the image.

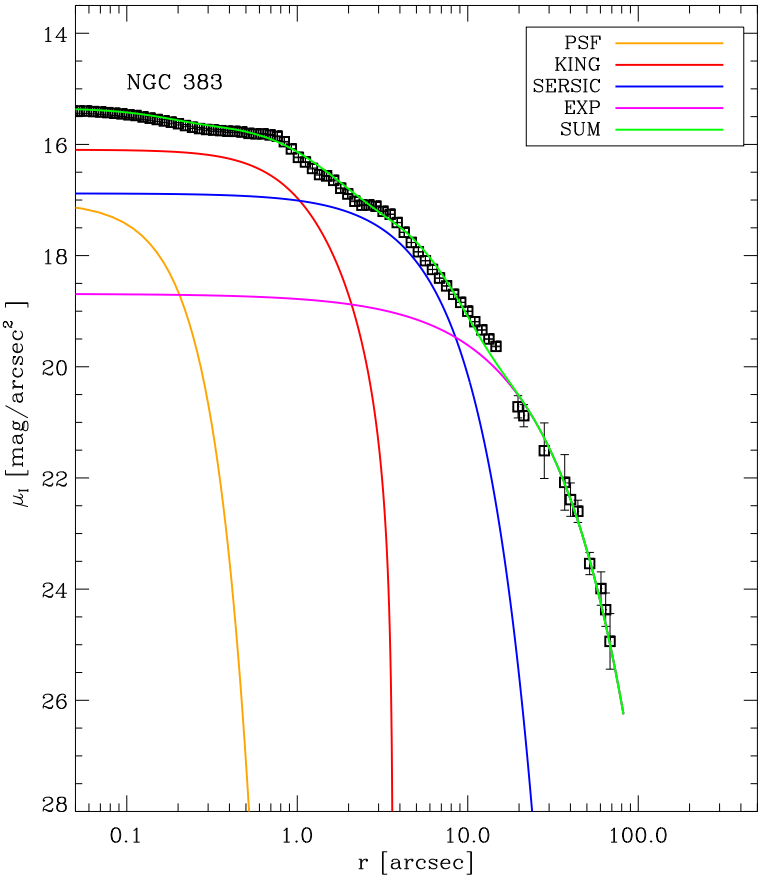

Figure 4.25: One-dimensional photometric decomposition of NGC 383 obtained by adopting the *WFPC2*/F814W PSF (yellow line), a King profile for the NSC (red line), a Sérsic bulge (blue line), and an exponential disc (magenta line). The green line shows the total surface brightness obtained summing all the contributions.

The guesses for the free parameters were derived by parametric fit of the elliptically-averaged surface brightness radial profile, ellipticity and position angle of the galaxy (I_e, r_e, n, I_0, h, $I_{0,k}$, r_c, r_t), and by the analysis of the ellipticity, by interpolating the one dimensional surface-brightness distribution of NGC 383 with the MPFIT routine.

The fit is improved by the addition of a nuclear component, namely a PSF

following a Moffat law (Moffat 1969)

$$I_{\rm PSF} = I_{0,\rm PSF}(1 + \frac{r}{\alpha}^2)^{-\beta} \tag{4.26}$$

where α and β are seeing dependent parameters, linked with $\alpha = \frac{\rm FWHM}{(2\cdot\sqrt{2^{(1/\beta)}-1})}$. Figure 4.26 shows the best-fitting model of the surface-brightness distribution of NGC 383 as results from GASP2D.

Then, by using the best-fitting parameters, we built the two-dimensional images of:

- the NSC (from the King profile, Figure 4.27a)
- the galaxy without the contribution of the NSC (Figure 4.27b).

4.4.7 Deprojected stellar density with a NSC

The deprojected luminosity density of the NSC was recovered using the MGE method on the image of the NSC built after the two-dimensional photometric decomposition of NGC 383 as shown in Figure 4.28 and 4.29. The surface brightness of the NSC is well described by 3 Gaussians. We also recovered the deprojected luminosity density of the galaxy excluding the contribution of the NSC, as shown in Figure 4.28 and in Figure 4.30. The surface brightness of the galaxy without the contribution of the NSC is well described by 7 circular Gaussians. We noticed that for radii larger than the tidal radius of the NSC, the surface brightness of the model galaxy is very similar to the observed one. Figure 4.31 shows the deprojected surface brightness, stellar luminosity density, and circular velocity profiles (assuming $(M/L)_*$=1) for the stellar mass profile of the NSC of NGC 383 and of the galaxy without the NSC. The comparison between the deprojected stellar mass profile of NGC 383 and the model of the total galaxy obtained as a sum of the NSC and the galaxy model without the NSC is also shown with the corresponding residuals.

Table 4.8 lists all the parameters we obtained from the MGE photometric analysis of the galaxy components.

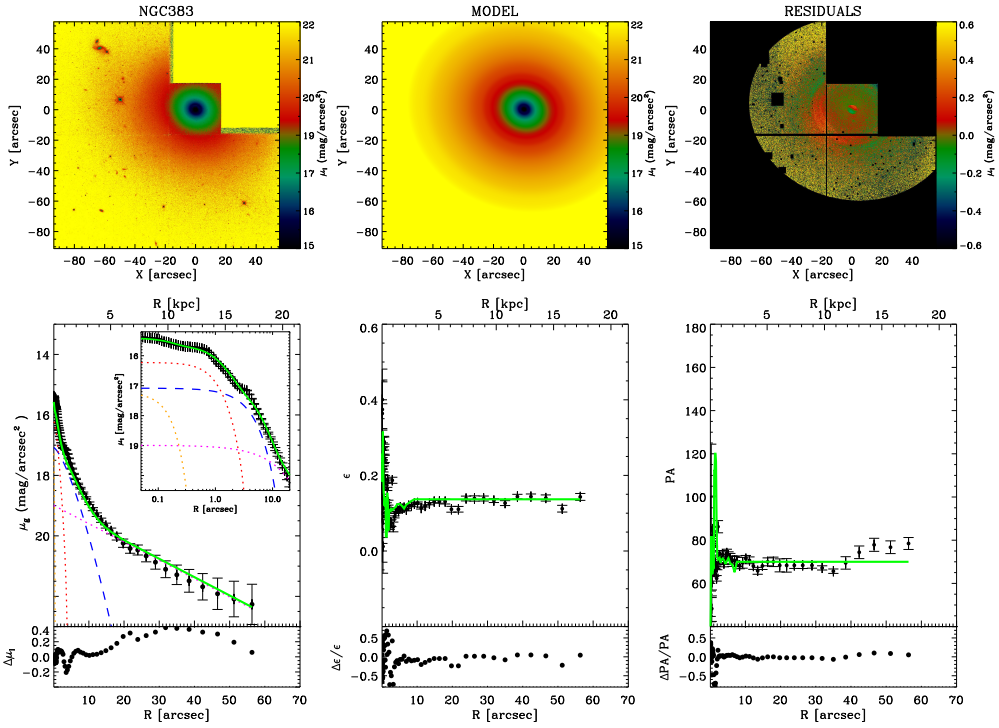

Figure 4.26: Two-dimensional photometric decomposition of NGC 383. Upper panels (from left to right): Map of the observed, modelled, and residual (observed-modelled) surface-brightness distribution of the galaxy. The surface-brightness range of each image is indicated at the right of the panel. In each panel the spatial coordinates with respect to the galaxy centre are given in arcsec. Lower panels (from left to right): Ellipse-averaged radial profile of surface-brightness, position angle, and ellipticity measured in the observed (points with error-bars) and modelled image (green line). The blue dashed and the magenta dotted lines represent the intrinsic surface-brightness contribution of the bulge and disc, respectively. The red and yellow dotted lines represent the intrinsic surface-brightness contribution of the NSC and PSF, respectively. The difference between the ellipse-averaged radial profiles extracted from the observed and modelled images is also shown.

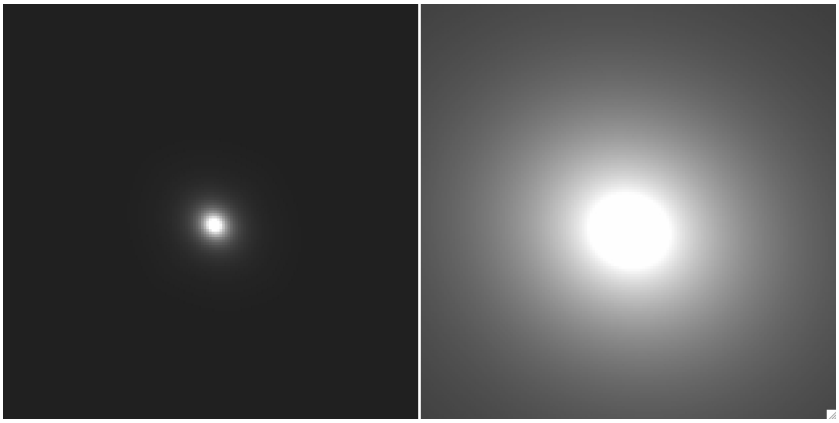

Figure 4.27: Images of the NSC of NGC 383 without the galaxy (left-hand panel) and of the modelled galaxy without the NSC (right-hand panel). The fields of view are 7 $\times$ 7 arcsec^2. The gray-scales and orientation are kept the same.

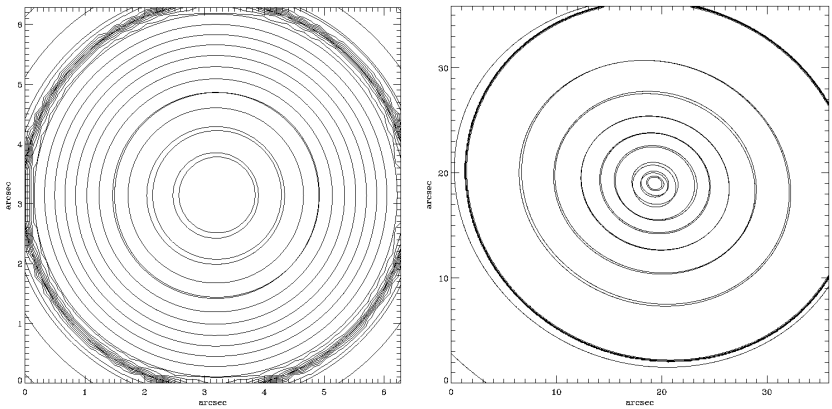

Figure 4.28: Contour plots of the images of the NSC of NGC 383 (left panel) and of the galaxy excluding the contribution of the NSC (right-hand panel) with the logarithmically-spaced contours of the MGE best-fitting models of the surface brightness. Orientation is kept the same in the two images.

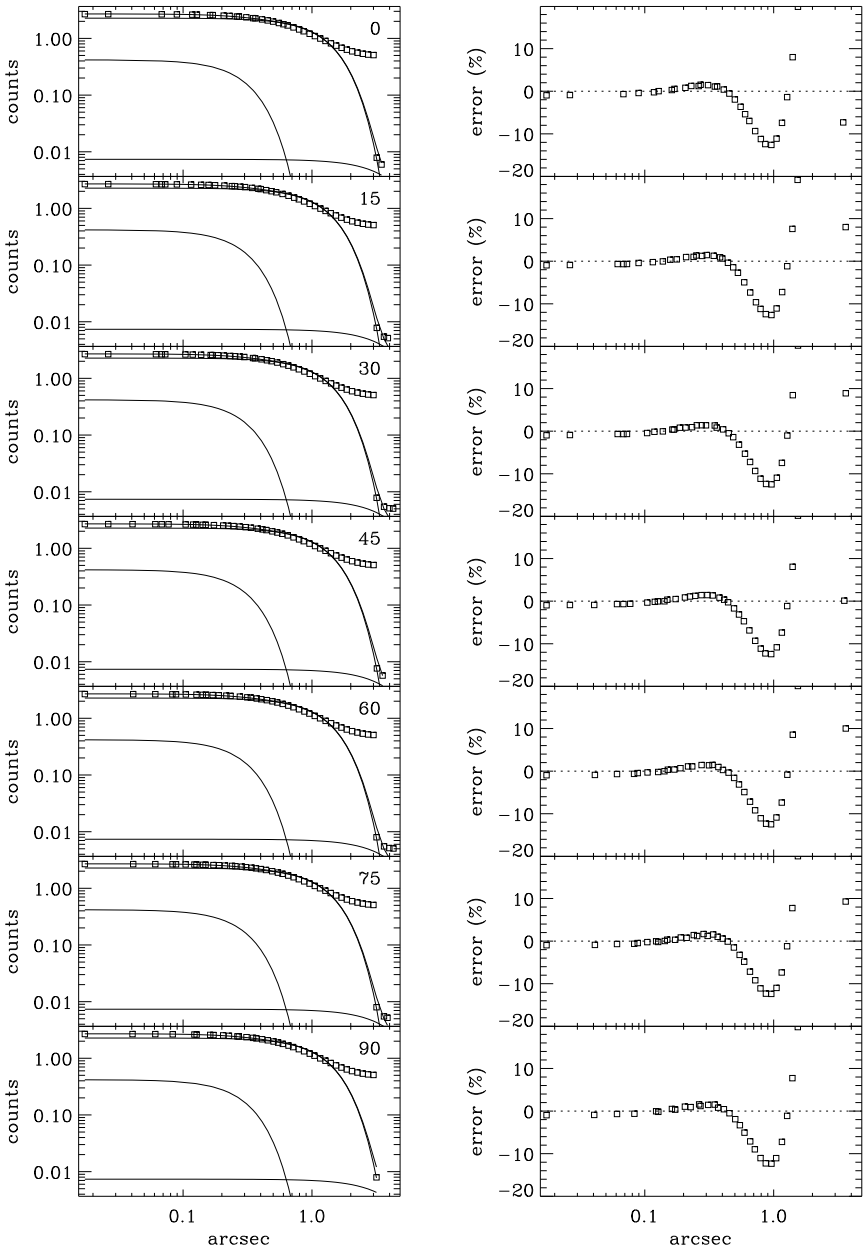

Figure 4.29: Left panels: From top to bottom the fits of the model NSC of NGC 383 measured along different sectors from the major to the minor axis are shown. Right panels: Percentage errors along the profile for different sectors.

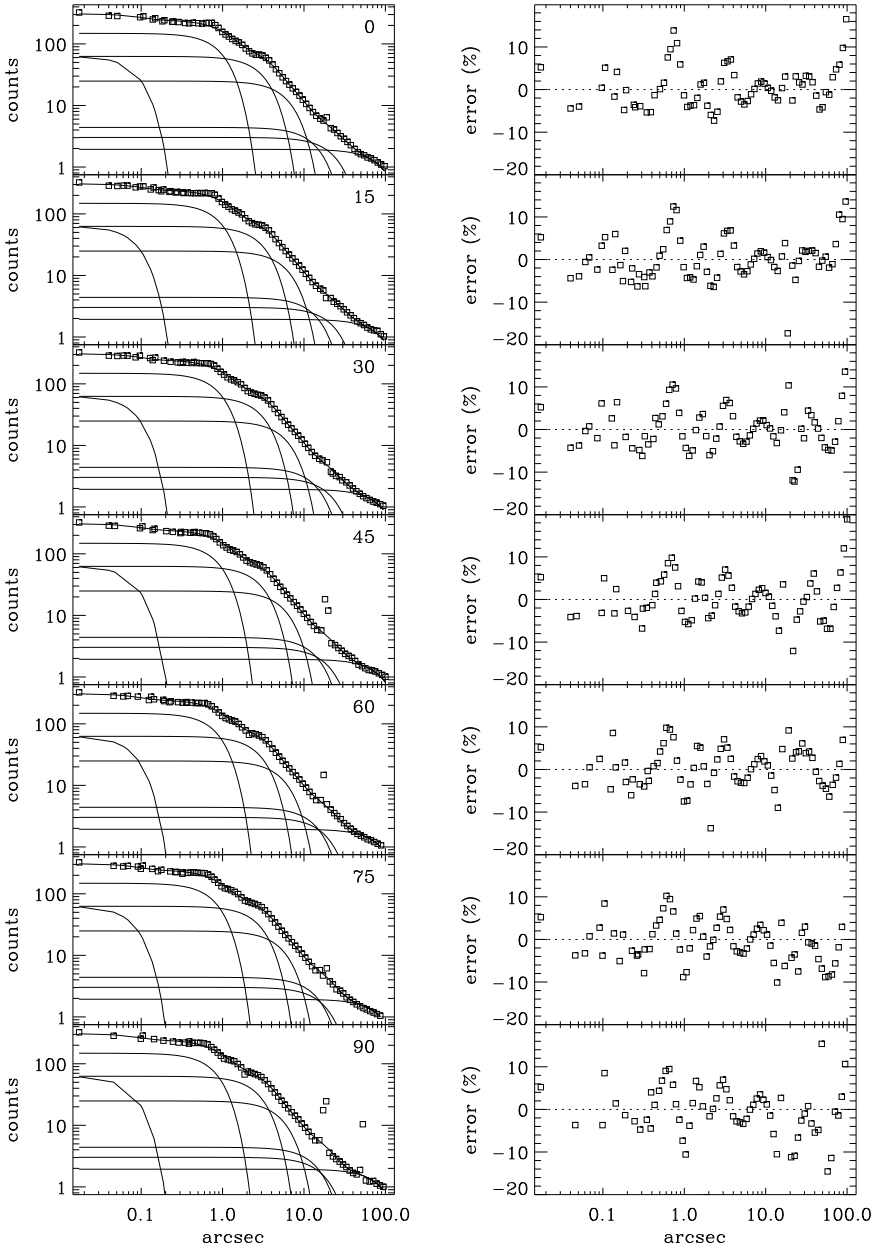

Figure 4.30: Left panels: From the top to the bottom are shown the model fit of the model galaxy without the NSC measured along different sectors from the major to the minor axis. Right panels: Percentage errors along the profile for different sectors.

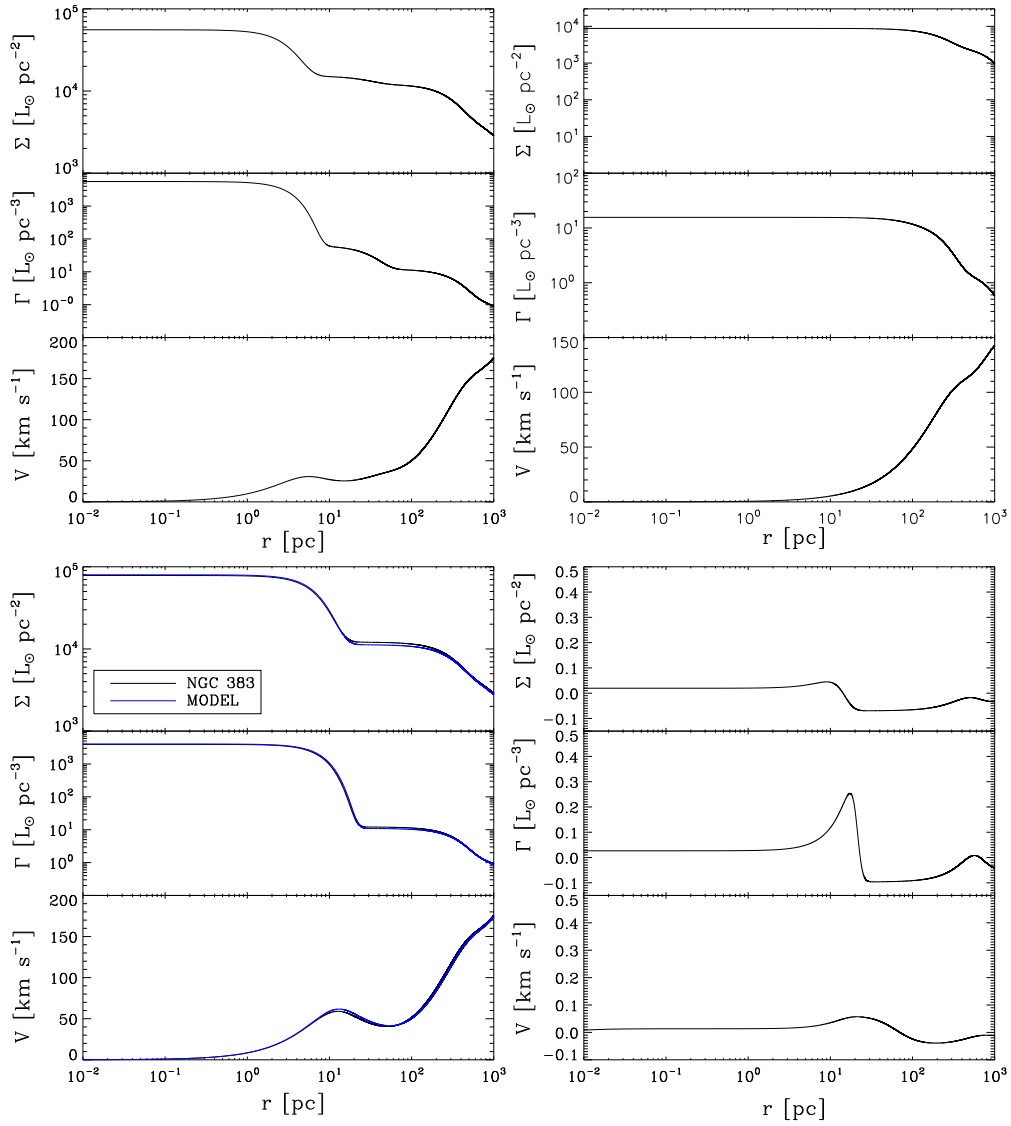

Figure 4.31: Top panel: Deprojection steps for the stellar mass profile of the NSC of NGC 383 (left-hand panel) and of the galaxy without the NSC (right-hand panel). From top to bottom: multi-Gaussian fit to the surface brightness profile derived from the images of the models; deprojected stellar luminosity density profile, and circular velocity curve assuming $(M/L)_*$= 1. Bottom panel: Comparison between the deprojected stellar mass profile of NGC 383 (black line) and the model of the total galaxy (blue line) obtained as a sum of the NSC and the galaxy model without the NSC. The corresponding residuals are shown in the right-hand panel.

Table 4.8: Parameters of the surface brightness of the NSC of NGC 383 obtained from the multi-Gaussian expansion.

Gaussian	$I_{\rm G}$	$\sigma_{\rm G}$		$q_{\rm obs}$	$q_{\rm G}$	$L_{\rm G}$
	$[{\rm L}_\odot {\rm pc}^{-2}]$	[arcsec]	[pc]			$[{\rm L}_{\odot,F814W}]$
(1)	(2)	(3)	(4)	(5)	(6)	(7)
			NSC			
16.56	0.222	68.36	1.000	1.000	0.0975	4.86×10^6
89.91	0.940	89.00	0.999	0.999	0.1241	$4.71.\times 10^7$
0.29	3.060	40.47	1.000	1.000	0.0001	1.61×10^5
		GALAXY	WITHOUT	NSC		
53095.06	0.020	6.20	1.000	1.000	3413.978	$1.28. \times 10^8$
5410.67	0.796	244.78	0.868	0.851	8.991	1.77×10^9
2511.76	2.549	783.54	0.918	0.908	1.293	8.89×10^9
974.68	5.249	1613.44	0.848	0.829	0.247	1.35×10^{10}
190.46	11.158	3429.50	1.000	1.000	0.022	1.41×10^{10}
122.44	22.018	6767.66	0.781	0.752	0.007	2.75×10^{10}
65.023	95.490	29351.03	1.000	1.000	0.0001	3.5×10^{11}

NOTES. — Col. (1): Gaussian component. Col. (2): central intensity of the Gaussian component. Cols. (3)-(4): Width of the Gaussian component in arcsec and in pc. Cols. (5)-(6): Observed and intrinsic axial ratio of the Gaussian component. Col. (7): I-band luminosity of the Gaussian component.

4.5 Dynamical modelling

4.5.1 Ionised-gas dynamics

To model the ionised-gas kinematics we used the method described in Coccato et al. (2006) and Dalla Bontà et al. (2009). We generated a synthetic velocity field assuming that the ionised gas is moving in circular orbits in an infinitesimally thin disc centred at the nuclear location, under the combined gravitational potential of the stars and SBH. The model is projected onto the plane of the sky for a given inclination of the gaseous disc, and then degraded to simulate the actual setup of the spectroscopic observations. The latter step includes accounting for width and location of each slit, *STIS*/PSF, and charge bleeding between adjacent CCD pixels. The free parameters of the model are the mass $M_\bullet$ of the SBH, the inclination i of the disc, and the mass-to-light ratio $(M/L)_*$ of the stellar component.

The mass of the SBH is determined by finding the model parameters that produce the best match to the observed velocity curve. This modelling technique is similar to that adopted by Barth et al. (2001) and Marconi & Hunt (2003) to analyse *STIS* spectra obtained along parallel positions across the nuclei of NGC 3245 and NGC 4041, respectively.

Let (r, ϕ, z) be cylindrical coordinates and consider the gaseous disc in the (r, ϕ) plane with its centre in the origin. In the case of a spherical mass distribution, the gas circular velocity $v_{\rm c}$ at a given radius r is

$$v_{\rm c}(r) = \left[\frac{GM(r)}{r}\right]^{\frac{1}{2}} = \left[\left(\frac{M}{L}\right)_{*} v_{*}^{2}(r) + \frac{GM_{\bullet}}{r}\right]^{\frac{1}{2}} \tag{4.27}$$

where M is the total mass enclosed by the circular orbit of radius r, $(M/L)_{*}$ is the (constant) mass-to-light ratio of the stellar component (and dark matter halo) and v_{*} is the circular velocity of radius r for a stellar component with $(M/L)_{*} = 1$. The radial profile of v_{*} is derived from the observed surface-brightness distribution in Section 4.4.5. The velocity dispersion of the gaseous disc is assumed to be isotropic with a Gaussian radial profile

$$\sigma(r) = \sigma_0 + \sigma_1 \exp\left(\frac{-r^2}{2r_{\sigma}^2}\right). \tag{4.28}$$

Then we assume that the flux of the gaseous disc has an exponential radial profile

$$F(r) = F_0 + F_1 \exp\left(\frac{-r}{F_{\rm r}}\right). \tag{4.29}$$

To project the velocity field of the gaseous disc on the sky plane, we considered (x, y, z) be Cartesian coordinates with the origin in the centre of the gas disc, y-axis aligned along the apparent major axis of the galaxy, and z-axis along the line of sight directed towards the observer. The sky plane is confined to the (x, y) plane. If the gaseous disc has an inclination angle i (with $i = 0^{\circ}$ corresponding to the face-on case), at a given sky point with coordinates (x, y), the observed gas velocity $v(x, y)$ is

$$v(x, y) = v_{\rm c}(x, y) \sin i \cos \phi \tag{4.30}$$

where

$$\begin{aligned} y &= r\cos\phi, \\ r &= \left(\frac{x^2}{\cos^2 i} + y^2\right)^{\frac{1}{2}}. \end{aligned} \tag{4.31}$$

We assumed that the velocity distribution of the gas at position (x, y) is a Gaussian with mean $v(x, y)$, dispersion $\sigma(x, y)$ and area $F(x, y)$. Then, we took into account the slit orientation. Let (ξ, η, ζ) be Cartesian coordinates with the origin in the *STIS* focal plane, ξ- axis aligned with the direction of the slit width, η-axis aligned with the direction of the slit length and ζ-axis along the line of sight directed towards the observer and crossing the centre of the gas disc. The *STIS* focal plane corresponds to the (ξ, η) plane. The (x, y) and (ξ, η) coordinate systems are related by the transformation

$$\begin{aligned} x &= \xi\cos\theta - \eta\sin\theta, \\ y &= \xi\sin\theta - \eta\cos\theta, \end{aligned} \tag{4.32}$$

where θ is the angle between the slit direction and the disc major axis. At position (ξ, η), the flux contribution due to gas with a line-of-sight velocity v in the range $[v\ \delta v/2, v + \delta v/2]$ is given by

$$F(v|\xi,\eta) = \int_{v-\delta v/2}^{v+\delta v/2} \frac{F(\xi,\eta)}{\sigma(\xi,\eta)\sqrt{2\pi}} \exp\frac{[v' - v(\xi,\eta)]^2}{2\sigma(\xi,\eta)^2} \mathrm{d}v' \tag{4.33}$$

where δv is the velocity resolution of the model. For a given line-of-sight velocity $\widehat{v}$, $F(\widehat{v})$ is the "monochromatic" image of the gas velocity field observed at $\lambda = \lambda_0(1 + \widehat{v}/c)$ for a rest-frame wavelength λ_0.

The line-of-sight velocity distribution (LOSVD) predicted by the model at position (ξ, η) on the focal plane is

$$S(v|\xi,\eta) = F(v|\xi,\eta) * \mathrm{PSF}(\xi,\eta) \tag{4.34}$$

and takes into account the diffraction of light through the *HST* and *STIS* aperture.

For each position η along the slit, the LOSVD predicted by the model is

given by the contribution of all the points on the focal plane inside the slit

$$S(v|\eta) = \int_{\xi_c - w/2}^{\xi_c + w/2} S[v + v_d M_a(\xi' - \xi_c)|\xi', \eta] d\xi' \tag{4.35}$$

where ξ_c is the ξ position of the slit centre, w is the slit width, v_d is the velocity bin along the wavelength direction in the spectral range of interest and M_a is the anamorphic magnification factor which accounts for the different scale in the wavelength and spatial direction on the focal plane. For *STIS* in the observed spectral range, $v_d = 50.4$ km s^{-1} pixel^{-1}. The velocity offset $v_d M_a(\xi - \xi_c)$ is the shift due to the non-zero width of the slit and its projection on to the *STIS* CCD. It accounts for the fact that the wavelength recorded for a photon depends on the position $(\xi - \xi_c)$ at which the photon enters the slit along the ξ-axis (Barth et al. 2001; Maciejewski & Binney 2001). This effect is sketched in Figure 4.32.

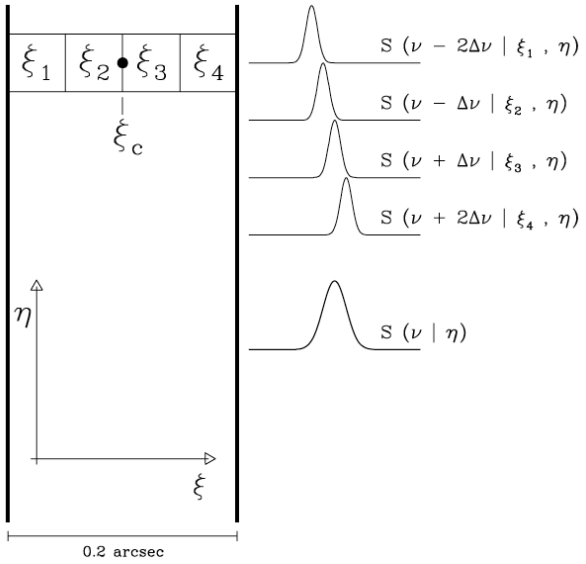

Figure 4.32: Schematic representation of the velocity shift caused by the non-zero width of the slit. The spectra generated along the slit width in pixels of coordinates (ξ_1, η), (ξ_2, η), (ξ_3, η), and (ξ_3, η) are characterised by a velocity offset $\Delta v(\xi_i - \xi_c)$, where $i = 1, 2, 3, 4$ and ξ_c corresponds to the slit centre. The resulting spectrum is $S(v|\eta)$. Figure from Coccato et al. (2006).

The free parameters in our model are the mass $M_\bullet$ of the SBH, the mass-

to-light ratio $(M/L)_*$ of the stellar component (and dark matter halo), the inclination i, the parameters σ_0, σ_1 and r_σ of the Gaussian radial profile of the intrinsic velocity dispersion of the gas, and the parameters F_0, F_1 and r_F of the exponential radial profile of the gas flux. Because of the large number of parameters, it is highly desirable to constrain as many as possible of them. Although i can be estimated from the minor-to-major axial ratio of the dust disc, which can be measured from the images, previous studies (Ferrarese et al. 1996; Ferrarese & Ford 1999; Sarzi et al. 2001; Shapiro et al. 2006) have shown that slight warps are common. When the ionised-gas emission arises predominantly from the innermost region of the dust disc, it is therefore best to treat i as a free parameter, as done by Dalla Bontà et al. (2009). We initially considered a grid of models in which each point is determined by $M_\bullet$, i, and $(M/L)_*$. For each model we explored several combinations for σ_0, σ_1, r_σ, F_0, F_1, and r_F in order to match the observations. In principle, the exact characterisation of the flux and the velocity dispersion affects the recovered velocity field, and therefore σ_0, σ_1, r_σ, F_0, F_1, and r_F should be treated as free parameters in the model, along with $M_\bullet$, i, and $(M/L)_*$. However, previous studies (Verdoes Kleijn et al. 2000; Barth et al. 2001; Coccato et al. 2006) have found that they are fairly insensitive to the values of $M_\bullet$, i, and $(M/L)_*$. Thus, we run a set of preliminary models in order to find the shape of the intrinsic flux and velocity dispersion profiles that are required to match our data, within the typical range of our key model parameters. We recovered the optimal values of the flux and velocity dispersion parameters by minimising the χ^2_F and χ^2_σ as defined by

$$\begin{aligned} \chi^2_F &= \sum \frac{(F - F_\mathrm{mod})^2}{\delta F}, \\ \chi^2_\sigma &= \sum \frac{(\sigma - \sigma_\mathrm{mod})^2}{\delta \sigma} \end{aligned} \tag{4.36}$$

where $F \pm \delta F$ and $\sigma \pm \delta\sigma$ are the observed flux and velocity dispersion along the major axis, respectively, and F_mod and σ_mod are the corresponding model flux and velocity dispersion, respectively. We then explored a grid of $M_\bullet$, i, and $(M/L)_*$, where at each point of the grid we used the optimised parameters for the flux and velocity dispersion. For each model, we calculated

$$\chi^2 = \sum \frac{(v - v_\mathrm{mod})^2}{\delta v} \tag{4.37}$$

where $v \pm \delta(v)$ and v_mod are the observed and the corresponding model velocity along the different slit positions, respectively, in order to obtain the best-fitting

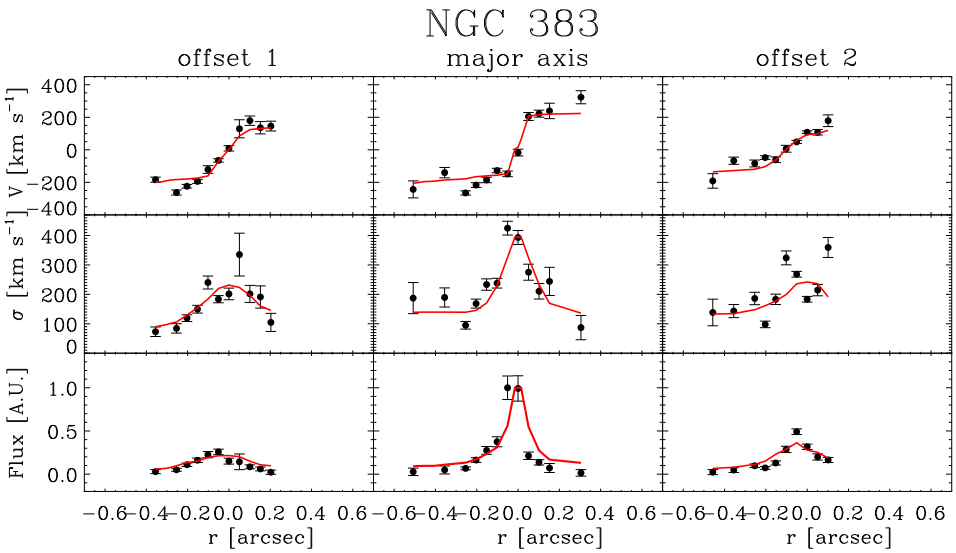

Figure 4.33: Observed [N II] $\lambda\lambda$6548, 6583 kinematics (filled circles) along with the best-fitting model (solid lines) for the SBH mass of NGC 383 obtained with $M_\bullet$=8.5 × 10^8 $M_\odot$, i=42.5 °, and $(M/L)_*$=5.3 $M_\odot/L_\odot$. The observed and modelled velocity curve (top panels), velocity dispersion radial profile (central panels), and flux radial profile (bottom panels) are shown for the slit along the offset 1 (left panels), major axis (central panels), and offset 2 position (right panels) of the gas disc.

parameters of the model.

4.5.2 Dynamical model with a single CMO

We explored a three-dimensional grid of models with $0 \leq M_\bullet \leq 1.2 \times 10^9$ $M_\odot$ in 2.0×10^8 $M_\odot$ steps, $30° \leq i \leq 60°$ in 0.5° steps, and $0 \leq (M/L)_* \leq 9$ $M_\odot/L_\odot$ in 0.2 $M_\odot/L_\odot$ steps. Within this range, the intrinsic flux and velocity dispersion of the gas best able to reproduce the observable are $F(r) = 0.054 + 0.567 \exp \frac{-r}{0.024}$ and $\sigma(r) = 127.640 + 0.024 \exp \frac{-r}{0.270}$. The model adopts three parameters to fit 33 data points (the values of the rotational velocity), for a total of 30 degrees of freedom. The best model fitting the observed rotation curve ($\chi^2_{\rm min} = 603.2$) requires $M_\bullet = 8.5^{+1.8}_{-1.3} \times 10^8$ $M_\odot$, $i = 42°.5^{+7.6}_{-6.7}$ and $(M/L)_* = 5.3^{+2.7}_{-2.1}$ $M_\odot/L_\odot$ in the I-band (Figure 4.33). The errors are quoted at the 3σ confidence level. Figure 4.34 shows the 1σ, 2σ and 3σ confidence levels (following the $\Delta\chi^2$ variations expected for two free parameters, i.e., 2.30, 6.17 and 11.8; Press et al. 1992) in the two-dimensional space of two of the

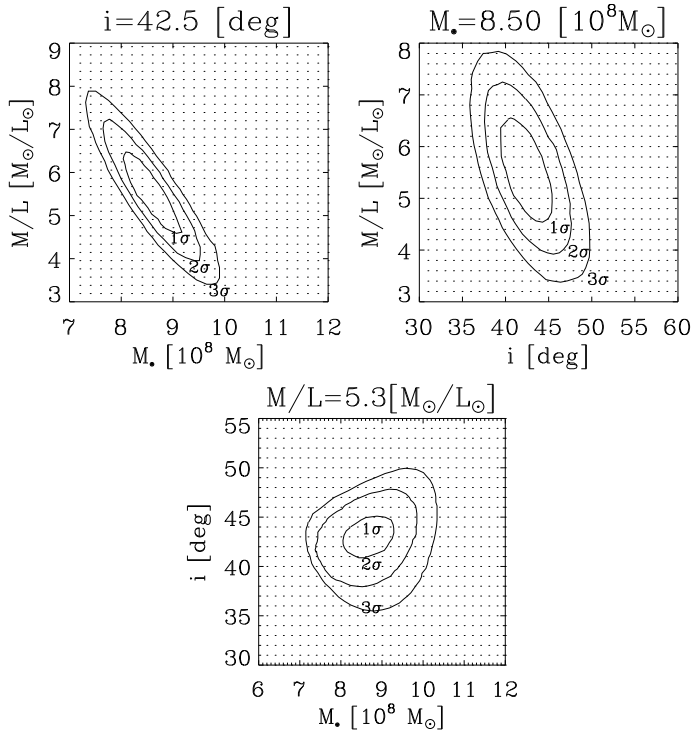

Figure 4.34: The locus of points of equal χ^2 values around the minimum χ^2_{min} value for the model of NGC 383. The 1σ, 2σ, and 3σ confidence levels expected for two free parameters are shown in the $M_\bullet - (M/L)_*$ plane with $i = 42°.5$ (top left-hand panel), $i - (M/L)_*$ plane with $M_\bullet$=8.5×10^8 $M_\odot$ (top right-hand panel), and i-$M_\bullet$ plane with $(M/L)_*$=5.3 $M_\odot/L_\odot$ (bottom panel). The grid of models explored is shown by the dots.

fitted parameters, where the third parameter is held fixed at the best fitted value listed above. Figure 4.35 shows 1σ, 2σ and 3σ confidence levels individually on $M_\bullet$, i, and $(M/L)_*$, according to the $\Delta\chi^2$ variations expected for one parameter (i.e., 1, 4, and 9; Press et al. 1992), marginalising over all the other parameters.

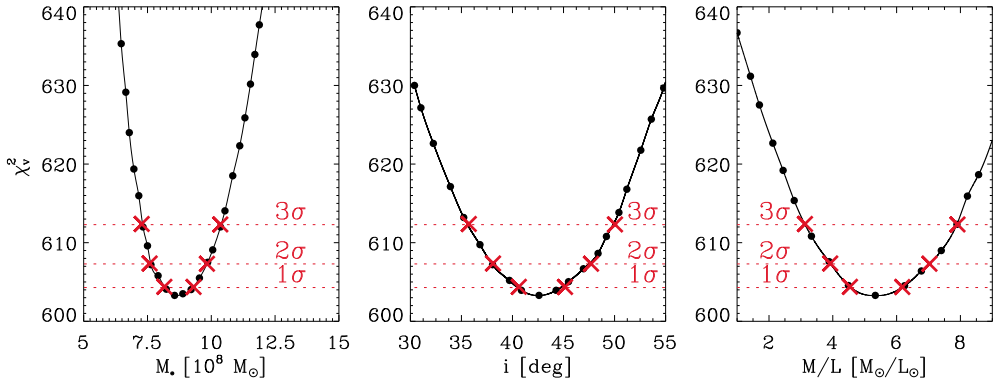

Figure 4.35: χ^2 distribution for NGC 383 as a function of $M_\bullet$ (left-hand panel), inclination (central panel), and $(M/L)_*$ (right-hand panel). The dotted horizontal lines indicate the 1σ, 2σ, and 3σ confidence levels on the best fitting values, marginalising over all the other parameters.

The inclination angle derived from modelling the ionised kinematic data $i = 42°.5^{+7.6}_{-6.7}$ is in good agreement with the inclination angle we derived from the analysis of the unsharp masked images ($i = 45°$). The best-fit value of $M_\bullet$ ($M_\bullet = 8.5^{+1.8}_{-1.3} \times 10^8$ M$_\odot$) is in agreement within the scatter with the expected value ($M_\bullet = 5.83 \times 10^8$ M$_\odot$) from the $M_\bullet - \sigma$ relation (Ferrarese & Ford 2005) and with the upper limits ($1.3{\times}10^9$ and $2.9{\times}10^8$ M$_\odot$ for $i = 33°$ and $i = 88°$, respectively) found by Beifiori et al. (2009).

4.5.3 Dynamical model with SBH and NSC

To disentangle the contribution of the masses of the NSC and SBH we run again the model assuming that the velocity profile is the result of the contribution of the SBH, NSC, and stellar component of the galaxy

$$v_c(r) = \left[\frac{GM(r)}{r}\right]^{\frac{1}{2}} = \left[\left(\frac{M}{L}\right)_* v_*^2(r) + \left(\frac{M}{L}\right)_{\rm NSC} v_{\rm NSC}^2(r) + \frac{GM_\bullet}{r}\right]^{\frac{1}{2}} \quad (4.38)$$

which is obtained from Equation 4.27 by including $v_{\rm NSC}$ and $(M/L)_{\rm NSC}$ which are the velocity and mass-to-light ratio of the NSC. Therefore, the free parameters of the new model are the mass $M_\bullet$ of SBH, the inclination i of the disc, and the mass-to-light ratio $(M/L)_*$ and $(M/L)_{\rm NSC}$ of the stellar component and

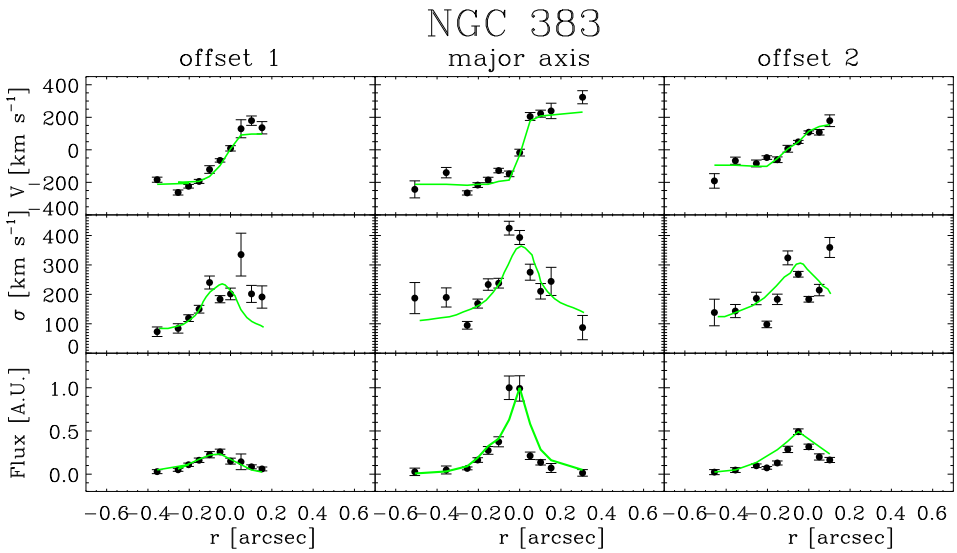

Figure 4.36: Observed [N II] $\lambda\lambda$6548, 6583 kinematics (filled circles) along with the best-fitting model (solid lines) for the SBH and NSC masses of NGC 383 obtained with $M_\bullet$=6.0 $\times$ 10^8 M$_\odot$, i=45.°5, $(M/L)_*$=6.7 M$_\odot$/L$_\odot$, and $(M/L)_{\rm NSC}$=3.0 M$_\odot$/L$_\odot$. The observed and modelled velocity curve (top panels), velocity dispersion radial profile (central panels), and flux radial profile (bottom panels) are shown for the slit along the offset 1 (left-hand panels), major axis (central panels), and offset 2 position (right-hand panels) of the gas disc.

NSC, respectively. We performed again the minimisation of the parameters of flux and velocity dispersion in a wide grid of values. Then, we explored a four-dimensional grid of models with $0 \leq M_\bullet \leq 1.2 \times 10^9$ M$_\odot$ in 2.0×10^8 M$_\odot$ steps, $30° \leq i \leq 60°$ in 0.5° steps, $0 \leq (M/L)_* \leq 9$ M$_\odot$/L$_\odot$, and $0 \leq (M/L)_{\rm NSC} \leq 9$ M$_\odot$/L$_\odot$ in 0.2 M$_\odot$/L$_\odot$steps. The model adopts four parameters to fit 33 data points (the values of the rotational velocity), for a total of 29 degrees of freedom. The best model fitting the observed rotation curve ($\chi^2_{\rm min}$ = 513.98) requires $M_\bullet = 6.0^{+1.8}_{-1.2} \times 10^8M_\odot$, $i = 45°.5^{+6.8}_{-7.1}$, $(M/L)_* = 5.2^{+1.8}_{-1.8}$ M$_\odot$/L$_\odot$, and $(M/L)_{\rm NSC} = 3.0^{+1.7}_{-1.3}$ M$_\odot$/L$_\odot$ in the I-band (Figure 4.36).

The errors are quoted at the 3σ confidence level. Figure 4.37 shows the 1σ, 2σ and 3σ confidence levels (following the $\Delta\chi^2$ variations expected for two free parameters, i.e., 2.30, 6.17 and 11.8 (Press et al. 1992) in the two-dimensional space of two of the fitted parameters, where the third and fourth parameters are held fixed at the best fitted values. Figure 4.38 shows 1σ, 2σ, and 3σ confidence levels individually on $M_\bullet$, i, $(M/L)_*$, and $(M/L)_{\rm NSC}$ according to the $\Delta\chi^2$

variations expected for one parameter (i.e., 1, 4, and 9; Press et al. 1992), marginalising over all the other parameters. The inclination angle derived from modelling the ionised kinematic data $i = 45.^{\circ}5^{+6.8}_{-7.1}$ is in good agreement with the inclination angle we derived from the analysis of the unsharp masked images ($i = 45^{\circ}$) and from the previous model ($i = 42.^{\circ}5^{+7.6}_{-6.7}$). The best-fit value of $M_{\bullet}$ ($M_{\bullet} = 6.0^{+1.8}_{-1.2} \times 10^8$ M$_{\odot}$) is in agreement within the scatter with the expected value ($M_{\bullet} = 5.83 \times 10^8$ M$_{\odot}$) measured from the $M_{\bullet}-\sigma$ relation (Ferrarese & Ford 2005) and with the upper limits (1.3×10^9 and 2.9×10^8 M$_{\odot}$ for $i = 33^{\circ}$ and $i = 88^{\circ}$, respectively) found by Beifiori et al. (2009).

4.6 Discussion and conclusions

We derived the total luminosity of the NSC in I-band following Larsen (2001). It is

$$. \; L_{I,\mathrm{K}} = \pi I_{0,\mathrm{K}} \left[r_{\mathrm{c}}^2 \log \left[1 + \left(\frac{r}{r_{\mathrm{c}}} \right)^2 \right] + \frac{r^2}{1+c^2} - \frac{4\pi r_{\mathrm{c}}^2}{\sqrt{1+c^2}} \cdot \left(\sqrt{1 + \left(\frac{r}{r_{\mathrm{c}}^2} \right)^2} - 1 \right) \right]$$

where $c = r_{\mathrm{c}}/r_{\mathrm{t}}$ is the concentration index, and $I_{0,\mathrm{K}}$, r_{c}, and r_{t} were obtained from the two-dimensional photometric decomposition described in Section 4.4.6. We obtained $L_{I,\mathrm{K}} = 2.95 \times 10^7$ M$_{\odot}$ corresponding to an absolute magnitude $M_{I,\mathrm{K}} = -2.5 \log L_{I,\mathrm{K}} + M_{\odot,I} = -14.6$. We found a mass of $M_{\mathrm{NSC}} = 8.9^{+5.0}_{-3.9}\times10^7$ M$_{\odot}$ considering the mass-to-light ratio of $(M/L)_{\mathrm{NSC}} = 3.0^{+1.7}_{-1.3}$ M$_{\odot}$/L$_{\odot}$ obtained from the dynamical model.

We compared the absolute magnitude and mass-to-light ratio of the NSC of NGC 383 to those of known nuclear star clusters in the I-band. The total magnitude of NGC 383 in the B band is -20.63 (de Vaucouleurs et al. 1991). Using the IRAF task SYNPHOT and taking into account the galaxy morphological type, we calculate the colour $B-I = 1.74$ and we obtained the I-band absolute magnitude of NGC 383, $M_I = -18.89$. We also derived the I-band absolute magnitude of the sample galaxies of Böker et al. (2002), Scarlata et al. (2004), Lauer et al. (2005), Walcher et al. (2005), De Propris et al. (2005), Seth et al. (2006), and Ferrarese et al. (2006a) which are known to host a NSC. Figure 4.40 shows the absolute magnitude of the sample NSCs as a function of the absolute magnitude of the host galaxy in the I band. The spiral galaxies NGC 2805 and NGC 7418 of Böker et al. (2002) are similar to NGC 383, since they have absolute magnitudes of -18.99 and -18.62, respectively. Their NSCs have a magnitude of -13.31 and -16.23, respectively. The late spiral NGC 6384 studied by Scarlata et al. (2004) has an I-band magnitude of -18.77 and its NSC has a magnitude of -12.45. Also three galaxies from the sample of Lauer

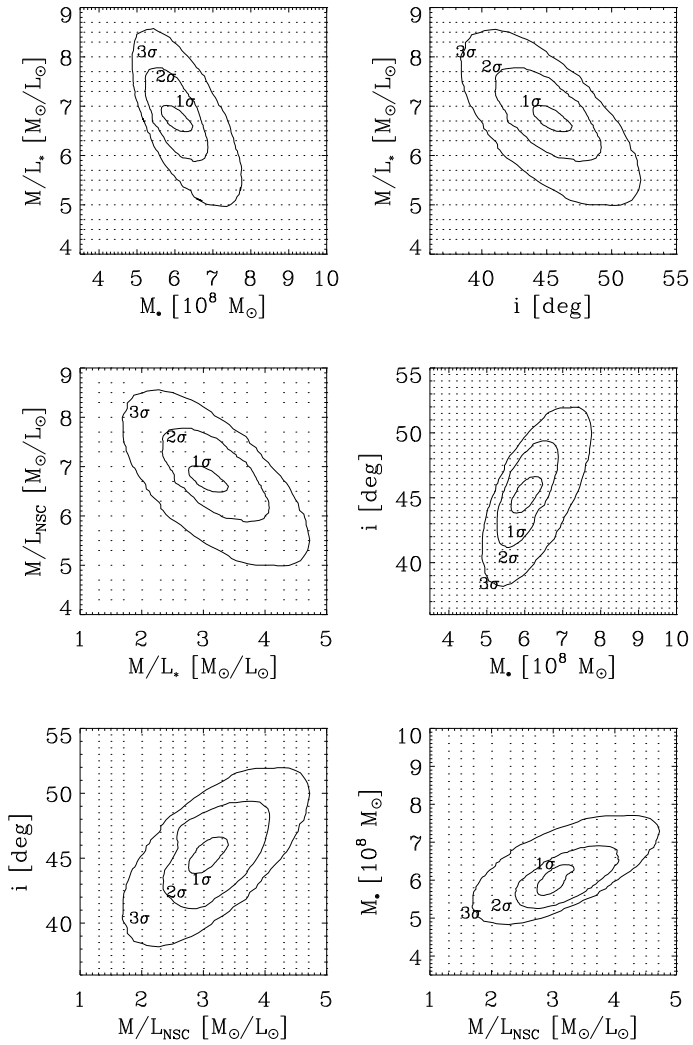

Figure 4.37: The locus of points of equal χ^2 values around the minimum χ^2_{min} value for the model of NGC 383. The 1σ, 2σ, and 3σ confidence levels expected for two free parameters are shown in the $M_\bullet - (M/L)_*$ (top left-hand panel), in the $i - (M/L)_*$ plane (top right-hand panel), in the $(M/L)_* - (M/L)_{\rm NSC}$ plane with $M_\bullet$=8.5 $\times$ 10^8 $M_\odot$ (middle left-hand panel), $M_\bullet$-i (middle right-hand panel), $(M/L)_{\rm NSC} - i$ (bottom left-hand panel), and $(M/L)_{\rm NSC}$–$M_\bullet$ (bottom right-hand panel) planes marginalising over all the other parameters. The grid of models explored is shown by the dots.

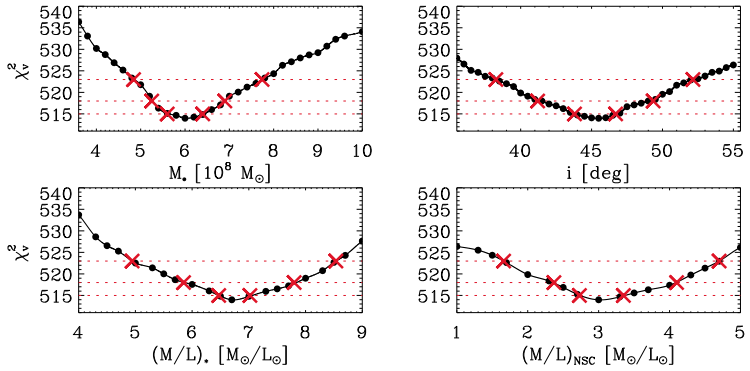

Figure 4.38: χ^2 distribution for NGC 383 as a function of $M_\bullet$ (top left-hand panel), inclination (top right-hand panel), $(M/L)_*$ (bottom left-hand panel), and $(M/L)_{\rm NSC}$ (bottom right-hand panel). The dotted horizontal lines indicate the confidence levels on the best-fitting values, marginalising over all the other parameters.

et al. (2005) have absolute magnitudes comparable with NGC 383. They are the lenticular galaxies NGC 1023 and NGC 3384, and the elliptical NGC 1427, which have -19.24, -18.61, and -19.53. Their NSCs have absolute magnitudes of -9.83, -10.23, and -10.73, respectively.

Furthermore, the mass-to-light ratio of the NSC of NGC 383 $(M/L)_{\rm NSC} = 3.0^{+1.7}_{-1.3}$ $M_\odot/L_\odot$ is in good agreement with those of the NSCs studied by Rossa et al. (2006) who found $0 \leq (M/L)_{\rm NSC} \leq 8.18$ $M_\odot/L_\odot$ in the I band.

Then we compared the masses of the CMO of NGC 383 with those of the SBH and NSC found to coexist in some galaxies. Table 4.9 lists the galaxies hosting both a SBH and NSC in the nucleus whose masses where measured in literature and Figure 4.39 shows the comparison between the CMOs of NGC 383 and the CMOs of other galaxies. NGC 383 has the highest value of central stellar velocity dispersion. The sample galaxies show a wide range of velocity dispersions, indicating that a clear separation between galaxies which host NSCs and galaxies which host SBHs (Ferrarese et al. 2006) is ruled out. On the contrary there is a transition region for galaxies where the nuclei can host both a SBH and a NSC. The $M_\bullet/M_{\rm NSC}$ ratio ranges between 0.01 and 12. The mass of the NSCs exceeds that of SBHs, for galaxies with $\sigma \geq 150$ km s^{-1}, while in other cases the SBH is more massive than the NSC, as in NGC 383.

Table 4.9: Masses of coexisting SBHs and NSCs.

Galaxy	Morph. Type	D [Mpc]	σ [km s^{-1}]	$M_\bullet$ [M$_\odot$]	Reference	$M_{\rm NSC}$ [M$_\odot$]	Reference
(1)	(2)	(3)	(4)	(5)	(6)	(7)	(8)
MW	Sbc	0.0083	105	4.30×10^6	Genzel et al. (2010)	2.9×10^7	Launhardt et al. (2002)
M31	Sb	0.774	169	1.43×10^8	Bender et al. (2005)	3.5×10^7	Kormendy & Bender (1999)
M33	SA	0.82	24	$\leq 1.5\times 10^3$	Gebhardt et al. (2001)	1.0×10^6	Kormendy & McClure (1993)
NGC 205	E5	0.82	15	$\leq 2.4\times 10^4$	Jones et al. (1996)	1.4×10^6	De Rijcke et al. (2006)
NGC 1023	SB0	10.81	205	4.13×10^7	Bower et al. (2001)	0.99×10^7	Lauer et al. (2005)
NGC 3115	S0	9.54	230	8.97×10^8	Emsellem et al. (1999)	1.04×10^7	Kormendy et al. (1996a)
NGC 3384	SB0	11.49	146	1.08×10^7	Schulze & Wisotzki (2011)	2.3×10^7	Seth et al. (2008b)
NGC 4026	S0	13.35	180	1.8×10^8	Gültekin et al. (2009)	1.44×10^7	Lauer et al. (2005)
NGC 4395	Sd	4.3	30	3.6×10^5	Peterson et al. (2005)	3.5×10^6	Seth et al. (2008b)
NGC 7457	S0	12.53	67	0.90×10^7	Schulze & Wisotzki (2011)	2.7×10^7	Seth et al. (2008b)

Notes. — Col.(1): Galaxy name. Col.(2): Hubble type. Col.(3): Distance. Col.(4): Stellar velocity dispersion. Col.(5)-(6): Mass and reference of the SBH. Col.(7)-(8): Mass and reference of the NSC.

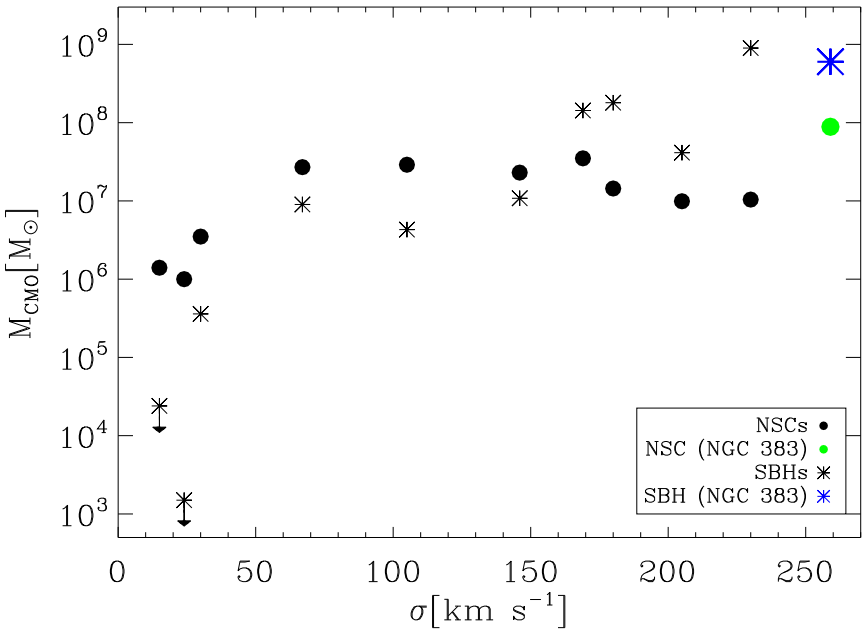

Figure 4.39: $M_{\rm NSC}$ and $M_\bullet$ as a function of velocity dispersion σ for galaxies where CMOs coexist. The black asterisks indicate SBHs and black points indicate NSCs. The blue asterisk and green point show the masses of the SBH and NSC of NGC 383, respectively. They are obtained with the dynamical model which disentangles the mass contribution of the two CMOs.

Then we explored the scaling relations that involve the mass of CMOs and global parameters of the host galaxy. Following Scott & Graham (2013) we show in Figure 4.41 the mass of CMOs as a function of the total magnitude, $M_{B,\rm gal}$, stellar velocity dispersion, σ, and virial mass of the galaxy $M_{\rm gal,dyn}$. The latter was obtained following Ferrarese et al. (2006a)

$$\mathcal{M}_{\rm gal,dyn} = \alpha r_{\rm e} \sigma^2 / G \tag{4.39}$$

where $\alpha = 5$ Cappellari et al. (2006). For NGC 383 $r_{\rm e} = 4.86$ arcsec is the effective radius of the bulge obtained from the two-dimensional photometric decomposition, $\sigma_* = 259$ km s^{-1} is the central stellar velocity dispersion from Garcia-Rissmann et al. (2005), and $\mathcal{M}_{\rm Gal,dyn} = 1.09 \times 10^{11} {\rm M}_\odot$. The masses of the SBH measured from both dynamical models obey the relations found by Scott & Graham (2013). Finally, the NSC and SBH of NGC 383 confirm the result for which the mass of the SBH is higher than that of the NSC for a given

mass of the galaxy. Moreover, our masses are in good agreement with the other CMOs and best-fitting relations by Scott & Graham (2013). Therefore, we confirm that for NGC 383 the NSC and SBH follow different scaling relations with global properties of the host galaxy.

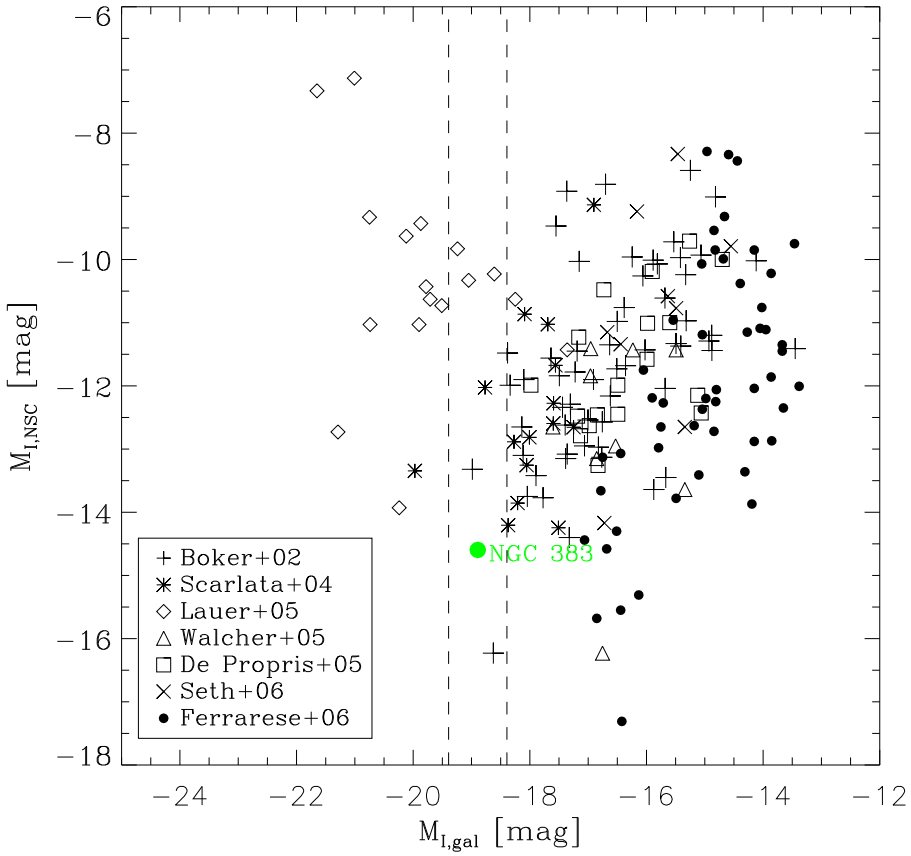

Figure 4.40: *I*-band absolute magnitude of NSCs from the sample of Böker et al. (2002), Scarlata et al. (2004), Lauer et al. (2005), Walcher et al. (2005), De Propris et al. (2005), and Seth et al. (2006) as a function of the absolute magnitude of their host galaxies. The dashed lines bracket the range where galaxies have similar magnitudes to NGC 383.

Our main conclusions can be summarised as follows.

- We presented a dynamical analysis aimed at constraining the mass of the CMO in the lenticular galaxy NGC 383 at a distance of 63.4 Mpc. The central stellar velocity dispersion is consistent with a putative SBH with

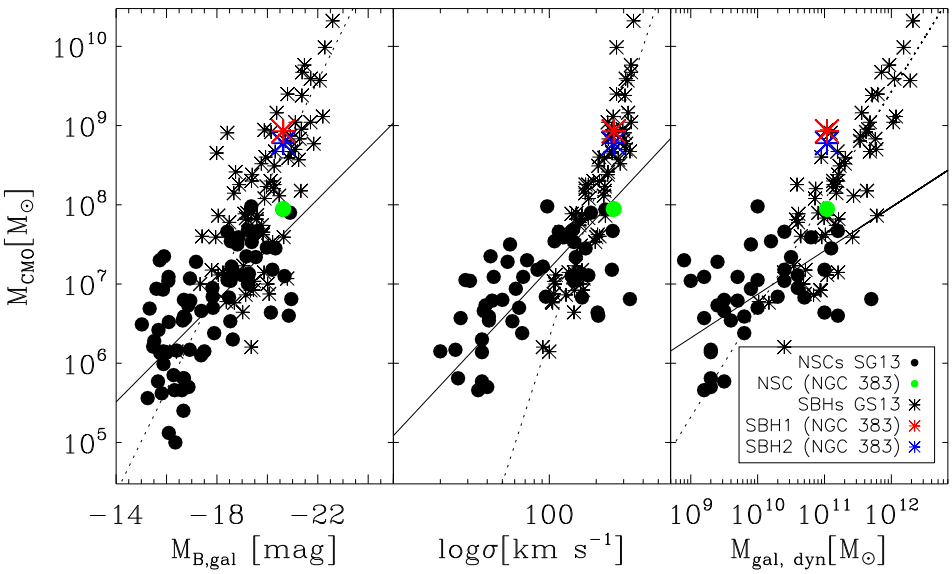

Figure 4.41: $M_{\rm NSC}$ and $M_\bullet$ as a function of galaxy magnitude M_B (left-hand panel), stellar velocity dispersion σ (middle panel), and dynamical mass $M_{\rm gal,dyn}$ (right-hand panel). The black asterisks indicate SBHs and black points indicate NSCs. The mass of the SBH of NGC 383 measured by the dynamical model not disentangling the NSC contribution is shown in red. The blue asterisk and green point show the masses of the SBH and NSC of NGC 383, respectively. They are obtained with the dynamical model which disentangles the mass contribution of the two CMOs. The dashed and solid lines indicate the best-fitting relations from Scott & Graham (2013) for SBHs and NSCs, respectively.

a mass of $M_\bullet = 5.8 \times 10^8$ M$_\odot$.

- From the visual inspection of *HST* images we found that the galaxy hosts a NSC in its centre. By performing the two-dimensional photometric decomposition we were able to obtain a model of the surface-brightness distribution of the NSC, bulge and disc of NGC 383.

- The *HST*/*WFPC2* image in the F814W filter was used to constrain the luminosity profile of the galaxy, while *STIS*/G750M spectra were measured to derive the rotation velocity and velocity dispersion profiles of the ionised gas from the [N II] λ6583 emission line. Three slit positions parallel to the galaxy major axis are considered: the first placed at −0.076 arcsec from the photometric major axis, and the others placed at −0.178 and +0.100 arcsec from the galaxy centre, respectively.

- The regular morphology and kinematics observed for the ionised gas led to the measurement of the SBH mass of $M_\bullet = 8.5^{+1.8}_{-1.3} \times 10^8$ $M_\odot$ (where the uncertainties represent 3σ errors). The SBH mass is consistent both with the $M_\bullet - \sigma$ relation (Ferrarese & Ford 2005) and with the upper limits found by Beifiori et al. (2009).

- When the contribution of the NSC to the CMO mass is taken into account, the best-fit dynamical model gives a mass of $M_\bullet = 6.0^{+1.8}_{-1.2} \times 10^8$ $M_\odot$. Combining the best-fitting value of $(M/L)_{\rm NSC}$=3.0 $M_\odot/L_\odot$ and the structural parameters of the best-fit model of the NSC, we found a mass of $M_{\rm NSC} = 8.9^{+5.0}_{-3.9} \times 10^7$ $M_\odot$.

- The masses of the SBH we found in both dynamical models are consistent within the errors and are in good agreement with the scaling relations found by Scott & Graham (2013).

- The mass and the mass-to-light ratio $(M/L)_{\rm NSC}$ of the NSC are consistent with previous studies of NSCs. Furthermore, $M_{\rm NSC}$ is in good agreement with the scaling relations found by Scott & Graham (2013).

- We also found that, for a given property of NGC 383, the SBH is more massive than the NSC, as predicted by Ferrarese et al. (2006a). In this sense, we confirmed that the NSC and SBH of NGC 383 follow different scaling relations with global properties of the host galaxy.

Bibliography

Abel, T., Bryan, G. L., & Norman, M. L. 2000, ApJ, 540, 39

Agarwal, M. & Milosavljević, M. 2011, ApJ, 729, 35

Aller, M. C. & Richstone, D. O. 2007, ApJ, 665, 120

Andersen, D. R., Walcher, C. J., Böker, T., Ho, L. C., van der Marel, R. P., Rix, H.-W., & Shields, J. C. 2008, ApJ, 688, 990

Antonini, F., Capuzzo-Dolcetta, R., Mastrobuono-Battisti, A., & Merritt, D. 2012, ApJ, 750, 111

Antonini, F. 2013, ApJ, 763, 62

Antonucci, R. 1993, ARA&A, 31, 473

Baggett, S., et al. 2002, HST WFPC2 Data Handbook, v. 4.0 (STScI: Baltimore)

Bailyn, C. D., Jain, R. K., Coppi, P., & Orosz, J. A. 1998, ApJ, 499, 367

Balcells, M., Graham, A. W., Domínguez-Palmero, L., & Peletier, R. F. 2003, ApJ, 582, L79

Balcells, M., Graham, A. W., & Peletier, R. F. 2007, ApJ, 665, 1084

Balick, B. & Brown, R. L. 1974, ApJ, 194, 265

Barth, A. J., Sarzi, M., Rix, H., Ho, L. C., Filippenko, A. V., & Sargent, W. L. W. 2001, ApJ, 555, 685

Barth, A. J., Ho, L. C., & Sargent, W. L. W. 2002, AJ, 124, 2607

—. 2003, ApJ, 583, 134

Barth, A. J., Strigari, L. E., Bentz, M. C., Greene, J. E., & Ho, L. C. 2009, ApJ, 690, 1031

Barway, S. & Kembhavi, A. 2007, ApJ, 662, L67

Bassino, L. P., Muzzio, J. C., & Rabolli, M. 1994, ApJ, 431, 634

Bastian, N., Saglia, R. P., Goudfrooij, P., Kissler-Patig, M., Maraston, C., Schweizer, F., & Zoccali, M. 2006, A&A, 448, 881

Batcheldor, D. et al. 2005, ApJS, 160, 76

Becklin, E. E. & Neugebauer, G. 1968, ApJ, 151, 145

Bedin, L. R., Piotto, G., Anderson, J., Cassisi, S., King, I. R., Momany, Y., & Carraro, G. 2004, ApJ, 605, L125

Begelman, M. C., Volonteri, M., & Rees, M. J. 2006, MNRAS, 370, 289

Begelman, M. C., Rossi, E. M., & Armitage, P. J. 2008, MNRAS, 387, 1649

Beifiori, A., Sarzi, M., Corsini, E. M., Dalla Bontà, E., Pizzella, A., Coccato, L., & Bertola, F. 2009, ApJ, 692, 856

Beifiori, A., Courteau, S., Corsini, E. M., & Zhu, Y. 2012, MNRAS, 419, 2497

Bekki, K., Couch, W. J., & Drinkwater, M. J. 2001, ApJ, 552, L105

Bekki, K., Couch, W. J., Drinkwater, M. J., & Shioya, Y. 2004, ApJ, 610, L13

Bekki, K., Couch, W. J., & Shioya, Y. 2006, ApJ, 642, L133

Bekki, K. 2007, PASA, 24, 77

Bekki, K. & Graham, A. W. 2010, ApJ, 714, L313

Bender, R., Doebereiner, S., & Moellenhoff, C. 1988, A&AS, 74, 385

Bender, R. et al. 2005, ApJ, 631, 280

Bendinelli, O. 1991, ApJ, 366, 599

Bentz, M. C. et al. 2010, ApJ, 716, 993

Bertola, F. & Corsini, E. M. 1999, in IAU Symposium 186, Galaxy Interactions at Low and High Redshift, ed. J. E. Barnes & D. B. Sanders (Dordrecht: Kluwer), 149

Bertola, F., Corsini, E. M., Vega Beltrán, J. C., Pizzella, A., Sarzi, M., Cappellari, M., & Funes, J. G. 1999, ApJ, 519, L127

Binggeli, B. & Cameron, L. M. 1993, A&AS, 98, 297

Binney, J. & Merrifield, M. 1998, Galactic Astronomy (Princeton: Princeton University Press)

Böker, T., Falcón-Barroso, J., Schinnerer, E., Knapen, J. H., & Ryder, S. 2008, AJ, 135, 479

Böker, T., Laine, S., van der Marel, R. P., Sarzi, M., Rix, H., Ho, L. C., & Shields, J. C. 2002, AJ, 123, 1389

Böker, T., Sarzi, M., McLaughlin, D. E., van der Marel, R. P., Rix, H., Ho, L. C., & Shields, J. C. 2004, AJ, 127, 105

Bond, J. R., Arnett, W. D., & Carr, B. J. 1984, ApJ, 280, 825

Booth, C. M. & Schaye, J. 2009, MNRAS, 398, 53

Bower, G. A. et al. 2001, ApJ, 550, 75

Bower, G. C., Falcke, H., Herrnstein, R. M., Zhao, J.-H., Goss, W. M., & Backer, D. C. 2004, Science, 304, 704

Braatz, J. A., Wilson, A. S., & Henkel, C. 1994, ApJ, 437, L99

—. 1996, ApJS, 106, 51

Bromm, V., Coppi, P. S., & Larson, R. B. 2002, ApJ, 564, 23

Bromm, V. & Loeb, A. 2003, ApJ, 596, 34

Brown, C. K. & Magorrian, J. 2013, MNRAS, 431, 80

Bruzual, G. & Charlot, S. 2003, MNRAS, 344, 1000

Burkert, A. & Silk, J. 2001, ApJ, 554, L151

Butcher, H. R., van Breugel, W., & Miley, G. K. 1980, ApJ, 235, 749

Butler, D. J. & Martínez-Delgado, D. 2005, AJ, 129, 2217

Caon, N., Capaccioli, M., & D'Onofrio, M. 1993, MNRAS, 265, 1013

Cappellari, M. 2002, MNRAS, 333, 400

Cappellari, M. et al. 2006, MNRAS, 366, 1126

Cappellari, M., Neumayer, N., Reunanen, J., van der Werf, P. P., de Zeeuw, P. T., & Rix, H. 2009, MNRAS, 394, 660

Capuzzo-Dolcetta, R. 1993, ApJ, 415, 616

Capuzzo-Dolcetta, R. & Miocchi, P. 2008a, ApJ, 681, 1136

—. 2008b, MNRAS, 388, L69

Carollo, C. M., Danziger, I. J., & Buson, L. 1993, MNRAS, 265, 553

Carollo, C. M., Franx, M., Illingworth, G. D., & Forbes, D. A. 1997, ApJ, 481, 710

Carollo, C. M., Stiavelli, M., & Mack, J. 1998, AJ, 116, 68

Carollo, C. M., Stiavelli, M., Seigar, M., de Zeeuw, P. T., & Dejonghe, H. 2002, AJ, 123, 159

Cen, R. 2001, ApJ, 560, 592

Cheung, A. C., Cudaback, D. D., Rank, D. M., Thornton, D. D., Townes, C. H., & Welch, W. J. 1969, BAAS, 1, 236 236

Chilingarian, I. V., Sil'Chenko, O. K., Afanasiev, V. L., & Prugniel, P. 2007, Astronomy Letters, 33, 292

Coccato, L., Sarzi, M., Pizzella, A., Corsini, E. M., Dalla Bontà, E., & Bertola, F. 2006, MNRAS, 366, 1050

Combes, F. & Sanders, R. H. 1981, A&A, 96, 164

Corbett, E. A., Croom, S. M., Boyle, B. J., Netzer, H., Miller, L., Outram, P. J., Shanks, T., Smith, R. J., & Rhook, K. 2003, MNRAS, 343, 705

Corsini, E. M. et al. 1999, A&A, 342, 671

Corsini, E. M., Méndez-Abreu, J., Pastorello, N., Dalla Bontà, E., Morelli, L., Beifiori, A., Pizzella, A., & Bertola, F. 2012, MNRAS, 423, L79

Côté, P. et al. 2004, ApJS, 153, 223

Côté, P. et al. 2006, ApJS, 165, 57

Courteau, S. 1997, AJ, 114, 2402

Crane, P. et al. 1993, AJ, 106, 1371

Cretton, N. & van den Bosch, F. C. 1999, ApJ, 514, 704

Dalla Bontà, E., Ferrarese, L., Corsini, E. M., Miralda-Escudé, J., Coccato, L., Sarzi, M., Pizzella, A., & Beifiori, A. 2009, ApJ, 690, 537

Davidge, T. J. 2000, AJ, 119, 748

Davies, J. I. & Phillipps, S. 1988, MNRAS, 233, 553

Davies, R. I. et al. 2006, ApJ, 646, 754

Davis, T. A., Bureau, M., Cappellari, M., Sarzi, M., & Blitz, L. 2013, Nature, 494, 328

De Lorenzi, F., Hartmann, M., Debattista, V. P., Seth, A. C., & Gerhard, O. 2013, MNRAS, 429, 2974

De Lucia, G., Springel, V., White, S. D. M., Croton, D., & Kauffmann, G. 2006, MNRAS, 366, 499

De Propris, R., Phillipps, S., Drinkwater, M. J., Gregg, M. D., Jones, J. B., Evstigneeva, E., & Bekki, K. 2005, ApJ, 623, L105

De Rijcke, S., Prugniel, P., Simien, F., & Dejonghe, H. 2006, MNRAS, 369, 1321

de Vaucouleurs, G., de Vaucouleurs, A., Corwin, Jr., H. G., Buta, R. J., Paturel, G., & Fouque, P. 1991, Third Reference Catalogue of Bright Galaxies (Springer-Verlag: Berlin)

Debattista, V. P., Corsini, E. M., & Aguerri, J. A. L. 2002, MNRAS, 332, 65

Debattista, V. P. & Sellwood, J. A. 2000, ApJ, 543, 704

Denney, K. D. et al. 2010, ApJ, 721, 715

Devecchi, B. & Volonteri, M. 2009, ApJ, 694, 302

Di Matteo, T., Colberg, J., Springel, V., Hernquist, L., & Sijacki, D. 2008, ApJ, 676, 33

di Nella, H., Garcia, A. M., Garnier, R., & Paturel, G. 1995, A&AS, 113, 151

Dressel, L. et al. 2007, STIS Data Handbook, v. 5.0 (Baltimore: STScI)

Dressler, L. 2011, HST WFC3 Instrument Handbook, v. 4.0 (Baltimore: STScI)

Dubois, Y., Pichon, C., Haehnelt, M., Kimm, T., Slyz, A., Devriendt, J., & Pogosyan, D. 2012, MNRAS, 423, 3616

Durrell, P. R. 1997, AJ, 113, 531

Ebisuzaki et al. 2001, ApJ, 562, L19

Eckart, A. & Genzel, R. 1997, BAAS, 29, 1366

Ekers, R. D., Goss, W. M., Schwarz, U. J., Downes, D., & Rogstad, D. H. 1975, A&A, 43, 159

Emsellem, E., Monnet, G., & Bacon, R. 1994, A&A, 285, 723

Emsellem, E., Bacon, R., Monnet, G., & Poulain, P. 1996, A&A, 312, 777

Emsellem, E., Dejonghe, H., & Bacon, R. 1999, MNRAS, 303, 495

Emsellem, E. et al. 2004, MNRAS, 352, 721

Emsellem, E. & van de Ven, G. 2008, ApJ, 674, 653

Emsellem, E. 2013, MNRAS, 433, 1862

Erwin, P. & Gadotti, D. A. 2012, Advances in Astronomy, 2012

Faber, S. M. et al. 1997, AJ, 114, 1771

Falcón-Barroso, J., Peletier, R. F., & Balcells, M. 2002, MNRAS, 335, 741

Falcón-Barroso, J. et al. 2004, MNRAS, 350, 35

Falcón-Barroso, J. et al. 2006, MNRAS, 369, 529

Farr, W. M., Sravan, N., Cantrell, A., Kreidberg, L., Bailyn, C. D., Mandel, I., & Kalogera, V. 2011, ApJ, 741, 103

Feoli, A. & Mancini, L. 2009, ApJ, 703, 1502

Ferland, G. J., Peterson, B. M., Horne, K., Welsh, W. F., & Nahar, S. N. 1992, ApJ, 387, 95

Ferrarese, L., van den Bosch, F. C., Ford, H. C., Jaffe, W., & O'Connell, R. W. 1994, AJ, 108, 1598

Ferrarese, L., Ford, H. C., & Jaffe, W. 1996, ApJ, 470, 444

Ferrarese, L. & Ford, H. C. 1999, ApJ, 515, 583

Ferrarese, L. & Merritt, D. 2000, ApJ, 539, L9

Ferrarese, L. 2002, ApJ, 578, 90

Ferrarese, L. & Ford, H. 2005, Space Science Reviews, 116, 523

Ferrarese, L. et al. 2006a, ApJ, 644, L21

Ferrarese, L. et al. 2006b, ApJS, 164, 334

Figer, D. F., McLean, I. S., & Morris, M. 1999, ApJ, 514, 202

Figer, D. F. et al. 2002, ApJ, 581, 258

Filippenko, A. V. & Halpern, J. P. 1984, ApJ, 285, 458

Filippenko, A. V. & Sargent, W. L. W. 1989, ApJ, 342, L11

Fraix-Burnet, D., Golombek, D., & Macchetto, F. D. 1991, AJ, 102, 562

Franceschini, A., Vercellone, S., & Fabian, A. C. 1998, MNRAS, 297, 817

Freedman, W. L. et al. 2001, ApJ, 553, 47

Freeman, K. C. 1970, ApJ, 160, 811

Freeman, K. C. 1993, in ASP Conf. Ser. 48, The Globular Cluster-Galaxy Connection, ed. G. H. Smith & J. P. Brodie (San Francisco: ASP), 608

Fruchter, A., Sosey, M., Hack, W., Dressel, L., Koekemoer, A. M., Mack, J., Mutchler, M., & Pirzkal, N. 2009, HST MultiDrizzle Handbook, v. 3.0 (Baltimore: STScI)

Fryer, C. L. & Kalogera, V. 2001, ApJ, 554, 548

Gao, L., Yoshida, N., Abel, T., Frenk, C. S., Jenkins, A., & Springel, V. 2007, MNRAS, 378, 449

Garcia, A. M. 1993, A&AS, 100, 47

Garcia-Rissmann, A., Vega, L. R., Asari, N. V., Cid Fernandes, R., Schmitt, H., González Delgado, R. M., & Storchi-Bergmann, T. 2005, MNRAS, 359, 765

Gebhardt, K., Pryor, C., Williams, T. B., & Hesser, J. E. 1995, AJ, 110, 1699

Gebhardt, K. et al. 2000a, ApJ, 539, L13

Gebhardt, K. et al. 2000b, ApJ, 539, L13

Gebhardt, K. et al. 2001, AJ, 122, 2469

Gebhardt, K. et al. 2003, ApJ, 583, 92

Gebhardt, K., Rich, R. M., & Ho, L. C. 2005, ApJ, 634, 1093

Gebhardt, K. et al. 2007, ApJ, 671, 1321

Gebhardt, K. & Thomas, J. 2009, ApJ, 700, 1690

Gebhardt, K., Adams, J., Richstone, D., Lauer, T. R., Faber, S. M., Gültekin, K., Murphy, J., & Tremaine, S. 2011, ApJ, 729, 119

Geha, M., Guhathakurta, P., & van der Marel, R. P. 2002, AJ, 124, 3073

Genzel, R. & Townes, C. H. 1987, ARA&A, 25, 377

Genzel, R., Hollenbach, D., & Townes, C. H. 1994, Reports on Progress in Physics, 57, 417

Genzel, R. 1996, in IAU Symposium 174, Dynamical Evolution of Star Clusters: Confrontation of Theory and Observations, ed. P. Hut & J. Makino (Dordrecht: Kluwer), 81

Genzel, R., Eckart, A., Ott, T., & Eisenhauer, F. 1997, MNRAS, 291, 219

Genzel, R., Pichon, C., Eckart, A., Gerhard, O. E., & Ott, T. 2000, MNRAS, 317, 348

Genzel, R., Eisenhauer, F., & Gillessen, S. 2010, Reviews of Modern Physics, 82, 3121

Ghez, A. M., Klein, B. L., Morris, M., & Becklin, E. E. 1998, ApJ, 509, 678

Ghez, A. M., Morris, M., Becklin, E. E., Tanner, A., & Kremenek, T. 2000, Nature, 407, 349

Ghez, A. M. et al. 2003, ApJ, 586, L127

Ghez, A. M., Salim, S., Hornstein, S. D., Tanner, A., Lu, J. R., Morris, M., Becklin, E. E., & Duchêne, G. 2005, ApJ, 620, 744

Ghez, A. M. et al. 2008, ApJ, 689, 1044

Gillessen, S., Eisenhauer, F., Trippe, S., Alexander, T., Genzel, R., Martins, F., & Ott, T. 2009, ApJ, 692, 1075

Gnerucci, A., Marconi, A., Capetti, A., Axon, D. J., & Robinson, A. 2010, A&A, 511, A19

Gnerucci, A., Marconi, A., Capetti, A., Axon, D. J., Robinson, A., & Neumayer, N. 2011, A&A, 536, A86

González Delgado, R. M., Pérez, E., Cid Fernandes, R., & Schmitt, H. 2008, AJ, 135, 747

Gordon, K. D., Hanson, M. M., Clayton, G. C., Rieke, G. H., & Misselt, K. A. 1999, ApJ, 519, 165

Graham, A. W., Trujillo, I., & Caon, N. 2001, AJ, 122, 1707

Graham, A. W., Erwin, P., Caon, N., & Trujillo, I. 2003, in RevMexAA Conf. Ser. 17, Galaxy Evolution: Theory & Observations, ed. V. Avila-Reese, C. Firmani, C. S. Frenk, & C. Allen (Cozumel: Universidad Nacional Autònoma de México), 196

Graham, A. W. & Driver, S. P. 2007, ApJ, 655, 77

Graham, A. W. 2008, ApJ, 680, 143

Graham, A. W. & Li, I. 2009, ApJ, 698, 812

Graham, A. W. & Spitler, L. R. 2009, MNRAS, 397, 2148

Graham, A. W., Onken, C. A., Athanassoula, E., & Combes, F. 2011, MNRAS, 412, 2211

Graham, A. W., 2012, MNRAS, 422, 1586

Greene, J. E., Ho, L. C., & Barth, A. J. 2008, ApJ, 688, 159

Grier, C. J. et al. 2012, ApJ, 755, 60

Gu, Q., Melnick, J., Cid Fernandes, R., Kunth, D., Terlevich, E., & Terlevich, R. 2006, MNRAS, 366, 480

Gültekin, K. et al. 2009, ApJ, 698, 198

Haiman, Z. 2013, in Ap&SS Library 396, The First Galaxies, ed. T. Wiklind, B. Mobasher, & V. Bromm (Berlin: Springer-Verlag), 293

Halliday, C., Davies, R. L., Kuntschner, H., Birkinshaw, M., Bender, R., Saglia, R. P., & Baggley, G. 2001, MNRAS, 326, 473

Häring, N. & Rix, H. 2004, ApJ, 604, L89

Harms, R. J. et al. 1994, ApJ, 435, L35

Harris, W. E. 1996, AJ, 112, 1487

Hartmann, M., Debattista, V. P., Seth, A., Cappellari, M., & Quinn, T. R. 2011, MNRAS, 418, 2697

Hartmann, M., Debattista, V. P., Cole, D. R., Valluri, M., Widrow, L. M., & Shen, J. 2013, MNRAS, in press (arXiv: 1309.2634)

Héraudeau, P. & Simien, F. 1998, A&AS, 133, 317

Héraudeau, P., Simien, F., Maubon, G., & Prugniel, P. 1999, A&AS, 136, 509

Hernquist, L. 1990, ApJ, 356, 359

Herrnstein, J. R. 1999, BAAS, 31, 921

Heyer, I. et al. 2004, WFPC2 Instrument Handbook, v. 9.0 (Baltimore: STScI)

Ho, L. C. 2008, ARA&A, 46, 475

Ho, L. C., Filippenko, A. V., & Sargent, W. L. W. 1997, ApJS, 112, 315

Ho, L. C., Sarzi, M., Rix, H., Shields, J. C., Rudnick, G., Filippenko, A. V., & Barth, A. J. 2002, PASP, 114, 137

Holley-Bockelmann, K. & Richstone, D. O. 2000, ApJ, 531, 232

Holtzman, J. A., Burrows, C. J., Casertano, S., Hester, J. J., Trauger, J. T., Watson, A. M., & Worthey, G. 1995, PASP, 107, 1065

Hopkins, P. F., Hernquist, L., Cox, T. J., Di Matteo, T., Robertson, B., & Springel, V. 2006, ApJS, 163, 1

Hopkins, P. F., Hernquist, L., Cox, T. J., Robertson, B., & Krause, E. 2007a, ApJ, 669, 45

—. 2007b, ApJ, 669, 67

Hopkins, P. F., Murray, N., & Thompson, T. A. 2009, MNRAS, 398, 303

Houghton, R. C. W., Magorrian, J., Sarzi, M., Thatte, N., Davies, R. L., & Krajnović, D. 2006, MNRAS, 367, 2

Hu, J. 2008, MNRAS, 386, 2242

Jedrzejewski, R. I. 1987, MNRAS, 226, 747

Johnson, J. L., Whalen, D. J., Fryer, C. L., & Li, H. 2012, ApJ, 750, 66

Jones, D. H. et al. 1996, ApJ, 466, 742

Kazantzidis, S. et al. 2005, ApJ, 623, L67

Keel, W. C. 1988, ApJ, 329, 532

Kim Quijano, J. et al. 2007, STIS Instrument Handbook, v.8.0 (Baltimore: STScI)

King, I. 1962, AJ, 67, 471

Kinney, A. L., Calzetti, D., Bohlin, R. C., McQuade, K., Storchi-Bergmann, T., & Schmitt, H. R. 1996, ApJ, 467, 38

Koleva, M., de Rijcke, S., Prugniel, P., Zeilinger, W. W., & Michielsen, D. 2009, MNRAS, 396, 2133

Komossa, S. & Böhringer, H. 1999, A&A, 344, 755

Kormendy, J. & Illingworth, G. 1982, ApJ, 256, 460

Kormendy, J. & Richstone, D. 1992, ApJ, 393, 559

Kormendy, J. & McClure, R. D. 1993, AJ, 105, 1793

Kormendy, J., Dressler, A., Byun, Y. I., Faber, S. M., Grillmair, C., Lauer, T. R., Richstone, D., & Tremaine, S. 1994, in ESO Conf. 49, Dwarf Galaxies, ed. G. Meylan & P. Prugniel (Garching: ESO), 147

Kormendy, J. & Richstone, D. 1995, ARA&A, 33, 581

Kormendy, J. & Bender, R. 1996, ApJ, 464, L119

Kormendy, J. et al. 1996a, ApJ, 473, L91

Kormendy, J. et al. 1996b, ApJ, 459, L57

Kormendy, J. & Bender, R. 1999, ApJ, 522, 772

Kormendy, J. 2001, in ASP Conf. Ser. 230: Galaxy Disks and Disk Galaxies, ed. J. G. Funes & E. M. Corsini (San Francisco: ASP), 247

Kormendy, J. & Gebhardt, K. 2001, in AIP Conf. Proc. 586, Relativistic Astrophysics, ed. J. C. Wheeler & H. Martel (New York: American Institute of Physics), 363

Kormendy, J. 2004, in Carnegie Observatories Astrophysics Ser., Coevolution of Black Holes and Galaxies, ed. L. C. Ho (Cambridge: Cambridge University Press), 1

Kormendy, J. & Kennicutt, Jr., R. C. 2004, ARA&A, 42, 603

Kormendy, J., Gebhardt, K., Fisher, D. B., Drory, N., Macchetto, F. D., & Sparks, W. B. 2005, AJ, 129, 2636

Kormendy, J. & Bender, R. 2011, Nature, 469, 377

Kormendy, J. & Ho, L. C. 2013a, ARA&A, 51, 511

—. 2013b, ARA&A, in press (arXiv: 1308.6483)

Kornei, K. A. & McCrady, N. 2009, ApJ, 697, 1180

Krajnović, D. & Jaffe, W. 2004, A&A, 428, 877

Krajnović, D., McDermid, R. M., Cappellari, M., & Davies, R. L. 2009, MNRAS, 1306

Krist, J. & Hook, R. 1999, Tiny Tim User's Guide (Baltimore: STScI)

Kuntschner, H. et al. 2010, MNRAS, 408, 97

Lara, L., Cotton, W. D., Feretti, L., Giovannini, G., Venturi, T., & Marcaide, J. M. 1997, ApJ, 474, 179

Larsen, S. S. 2001, AJ, 122, 1782

Larsen, S. S., Brodie, J. P., & Hunter, D. A. 2004, AJ, 128, 2295

Lauer, T. R. et al. 1993, AJ, 106, 1436

Lauer, T. R. et al. 1995, AJ, 110, 2622

Lauer, T. R. et al. 1996, ApJ, 471, L79

Lauer, T. R., Faber, S. M., Ajhar, E. A., Grillmair, C. J., & Scowen, P. A. 1998, AJ, 116, 2263

Lauer, T. R. et al. 2002, AJ, 124, 1975

Lauer, T. R. et al. 2005, AJ, 129, 2138

Lauer, T. R., Tremaine, S., Richstone, D., & Faber, S. M. 2007, ApJ, 670, 249

Launhardt, R., Zylka, R., & Mezger, P. G. 2002, A&A, 384, 112

Layden, A. C. & Sarajedini, A. 2000, AJ, 119, 1760

Ledo, H. R., Sarzi, M., Dotti, M., Khochfar, S., & Morelli, L. 2010, MNRAS, 407, 969

Leigh, N., Böker, T., & Knigge, C. 2012, MNRAS, 424, 2130

Li, Y., Haiman, Z., & Mac Low, M.-M. 2007, ApJ, 663, 61

Lodato, G. & Natarajan, P. 2006, MNRAS, 371, 1813

Long, K. S., Charles, P. A., & Dubus, G. 2002, ApJ, 569, 204

Lotz, J. M., Telford, R., Ferguson, H. C., Miller, B. W., Stiavelli, M., & Mack, J. 2001, ApJ, 552, 572

Lotz, J. M., Miller, B. W., & Ferguson, H. C. 2004, ApJ, 613, 262

Lynden-Bell, D. 1969, Nature, 223, 690

Lyubenova, M. et al. 2013, MNRAS, 431, 3364

Maciejewski, W. & Binney, J. 2001, MNRAS, 323, 831

Maciejewski, W., Teuben, P. J., Sparke, L. S., & Stone, J. M. 2002, MNRAS, 329, 502

Maciejewski, W. 2004, in ASS Library 315, How Does the Galaxy Work?, ed. E. J. Alfaro, E. Pérez, & J. Franco (Dordrecht: Kluwer), 265

Mackey, A. D. & Gilmore, G. F. 2003, MNRAS, 340, 175

Madau, P. & Rees, M. J. 2001, ApJ, 551, L27

Magorrian, J. 1999, MNRAS, 302, 530

Magorrian, J. et al. 1998, AJ, 115, 2285

Maoz, D., Filippenko, A. V., Ho, L. C., Rix, H., Bahcall, J. N., Schneider, D. P., & Macchetto, F. D. 1995, ApJ, 440, 91

Maoz, E. 1998, ApJ, 494, L181

Maraston, C. 1998, MNRAS, 300, 872

—. 2005, MNRAS, 362, 799

Marconi, A. & Hunt, L. K. 2003, ApJ, 589, L21

Marconi, A., Pastorini, G., Pacini, F., Axon, D. J., Capetti, A., Macchetto, D., Koekemoer, A. M., & Schreier, E. J. 2006, A&A, 448, 921

Markwardt, C. B. 2009, in ASP Conf. Ser. 411, Astronomical Data Analysis Software and Systems 18, ed. D. A. Bohlender, D. Durand, & P. Dowler (San Francisco: ASP), 251

Martel, A. R. et al. 1999, ApJS, 122, 81

Marulli, F., Bonoli, S., Branchini, E., Moscardini, L., & Springel, V. 2008, MNRAS, 385, 1846

Masters, K. L., Springob, C. M., Haynes, M. P., & Giovanelli, R. 2006, ApJ, 653, 861

Mayer, L., Kazantzidis, S., Escala, A., & Callegari, S. 2010, Nature, 466, 1082

Mc Master, M. & Biretta, E. A. 2008, WFPC2 Instrument Handbook, v. 10.0 (Baltimore: STScI)

McConnell, N. J., Ma, C.-P., Gebhardt, K., Wright, S. A., Murphy, J. D., Lauer, T. R., Graham, J. R., & Richstone, D. O. 2011, Nature, 480, 215

McConnell, N. J., Chen, S.-F. S., Ma, C.-P., Greene, J. E., Lauer, T. R., & Gebhardt, K. 2013, ApJ, 768, L21

McDermid, R. M. et al. 2006, MNRAS, 373, 906

McLaughlin, D. E. 1999, AJ, 117, 2398

McLaughlin, D. E. & van der Marel, R. P. 2005, ApJS, 161, 304

McLaughlin, D. E., King, A. R., & Nayakshin, S. 2006, ApJ, 650, L37

McLure, R. J. & Dunlop, J. S. 2002, MNRAS, 331, 795

Méndez-Abreu, J., Aguerri, J. A. L., Corsini, E. M., & Simonneau, E. 2008, A&A, 478, 353

Merritt, D. 2009, ApJ, 694, 959

Meylan, G., Sarajedini, A., Jablonka, P., Djorgovski, S. G., Bridges, T., & Rich, R. M. 2001, AJ, 122, 830

Mihos, J. C. & Hernquist, L. 1994, ApJ, 437, L47

Miller, J. M., Fabian, A. C., & Miller, M. C. 2004, ApJ, 607, 931

Milosavljević, M. 2004, ApJ, 605, L13

Miocchi, P., Capuzzo Dolcetta, R., Di Matteo, P., & Vicari, A. 2006, ApJ, 644, 940

Miralda-Escudé, J. & Kollmeier, J. A. 2005, ApJ, 619, 30

Miyoshi, M., Moran, J., Herrnstein, J., Greenhill, L., Nakai, N., Diamond, P., & Inoue, M. 1995, Nature, 373, 127

Moffat, A. F. J. 1969, A&A, 3, 455

Monnet, G., Bacon, R., & Emsellem, E. 1992, A&A, 253, 366

Monaco, P., Salucci, P., & Danese, L. 2000, MNRAS, 311, 279

Monaco, L., Bellazzini, M., Ferraro, F. R., & Pancino, E. 2005, MNRAS, 356, 1396

Morelli, L. et al. 2004, MNRAS, 354, 753

Morelli, L., Cesetti, M., Corsini, E. M., Pizzella, A., Dalla Bontà, E., Sarzi, M., & Bertola, F. 2010, A&A, 518, A32

Murray, N. & Chiang, J. 1997, ApJ, 474, 91

Nayakshin, S., Wilkinson, M. I., & King, A. 2009, MNRAS, 398, L54

Nayakshin, S. & Power, C. 2010, MNRAS, 402, 789

Nelder, J. A. & Mead, R. 1965, Computer Journal, 7, 308

Nelson, C. H. & Whittle, M. 1995, ApJS, 99, 67

Neufeld, D. A. & Melnick, G. J. 1991, ApJ, 368, 215

Neumayer, N., Cappellari, M., Reunanen, J., Rix, H., van der Werf, P. P., de Zeeuw, P. T., & Davies, R. I. 2007, ApJ, 671, 1329

Neumayer, N., Walcher, C. J., Andersen, D., Sánchez, S. F., Böker, T., & Rix, H.-W. 2011, MNRAS, 413, 1875

Noel-Storr, J., Baum, S. A., & O'Dea, C. P. 2007, ApJ, 663, 71

Noel-Storr, J., Baum, S. A., Verdoes Kleijn, G., van der Marel, R. P., O'Dea, C. P., de Zeeuw, P. T., & Carollo, C. M. 2003, ApJS, 148, 419

Noordermeer, E. et al. 2008, MNRAS, 384, 943

Nowak, N., Saglia, R. P., Thomas, J., Bender, R., Pannella, M., Gebhardt, K., & Davies, R. I. 2007, MNRAS, 379, 909

Nowak, N., Saglia, R. P., Thomas, J., Bender, R., Davies, R. I., & Gebhardt, K. 2008, MNRAS, 391, 1629

Nowak, N., Thomas, J., Erwin, P., Saglia, R. P., Bender, R., & Davies, R. I. 2009, MNRAS, 403, 646

Oke, J. B. 1974, ApJS, 27, 21

O'Leary, R. M., Rasio, F. A., Fregeau, J. M., Ivanova, N., & O'Shaughnessy, R. 2006, ApJ, 637, 937

Osterbrock, D. E. 1989, Astrophysics of Gaseous Nebulae and Active Galactic Nuclei (Sausalito: University Science Books)

Owen, F. N., O'Dea, C. P., & Keel, W. C. 1990, ApJ, 352, 44

Özel, F., Psaltis, D., Narayan, R., & McClintock, J. E. 2010, ApJ, 725, 1918

Pastorini, G. et al. 2007, A&A, 469, 405

Paudel, S., Lisker, T., & Janz, J. 2010, ApJ, 724, L64

Pavlovsky, C. et al. 2004, ACS Instrument Handbook, v. 5.0 (Baltimore: STScI)

—. 2006, ACS Data Handbook, v. 5.0 (Baltimore: STScI)

Peng, C. Y., Ho, L. C., Impey, C. D., & Rix, H.-W. 2002, AJ, 124, 266

Peterson, B. M. 2004, in IAU Symposium 222, The Interplay Among Black Holes, Stars and ISM in Galactic Nuclei, ed. T. Storchi-Bergmann, L. C. Ho, & H. R. Schmitt (Cambridge: Cambridge University Press), 15

Peterson, B. M. et al. 2005, ApJ, 632, 799

Peterson, B. M. & Bentz, M. C. 2006, New Astronomy Review, 50, 796

Pizzella, A., Corsini, E. M., Morelli, L., Sarzi, M., Scarlata, C., Stiavelli, M., & Bertola, F. 2002, ApJ, 573, 131

Pizzella, A., Corsini, E. M., Dalla Bontà, E., Sarzi, M., Coccato, L., & Bertola, F. 2005, ApJ, 631, 785

Portaluri, E., Corsini, E. M., Morelli, L., Hartmann, M., Dalla Bontà, E., Debattista, V. P., & Pizzella, A. 2013, MNRAS, 433, 434

Portegies Zwart, S. F., Dewi, J., & Maccarone, T. 2004, MNRAS, 355, 413

Pota, V., Graham, A. W., Forbes, D. A., Romanowsky, A. J., Brodie, J. P., & Strader, J. 2013, MNRAS, 433, 235

Press, W. H., Teukolsky, S. A., Vetterling, W. T., & Flannery, B. P. 1992, Numerical Recipes in FORTRAN. The Art of Scientific Computing (2nd ed.; Cambridge: Cambridge University Press)

Quinlan, G. D. & Shapiro, S. L. 1987, ApJ, 321, 199

—. 1989, ApJ, 343, 725

—. 1990, ApJ, 356, 483

Rasio, F. A., Freitag, M., & Gürkan, M. A. 2004, in Carnegie Observatories Centennial Symposia, Coevolution of Black Holes and Galaxies, ed. L. C. Ho (Cambridge: Cambridge University Press), 138

Ravindranath, S., Ho, L. C., Peng, C. Y., Filippenko, A. V., & Sargent, W. L. W. 2001, AJ, 122, 653

Reader, J. & Corliss, C. H. 1998, Handbook of Chemistry and Physics (Boca Raton: CRC)

Rees, M. J. 1978, The Observatory, 98, 210

—. 1984, ARA&A, 22, 471

Reines, A. E., Sivakoff, G. R., Johnson, K. E., & Brogan, C. L. 2011, Nature, 470, 66

Rest, A., van den Bosch, F. C., Jaffe, W., Tran, H., Tsvetanov, Z., Ford, H. C., Davies, J., & Schafer, J. 2001, AJ, 121, 2431

Rix, H.-W. & White, S. D. M. 1990, ApJ, 362, 52

Rossa, J., van der Marel, R. P., Böker, T., Gerssen, J., Ho, L. C., Rix, H.-W., Shields, J. C., & Walcher, C.-J. 2006, AJ, 132, 1074

Rusli, S. P. et al. 2013, AJ, 146, 45

Sakai, S., Giovanelli, R., & Wegner, G. 1994, AJ, 108, 33

Salpeter, E. E. 1955, ApJ, 121, 161

Sancisi, R., van Woerden, H., Davies, R. D., & Hart, L. 1984, MNRAS, 210, 497

Sandage, A. & Tammann, G. A. 1981, Revised Shapley-Ames Catalog of Bright Galaxies (Washington: Carnegie Institute of Washington)

Sandage, A. & Bedke, J. 1994, The Carnegie Atlas of Galaxies, (Washington: Carnegie Institute of Washington)

Santoro, F. & Shull, J. M. 2006, ApJ, 643, 26

Sarzi, M., Rix, H., Shields, J. C., Rudnick, G., Ho, L. C., McIntosh, D. H., Filippenko, A. V., & Sargent, W. L. W. 2001, ApJ, 550, 65

Sarzi, M., Rix, H., Shields, J. C., Ho, L. C., Barth, A. J., Rudnick, G., Filippenko, A. V., & Sargent, W. L. W. 2005, ApJ, 628, 169

Sarzi, M. et al. 2006, MNRAS, 366, 1151

Scarlata, C. et al. 2004, AJ, 128, 1124

Schinnerer, E., Böker, T., & Meier, D. S. 2003, ApJ, 591, L115

Schinnerer, E., Böker, T., Meier, D. S., & Calzetti, D. 2008, ApJ, 684, L21

Schlegel, D. J., Finkbeiner, D. P., & Davis, M. 1998, ApJ, 500, 525

Schödel, R. et al. 2002, Nature, 419, 694

Schödel, R., Ott, T., Genzel, R., Eckart, A., Mouawad, N., & Alexander, T. 2003, ApJ, 596, 1015

Schödel, R. et al. 2007, A&A, 469, 125

Schulze, A. & Wisotzki, L. 2011, A&A, 535, A87

Schwarzschild, M. 1979, ApJ, 232, 236

Scorza, C. & Bender, R. 1995, A&A, 293, 20

Scorza, C. & van den Bosch, F. C. 1998, MNRAS, 300, 469

Scott, N. & Graham, A. W. 2013, ApJ, 763, 76

Scott, N., Graham, A. W., & Schombert, J. 2013, ApJ, 768, 76

Seifert, W. & Scorza, C. 1996, A&A, 310, 75

Sellwood, J. A. 2008, ApJ, 679, 379

Sellwood, J. A. & Debattista, V. P. 2009, MNRAS, 398, 1279

Sérsic, J. L. 1968, Atlas de Galaxias Australes (Cordoba: Observatorio Astronomico)

Seth, A. C., Dalcanton, J. J., & de Jong, R. S. 2005, AJ, 129, 1331

Seth, A. C., Dalcanton, J. J., Hodge, P. W., & Debattista, V. P. 2006, AJ, 132, 2539

Seth, A. C., Agüeros, M., Lee, D., & Basu-Zych, A. 2008a, ApJ, 678, 116

Seth, A. C., Blum, R. D., Bastian, N., Caldwell, N., & Debattista, V. P. 2008b, ApJ, 687, 997

Seth, A. C. et al. 2010, ApJ, 714, 713

Shankar, F., Salucci, P., Granato, G. L., De Zotti, G., & Danese, L. 2004, MNRAS, 354, 1020

Shapiro, S. L. 2004, in Carnegie Observatories Centennial Symposia, Coevolution of Black Holes and Galaxies, ed. L. C. Ho (Cambridge: Cambridge University Press), 103

Shapiro, K. L., Cappellari, M., de Zeeuw, T., McDermid, R. M., Gebhardt, K., van den Bosch, R. C. E., & Statler, T. S. 2006, MNRAS, 370, 559

Shen, Z.-Q., Lo, K. Y., Ho, P. T. P., & Zhao, J. 2005, in ASP Conf. Ser 340, Future Directions in High Resolution Astronomy, ed. J. Romney & M. Reid (San Francisco: ASP), 263

Shen, J. & Gebhardt, K. 2010, ApJ, 711, 484

Shields, G. A., Gebhardt, K., Salviander, S., Wills, B. J., Xie, B., Brotherton, M. S., Yuan, J., & Dietrich, M. 2003, ApJ, 583, 124

Shields, J. C., Walcher, C. J., Böker, T., Ho, L. C., Rix, H., & van der Marel, R. P. 2008, ApJ, 682, 104

Shlosman, I. & Begelman, M. C. 1989, ApJ, 341, 685

Sil'chenko, O. K. 1997, Astronomy Reports, 41, 567

—. 1999, AJ, 117, 2725

Silge, J. D. & Gebhardt, K. 2003, AJ, 125, 2809

Silge, J. D., Gebhardt, K., Bergmann, M., & Richstone, D. 2005, AJ, 130, 406

Silk, J., Wyse, R. F. G., & Shields, G. A. 1987, ApJ, 322, L59

Simien, F. & Prugniel, P. 1997, A&AS, 122, 521

—. 1998, A&AS, 131, 287

Siopis, C. et al. 2009, ApJ, 693, 946

Soltan, A. 1982, MNRAS, 200, 115

Stadel, J. G. 2001, PhD thesis, University of Washington

Steinmetz, M. & Navarro, J. F. 2002, New Astronomy, 7, 155

Stephens, A. W. & Frogel, J. A. 2002, AJ, 124, 2023

Stiavelli, M., Miller, B. W., Ferguson, H. C., Mack, J., Whitmore, B. C., & Lotz, J. M. 2001, AJ, 121, 1385

Tegmark, M., Silk, J., Rees, M. J., Blanchard, A., Abel, T., & Palla, F. 1997, ApJ, 474, 1

Terlevich, E., Diaz, A. I., & Terlevich, R. 1990, MNRAS, 242, 271

Thim, F., Hoessel, J. G., Saha, A., Claver, J., Dolphin, A., & Tammann, G. A. 2004, AJ, 127, 2322

Thomas, D., Maraston, C., & Bender, R. 2003, MNRAS, 339, 897

Tonry, J. L., Blakeslee, J. P., Ajhar, E. A., & Dressler, A. 2000, ApJ, 530, 625

Tonry, J. L., Dressler, A., Blakeslee, J. P., Ajhar, E. A., Fletcher, A. B., Luppino, G. A., Metzger, M. R., & Moore, C. B. 2001, ApJ, 546, 681

Tran, H. D., Tsvetanov, Z., Ford, H. C., Davies, J., Jaffe, W., van den Bosch, F. C., & Rest, A. 2001, AJ, 121, 2928

Tremaine, S. D., Ostriker, J. P., & Spitzer, Jr., L. 1975, ApJ, 196, 407

Tremaine, S. 1995, AJ, 110, 628

Tremaine, S. et al. 2002, ApJ, 574, 740

Trujillo, I., Erwin, P., Asensio Ramos, A., & Graham, A. W. 2004, AJ, 127, 1917

Tully, R. B. 1988, Nearby Galaxies Catalog (Cambridge: Cambridge University Press)

Turner, M. L., Côté, P., Ferrarese, L., Jordán, A., Blakeslee, J. P., Mei, S., Peng, E. W., & West, M. J. 2012, ApJS, 203, 5

Urry, C. M. & Padovani, P. 1995, PASP, 107, 803

Valluri, M., Merritt, D., & Emsellem, E. 2004, ApJ, 602, 66

van den Bosch, F. C. & de Zeeuw, P. T. 1996, MNRAS, 283, 381

van den Bosch, F. C. 1998, ApJ, 507, 601

van den Bosch, F. C. & Emsellem, E. 1998, MNRAS, 298, 267

van den Bosch, F. C., Jaffe, W., & van der Marel, R. P. 1998, MNRAS, 293, 343

van den Bosch, R. C. E., Gebhardt, K., Gültekin, K., van de Ven, G., van der Wel, A., & Walsh, J. L. 2012, Nature, 491, 729

van der Kruit, P. C. & Searle, L. 1981, A&A, 95, 105

van der Marel, R. P. & van den Bosch, F. C. 1998, AJ, 116, 2220

van der Marel, R. P. 2004, in Carnegie Observatories Centennial Symposia, Coevolution of Black Holes and Galaxies, ed. L. C. Ho (Cambridge: Cambridge University Press), 37

van der Marel, R. P., Rossa, J., Walcher, C. J., Boeker, T., Ho, L. C., Rix, H.-W., & Shields, J. C. 2007, in IAU Symposium 241, Stellar Populations as Building Blocks of Galaxies, ed. A. Vazdekis & R. Peletier (Cambridge: Cambridge University Press), 475

van der Marel, R. P. & Anderson, J. 2010, ApJ, 710, 1063

van Dokkum, P. G. 2001, PASP, 113, 1420

Vazdekis, A. 1999, ApJ, 513, 224

Vazdekis, A., Sánchez-Blázquez, P., Falcón-Barroso, J., Cenarro, A. J., Beasley, M. A., Cardiel, N., Gorgas, J., & Peletier, R. F. 2010, MNRAS, 404, 1639

Verdoes Kleijn, G. A., Baum, S. A., de Zeeuw, P. T., & O'Dea, C. P. 1999, AJ, 118, 2592

Verdoes Kleijn, G. A., van der Marel, R. P., Carollo, C. M., & de Zeeuw, P. T. 2000, AJ, 120, 1221

Verdoes Kleijn, G. A., van der Marel, R. P., & Noel-Storr, J. 2006a, AJ, 131, 1961

—. 2006b, AJ, 131, 1961

Vesperini, E. & Trenti, M. 2010, ApJ, 720, L179

Volonteri, M. & Natarajan, P. 2009, MNRAS, 400, 1911

Volonteri, M. & Begelman, M. C. 2010, MNRAS, 409, 1022

Wagner, S. J. & Appenzeller, I. 1988, A&A, 197, 75

Walcher, C. J., van der Marel, R. P., McLaughlin, D., Rix, H.-W., Böker, T., Häring, N., Ho, L. C., Sarzi, M., & Shields, J. C. 2005, ApJ, 635, 741

Walcher, C. J., Böker, T., Charlot, S., Ho, L. C., Rix, H.-W., Rossa, J., Shields, J. C., & van der Marel, R. P. 2006, ApJ, 649, 692

Wallerstein, G., Gilroy, K. K., Zethson, T., Johansson, S., & Hamann, F. 2001, PASP, 113, 1210

Weedman, D. W. 1983, ApJ, 266, 479

Wehner, E. H. & Harris, W. E. 2006, ApJ, 644, L17

Whitmore, B. C. & Kirshner, R. P. 1981, ApJ, 250, 43

Willott, C. J., McLure, R. J., & Jarvis, M. J. 2003, ApJ, 587, L15

Worthey, G. 1994, ApJS, 95, 107

Wyse, R. F. G., Gilmore, G., & Franx, M. 1997, ARA&A, 35, 637

Yoshida, N., Omukai, K., Hernquist, L., & Abel, T. 2006, ApJ, 652, 6

Younger, J. D., Hopkins, P. F., Cox, T. J., & Hernquist, L. 2008, ApJ, 686, 815

Zacharias, N., Monet, D. G., Levine, S. E., Urban, S. E., Gaume, R., & Wycoff, G. L. 2005, NOMAD Catalog (Strasbourg: CDS)

Zheng, X. Z. et al. 2009, ApJ, 707, 1566